Digitized Theses   Digitized Special Collections

1989

Motion-induced Wind Forces On Chimneys And Tall Buildings

Andrew Steckley

Recommended Citation

Steckley, Andrew, "Motion-induced Wind Forces On Chimneys And Tall Buildings" (1989). *Digitized Theses*. 1853.
https://ir.lib.uwo.ca/digitizedtheses/1853

NOTICE

AVIS

The quality of this microform is heavily dependent upon the quality of the original thesis submitted for microfilming. Every effort has been made to ensure the highest quality of reproduction possible.

If pages are missing, contact the university which granted the degree.

Some pages may have indistinct print especially if the original pages were typed with a poor typewriter ribbon or if the university sent us an inferior photocopy.

Reproduction in full or in part of this microform is governed by the Canadian Copyright Act, R.S.C. 1970, c. C-30, and subsequent amendments.

La qualité de cette microforme dépend grandement de la qualité de la thèse soumise au microfilmage. Nous avons tout fait pour assurer une qualité supérieure de reproduction.

S'il manque des pages, veuillez communiquer avec l'université qui a conféré le grade.

La qualité d'impression de certaines pages peut laisser à désirer, surtout si les pages originales ont été dactylographiées à l'aide d'un ruban usé ou si l'université nous a fait parvenir une photocopie de qualité inférieure.

La reproduction, même partielle, de cette microfo.me est soumise à la Loi canadienne sur le droit d'auteur, SRC 1970, c. C-30, et ses amendements subséquents.

Canada

Motion-Induced Wind Forces
on
Chimneys and Tall Buildings

by
Andrew Steckley

Faculty of Engineering Science

Submitted in partial fulfillment
of the requirements for the degree of
Doctor of Philosophy

Faculty of Graduate Studies
The University of Western Ontario
London, Ontario
June 1989

Canadä

ABSTRACT

This thesis describes the development of a Pivot Mode Activator System (PMA) for the measurement of motion-induced forces on wind tunnel models of tall structures. The impetus for this was the desire to refine the established base balance wind tunnel technique of predicting wind loads. The system developed forces a sinusoidal oscillation of the test model in a pivoting mode about its base at controlled amplitude and frequency. The wind forces acting on the model are measured, and the motion-induced forces are extracted by correlating the total force with the motion. In this way, both the in-phase and out-of-phase components of the motion-induced forces are distinguished. These quantities are denoted by a complex aerodynamic impedance whose real and imaginary parts correspond to aerodynamic stiffness and damping parameters.

As a demonstration of the use of the system, two substantial experimental studies have been carried out. The first is a comprehensive study of a square prism. This study provides extensive data on the aerodynamic impedance for tip oscillation amplitudes less than about 15% of the model width. The effects of varying the turbulence intensity of the wind and the aspect ratio of the model are also investigated. To complement these results, additional experiments have been carried out for the same model shape. These include forced oscillation experiments on a pressure model which provide information about the spatial and spectral distribution of the forces, as well as free oscillation experiments on several aeroelastic model structures. Rms response predictions based on base balance data, augmented with the measured data on motion-induced forces, are found to agree very well with the corresponding results from an aeroelastic model test.

The second experimental study involved base balance experiments and PMA experiments on various cross-sectional shapes. This study provides a large data set,

which along with some judicious interpolation, is expected to be of valuable use to designers of tall chimneys.

The Pivot Mode Activator System has surpassed the initial design expectations. The aerodynamic impedance for a model can be measured with a high degree of resolution. It is hoped that the system will provide a means for expediting fundamental research into motion-induced force models as well as contributing to practical wind tunnel studies.

ACKNOWLEDGEMENTS

preparation of the figures. I am grateful to the office staff just for putting up with me.

I cannot forget to thank Tim Horton, without whose coffee this work would not have been completed.

Finally, I would like to thank Peg for her patience and her support during the last months.

"Peace of mind isn't at all superficial to technical work. It's the whole thing. That which produces it is good work and that which destroys it is bad work."

Robert Pirsig

Zen and the Art of Motorcycle Maintenance

"What objectivity and the study of philosophy require is not an 'open mind,' but an *active mind*—a mind able and eagerly willing to examine ideas, but to examine them *critically.*"

Ayn Rand

Philosophy: Who Needs It

Contents

CONTENTS

CONTENTS

CONTENTS

List of Figures

LIST OF FIGURES

LIST OF FIGURES

List of Tables

Nomenclature

Following is a list of some of the variables used in this thesis which is intended to assist the reader. Not all variables are included. Variables associated with specific models from previous sources and described in Chapter 3, for example, are not included nor are variables which are clearly defined or redefined in the text for local use. Various subscripted variables such as spectral quantities are not individually specified. First reference should be made to the text where first used.

a	power law profile exponent
$a(t)$	amplitude function
A_B	background contribution
A_R	resonant contribution
B	characteristic length, (width of structure)
$C_a[z]$	per unit height damping coefficient at z
C_D	drag coefficient
C_l	coefficient of random component of generalised force
C_m	coefficient of motion correlated generalised force
C_M	moment coefficient
C_X	coefficient of X direction moment
C_Y	coefficient of Y direction moment
E	Young's modulus
f	frequency
$\hat{f}$	frequency at which maximum in spectrum occurs
f_b	balancing frequency
f_r	response frequency
f_s	frequency of structure (in still air)

NOMENCLATURE

f_v	vortex shedding frequency
f_D	drag force per unit height
$F(t)$	generalised force as a function of time
$F_A(t)$	aerodynamic force
F_D	generalised force in the drag direction
F_L	generalised force in lift direction
$F_l(t)$	random component of generalised force as a function of time
$F_m(t)$	motion correlated generalised force as a function of time
F_y	across wind force
g	peak factor
G_a	dimensionless complex aerodynamic impedance
	$= \alpha + i\beta$
G_a^*	modified dimensionless aerodynamic impedance
	$= \alpha^* + i\beta^*$
H	height of structure
h_i	height of level i
$H_a(f)$ or $H_a(\omega)$	aeroelastic admittance function (of frequency)
$H(f)$ or $H(\omega)$	mechanical admittance function (of frequency)
I_M	mass moment of inertia of the model
I_m	mass moment of inertia of the calibration mass model
$i(z)$	influence function as a function of vertical location
K_a	complex aerodynamic impedance with dimensions $[\frac{force}{length}]$
$k_a(t)$	impulse response function, resisting moment due to deflection
K_s	generalised stiffness of structure
L_m	scale of turbulence, $\frac{\lambda_m}{2\pi}$ where
	λ_m is the wavelength at which $fS(f)$ is maximum
M_s	generalised mass of structure
p	velocity pressure of mean flow

NOMENCLATURE

	$= \frac{1}{2}\rho_a V^2$
q	modal force
r	a general response quantity
R_{ii}	auto-correlation function of quantity i
R_{ij}	cross-correlation function between quantities i and j
S_{ii} or S_i	auto-spectral density of quantity i
S_{ij}	cross-spectral density of quantities i and j
T_{ij}	transfer function between quantities i and j
t	time
V	mean flow velocity
V_c	critical velocity of vortex shedding
V_g	gradient velocity
V_o	onset velocity for galloping behavior
V_r	reduced velocity
	$= V/fB$
V_A	voltage signal A
V_W	voltage signal W
$W(t)$	wind-induced moment as a function of time
$w(z)$	wind force per unit height
$W_i(t)$	random component of wind moment as a function of time
$W_m(t)$	motion correlated wind moment as a function of time
x	along wind displacement
Y	dimensionless tip deflection
	$= y/B$
y	response, (when specific: tip deflection)
$\tilde{y}$	rms response
$\bar{y}^2$	variance of response
$\hat{y}$	expected maximum (peak) response

NOMENCLATURE

$\breve{y}$		expected minimum response
z_g		gradient height
z		vertical location
α		real part of aerodynamic impedance
		(aerodynamic stiffness parameter)
α_{QS}		quasi-steady estimate of aerodynamic stiffness parameter
α^*		real part of modified aerodynamic impedance
β	Chapter 2:	a mode shape descriptor value
	elsewhere:	imaginary part of aerodynamic impedance
		(aerodynamic damping parameter)
β_{QS}		quasi-steady estimate of aerodynamic damping parameter
β^*		imaginary part of modified aerodynamic impedance
λ_L		length scale factor
λ_M		mass scale factor
λ_T		time scale factor
λ_ρ		density scale factor
$\mu(z)$		mode shape as a function of vertical location
η		dimensionless mass parameter
		$= \rho_a / \rho_s$
$\phi(t)$		phase function
ρ_a		density of air
ρ_s		structural density
τ		time lag
θ		wind angle of attack (azimuthal angle)
Θ		phase of the complex aerodynamic impedance
ω		circular frequency
		$= 2\pi f$
ω_r		circular response frequency

NOMENCLATURE

	$= 2\pi f_r$
ω_s	natural circular frequency of structure in still air
	$= 2\pi f_s$
ω_v	vortex shedding frequency
	$= 2\pi f_v$
ζ_a	"aerodynamic damping" as a fraction of critical
ζ_s	structural damping as a fraction of critical
S	Strouhal number or Strouhal frequency

Part I

BACKGROUND

Chapter 1
Scope of the Study

1.1 Introduction

This thesis describes the design, development, and demonstration of a new wind tunnel experimental technique for the measurement of motion-induced forces and the prediction of their effects on tall slender structures.

The prediction of wind-induced loading and response of tall buildings, towers, chimneys, and other large structures is an important consideration for the structural design engineer. Although building codes offer important and helpful estimates of the wind loading, the analytical procedures on which they are based are not sufficiently developed for confident application to taller or more complex structures. Only the along-wind response procedures are well established. Despite significant advances in computational fluid dynamics, the complexity of the flow fields associated with the action of the turbulent shear flow on these complex bluff bodies necessitates the use of experimental or modelling approaches. Even at the present explosive rate of growth in computer speed and memory capabilities, it will be some time before these problems will become tractable by computational analyses alone. When this does eventually occur, experimental modelling techniques will remain a vital, albeit less often required, tool for demonstrating various phenomena, validating theoretical and numerical models, and developing fundamental understandings of the underlying physical mechanisms.

In the meantime, modelling techniques are in many cases the only avail-

able means of estimating wind loads and their effects. It is often necessary to carry out experiments in a boundary layer wind tunnel in which the full scale structure and its wind environment are simulated. The response information of interest may include: displacements and accelerations, base bending moments and shears, or pressure distributions.

Modelling the wind environment requires, in general, matching the vertical variation of mean wind speeds, and the spectral characteristics, including intensities and scales expected to be seen in full scale. The boundary layer is usually considered to be locally stationary. Wind effects for particular cases of mean wind speed and direction are determined experimentally and then combined with statistical models of wind speed and direction for the particular geographic location.

With regard to modelling the structure itself, two techniques that have evolved in the modelling process are:

1. the use of an *aeroelastic model*

2. the dynamic *base balance technique*

Before describing these techniques further and comparing their advantages and disadvantages, some discussion of the flow-induced forces is in order.

Very broadly, the dynamic forces induced by the wind on a structure may be divided into three classes.

- Turbulence or buffeting: This is due to rapid changes in the wind velocity, that is, changes in the wind speed and in the angle of attack.

- Wake effects: These are due to the unsteady nature of the wake behind

a bluff body which occurs even in smooth flow. Vortex shedding is one example, which is often identified.

- Motion-induced forces: This refers to aerodynamic forces which are induced by the motion of the structure through the fluid.

The three classifications are by no means independent. For example, turbulence can influence both the wake effects and the motion-induced forces. The motion of the structure may also alter as well as supplement the wake forces acting on the structure. Nevertheless, conceptual division into the three classes is helpful in examining the two wind tunnel modelling techniques presently in use and, in addition, a third technique which forms the main thrust of this thesis.

1.2 Aeroelastic Modelling

Basically the aeroelastic modelling approach attempts to model the complete aeroelastic process. The model is designed to not only have the exterior geometry of the prototype structure, but also all of the relevant structural parameters such as mass and stiffness distributions, and effective damping. Consequently the model responds to the flow in the same way as the prototype would. In turn, any effects that the responding structure has on the flow are also modelled. The approach requires that certain modelling criteria are met so that there exists appropriate similarity in the dynamic behavior of the model and that of the full scale structure. Similarity implies that the relative magnitudes of all significant forces are the same in both model and full scale. For a discussion of similarity requirements in general and as applied to a wide range of problems in practical fluid dynamics, the reader is referred to Hertig[37]. Isyumov [40] has summarised the modelling criteria for wind

tunnel testing of tall structures. Specifically this requires that the following ratios are considered:

$$\text{mass:} \qquad \frac{\rho_s}{\rho_a} \qquad \frac{\textit{inertial forces of structure}}{\textit{inertial forces of flow}}$$

$$\text{stiffness:} \qquad \frac{E}{\rho_a V^2} \qquad \frac{\textit{elastic forces}}{\textit{inertial forces of flow}}$$

$$\text{damping:} \qquad \zeta_s \qquad \frac{\textit{dissipated energy per cycle}}{\textit{structural kinetic energy}}$$

The proper modelling of the flow environment in a wind tunnel is of course a prerequisite to the technique. High Reynolds number flow is assumed. In other words, the viscous forces of the fluid are considered negligible relative to the inertial forces of the same. This assumption must be given due consideration in cases which are sensitive to Reynolds number. For tall structures such as buildings, chimneys or towers, gravity forces contribute little to the restoring forces of the structure, and so Froude number scaling, which concerns the ratio of gravity forces to fluid inertial forces, is not considered. This is in contrast to the modelling of long span bridges or flexible roof structures, for example.

In most cases, the air density in model and full scale is the same, and so the first condition requires that the effective density of the structure also be the same at both scales, thus $\lambda_\rho = 1$. Once a length scale, λ_L, is chosen, then the mass scaling required is $\lambda_M = \lambda_L^3 \lambda_\rho$. Meeting the second condition subsequently dictates appropriate stiffness and time scales. Hence the velocity scale of the flow, $\lambda_V = \lambda_L / \lambda_T$ is also defined. The third condition combines the length, mass, and time scales so that the rate of energy dissipation is appropriately modelled. This similarity condition is implicitly met in requiring that the effective viscous damping as a fraction of critical is the same in model and full scales.

For complete and proper modelling of the aeroelastic effects, the scales discussed above must be the same for all modes of vibration of the structure which

are considered significant. Hence the ratio of frequencies of any two modes must be the same in both model and full scale.

For many tall structures, it is sufficient to consider only the first two fundamental sway modes of the structure and, furthermore, to consider the displacement modes as linear functions of height in each of two orthogonal independent directions. These approximations have given rise to the so called "stick model" approach where the model is designed to vibrate elastically in two rotational degrees of freedom, each pivoting about a point at the base of the model. The scaling conditions are applied to the generalised mass, generalised stiffness, and damping as a fraction of critical for each mode independently. A single degree of freedom version of this type of aeroelastic model has been used in the experimental portion of this study and will be described in a later chapter.

In cases where the significant modes are more three dimensional or where higher modes are significant, multi-degree of freedom aeroelastic models are used. In general these rely on a lumped element approximation of the structure, although in some cases, continuous or distributed element models have been used, particularly for slender towers where several modes have been considered important [41,43]. For most tall buildings, a model with four or five lumped elements is sufficient. Details of these modelling procedures can be found elsewhere[40,77]. Figure 1.1 shows an example of an aeroelastic model for a tall building.

The design and construction of an aeroelastic model can be a time consuming and relatively expensive process. The testing procedures involved are also relatively extensive. Tests must be carried out for a range of wind speeds which each represent a different full scale speed. This is important in order to capture any phenomena which are related to a limited or critical range of wind speeds, such as vortex-induced excitations. These tests must also be carried out for different
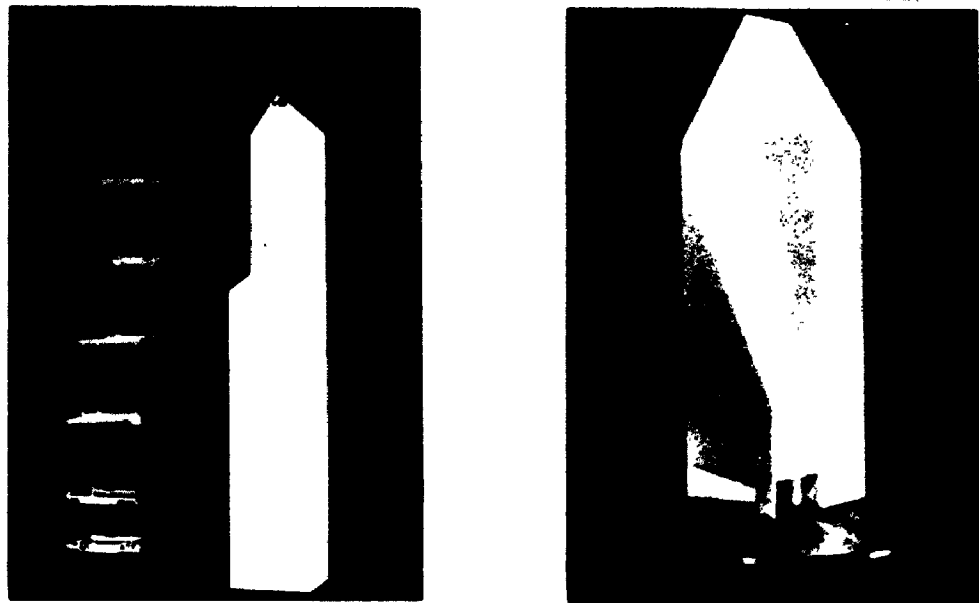
Figure 1.1: Examples of Aeroelastic and Base Balance Wind Tunnel Models

directions of wind as well.

Often the loading information from the wind tunnel testing is required by the engineers before the final design is complete. Indeed, the information on wind loading often contributes to some modifications of the structural design of the prototype. Since the wind tunnel testing is at that point completed, extrapolations of the results to the new design must be relied upon, or, alternatively, another iteration of wind tunnel testing must be carried out with appropriate model redesign and construction.

1.3   Base Balance Technique

The base balance technique offers a relatively economical and expeditious alternative to the more involved aeroelastic procedure. Figure 1.1 includes a photograph of a base balance model. The technique involves the use of a very stiff high frequency balance-model system which models only the exterior geometry of the structure and makes complementary use of analytical techniques to determine the final wind-induced response. The wind tunnel study may be carried out at a stage in the design when only the exterior geometry of the structure has been fixed. When they become available, the remaining structural properties are combined analytically with the wind tunnel data to determine full-scale responses.

Figure 1.2 shows a diagrammatic representation which compares the aeroelastic and base balance techniques. The measured quantity in the aeroelastic procedure is the final response spectrum. In the base balance technique, on the other hand, it is the spectrum of modal force which is measured experimentally. The final response of the structure to that modal force is then determined analytically. Changes in the structural properties can be readily accommodated by iteration of the analytical procedures. Parametric studies wherein the responses are predicted as functions of the structural parameters are often feasible. Importantly, it is unnecessary to retest a new wind tunnel model unless significant changes in the exterior geometry are made.

The aeroelastic modelling remains the most complete form of wind tunnel simulation; however, the base balance technique offers the very desirable advantages of economy and flexibility. Although there are several assumptions inherent in the approach, there are also reasonable modifying procedures which can be made to accommodate most cases in which the assumptions do not strictly apply; these will
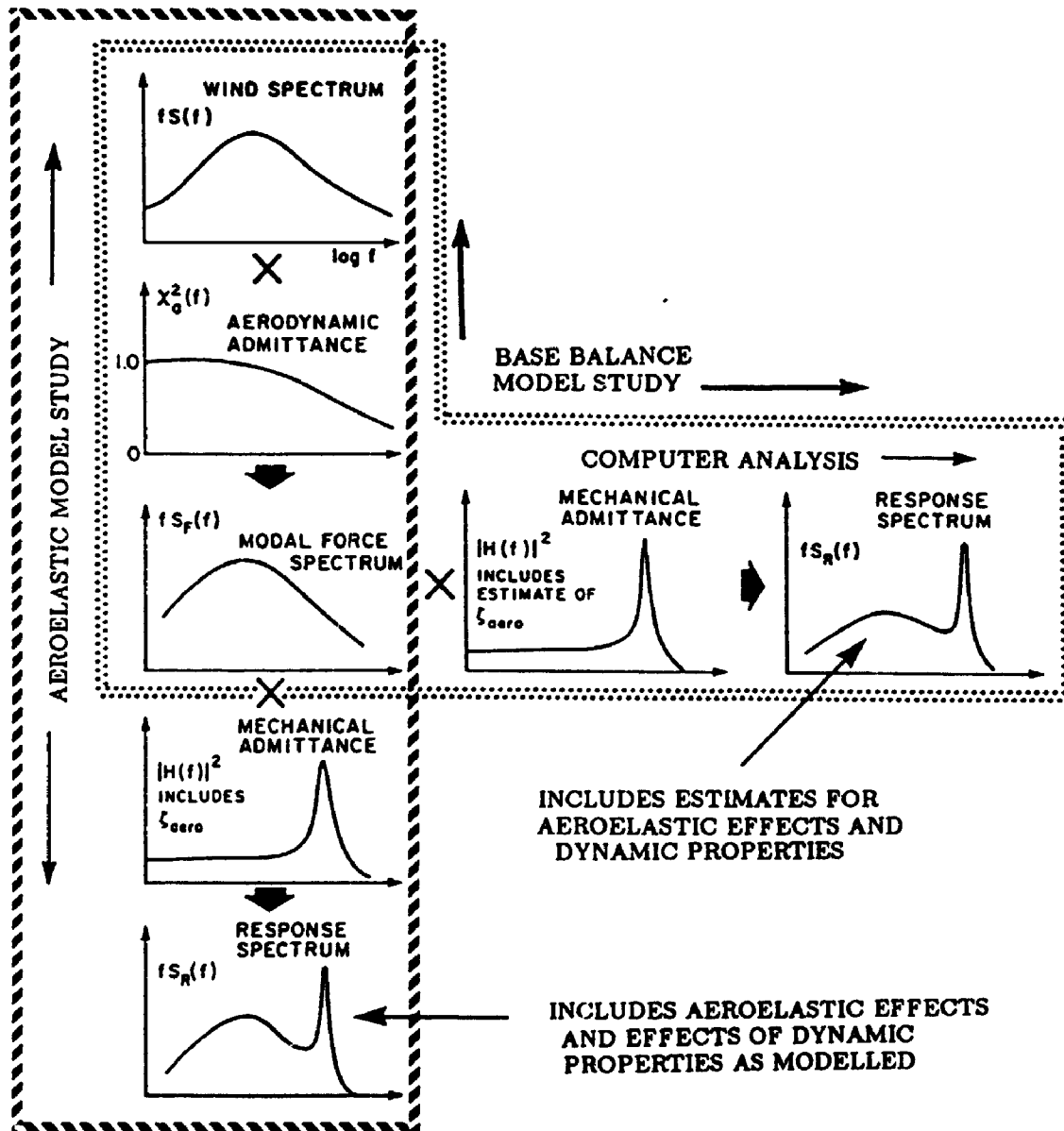
Figure 1.2: Schematic Comparison of Aeroelastic and Base Balance Techniques

be discussed further in the next chapter. The main exception to this is the exclusion of motion-induced forces. While the turbulence and buffeting are provided by the correctly modelled flow, and the wake effects are created by the correctly modelled geometry, the stationary model used in the base balance technique simply cannot affect the flow in the same way that the responding aeroelastic model can. Hence any motion-induced forces are absent in the base balance technique.

1.4   An Alternative Approach

The motion-induced aerodynamic force represents a relatively small proportion of the total motion producing force acting on a tall structure. It is typically no more than a few percent of the inertial force. However, because part of the motion-induced force acts systematically in phase with the velocity, its effect on the response can be substantial. Forces which act in phase with velocity act effectively like damping forces. Unlike the structural damping, however, the *aerodynamic damping* may be negative implying that there is net work being performed on the structure by the flow. Hence there is a gain of energy by the structure. This can effectively reduce or even negate the total damping available to the structure. In the latter event, the structural motion will increase until either structural failure occurs, or until nonlinear structural elasticity or altered flow conditions restore sufficient damping.

Simply neglecting the motion-induced forces in the base balance approach can therefore produce either conservative or grossly unconservative results depending on the particular conditions. Methods of including them are therefore highly desirable. The suggestion put forth here is to augment the base balance technique with experimentally derived data on the motion-induced forces acting on the model of interest. Specifically, it is suggested that

the rigid base balance model be forced to oscillate in a pivot mode, which is the same mode shape assumed in the base balance technique, and the motion-induced forces be measured. These data would then be used conjointly with the base balance results to produce more reliable response estimates.

The main advantage of this approach over the more complete aeroelastic approach is that the wind tunnel testing is still independent of the actual structural properties. Like the base balance approach, it can readily accommodate changes in those properties, or allow parametric studies, without requiring retesting of each case. Such calculations are carried out in the analytical portion of the wind study. Only the basic geometry is required to perform the experimental portion.

While there would be some additional wind tunnel tests required over the regular base balance experiments, there is still a great overall savings in the design and construction effort of the model required, as compared to that of an aeroelastic model.

There are some simplifying assumptions which can minimise the amount of extra wind tunnel tests required. These will be discussed further in a later chapter.

1.5 Aims of the Study

The <u>principal aim</u> of this study is to design a routine experimental system to augment the base balance technique by providing information about the motion-induced forces acting on a structure. This information would be used conjointly with base balance results to produce more reliable response

estimates.

The demonstration of the system in application to a typical research problem constitutes a separate part of the study.

In the process of designing and demonstrating the system, two secondary goals developed which also form significant parts of the study. The first was the provision of a comprehensive set of matched experiments on a particular bluff body, a square prism, with which theoretical predictive models of motion-induced forces may be tested and developed. The second was the provision of a data base including several shapes of bluff bodies which can assist in the basic design process of tall chimneys or slender buildings. This data base includes extensive base balance results as well as results from the system developed for measuring motion-induced forces. It is intended to allow the designer to obtain preliminary wind load estimates for a wide range of cross-sectional shapes.

1.6 Preview

The thesis is divided into five parts as follows.

Part I, containing Chapters 1-3, provides some background for the study:

Following this introductory chapter, Chapter 2 reviews the base balance technique currently in wide use. It describes the basic procedure, the underlying assumptions, and the various modifications used to accommodate practical cases which deviate from those assumptions. This review is intended to stand independently as well as to provide a point of departure for the current work.

Chapter 3 reviews the current state of knowledge regarding motion-induced forces. Some theoretical models are described, and their advantages and disadvantages highlighted. Previous experimental approaches are also discussed. The reasons behind the approach taken with the proposed experimental system is also clarified by this review.

Part II, containing Chapters 4-6, describes the development of the Pivot Mode Activator System. This is the system developed for the measurement of motion-induced forces using a rigid base balance model. It includes experimental and analytical components:

Chapter 4 describes the hardware of the system. A functional overview is first given and then particular subcomponents are described in more detail. Both the mechanical activator and the electronic signal processor are outlined.

Chapter 5 discusses the calibration and experimental procedures which have been developed. The system is quite sensitive to the dynamic forces present in the activator and a specific procedure is required to account for the potential contaminating forces. For this reason, a full chapter has been devoted to describing this portion of the work.

. Chapter 6 outlines the analytical procedures which have been developed. This includes a discussion of appropriate notation to describe the motion-induced

forces, and then the various computational methods of extracting the desired quantities from the raw experimental data.

Part III, containing Chapters 7 and 8 describes the experimental studies. The main purpose of these studies was to demonstrate the use of the Pivot Mode Activator System. The first is more research oriented while the second, although extensive, is a more routine program of data aquisition:

Chapter 7 reports a comprehensive set of experiments carried out on the square prism. These experiments included measurements of the motion-induced forces using the Pivot Mode Activator System which investigated the effects of oscillation amplitude, turbulence level of the approaching flow, and aspect ratio of the model. Some qualitative comparisons are made with previous findings involving square prism. To complement the results, experiments were also carried out on a stationary model using the regular base balance technique. An investigation was then carried out on the vertical variation and correlation of the motion-induced forces. These tests used a pressure model forced to oscillate at various amplitudes and from these a great deal of data was accumulated. Only the results pertinent to the current study are included. The data set in its entirety is included in a separate report[74]. "Free" oscillation or aeroelastic experiments were also carried out on the square prism with several different sets of structural properties. These tests provided a set of results with which to compare predictions derived from the other tests. Different methods of carrying out those predictions are looked at and some insight into the nature of motion-induced forces in the range of vortex shedding is gained by this. Together these set of experiments provide a set of matched results under controlled conditions. It is hoped that they can thus be used to test and develop predictive models of motion-induced forces.

Chapter 8 provides a large set of results from experiments on several

different shapes of prisms. In contrast to the previous chapter, this one is of a more routine and practical nature. The experiments include both base balance tests and pivot mode activator tests. This data base provides an extensive set of information which can be used by designers of tall chimneys and slender buildings. Again, in the interests of space, only the main results of these tests sufficient for the present purpose are included here. The complete set of data is reported separately[78] in a form more suitable for use by design engineers.

Part IV contains the concluding Chapter 9. This chapter summarises the main findings which resulted from the studies in Parts II and III with respect to the development of motion-induced forces in general and the practical use and improvement of the Pivot Mode Activator System. Some recommendations for further studies are then discussed.

The Bibliography and Appendices then follow as **Part V**.

Chapter 2
Review of the Base Balance Technique

2.1 Introduction

In order to predict the wind-induced loading and response of tall buildings, towers, and chimneys, it is often necessary to carry out experiments in a boundary layer wind tunnel in which the full scale structure and its wind environment are modelled. The measured responses of interest may include: displacements and accelerations, base bending moments and shears, or pressure distributions. If certain modelling criteria are conformed to, then the model responses may be scaled up to full scale. The modelling techniques involved here have been well developed[37,40].

Complete wind tunnel simulation of a structure involves modelling all of the relevant structural parameters such as exterior geometry, mass and stiffness distributions, and effective damping. The design and construction of an aeroelastic model for this purpose can be both time consuming and expensive. Furthermore, once the test is carried out, only limited extrapolations of the responses can be made should the structural parameters change in the course of the design. Although aeroelastic modelling remains the most complete form of wind tunnel simulation, more economical and flexible procedures are desired.

The use of the "high frequency base balance technique" developed by Tschanz [84] is now a widely accepted technique for wind tunnel model studies[21,81]. It offers a relatively economical and expeditious alternative to the more involved

16

aeroelastic procedure. The technique involves the use of a very stiff high frequency balance-model system which models only the exterior geometry of the structure. The wind tunnel study may be carried out at a stage in the design when only the exterior geometry of the structure has been fixed. When they become available, the remaining structural properties are combined analytically with the wind tunnel data to determine full-scale responses. The measured quantity in the aeroelastic procedure is the final response. In the base balance technique, on the other hand, it is the spectrum of modal force which is measured experimentally. The final response of the structure to that modal force is then determined analytically. Changes in the structural properties can be readily accommodated by iteration of the analytical procedures. Parametric studies wherein the responses are predicted as functions of the structural parameters are often feasible. Importantly, it is unnecessary to retest a new wind tunnel model unless significant changes in the exterior geometry are made.

The idea of measuring the modal force spectrum and then calculating the response as it would occur for varying structural parameters had been considered prior to the development of the current base balance technique. Saunders and Melbourne[67] attempted to record the modal spectrum by measuring it as seen through the mechanical admittance of an aeroelastic model. By knowing the modal properties, reverse calculation yielded the modal spectrum which could then be combined with the desired structural properties. The major difficulty with this procedure is the errors introduced through the aeroelastic model properties, in particular the estimate of the damping. Measurements of modal force have also been made using pressure models [75,76,88]. This, however, involves integration of simultaneous pressure transducer responses and therefore has limited applications. A closer precursor to the design by Tschanz was described by Whitbread[92]. The development of the base balance technique has greatly reduced the difficulties in

the modal force measurement.

The base balance technique can also be used for nonlinear response analysis; the details of this procedure are dealt with by Tschanz [84]. This is a less common application, however.

2.2   Basic Assumptions

The fundamental premise of the base balance technique is that the generalised or modal forces due to the wind forces can be estimated from the measured base moments experienced by a stationary model. The modal force is defined as the integral of the applied force weighted by the mode shape at the point of application. This is shown graphically in Figure 2.1 for a vertical structure subject to wind-induced force in the direction of its fundamental sway modal deflection. $w(z)$ and $\mu(z)$ are the wind force and the mode shape as functions of height, H is the height and $F(t)$ is the generalised force.

A fortuitously similar quantity to the modal force occurs in the more easily measured base bending moment. In this case, the applied forces incur a weighting naturally through the moment arm influence line as shown in the figure. When the mode shape, $\mu(z)$, is proportional to the influence function, $i(z)$, then the modal force and the base overturning moment are also proportional.

Similar expressions to those shown in the figure could be written for the twist modal force or modal torque. In this case, the loading is the torque per unit height and the base torque influence line is unit constant over the height of the structure.

Mode Shape

$\mu(z)$

Modal Force

EXACT REQUIRED

$$F(t) = \int_0^H w(z,t)\mu(z)dz$$

z $w(z,t)$

WIND FORCE

ESTIMATE FROM BASE MOMENT

$i_1(z)$

Base Moment

$$M_b(t) = \int_0^H w(z,t)i_1(z)dz$$

$$i_1(z) = z$$

IMPROVED ESTIMATE

1.0

Moment at h

$$M_h(z) = \int_h^H w(z,t)i_2(z)dz$$

P

h

$$i_2(z) = z - h \ : \ z \geq h$$
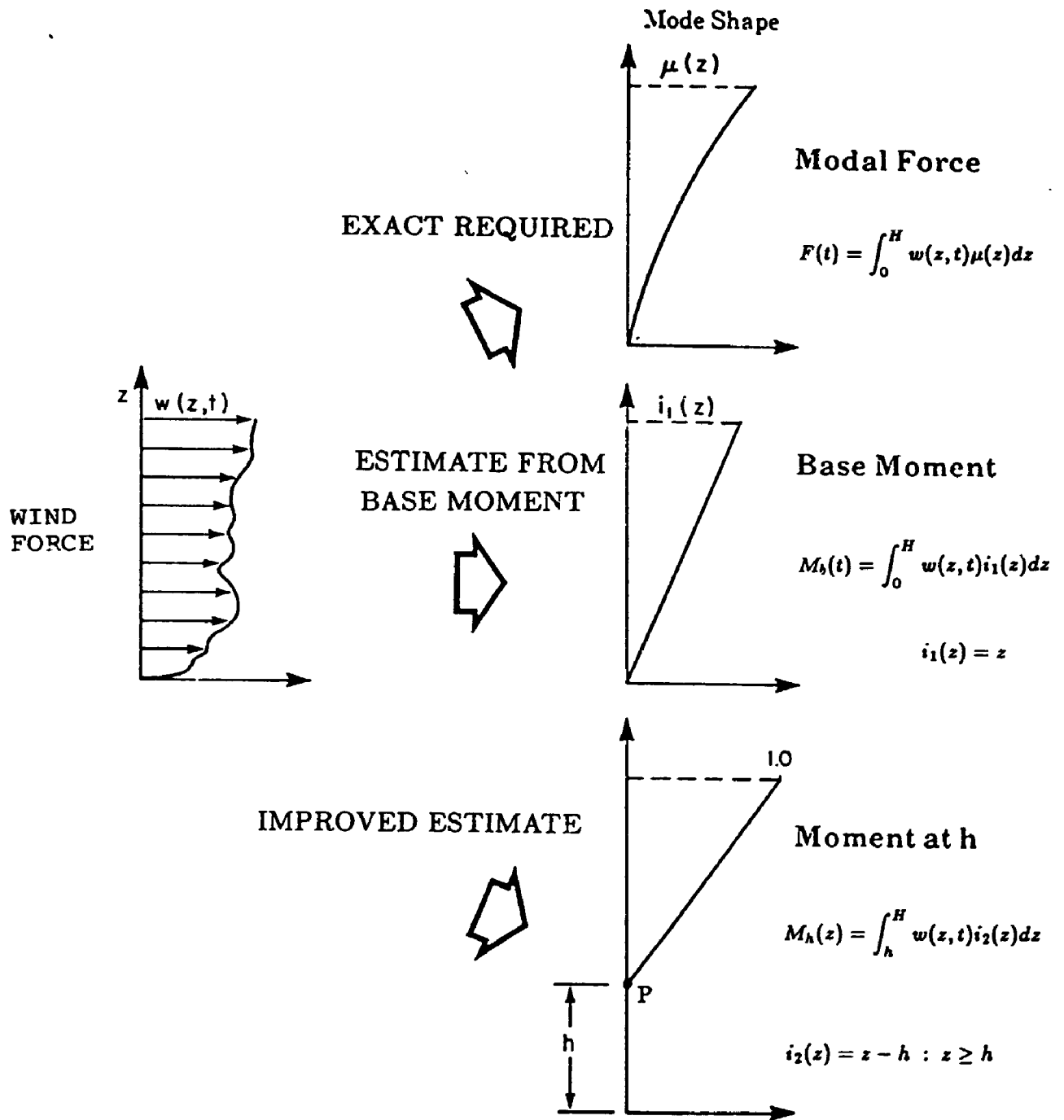
Figure 2.1: Estimation of Sway Modal Forces

The base moments, including two overturning moments and the base torque, represent direct measurements of the modal forces on a structure when the following conditions are met:

- The balance-model system is essentially rigid, with a high natural frequency, so that the measured moments are not significantly amplified by the mechanical admittance of the system in the frequency range of interest.

- The first three natural modes of the structure are decoupled and geometrically orthogonal in two sway directions and one twist direction.

- The fundamental sway mode shapes are linear functions of height and pivot at a point where the moments are measured.

- The fundamental twist mode shape is constant over the height of the structure.

- There are no significant motion-induced forces involved and so the nature of the forcing remains the same on a responding structure as it is on a stationary structure.

In practice these conditions are never fully met.

The technique is also limited in that only the fundamental modes in each direction can be reasonably estimated. It must be assumed that contributions to the response from higher modes are negligible. Also no information as to how the loads are distributed over the structure is derived from the base balance technique. This must be estimated or measured in a companion study of local pressures.[1]

---

[1] A "second generation" base balance approach has been suggested[87] which provides some limited information regarding the distribution of loads. This will potentially allow an experimental consideration of non-linearly varying mode shapes. The technique, however, is still under development.

2.3   Basic Approach

With the assumptions outlined in the previous section, the spectrum of generalised force may be determined directly from the spectrum of moment:

$$S_{FF}(f) = \frac{1}{H^2} S_{MM}(f) \qquad (2.1)$$

The calculation of the response of a linear single degree of freedom system to the generalised force is a straightforward process based on random vibration theory[15]. The variance of the response is given by

$$\bar{y}^2 = \frac{1}{K_s^2} \int_0^\infty |H(f)|^2 S_{FF}(f) df \qquad (2.2)$$

where $|H(f)|$ is the modulus of the mechanical admittance function:

$$H(f) = \frac{1}{\left(1 - (\frac{f}{f_r})^2\right) + i2\varsigma_s(\frac{f}{f_s})} \qquad (2.3)$$

In most cases, Equation 2.2 may be approximated by splitting the integral between a quasi-static background and a resonant component:

$$\bar{y}^2 = [A_B + A_R] = \frac{1}{K_s^2} \left[\int_0^{f_s} S_{FF}(f) df + \frac{\pi f_s S_{FF}(f_s)}{4\varsigma_s} \right] \qquad (2.4)$$

A slightly different simplification carries the integral out to infinity. The rms response may then be expressed as:

$$\tilde{y} = \frac{\sigma_F}{K_s} \sqrt{1 + \frac{\pi f_s S_{FF}(f_s)}{4\varsigma_s \sigma_F^2}} \qquad (2.5)$$

The peak response may then be estimated as:

$$\hat{y} = \bar{y} + g\tilde{y} \qquad (2.6)$$

where g is an appropriate peak factor. The details of these procedures are covered in greater detail elsewhere[22].

It is often assumed that the approximate expression, Equation 2.5, represents a conservative estimate of the rms response because, although the first term accounts for the background portion of the spectrum without dynamic amplification, the second term includes an exaggerated contribution. However, these compensatory contributions result in conservatism only if the spectrum of generalised force is sufficiently broadband. (It is also necessary that the natural frequency of the structure is of relatively high frequency and lightly damped.) In the contrived case of white noise excitation, the approximation is always conservative. **If the spectrum is very peaky, as is common for the excitation in the lift direction, Equation 2.5 is likely to underestimate the response.**

An indication that the approximation is likely to be conservative is given by considering, in an approximate way, a ratio of the compensating contributions previously mentioned. This results in the following condition:

$$\frac{S_{FF}(\hat{f})}{S_{FF}(f_s)} \left[\frac{1}{\left(1 - (\frac{\hat{f}}{f_s})^2\right)^2} - 1 \right] \ll 1 \tag{2.7}$$

where $\hat{f}$ indicates the frequency at which the maximum value of the spectral density function occurs. Where this condition is not met, or where the conditions of a high frequency lightly damped structure are not met, it is best to resort to the full expression, Equation 2.2.

2.4 Adjustments for Base Balance System Mechanical Admittance

It is necessary that the base moments used to represent the modal forces be moments as measured on a nearly rigid model. If the balance-model system responds dynamically to the wind loading, then the measured base moments will include the inertial

loading effects of the system itself. If the motions are large, then the aerodynamic interaction of the model with the wind could also contaminate the measurements. It is therefore attempted to make the balance-model system as stiff as possible while still being sensitive enough to provide reasonable signal strength. In this way the frequency range of interest falls at the low end of the mechanical admittance function of the balance-model system. In this range, the dynamic amplifications are small as illustrated in Figure 2.2. In some cases the natural frequency of the system cannot be raised sufficiently high and the base moment measurements are amplified. There is in principle no difficulty in adjusting the spectral density measurements to account for this, providing that the mechanical admittance of the system is well identified and may be treated as linear and uncoupled. It is assumed, however, that the frequency is still high enough that the model motion is insignificant.

2.5   Adjustments for Mode Shape

The assumption of a constant twist mode shape with height is never true for real structures. A typical twist mode shape for a very tall building lies somewhere between a constant and a linear function of height. In practical cases the majority of the contribution to the torsional modal force comes from the upper half of the structure. Experimental measurements of the modal force made by Tallin and Ellingwood[82] confirm this.

The measurement of the base torque from the base balance may be made more representative of the generalised torque by artificially sheltering the lower portion of the model in such a way that the aerodynamic interference of the sheltering device is minimal. A more convenient method of adjustment was suggested by Tschanz[84]. He argued that a realistic measure of the relative values of generalised

RANGE OF BUILDING
RESPONSES

$\text{LOG}\left\{ f \, S_F(f) \right\}$

Typical spectrum of wind forces,
aerodynamic admittance of model
shape included

LOG f

X

$$|H(f)|^2 = \frac{1}{\left[1 - \left(\frac{f}{f_o}\right)^2\right]^2 + 4\xi^2\left(\frac{f}{f_o}\right)^2}$$

$\text{LOG}\,|H(f)|^2$

WITH ATTENUATION
FROM ELECTRONIC
FILTER

Mechanical transfer function of a
transducer with a fundamental frequency
f_o and a damping ratio ξ of
critical damping

1.0

LOG f

=

f_o

$\text{LOG}\left\{ f \, S_R(f) \right\}$

Typical spectrum of actual measured
and ideal force output from a transducer

ACTUAL, NON - FILTERED

FILTERED

IDEAL

LOG f

Figure 2.2: Dynamic Response of the Base Balance-Model System

torques associated with a constant mode shape and a linear one is given by the ratio of the measured base shear and measured base moment. Some experimental comparisons have also been made with respect to this area [11]. It is generally agreed that a value of about .70 represents an adequate empirical adjustment factor to apply to measured base torques.

Although approximating the sway mode shapes by a linear function is sufficient in many cases, tall buildings and structures having mode shapes which significantly deviate from this approximation are not uncommon. The variation in mode shape can have a significant effect on the similarity of the modal force and the measured base moment spectral densities. Measurements aimed at quantifying these effects have been carried out[88] and some examples are illustrated in Figure 2.3. The model used in these experiments was a simple square building of aspect ratio 5:1, instrumented to measure area loads at several heights. These area loads were weighted and combined on-line to provide measures of modal forces corresponding to different mode shapes of the form:

$$\mu(z) = (\frac{z}{H})^\beta \tag{2.8}$$

where the parameter, β, took on various values indicated. The case of $\beta = 1.0$ corresponds to the measured overturning moment and $\beta = 0.0$ corresponds to the measured base shear. These spectra are for a normal wind direction and an open country upwind terrain.

Mode shapes which are best described by β values of 1.5 or higher are not uncommon. The effect which this deviation from a linear function has on final predicted peak response differs depending on the type of response considered. The most notably affected response is the predicted acceleration. Unlike the predicted base moments, the accelerations have no mean component to diminish the errors incurred from the base balance estimate of the dynamic component. Also in the case
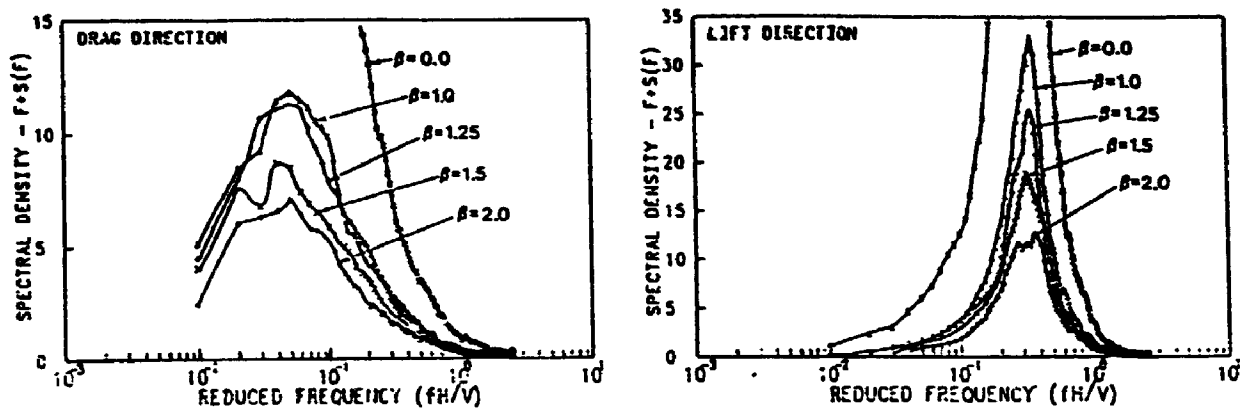
Figure 2.3: Modal Force Spectra for Various Mode Shapes: $\mu(z) = (z/H)^\beta$

of accelerations, the mode shape appears in the analytical portion of the response estimate as well as the measured portion. This accentuates the errors arising from the assumption of a linear mode shape.

Quasi-steady theory can be used to determine an adjustment factor to be applied to the measured moments from the base balance. This adjustment makes the measured moments more representative of the modal forces associated with the non-linear[2] mode shape. It is determined by estimating the drag response of the structure following the approach outlined by Davenport[19,18] assuming first the correct non-linear mode shape and then the assumed linear one. The ratio of these estimates provides an adjustment to be applied to the instantaneous measured overturning moment or, when squared, an adjustment for the measured spectral densities. Although the quasi-steady approach used applies to the drag direction only, the adjustment has been ..und to apply surprisingly well to other directions too. This is covered in greater detail elsewhere [88]. Figure 2.4 shows comparisons of the necessary adjustment as measured experimentally and as determined by the quasi-steady approach. The latter is denoted as the mathematical model in the figure.

---

[2]non-linearly varying with height
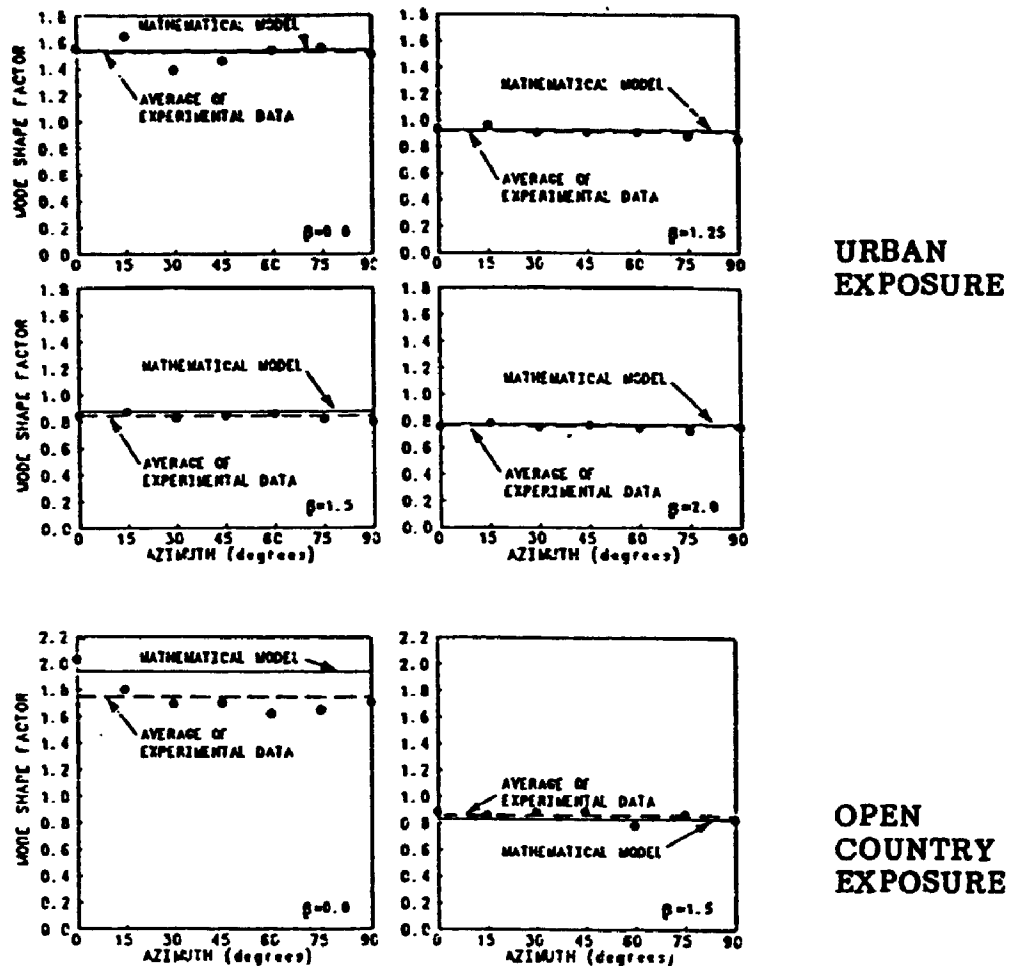
Figure 2.4: Experimental and Analytical Generalised Force Spectrum Mode Shape Correction Factors for a Various Mode Shapes and Wind Angles[88]

Experience so far has indicated that the mathematical model is quite appropriate even for buildings in relatively built-up surroundings.

In situations where estimates are desired before any mode shape information is available, it may be unavoidable to assume a linear mode shape in calculating the model mass and to accordingly apply no adjustments to the measured moments. In other cases, a good estimate of the mode shape may be available and used to calculate the modal mass, but a suitable adjustment for the modal spectrum may be still in question and hence neglected. For realistic mode shapes, these

procedures produce significantly different estimates of response, particularly in the accelerations. The effect of mode shape variation on accelerations as predicted by these different methods for a simple square building has been covered elsewhere[88] and is shown in Figure 2.5.

Equation 2.8 may not always provide the best description of the mode shape. Some typical mode shapes are better described by a linearly varying function which intersects the axis at some point, P, located above the base as shown in the lower diagram of Figure 2.1. This function also represents the influence function for overturning moments measured at P. When this mode shape is known at the time of the tunnel tests, an improved measure of the modal force can be made by using the moments at P. Unfortunately it is not always convenient to measure moments at this point. An approximation can be made by combining simultaneously measured base moments and base shears:

$$M_P(t) = M_b(t) - S_b(t)z_P \tag{2.9}$$

It is assumed here that the contribution to the base shear below the point, P, is negligible. This is a reasonable assumption in most cases, particularly where the lower portion of the structure is sheltered by other buildings. This approach has been used in practice[27].

2.6 Treatment of Coupled Degrees of Freedom

Many structures, particularly buildings of more complex design, exhibit coupling between the sway and twist motions. Where coupling is significant, a multi-degree of freedom aeroelastic model study is a necessary alternative to the base balance technique. For cases where the coupling is less significant, methods of adapting the technique in order to include the effects of the coupling are highly desirable.
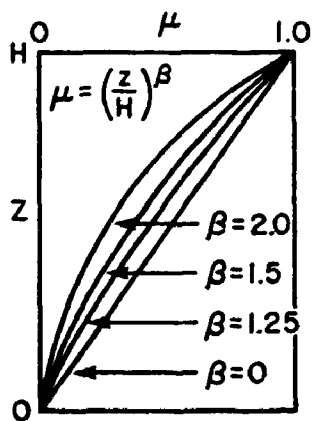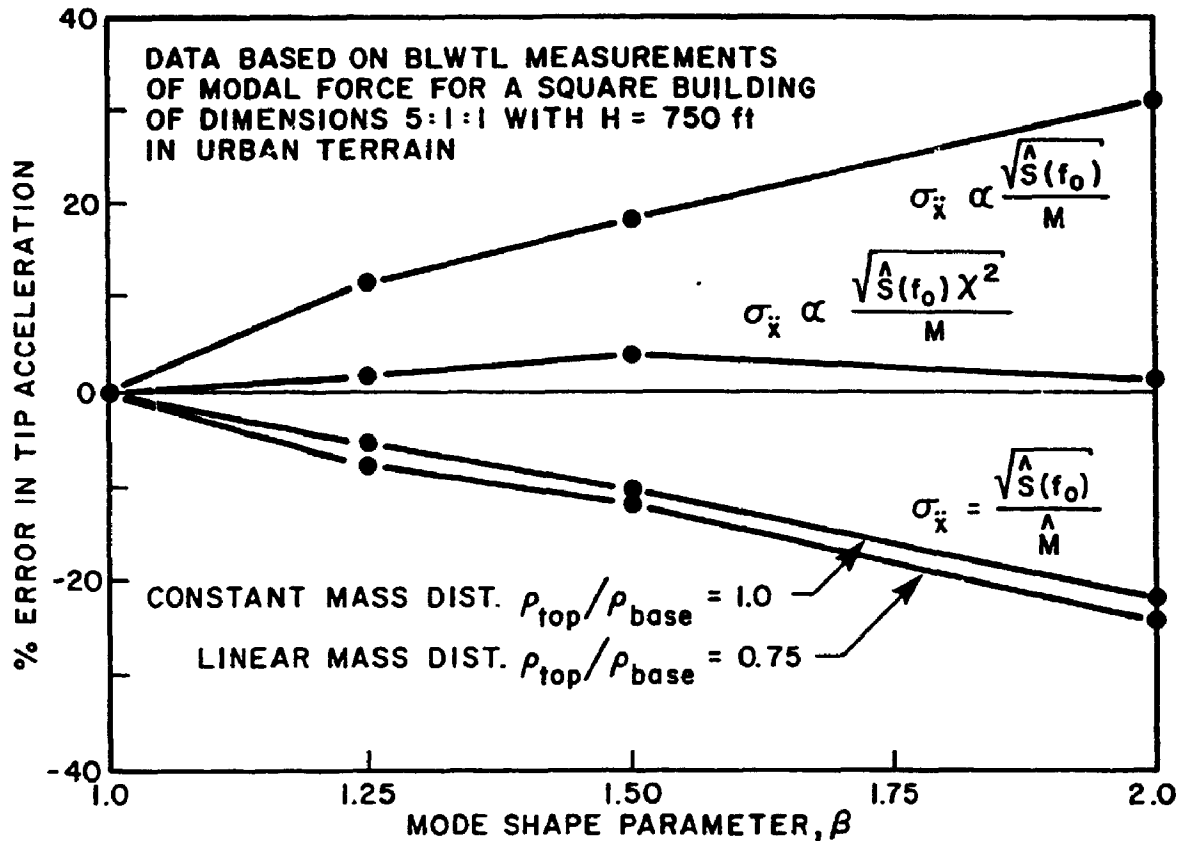
Figure 2.5: Tip Acceleration Error Arising from Various Mode Shape Assumptions (after [88])

Ideally, a relatively complete approach would proceed as follows. The complete spectral density matrix of the actual modal forces, including cross-spectra would be measured as seen in any convenient system of coordinates. This system may not necessarily be the modal coordinate system. The spectral density matrix would then be combined with the mechanical admittance matrix as defined in consistent coordinates to get the spectral density of the the response. Since the mechanical admittance is most easily defined in the modal coordinates, it would be prudent to first transform the spectral density matrix of modal forces to the modal coordinate system.

The practical difficulty is of course the measurement of the modal forces. The base moments only represent *approximations* to the modal forces and furthermore only do so when measured in the modal coordinates.[3] Coupled degrees of freedom represent a further complexity in making these representative measurements. Some progress can be made in cases where it can be assumed that the base moments and torque represent proportional measures of separate modal forces. This means that the twist response is largely contained in one mode and that the sway modes, although with coupled degrees of freedom, still lie in basically vertical planes. It then becomes valid to measure the base moments and torque in a predefined coordinate system and then transform them to modal coordinates. The measurement of cross-spectra as well as auto-spectra extends the data acquisition effort, but this is not considered prohibitive. Consideration must still be given to the poorer representation for the twist mode provided by the base torque.

For lightly damped systems with well separated frequencies, it is an accepted practice to neglect the off-diagonal terms of both the spectral density

---

[3]In applications of the base balance technique to uncoupled situations, the mode shapes may not be fully known at the time of testing, but it is expected they are known to the extent of the principal directions of sway in order to measure the moments about the appropriate axes.

matrix of the modal force and the mechanical admittance matrix. These terms contribute little to the final response. The response spectrum for each mode is then defined by:

$$S_{rr}(f) = |H(f)|^2 S_{qq}(f) \qquad (2.10)$$

Neglecting the cross terms only applies to the matrices after transformation to the modal coordinates. In general, the cross-spectra measured in standard or predefined coordinates can make significant contributions to the auto-spectra of the modal coordinate system. Note also, that by the very nature of coupled systems, the frequencies may not be well separated. Only a few percent separation in frequency is necessary to diminish the cross-modal response, but in situations where this cannot be ensured, it may be advisable to consider these effects.

The suggested treatment of this special case of a coupled system is summarised in Figure 2.6

A limited set of experiments has been carried out to determine the effect of these complexities on the final predicted response. A building of relatively complex geometry was tested in homogeneous suburban ' rrain. The full spectral density matrix of overturning moments was measured in a standard coordinate system for two wind directions differing by 45°. A coupled mode system in two degrees of freedom only was assumed as shown in Figure 2.7. The twist or torsional mode was not considered. The frequencies were assumed to be well separated. A reasonably extreme isotropic wind climate was defined with 10 and 100 year return gradient wind sp eds of 85 and 100 mph respectively. Estimates of 10-year return accelerations and 100 year return base moments were made according to the following three variations in method.

standard coordinates

$M_X(t)$ ⟶
$M_Y(t)$ ⟶
$M_T(t)$ ⟶
$\begin{bmatrix} \text{Spectral Density} \\ \text{Matrix in} \\ \text{standard coordinates} \end{bmatrix} = \underline{S}_f$

$q = \underline{A}\,\underline{x}$

Transform to modal coordinates $\underline{S}_q = \underline{A\,S_f\,A^T}$

modal coordinates

$\begin{bmatrix} \text{Spectral Density} \\ \text{Matrix in} \\ \text{model coordinates} \end{bmatrix} = \underline{S}_q$

for lightly
damped systems
with well
separated
frequencies

drop off-diagonal terms

$S_{q_{11}}, S_{q_{22}}, S_{q_{33}}$ $\left(\begin{array}{c} \text{modal force} \\ \text{auto spectra} \end{array} \right)$

combine with diagonal
mechanical impedance
matrix

$\underline{S}_R = \underline{H S_q H^*}$

$S_R = \mid H \mid^2 S_q \left(\begin{array}{c} \text{modal response} \\ \text{auto spectra} \end{array} \right)$

Figure 2.6: Procedural Treatment of Coupled Sway Modes

1. The *full* measured spectral density matrix was transformed to the modal coordinate system.

2. The measured cross-spectra were neglected and *only the auto-spectra* were transformed.

3. The *coupled mode system* was ignored entirely and responses were estimated in the standard coordinate system.

Exemplary results for one of the wind directions are tabulated in Figure 2.7. These data, although limited, give some indication of the extent of procedural effects. Despite complex building geometry and significant degree of coupling, the effects on the final resultant accelerations and moments are modest. The relative contributions to these results from the modal directions, however, are significantly affected. **This would have further consequences when these results are combined with a strongly directional wind climate to predict responses at a specific geographic location.**

2.7 Motion-Induced Forces

In general a stationary model will not experience the same forces as a model which is able to respond as a real structure would. The motion of the structure imposes time dependent boundary conditions on the fluid flow around the structure. The flow in turn influences the motion of the structure. These complex interactions are such that the both the deterministic and the stochastic character of the forces may be significantly altered.

Unlike the situations considered in the previous sections, there are cur-

COUPLED COORDINATE SYSTEM
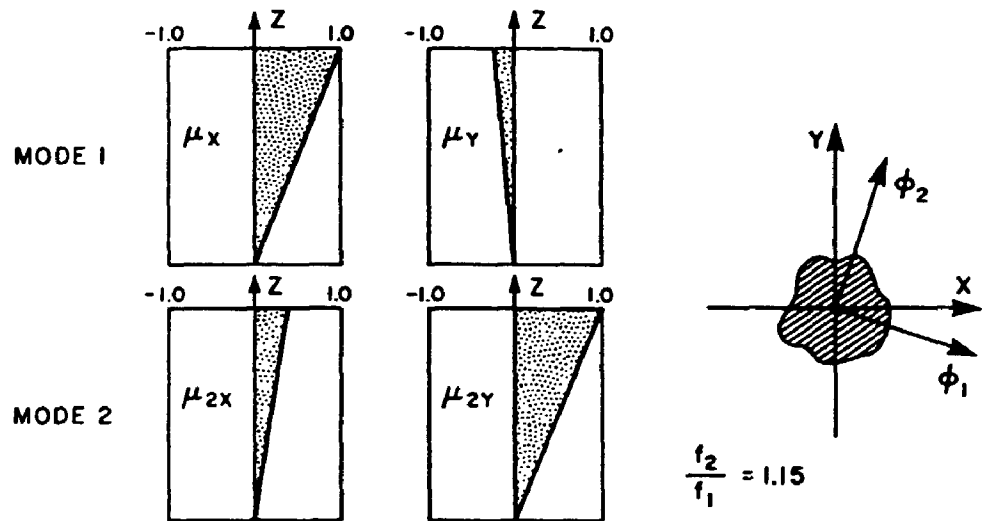
	Modal Coordinates			Standard Coordinate Disregarding Coupling		
Response	Units	Full Spectral Density Matrix	Diagonal Spectral Density Matrix	Response	Units	
a_{ψ_1}	milli-g	14	17	a_x	milli-g	17
a_{ψ_2}	"	14	13	a_y	"	12
a_R	"	18	19	a_R	"	19
M_{ψ_1}	$\times 10^6$ ft-lb	1100	1340	M_x	$\times 10^6$ ft-lb	1500
M_{ψ_2}	"	1600	1470	M_y	"	1400
M_R	"	1750	1790	M_R	"	1850

Figure 2.7: Effects of Various Assumptions in a Coupled System

rently no methods of treating motion-induced effects with the base balance approach beyond a cautionary approach to situations where unconservative estimates may be expected. Specifically this occurs when the natural frequency of the structure is near that associated with a vortex shedding peak in the force spectrum. The lack of such methods was the impetus for the current work. The following chapter is devoted to discussing motion-induced forces in greater detail.

Chapter 3
Motion-Induced Forces

3.1   A Definition

The term *motion-induced forces* appears throughout the literature of fluid dynamics, but precise definitions are not often stated. Taken literally, the term would include inertial forces and material damping forces of a structure, however this is not what is intended. It is generally understood to refer to fluid forces which are induced by the motion of a body through the fluid, yet even this is a somewhat loose definition. It is important to define the term because there is often a certain specificity implied in its usage. With subtly different connotations being held by a wide range of researchers from various fields, this can lead to confusion and misconceptions being ingrained in the descriptive models which are put forth. A reasonably precise definition is as follows:

> <u>Motion-Induced Forces</u> refer to any aerodynamic forces which are correlated to the motion of the structure relative to an inertial reference frame, and might more properly be called *motion correlated aerodynamic forces.*

This is not intended to be a universal definition since other applications may call for less specific or entirely different restrictions. It is intended only to define the term as it is used within the present study. Note that the word "correlated" as it is used above implies that there exists a non-trivial mathematical dependency between the aerodynamic force and the body motion.

Motion-induced forces should not be simply equated with *aeroelastic forces*. Aeroe..sticity is concerned with the study of phenomena in which there is significant interaction between structural motion and aerodynamic forces. It follows that aeroelastic phenomena will certainly involve motion-induced forces. The presented definition, however, is intended to separate reference to the aerodynamic forces inherently responsible for aeroelastic classification of a phenomenon from reference to the other forces, aerodynamic and structural, which are still significantly present in that situation. Hence, the term motion-induced forces does not include vortex shedding forces per se. These exist on a stationary structure where there can be no motion correlation. On the other hand, the so called lock-in phenomenon, may occur when the structure oscillates, and in this case the vortex shedding forces become, at least in part, motion-induced forces by definition. Also still present are additional aerodynamic and structural forces which play a significant role in the aeroelastic phenomenon.

To avoid possible confusion, it should also be noted that the aeroelastic modelling discussed in Chapter 1 is so called because of its ability to *include* aeroelastic effects. It does not mean that strong interaction of structural motion and aerodynamic forces are necessarily present in all aeroelastic model tests. In fact, some measure of the presence or absence of aeroelastic effects is given by the degree of agreement between results from aeroelastic tests and from base balance tests. Such comparisons have been made in various wind tunnel studies [77] and will be looked at in Chapter 7.

3.2   Aeroelastic Phenomena

There are a number of phenomena which are related to motion-induced forces and are therefore classified as aeroelastic. These include vortex-induced vibrations, across wind galloping, wake galloping, flutter, and torsional divergence. It is not difficult for the attentive sightseer to find relatively common examples of many of these, by watching hydro lines, stop signs, flagpoles, advertising banners, and the like.

Not all of these phenomena are significant concerns with respect to tall chimneys and buildings. Torsional divergence and certain kinds of flutter are associated with significant torsional motion. Their study is given much greater attention with respect to long afterbody or airfoil type structures such as wings or long span bridges. Flutter may also be associated with certain flexible structures such as the large side panels of rockets, or flexible roof structures. Classical flutter refers to a two degree of freedom phenomenon in which energy exchange between the modes takes place. Wake galloping refers to a special case of galloping where there is more than one bluff body structurally connected. A downstream body is then affected by the wake of an upstream one and its motion in turn affects the upstream body and its wake. This is a common problem observed with bundles of suspended power lines held parallel by mechanical spacers.

While generally, aeroelastic instabilities have been observed for chimneys, there is a potential for instability with very tall slender buildings. The most important instabilities can be classified as either vortex-induced vibrations or galloping, and so only these will be described here.[1]

---

[1] An additional aeroelastic effect (but not an instability) which has been identified for these structures is aerodynamic damping in the along wind direction. It is generally positive and therefore reduces structural response. A quasi-steady development of this is included in Chapter 7 and so will

3.2.1 Vortex-Induced Vibrations

Vortex shedding from bluff bodies is a phenomenon which has received considerable attention for some time. Strouhal [79], Bénard [5], and von Karman[90,89] made notable early contributions to the field. Today, dozens of papers a year continue to be published on experimental, and analytical aspects of the phenomenon. This is certainly due, in part, to the intriguing variety of effects associated with the phenomenon and our relatively poor understanding of the underlying mechanisms. More important than the simple academic interest, however, is the fact that vibrations due to the shedding process are one of the most prevalent problems in mechanical and fluid dynamics, affecting a wide range of structures such as power lines, towers, chimneys, marine cables, and aerospace structures.

It is important to distinguish vortex shedding, a strictly fluid dynamic phenomenon, from vortex-induced vibration, which is a fluid-elastic phenomenon occurring in the presence of vortex shedding.

When a body is immersed in a smooth fluid flow, the fluid must flow around the body. At low Reynolds number, the fluid can follow the contours of the body. This is depicted in Figure 3.1 for a circular cylinder at $Re \leq 5$. As the Reynolds number is increased, the inertial forces become relatively greater and the flow can no longer accelerate around the body surface. Flow separations occur at some points. Around $Re \approx 10$ for the circular cylinder, a stable pattern of two vortices called *Föppl* vortices is formed as shown in part (b) of the figure.

At still higher Reynolds number, free shear layers are set up as shown in Figure 3.2. For bodies with curved surfaces, such as a circular cylinder, the actual location of separation will vary widely over relatively minor changes in Reynolds

---

not be dealt with here.

Re < 5   REGIME OF UNSEPARATED FLOW

5 TO 15 < Re < 40   A FIXED PAIR OF FOPPL
                    VORTICES IN WAKE

40 < Re < 90 AND 90 < Re < 150
TWO REGIMES IN WHICH VORTEX
STREET IS LAMINAR

150 < Re < 300   TRANSITION RANGE TO TURBU-
                 LENCE IN VORTEX

$300 < Re \gtrsim 3 \times 10^5$ VORTEX STREET IS FULLY
                                   TURBULENT

$3 \times 10^5 \lesssim Re < 3.5 \times 10^6$

LAMINAR BOUNDARY LAYER HAS UNDERGONE
TURBULENT TRANSITION AND WAKE IS
NARROWER AND DISORGANIZED

$3.5 \times 10^6 < Re$
REESTABLISHMENT OF TURBU-
LENT VORTEX STREET

Figure 3.1: Regimes of Fluid Flow Across Circular Cylinders[10]
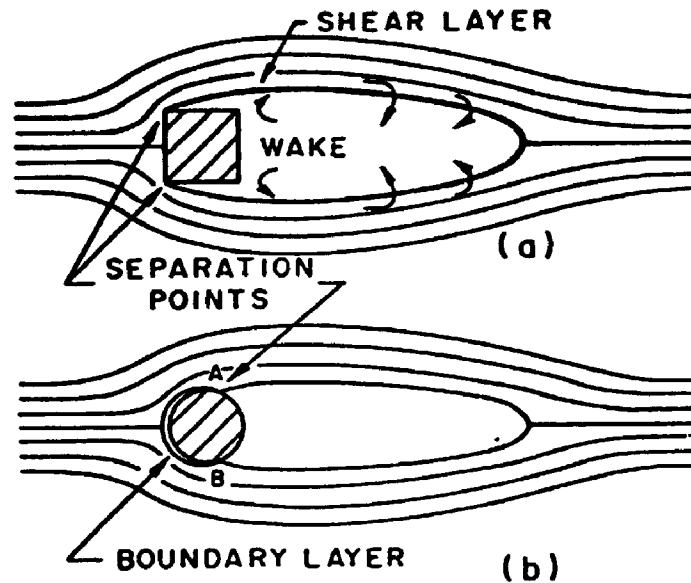
Figure 3.2: Wake Formation Past Bluff Bodies: (a) Sharp-Edged Body, (b) Circular Cylinder[26]

number and in the surface roughness. For sharp cornered bodies, on the other hand, the separation points tend to be much more stably located at leading corners where large accelerations in the flow would be otherwise required. The shearing in this vicinity causes the formation of vortices which contribute to the turbulent wake behind the body. By processes which are less understood, some of these vortices coalesce into larger ones which ultimately separate away from the body and migrate downstream. If the body is reasonably symmetric, the vortices of opposite rotation shedding from opposite sides of the body will organise themselves in an alternating succession proceeding downstream from the body. as shown in Figure 3.1(c). This is known as the von Karman vortex street, due to his analytical study of the process as a series of discrete vortices[90,89]. At still higher Reynolds number the transition to turbulent flow occurs, and the vortices are shed more randomly. Eventually a regime of turbulent regular vortex shedding is reached.

In one of the first systematic studies of vortex shedding, it was observed by Strouhal[79] that the frequency at which vortices are shed from one side of a
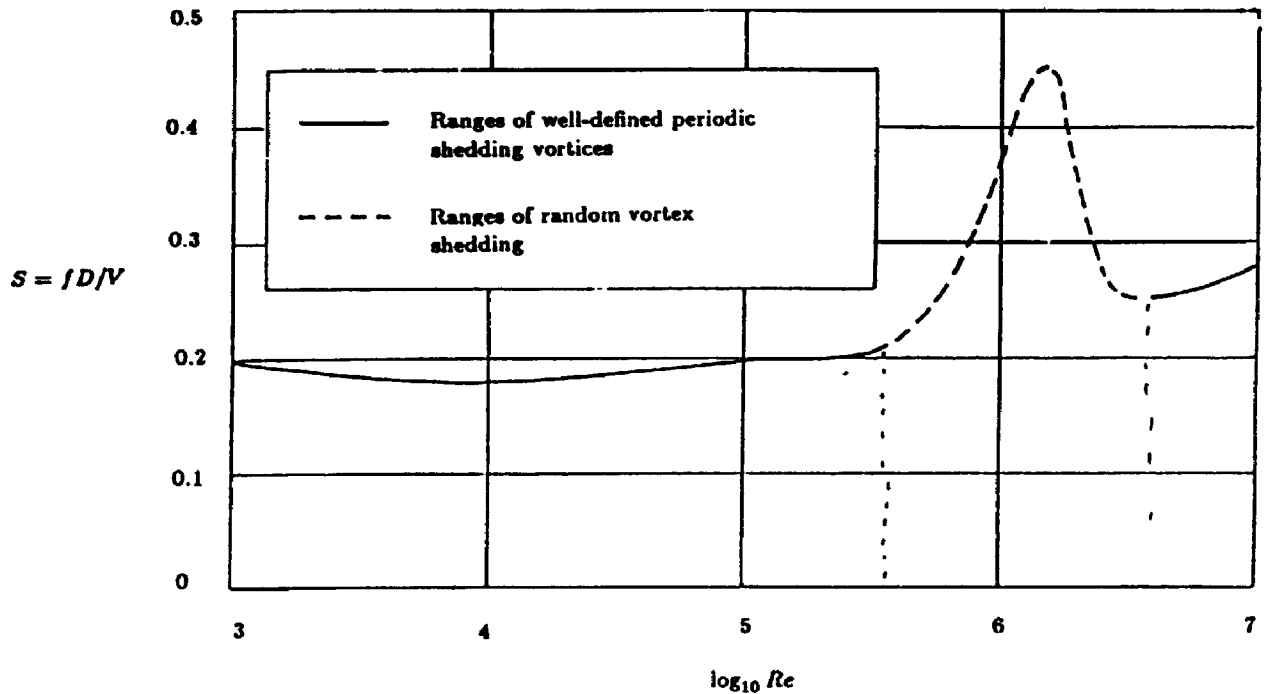
Figure 3.3: Variation of Strouhal Number with Reynolds Number for a Circular Cylinder[68]

bluff body, f_v, is related to the mean flow speed, V, and the size of the body, B, by a non-dimensional scaling parameter, which is now called the Strouhal frequency, or S. For a given cross-sectional shape, this parameter is reasonably insensitive to Reynolds number and is given by:

$$S = \frac{f_v B}{V} \qquad (3.1)$$

For two dimensional shapes, it typically takes on values in the range $0.25 \geq S \geq 0.14$. Figure 3.3 shows the variation of the Strouhal frequency over a wide range of Reynolds number for a circular cylinder.

The vortex shedding process has been observed over a wide range of physical scale. For example vortex shedding is the principle behind the Aeolian harp[70], in which musical tones are produced by the passing of air across the

harp's taut strings. At a much larger scale, satellite photographs of cloud patterns have shown trails of vortices as clouds move past the mountain peak of Guadaloupé Island off the coast of Mexico[69]. In this case the distance between successive vortices is on the order of 50 km.

The alternating action in the body wake imparts oscillatory forces on the body principally in the across wind direction. If the body is elastic, it will respond to those forces. It is conceivable that the body, under some conditions, may merely respond in an oscillatory fashion much like the buffeting action which occurs with along wind turbulence. However, it is the way in which an elastic structure responds and interacts with the vortex-induced forces which is the critical process underlying the vortex-induced vibration phenomenon and which differentiates it from simply across wind buffetting due to vortex shedding. It appears from all experimental data available, that the body motion and the vortex shedding interact in such a way that there is a net flux of energy from the fluid flow into the structure. In other words, with respect to the structure, a condition of *negative damping* is set up which acts to reduce the total damping available to the structure. Under certain conditions of structural properties which include sufficiently low structural damping and mass, oscillations of the body may be induced which grow in amplitude. The lower the damping of the structure, the greater are the amplitudes of the vortex-induced oscillations; however, even for negligible structural damping, the oscillations limit themselves to amplitudes on the order of the body dimensions. This suggests that there is a nonlinearity to the process; the flow and thereby the amount of negative damping it provides to the structure, is altered by the increasing amplitude of the body motion. The altered flow provides less net energy flux to the structure and so, at some amplitude, equilibrium of energies is again achieved.

If the flow velocity is increased past a certain range, the oscillations

diminish and cease. In fact, the vortex-induced oscillations are limited to a finite range of velocities where the frequency of shedding approximately coincides with the natural vibration frequency of the structure. There is also some suggestion that oscillations may occur at other frequency synchronisations such as when the vortices are shed at three times the body frequency[71,91,2].

Perhaps the most important feature of vortex-induced oscillations is the feedback which the body motion provides to the fluid flow. It is responsible for the self limiting nature of the oscillations as previously mentioned, but its presence is perhaps more clearly demonstrated by the so called lock-in effect. As the body responds to the forces resulting from the shedding of vortices, it provides time dependent boundary conditions to the fluid flow. The shedding of vortices is, consequently, affected to some extent. When the motion is large enough, the shedding of vortices becomes locked in to the body motion. If the velocity of the flow is then changed slightly, the vortices persist in shedding according to the body motion rather than the Strouhal frequency suggested by the flow velocity. If the velocity is changed sufficiently, however, the vortices again revert to the Strouhal shedding frequency. The results reported by Feng[34] for vortex-induced oscillation of a circular cylinder and reproduced in Figure 3.4 are most often quoted to illustrate the lock-in effect.

Hysteresis effects in the oscillation amplitude have also been observed in vortex-induced oscillation, see Figure 3.4 for example. Such effects have been verified by a number of researchers, however, there is not a clear relation between the occurrence of hysteresis and other experimental parameters. There is still a certain amount of debate as to the details, not to mention the causes, of the hysteresis observed. Greater detail regarding such debate can be found elsewhere[7].
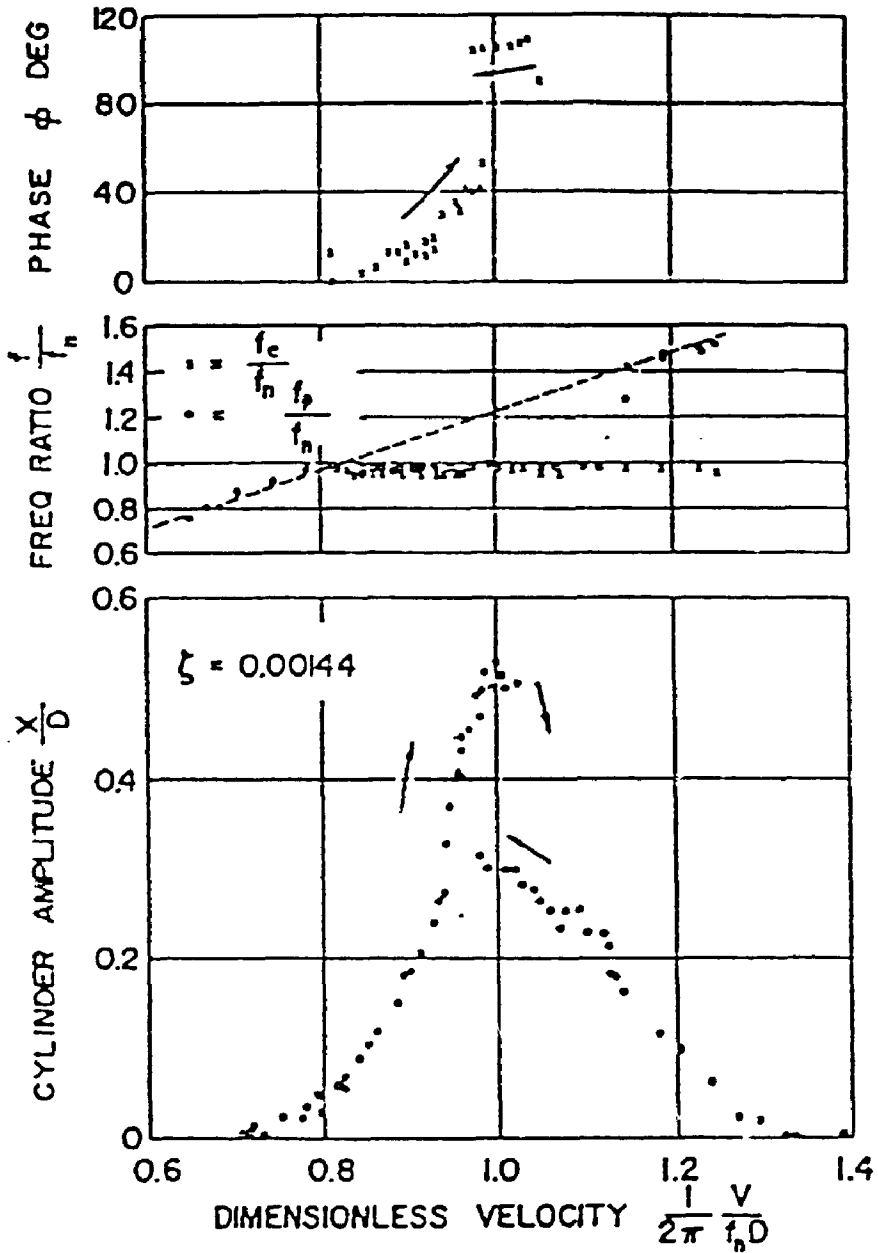
Figure 3.4: Vortex-Induced Effects on a Circular Cylinder[34]

3.2.2 Galloping

Galloping has been observed for some time in the large amplitude oscillations of suspended power lines and it is likely from observations of several lines strung in parallel and oscillating independently that the name originates. It has also been observed in guy wires, light stands, and tall chimneys.

The motion is generally a single degree of freedom oscillation perpendicular to the flow. It results from an aerodynamic instability associated with the cross-sectional shape of the body. A necessary, but not sufficient, condition for galloping is that a small cross wind motion perturbation of the body produces an increase in the perturbing aerodynamic force. Under assumptions of quasi-steady flow, this condition can be expressed by the well known Den Hartog's criterion[28]. Galloping is not possible for a structure which is axially symmetric such as a circular cylinder or wire; however, ice accumulating on suspended wires can alter a cross section which is otherwise stable. This particular problem has received much attention [29,51]. In smooth flow, galloping is also characterised by the existence of an onset or critical velocity at which the conditions of instability are reached and oscillations occur. Once galloping has begun, the amplitude of the oscillation generally increases with increasing wind speed and, unlike vortex-induced oscillations, may reach amplitudes which are many times the diameter of the body. Hysteresis may also occur in the oscillation amplitude as the velocity is increased and decreased.

Parkinson[60,58] was the first to treat the galloping problem analytically. He considered a two dimensional case using quasi-steady assumptions. Several researchers [71,80,91,65,48,49] have verified the theory for various experimental conditions and set-ups. Some illustrative results of Parkinson's which compare experiment and theory are reproduced in Figure 3.5. The critical wind speed at which
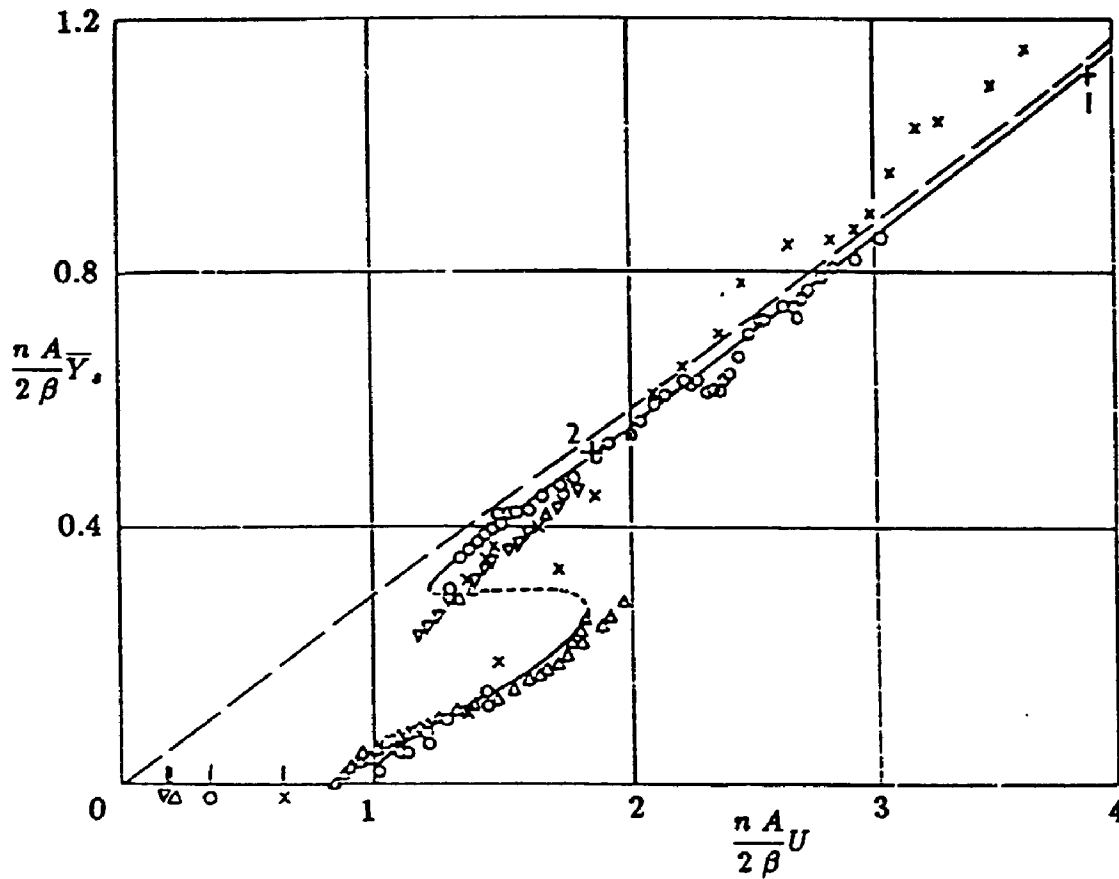
Collapsed amplitude-velocity characteristic. Theory: ——— Stable limit cycle, — — — Unstable limit cycle. Experiment: × β = ·00107, ○ β = ·00196, △ β = ·00364, ▽ β = ·00372, +1 β = ·0012, +2 β = ·0032

Reynolds numbers 4,000–20,000.

Figure 3.5: Amplitude-Velocity Characteristics from Theory and Experiment[58]

galloping begins, and the amplitude versus wind speed including hysteretic effects can be predicted quite well by the approach.

The theory is more successful at higher velocities, which is an expected consequence of the quasi-steady assumption. It breaks down at lower velocities and is inappropriate for speeds near and below the critical speed of vortex shedding. Hence if the vortex shedding range falls above·the predicted on-set velocity for galloping, the theory will not apply until well above this range.

In Chapter 7, galloping theory is compared with experimental results from the present research. Therefore a more detailed mathematical description is postponed until then. It is sufficient at this point to note that the approach involves identifying conditions of effective negative damping being supplied to the structure by the aerodynamic forces.

3.2.3 Interference between Galloping and Vortex-Induced Oscillations

The characteristic features of galloping and vortex-induced oscillations can be summarised as follows.

Vortex-Induced Oscillations	Galloping Oscillations
• flow-induced • body motion and flow interact	• self excited • quasi-steady – body motion does not significantly affect flow (at high reduced velocity)
• occurs in finite range of velocity near coincidences of vortex shedding and structural frequencies • hysteretic effects possible • motions self limiting on order of the body diameter • shedding process "locks-in" to body motion	• onset velocity after which amplitudes increase with velocity • hysteretic effects possible • motions may reach many diameters in amplitude

Galloping mechanisms are well understood in the sense that the occurrence and level of response can be predicted once certain aerodynamic properties of a cross section are known. Vortex-induced oscillations, on the other hand, have presented much greater difficulty. The interaction of the body motion and the flow adds considerable complexity to the problem over that of the galloping phenomenon. As a result, the present theories and models for predicting vortex-induced oscillations are somewhat primitive and unreliable. These will be commented on further in a later section. When conditions are such that both galloping and vortex-induced oscillations may be expected to be present, there is a further complexity introduced. This occurs when the speed is such that the frequency of vortex shedding is near the natural frequency of the structure, $f_v \approx f_s$, and at the same time, the quasi-steady aerodynamic forces provide sufficient negative damping to cancel the available structural damping.

In fact, it has been found [61,91,2] that when the galloping onset velocity, V_0 is *near* , but still higher than the range of vortex-induced oscillation , around

V_c, not only does the agreement with the quasi-steady galloping theory break down, but large amplitude vibrations may occur for wind speeds at which no vibrations would be expected if one considered either aeroelastic phenomenon separately. This is illustrated qualitatively in Figure 3.6. Vortex-induced oscillations begin at the speed expected, and then the oscillation amplitude increases with speed eventually approaching the expected values due to the galloping theory at higher velocities. When the range of vortex-induced oscillation falls above the onset velocity of galloping, oscillations may not occur when expected [35,33]. The expected galloping oscillations are suppressed until the vortex-induced lock-in effect or higher.

3.2.4   Influence of Turbulence

Most of the observations previously described have been in smooth flows. However, the effects of turbulence in the incident flow has also been noted. For example, Novak [48,50,49,52] has examined the galloping problem extensively and, based on energy considerations, extended Parkinson's approach to treat three dimensional bodies in turbulent shear flow. A surprising result of his experimental studies was that while increased turbulence generally diminished galloping behavior, in some cases it could produce galloping for mean speeds at which it did not occur in smooth flow. This was a result of the mean flow field around the body being altered by the presence of small scale turbulence.

Davenport[17,20] has emphasized the importance of including turbulence in wind tunnel model studies, because of the significant effects which it can have on tall structures as well as long structures such as bridges.

It is sufficient at this point to note that turbulence can have profound effects on aeroelastic phenomena. In some cases the wind loading is diminished,
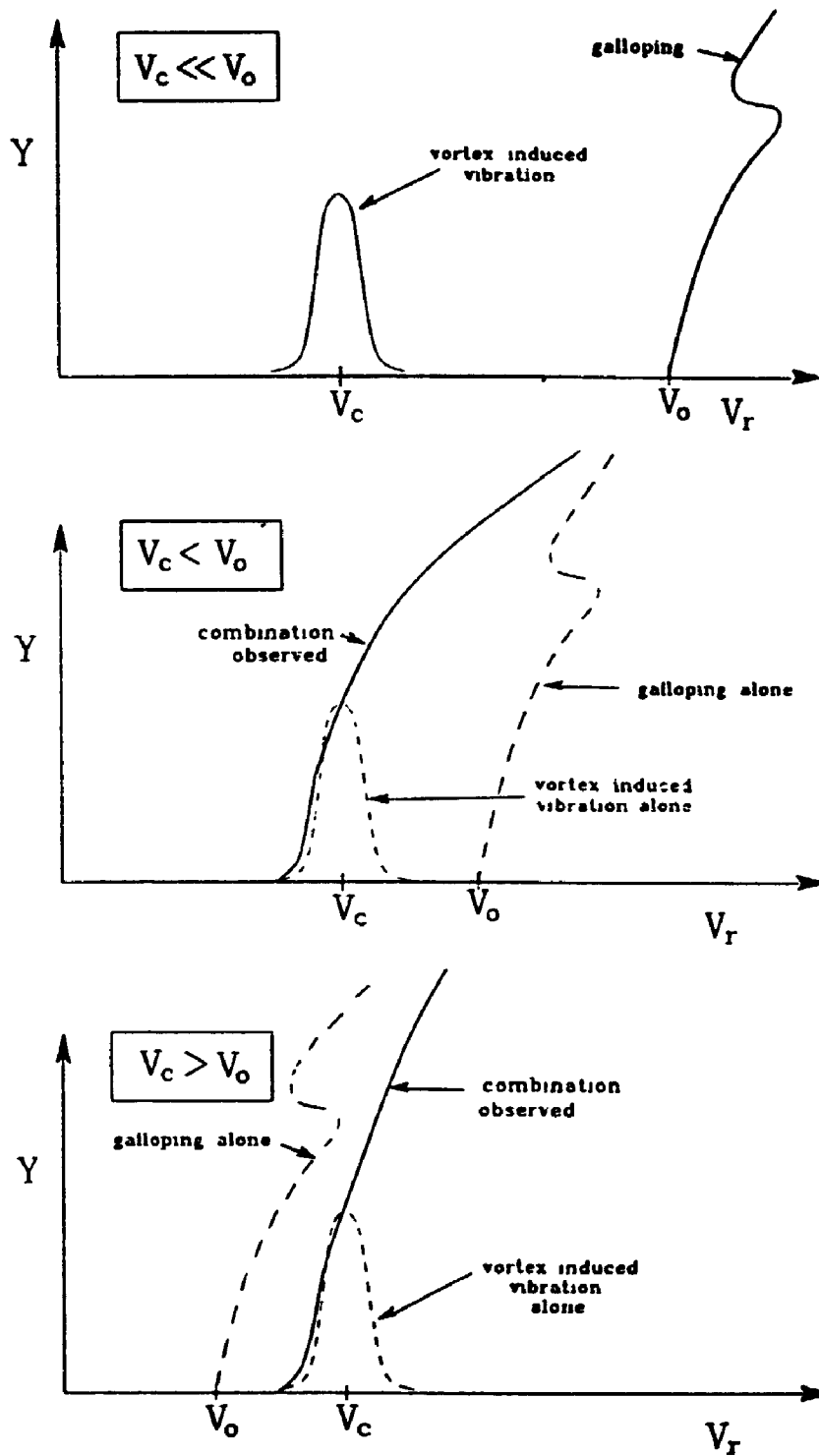
Figure 3.6: Combined Effects of Galloping and Vortex-Induced Vibration

but in other cases, instabilities may actually arise due to its presence. The varying effects of turbulence are not fully understood nor have they been fully identified, and so observations made in smooth flow cannot be readily extrapolated to turbulent flow.

3.2.5 Practical Effects on Tall Slender Structures

The main aeroelastic phenomena affecting tall slender structures have now been reviewed in some detail. The practical significance of these effects is worth highlighting.

Galloping oscillations are a potential problem for some very tall stacks and chimneys. The excessively large amplitudes associated with galloping can have disastrous affects.

Vortex oscillations are a more common problem for these structures and are a potential problem for very tall slender buildings. Although the amplitudes tend to be considerably smaller than those associated with galloping, they are still significant in magnitude. Moreover, because of lock-in effects, vortex-induced oscillations may have significant consequences on fatiguing of the structure.

As pointed out earlier, large amplitude oscillations may occur when vortex-induced vibrations and galloping interact and this may occur even at speeds that galloping theory alone would not predict. Such ranges of interaction are in fact possible for conditions that may be realistically encountered in the design of full scale towers and chimneys.

On the other hand, the interference between galloping and vortex-induced

oscillations may take on a beneficial role at speeds below vortex-induced vibration. It appears that the interference has the potential of quenching the galloping oscillations. This effect has been used advantageously in the design of cable trays on the Space Shuttle [33].

3.3 Experimental Approaches

Much of what follows in the present study is inherently concerned with the relationship between two experimental approaches in regards to motion-induced forces. For this reason, a brief discussion regarding these approaches is now undertaken. While this is done in the context of experiments, the real comparison which is of issue, is between motion-induced forces as they manifest themselves in practical situations and as they occur in a controlled experiment under forced oscillation.

3.3.1 Free Oscillation

The practical concern of motion-induced forces is their affect on real structures which are flexible, lightly damped, and subjected to the natural wind. While original recognition of the aeroelastic phenomena discussed in the previous sections have mainly occurred from practical observations, they have been verified over the years with controlled experiments using aeroelastic and hydroelastic models. These are here referred to as free oscillation experiments. Free oscillation, in general, refers to oscillation conditions which are free of any external forcing. In the context of the present study, however, the external wind force is assumed to be part of the natural conditions. Hence the term refers to conditions which are free of additional or artificial external forcing.

Such experiments can closely simulate practical or prototype situations. Experimental results such as those of Parkinson[58], Novak[48,50,49,52], and Feng[34], have contributed to the more detailed compilation of observations regarding both galloping and vortex-induced vibrations. Some examples have already been presented in Figures 3.4 and 3.5. They illustrate most of the features of these aeroelastic instabilities which have been summarised in the previous section.

Short of final practical applications, free oscillation experiments represent the ultimate testing ground for any models or theories of motion-induced forces and associated phenomena.

3.3.2 Forced Oscillation

The forced oscillation approach has been used extensively to investigate aeroelastic instabilities. It involves actively oscillating a model in a forced sinusoidal motion at controlled frequencies and amplitudes. The forces acting on the model and perhaps the flow around the model are then investigated. Some of the earliest experiments of this type were performed by Bishop and Hassan[9], and many subsequent investigators have used the approach. In most cases, the experiments have involved forced oscillation in a heaving mode[55,3,46], however, some research has been carried out using pivoting modes[83]. Forced oscillations are also sometimes used in practical wind studies of bridge section models to derive "flutter derivatives"[69,24,25].

In contrast to free oscillation aeroelastic experiments, forced oscillation experiments are primarily a research tool. They cannot be said to simulate practical situations of concern as an aeroelastic model test can. The approach does allow more control over the variables involved; the effects of oscillation amplitude and frequency can be separated and investigated one at time. However, more control

also means more interference with the natural phenomenon. For this reason, there is still some controversy over the use and representativeness of forced oscillation experiments. It is sufficient to acknowledge at this point, that great care must be taken in interpreting the results of forced oscillation experiments and in applying the results to situations of free oscillation.

Despite this cautionary note, it can be stated that a good deal of relevant information can be obtained from forced oscillation experiments. Details can be derived about the nature of the forces and the flow behavior which could not be feasibly obtained from even an extensive and meticulous set of aeroelastic experiments.

Other sources[7] have summarised the main observations which forced oscillation experiments have produced with respect to vortex-induced oscillation. (Less insight is gained from these experiments regarding the relatively well understood phenomenon of galloping).

3.4 Models of Vortex-Induced Oscillations

As previously mentioned, the current understanding of vortex-induced oscillations is relatively primitive. Several empirical models exist, which attempt to describe various aspects of the phenomenon and review papers describing the various models in use are published from time to time; see for example [66,59,57,69,30,39].

While it would be inappropriate not to include some description of these models here, a detailed discussion has been avoided. This is mainly because it is not within the scope of the present study to deal with the models in that manner. It is also due to the belief that most of the existing models conflict with some of the

essential features of vortex-induced vibration on a fundamental level.[2] Moreover these conflicts tend to undermine the finer details of the models and make further elaboration nugatory.

Vortex-induced vibration models, to date, generally fall into two categories; wake oscillator models, based on coupling the body motion with a nonlinear oscillator associated with the wake, and single degree of freedom models based on the idea of negative damping.

3.4.1 Wake Oscillator Models

The oscillator models have arisen principally from the observations of Bishop and Hassan[9] that the wake behind a bluff body exhibits some characteristics of a "nonlinear self-excited fluid oscillator." Their observations were based on both free oscillation and forced oscillation experiments. Probably the most well known of the oscillator models which followed, is that proposed by Hartlen and Currie[36]. It has been used as an example in what follows because it is also one of the simpler oscillator models and exemplifies some of the basic characteristics. Most of the oscillato models proposed since have been modifications or extensions of the basic idea. These have been applied in order to account for various additional features of the observed phenomena and to produce better comparisons with experimental data. Amongst these are the models of Skop and Griffin[70], Iwan and Blevins[44], Dowell[30], and Birkhoff[8]. Some models which attempt to include the effects of galloping as well have been proposed by Bouclin[13], and Corless[16].

For the limited purpose of summarising the models and exposing their

---

[2] This, perhaps bold, statement is supported by the very recent work of Billah[7], who has provided a comprehensive analysis of the current state of modelling vortex-induced oscillations.

merits and failings, it is helpful to discuss the models as a group and to adopt a general form of mathematical expression. The form below, with some change of notation, is that used by Billah[7] to describe smooth flov oscillator models.

$$\ddot{x} + 2\zeta_s\omega_s\dot{x} + \omega_s^2 x + \boxed{e\{x,\dot{x}\}} = \boxed{g(y,\dot{y},\ddot{y}) \equiv a_1 y + a_2\dot{y} + a_3\ddot{y}} \qquad (3.2)$$

$$\ddot{y} + \omega_v^2 y + \boxed{f\{y,\dot{y}\}} = \boxed{h(x,\dot{x},\ddot{x}) \equiv b_1 x + b_2\dot{x} + b_3\ddot{x}} \qquad (3.3)$$

where,

$$x \quad \longmapsto \quad \text{body position degree of freedom}$$
$$y \quad \longmapsto \quad \text{some degree of fieedom associated with the wake}$$
$$\left.\begin{array}{c} e\{\} \\ f\{\} \end{array}\right\} \quad \longmapsto \quad \text{NONLINEAR FUNCTIONS}$$
$$\left.\begin{array}{c} g() \\ h() \end{array}\right\} \quad \longmapsto \quad \text{LINEAR FUNCTIONS}$$

The function $e\{\ \}$ can serve to induce and to limit a vibration instability. In this sense it could include the functions which account for the galloping vibrations in the quasi-steady approach. This has been the approach of Bouclin[13] and Corless[16], for example. As to vortex-induced vibration models, the function $e\{\ \}$ has only been included in one — that proposed by Dowell [30] — where it served to limit the instability generated by other terms of the model's equations. But it is not necessary for $e\{\ \}$ to do this; that is, the remaining functions could serve the purpose.

The most prominent feature distinguishing the oscillator models is given by the function $f\{\ \}$. It is used to model the nonlinearity of the periodic wake and to account for its occurrence in the presence of a stationary body, wherein $x(t) \equiv 0$. To demonstrate this, consider the specific case of the Hartlen-Currie model. It uses

a lift force coefficient, C_L, as the wake degree of freedom and chooses a form for $f\{\}$ designed to make the left hand side of Equation 3.3 into a Van der Pol oscillator. For a stationary body, the equation describing the wake is then of the form,

$$\ddot{C}_L + \omega_v^2 C_L - \alpha_1 \dot{C}_L + \gamma_1 \dot{C}^3{}_L = 0 \tag{3.4}$$

with

$$\alpha_1 = \alpha \omega_v \tag{3.5}$$

$$\gamma_1 = \frac{\gamma}{\omega_v} \tag{3.6}$$

By appropriate choices of the parameters, ω_v, α, and γ, this can be made to give a solution for C_L which is in general agreement with experimer*. It should be emphasized that this is no surprise, and occurs by design. The form of the equation was chosen to simulate certain observations, namely that the wake acts like a periodic oscillator which is self-exciting, and self-limiting. These three qualities are respectively assured by the first two, the third, and the fourth terms of Equation 3.4, each being essentially the simplest mathematical form to do the job. In other words, the equation has no fat on it. *Any* periodic, self-excited, self-limiting phenomenon will necessarily have gross features in common with this mathematical representation, since it represents the essence of those qualities. The question to be asked of a particular oscillator model is how well it goes beyond this to model the behavior of the non-stationary body and wake system. It is at this point that any critical assessment of the models must begin.

The functions $g()$ and $h()$ serve to couple the equations and provide feedback between the wake oscillator and the body motion. It is particularly important to note that this is linear coupling, while the experimental observations suggest that a nonlinear coupling in fact exists between the body motion and the wake. The nonlinearity of the oscillator described by $f\{\}$ is sometimes mistakenly

thought to account for this interaction. It cannot. A second point worth noting is that, nonlinearity considerations aside, both $g(\ )$ and $h(\ )$ must be present to provide true feedback. If only one is considered, then the corresponding equation reduces to a case of forced oscillation with the forcing being defined by the solution of the remaining, independent, equation. This is clearly not the intention of the coupled oscillator model approach and should be kept in mind in what follows.

While Equation 3.3 succeeds, by the definition of $f\{\ \}$, in simulating the oscillator character of the wake of a stationary model, the motivating appeal of the oscillator model when first proposed, lay more in its behavior when a moving body is considered and the equations are coupled through some definition of $h(\ )$. In particular, if a forced oscillation situation is considered, so that the right hand side of Equation 3.3 is known, the nonlinear wake oscillator exhibits a synchronisation effect when $\omega_v \approx \omega_s$. This effect is a well recognised property of the forced Van der Pol oscillator[47,45] and very likely played an instigating role in Hartlen and Currie's original conception of their model since it is suggestive of the experimentally observed lock-in effect. But note that that the forced oscillation comparison is a contrived case. Not only is a control force term implicitly added to the first equation of the model, but it is done so in such a way as to effectively eradicate the function $g(\ )$. Hence feedback, which is the principal feature of the model beyond the basic oscillator concept, is destroyed. It is a crucial and neglected inadequacy of the model that the synchronisation effect is not well predicted[7] when feedback is restored, that is, when unforced or free vibration is considered and both equations are solved simultaneously.

As mentioned, various other models have been put forth which, through additional terms or alternative degrees of freedom, attempt to better describe the actual phenomena. However, it seems that, by and large, the existing oscillator models

fail to simulate the observed effects in regards to certain basic and phenomenologically distinguishing features. These failures may be summarised as follows[7]:

EXISTING COUPLED MODELS	ACTUAL PHENOMENON
• Body draws energy from the non-periodic flow	• Body draws energy from the periodic flow
• Body and wake oscillator both gain energy	• Body gains energy; wake oscillator transfers energy to the body
• The effect is due to frequency coalescing	• The effect is due to nonlinear interaction
• "Negative damping" condition not possible via body-wake interaction	• Body vibration initiated by "negative damping" condition

3.4.2   Single Degree of Freedom Models

Several models of vortex-induced vibration have been proposed which are aimed at a more practical and modest goal than is implied by the wake oscillator models. They attempt to simply predict those aspects of the vibrations which are of most concern for design purposes, namely the overall levels of response occurring for given system parameters.

It is reasonably convincing from the empirical observations that a strong coupling indeed occurs between the body motion and the action of the flow in the wake region. Nevertheless, these models consider the body motion as the only degree of freedom and discard attempts to model the wake in any direct sense. This approach is adopted for its mathematical simplicity and hence, in general, no

pretense of simulating the underlying mechanisms of the phenomenon is made.

For the present discussion consider a general form for the single degree of freedom models as:

$$\ddot{x} + \omega_s^2 x + 2\xi_s \dot{x} + \boxed{f\{x, \dot{x}\}} = \boxed{F_V(\omega_v t)} + \boxed{F_S(\omega_s t)} + \boxed{F_R(t)} \qquad (3.7)$$

Any "motion-induced" contributions to the phenomenon which come from the flow are included by one or more of the three functions, $f\{\ \}$, $F_V(\ )$, or $F_S(\ )$. The function $F_R(t)$, when included, describes the non-periodic random flow. The periodic forcing which comes from the flow is usually assumed to occur at one of the two frequencies, ω_v, or ω_s. The latter is used to account for the lock-in conditions. In some models, such as Staubli's[72], both are considered to be present at all times.

The magnitude of the forcing is dictated by empirically deduced force coefficients, which may be functions of the velocity as in the nonlinear model of Scanlan[69]:

$$\ddot{x} + \omega_s^2 x + 2\xi_s \dot{x} = \frac{\rho U^2 (2D)}{2m} \left[\overbrace{Y_1(K)\left(1 - \epsilon \frac{x^2}{D^2}\right)\frac{\dot{x}}{U} + Y_2(K)\frac{x}{D}}^{-f\{\}} + \overbrace{\frac{1}{2}C_L(K)\sin(\omega_v t + \phi)}^{F_V(\ )} \right]$$

$$(3.8)$$

where $K = \omega_s D/U$.

The use of experimental data in this manner sidesteps consideration of the underlying reasons that the force coefficients take the particular form or values that they do. Instead, the emphasis of the approach is on the resulting amplitude of the body response. In most models, only one of the forcing functions is considered

at a time and some ad hoc means of identifying lock-in and choosing between them is used.

In some models such as the ones proposed by Sarpkaya[66] or Staubli[72], the force coefficients and their variations provide the only contrib ations of the flow. That is, a function $f\{\ \}$, is not considered, nor is $F_R(t)$. When such a function as $f\{\ \}$ is used in these models, it provides a negative damping, which serves to initiate the body instability. In models such as Scanlan's above, the negative damping is nonlinear such that the amount of negative damping decreases with amplitude thereby limiting the instability as well. The function may also contribute an aerodynamic stiffness. This is generally considered to be of negligible consequence for small motions.

When $f\{\ \}$ is absent, the negative damping *effect* is instead given by the force coefficients of the functions $F_V(\ )$ and/or $F_S(\ )$. If only one of the three right hand side forcing functions is considered, then the difference is merely one of mathematical presentation. However, if $F_R(t)$ is also present, for example, then the force coefficients of either $F_S(\ )$ or $F_v(\ )$ provide damping of a slightly different nature since they serve to dissipate or add energy in respect of body motion at a specific frequency only. This is in contrast to damping provided from terms of the function $f\{\ \}$ which provides damping at all frequencies of body motion. Whether one or the other form of aerodynamic contribution to the body motion energy is more appropriate is a question which has not been addressed nor has the possible importance of this point for practical purposes been determined.

As a final specific example, consider the model proposed by Vickery and

Basu[1,85], in which the right hand side forcing terms are of the form:

$$w(t) = \overbrace{\frac{1}{2}\rho U^2 DC_L(t)}^{F_R(\,)} + \overbrace{4\omega_s^2\rho D^4\left(H_a Y sin(\omega_s t) + K_a Y cos(\omega_s t)\right)}^{F_S(\,)} \qquad (3.9)$$

In this model, the random forcing function $F_R(t)$ is considered in the first term on the right hand side. (Although it is expected to be, and is modelled as, narrow band about the frequency ω_s, it is not strictly a function which would be described by $F_S(\,)$.) A nonlinearity is included by making the force coefficient, K_a, a function of the response level, $\bar{y}$. While this model is considered to be based on "negative damping" it should be noted that it is unlike the negative damping of the Scanlan model. The negative damping effect which initiates the body motion is given by nonlinear force coefficients in a function of the $F_S(\,)$ type, and not by "viscous" damping terms in a nonlinear function of the $f\{\,\}$ type.

3.4.3 A Recently Proposed Model

A few additional comments are worth appending to this discussion due to the recent work of Billah[7]. He has carried out a comprehensive analysis of the current state of modelling vortex-induced oscillations. For a more detailed review of the models, and for insights towards future modelling attempts, this reference is highly recommended.

While many of the observations presented in the last few sections were made by the author during the present study, the overall set of conclusions regarding the inadequacies of the oscillator models, shown on page 60 is a reporting of Billah's findings. One further result of his study was the formulation of a new coupled oscillator model. It is somewhat more imposing with respect to the number of terms and the nature of coupling involved, than any of the previous models. However,

because it has resulted from a more careful consideration of all of the actually observed features of the phenomenon, and because it addresses, in particular, those aspects of previous models which have been found to be in contradiction with the experimental observations, this new model represents a significant departure from previous formulations. For this reason the actual model equations are reported here. The purpose is only to present the _form_ of the new model, for comparison to the previous models. For the more detailed discussion and analyses, which it deserves, the reader is referred to the original source.

The coupled equations are as follows:

$$\ddot{q}_1 + 2\omega_n \xi \dot{q}_1 + 2\alpha q_1 q_2 + 4\beta q_2 q_1^3 + (\gamma q_1 + \epsilon q_1^3)\dot{q}_2^2 = 0$$

$$\ddot{q}_2 + f(q_2, \dot{q}_2) + (2\omega_s)^2 q_2 + \alpha q_1^2 + \beta q_1^4 - 2(\gamma q_1 + \epsilon q_1^3)\dot{q}_1 \dot{q}_2 = 0$$

(3.10)

where q_1 and q_2 are a body and a wake degree of freedom respectively.

Perhaps the most significant departure from the general form of Equations 3.3, is that the coupling between the two equations is nonlinear. This coupling is created by all the terms containing both q_1 and q_2 or their derivatives.

3.5   Prelude to the Current Approach

In view of the practical effects that aeroelastic effects have on structures, the interest in investigating motion-induced forces, and determining reliable predictive procedures is more than academic. It is a current and active concern of designers. Design related methods of suppressing these aeroelastic effects do exist. For example helical strakes and porous shrouds have been shown to be quite effective in

disrupting the vortex shedding process on tall stacks[69]. Research is currently being carried out into the effect of holes through tall structures such as skyscrapers for mitigating vibrations[31,32], and into the advantages of deliberately designing the principal axes of the structure to be out of alignment with the primary directions of aerodynamic excitation[42]. However, these measures are not always feasible which leads us to the basic motivation for the current study.

A great need exists for efficient, reliable, and economical methods of estimating the aeroelastic effects on tall slender structures of conventional design.

When this problem was first tackled at the outset of this study, it was accepted somewhat out of necessity that the forced oscillation approach was an appropriate and feasible one to take. Some consideration was given to the possibility of developing more efficient aeroelastic model experiment techniques, perhaps involving a mounting rig on which stiff geometric models could be mounted and tested for easily adjusted mass, stiffness, and damping properties. The particular advantage which the forced oscillation approach had, however, was the potential to determine the motion-induced forces in isolation, that is independent of particular structural parameters. This suggested the possibility of predicting the response of the structure as a function of structural parameters, analytically, in a similar manner as currently practised with the base balance technique. Repeated tunnel testing would not be necessary, and the tests coulu be carried out without specific knowledge of expected properties other than the geometry. It was not until attempts were made to actually use the measured forced oscillation data, and to predict the outcome of free oscillation aeroelastic models that a legitimate confidence in the approach was ucquired.

Certain restrictions were adopted for the study. For example, only single

degree of freedom pivoting motion has been investigated. Some considerations of at least two degree of freedom motion would be in order for future investigation, however, it is not expected that those considerations will depreciate the present study and its findings.

The following chapters describe in detail the system for measuring motion-induced forces which was developed, the analysis techniques, and two significant experimental studies which were carried out to demonstrate the system. The system has been dubbed the Pivot Mode Activator System. For brevity, the acronym PMA has been used to refer to the system or to qualify results which have been obtained using it. Similarly the terms PP, BB and AERO have been used to refer to the forced oscillation pressure model, the base balance and the aeroelastic techniques respectively.

Part II

DEVELOPMENT OF THE PIVOT MODE ACTIVATOR SYSTEM

Chapter 4
Hardware

4.1 Introduction

The design of a device or system to routinely measure motion-induced forces presents some unique challenges. In many ways it must have the capabilities of a conventional sensitive base balance, criteria which are themselves somewhat demanding. In addition, for practical utility, it must be able to do the following:

- accommodate a reasonable geometric range of models which occur in practice, without any special adaptors or rigs being required

- activate the model at a controlled and monitored sinusoidal amplitude and frequency

- sense those forces acting on the model from external application; that is, independent of the internal inertial and elastic forces of the model-balance system

- finely resolve those forces; the ultimate forces of interest are no more than a few percent as large as the total wind force on the model, itself not a large signal relative to the inertial forces of the system

- correlate these forces with the motion of the model

- provide the necessary information without an excessive amount of additional wind tunnel time being required beyond the reg-

ular base balance approach

The system which has been designed has met these requirements although there are a few potential improvements which have been recommended for any future version and these will be discussed in Chapter 9.

The basic concept of the system is similar to the method used by some previous researchers[56]. Total forces on a model subjected to forced vibration are measured and the contaminating internal forces which are dependent on the particular model being used are subtracted out leaving, under ideal conditions, a signal which represents only the externally applied wind force.

The main hardware and procedural components of the system are:

- the activator device

- the signal processor

- the calibration and experimental procedures

- the data analysis procedures

In the current chapter the two main hardware components, the activator device and the signal processor, are described. Chapter 5 will describe some calibration and experimental procedures which have been found effective. Chapter 6 will detail the data analysis procedures.

4.2 The Pivot Mode Activator Device

4.2.1 Functional Overview

A photograph of the activator device is shown in Figure 4.1. Schematic diagrams are shown in Figures 4.2 and 4.3.

The main support plate sits flush with the wind tunnel floor. A pot like substructure on which the model is mounted is connected to the main support plate by two elastic pivots which lie along a common pivot axis as shown. The pivots allow the pot to rotate in one degree of freedom within a limited range. The pot is connected to a drive shaft which has an eccentric connection to a 3 horsepower variable speed DC motor located about a foot below the tunnel floor. The eccentricity of the drive shaft connection is exaggerated in the figure. It can be varied by an adjustment screw to obtain a range of oscillation amplitude and the variable speed DC motor can be operated over a range of frequency from about 1 Hz to well over 50 Hz. The result is an essentially sinusoidal forced oscillation of the test model in a pivoting mode of adjustable amplitude. In order to minimise the eccentric loading acting on the DC motor drive, a second auxiliary oscillation system is connected to the motor so that it operates 90° out of phase with the main oscillating system. An adjustable mass has been provided in the auxiliary system to tune the balancing of the main system if necessary.

The test model is actually mounted on a thin rigid mounting plate of smaller
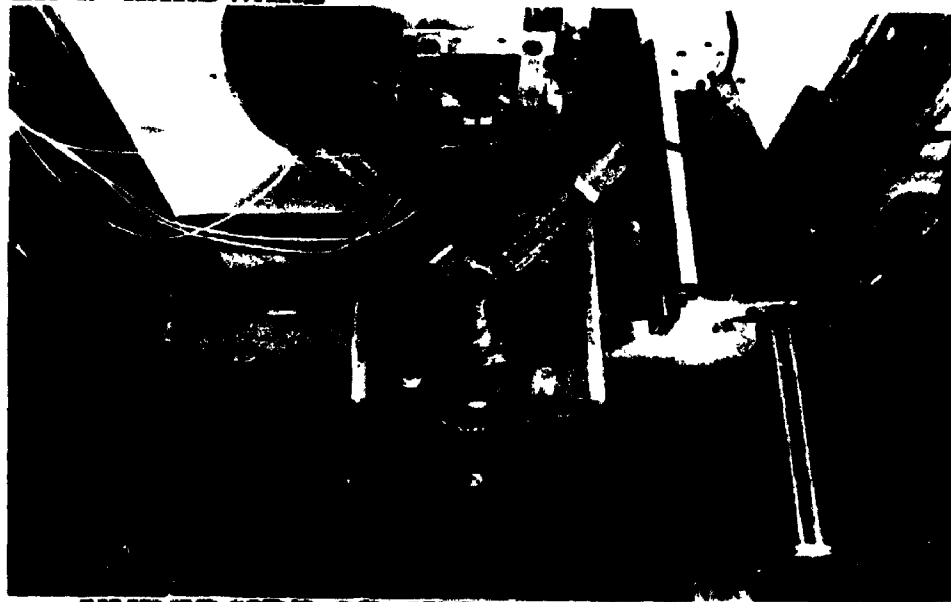
UNDERSIDE OF THE ACTIVATOR DEVICE
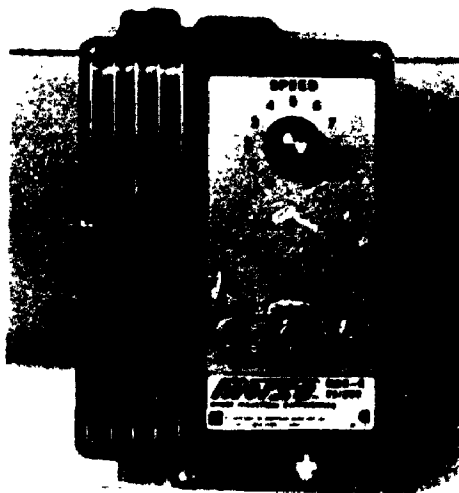
DC MOTOR SPEED CONTROLLER
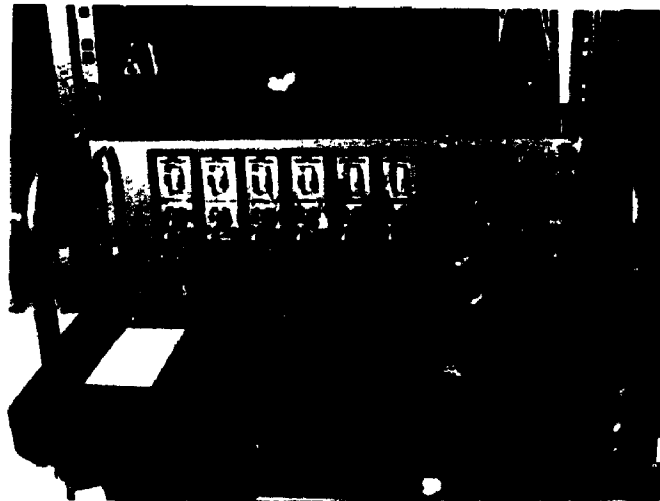
LOAD CELL DEDICATED AMPLIFIERS

PIVOT MODE ACTIVATOR SIGNAL PROCESSOR

Figure 4.1: Photographs of The Pivot Mode Activator System Hardware

2
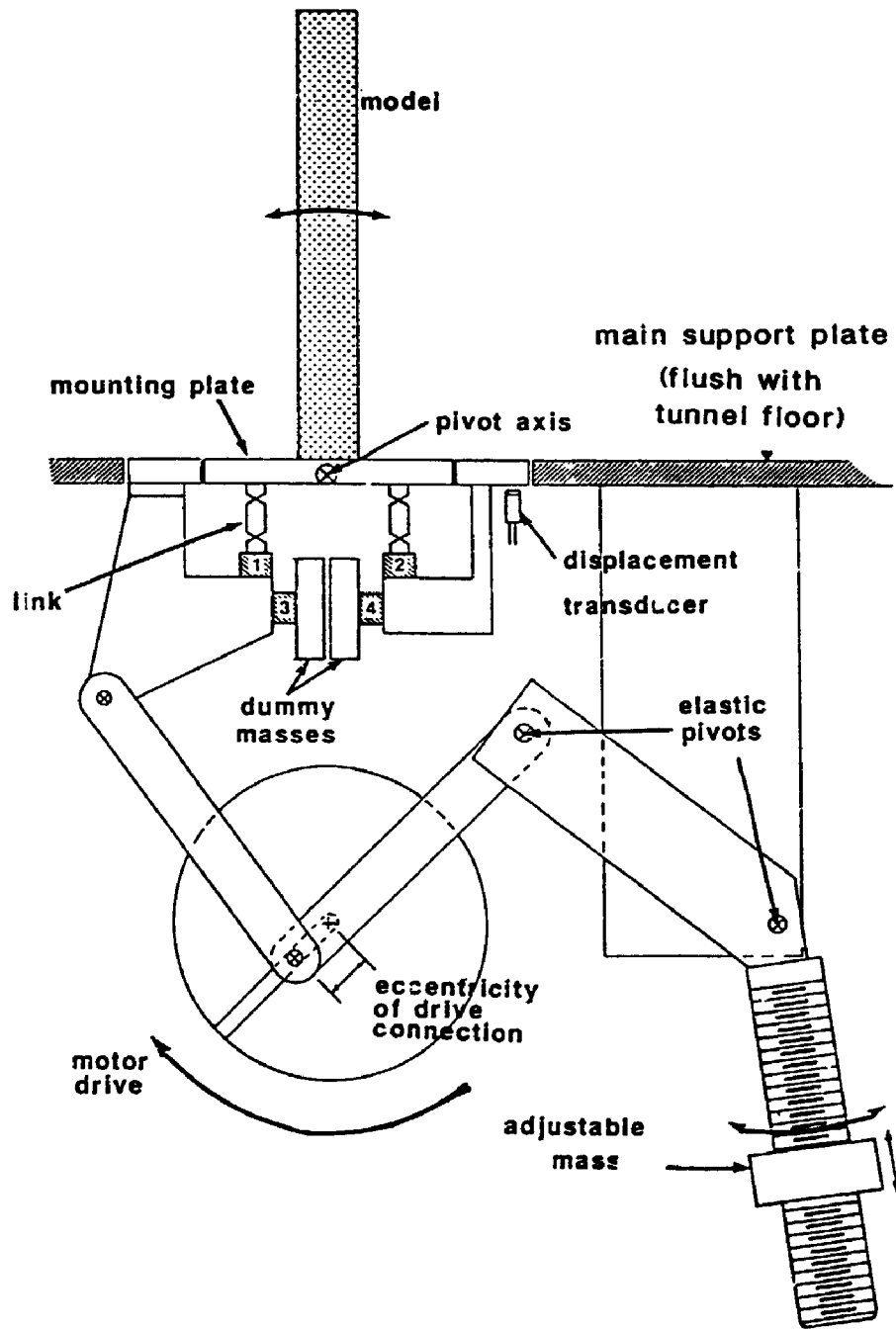
Figure 4.2: Schematic Diagram of the Pivot Mode Activator (PMA)
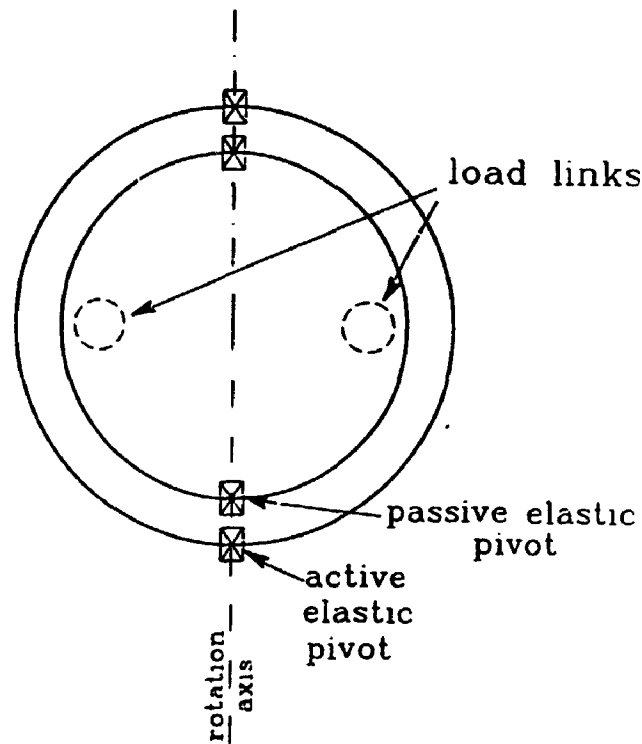
Figure 4.3: Top View of the Activator

diameter than the pot substructure. The mounting plate is connected to the pot by two more elastic pivots also located along the pivot axis and by two load transmitting links. The pivots take up essentially all loads acting on the model except moments about the pivot axis and some portion of the vertical lifting load. These loads are instead opposed by the vertically stiff links. The design also includes a mechanism for rotating the mounting position of the model about the vertical axis so that the oscillation will occur in a chosen direction relative to the model geometry.

Four piezo-electric crystal load cells are employed for the measurement of forces. These transducers are very stiff and robust and offer a higher degree of force resolution than conventional strain gauges. They are utilised in two pairs and are labelled 1 - 4 in the Figure 4.2. Load cells 1 and 2 are sensitive to forces

transmitted vertically through the links. Note that the model and pot substructure are designed to move as a unit with negligible relative motion. The load links and elastic pivots supporting the mounting plate are incorporated simply to channel the overturning moments as completely and purely as possible through load cells 1 and 2. Load cells 3 and 4 are connected rigidly to the lower region of the pot substructure. Attached to them are two small dummy masses of identical design. These load cells are sensitive to forces acting horizontally and therefore measure the inertial forces due to the dummy masses. This in turn provides a direct measure of the acceleration of the oscillating system as well as convenient signals which can be amplified and used to balance out the undesired inertial forces of the model.

For very small oscillations and for ideal linkage design only one of each load cell pair is necessary to provide the necessary experimental information; however, the load cells are employed in pairs in order to take advantage of the symmetry of contaminating loads in the system.

Particular subcomponents will now be discussed in more detail.

4.2.2 Elastic Pivots

The elastic pivots used in the activator device are cantilevered *Bendix Flexural Pivots*[1]. These are frictionless bearings of limited angular travel. Their construction can be seen shown in Figure 4.4.

---

[1] model no. 5012-400

Figure 4.4: Elastic Pivot Devices

There are ten of these pivots located throughout the activator. Eight are active in that they undergo cyclic angular deflections as the system oscillates. They are used in the drive linkage connections of the main and the auxiliary oscillating system. The last two pivots are passive and undergo negligible angular deflections. They are located along the rotation axis, between the model mounting unit and the oscillation pot. Their purpose is to provide load resistance to all loads acting on the model except the overturning moment of interest and to provide as little resistance to that as possible.

The main advantage of elastic pivots over regular bearings is that they are essentially frictionless and require no lubrication. They do, however, resist deflection elastically. By the geometry of their construction, this resistance is nonlinear particularly in the shearing directions. Furthermore, the data available from the manufacturer regarding the stiffnesses are limited and acknowledges considerable scatter. This all makes prediction of the dynamic influence of off-the-shelf pivots

difficult to predict and uncertain at best.

4.2.3 Load Cells

Four piezo-electric load cells are used in the activator[2]. Piezo-electric load cells offer distinct advantages over conventional transducers such as strain gage bridge systems. The cells are each constructed of two thin quartz disks or plates operating in a thickness compression mode and capped by hardened steel cylindrical members. This design offers a stiffness approaching that of a solid steel cylinder. The nominal sensitivity is 50 mV/lb with a range of ±100 lbs and a large physical overload capacity. The sensitivity is .002 lbs. These qualities make the devices excellent for the particular application. The main disadvantages are slow zero drifts and temperature effects, and an inability to pass DC.

The time constant of the particular cells used is 500 seconds allowing reasonably low frequency response. For the current application, however, only dynamic response above about 5 Hz was of concern, and so the amplifiers are run in AC mode. The amplifiers allow gains of 0, 10 or 20 dB. This adds some additional flexibility in balancing the outputs which is discussed in § 5.2.2.

The load cells are designed for axial load sensitivity, but some minor sensitivity to cross loads, particularly shearing, remains. Although optimum load paths

---

[2]Specifically, *Piezotronics* model 208A02 force transducers. The power and amplifier units for these particular transducers are *Piezotronics* model 484B.

have been designed in the activator, these cross sensitivities could still contaminate the outputs of individual load cells. Of less consequence, but notable, is that the construction of the cells is not completely symmetric and so when they are used in motion, their own mass adds some inertial loads which are directionally asymmetric. To minimise these contaminating effects, the cells have been used in pairs and installed so that the undesirable loads are cancelled out in practice. For example, in the case of load cells 1 and 2, any horizontal shear loads or vertical lift loads are cancelled out when the signals are differenced. At the same time, the overturning moments transmitted through the cells as axial loads are magnified as one cell will experience axial tension while the other experiences compression.

4.2.4 Load Links

The two load links shown in Figure 4.2 connect the model mounting unit to load cells 1 and 2. Their construction is detailed in Figure 4.5. They are designed to provide maximum axial stiffness and minimum lateral stiffness, while providing sufficient safety against buckling. The resulting ratio of axial to lateral stiffness is about 570. The minimum buckling loads are in excess of 150 lbs. They are constructed of hardened steel piano wire inserted in a machined body as indicated.
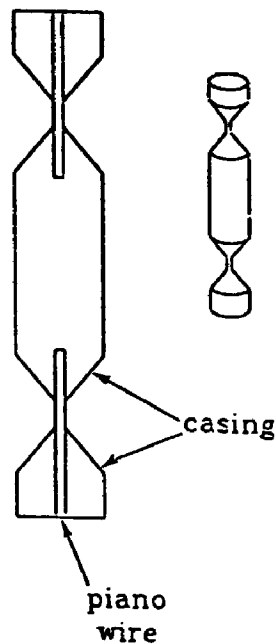
Figure 4.5: Load Link Construction

4.2.5 Drive Linkage

The two drive links are connected to the pot substructure and to the auxiliary oscillating system by pairs of elastic pivots. They are connected to the motor drive cam by greased bearings which allow full angular rotation. The eccentricity of the cam connection can be adjusted and locked at any location from 0 to .5 in. This represents a much larger range of angular motion than is expected to be of practical interest.

The two drive arms are about 6.4 in. between active connections. This length is sufficient to maintain a very nearly sinusoidal oscillation of the model while still keeping the whole device reasoι ʰly compact. Using the notation of Figure 4.6, the
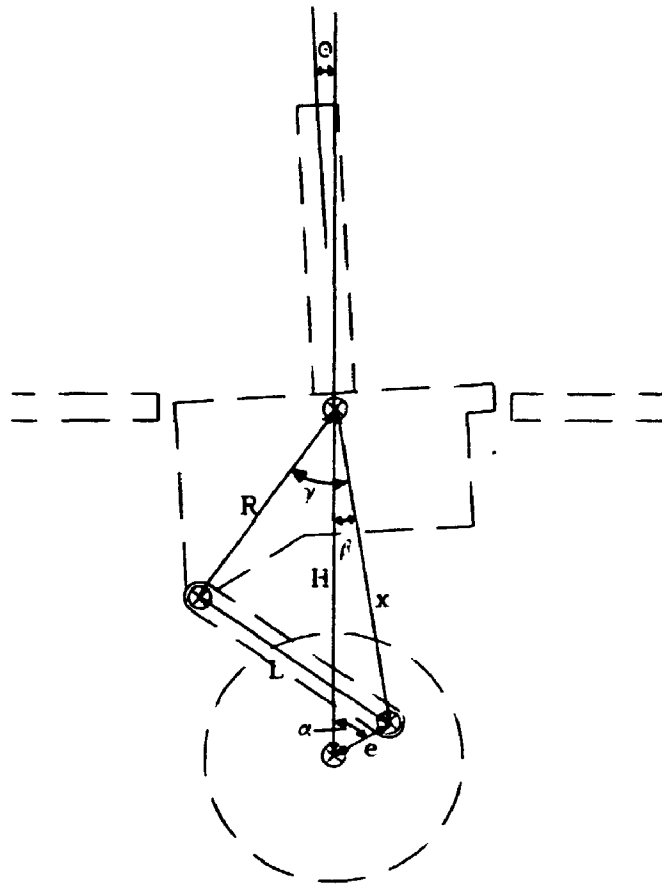
Figure 4.6: Linkage System Notation

actual path of motion is defined by following set of coupled equations:

$$\theta = \gamma - \beta - constant \tag{4.1}$$

where

$$\gamma = arccos\left[\frac{L^2 - x^2 - R^2}{-2xR}\right] \tag{4.2}$$

$$\beta = arcsin\left[\frac{e}{x}sin(\alpha)\right] \tag{4.3}$$

$$x = \sqrt{e^2 + H^2 - 2eHcos(\alpha)} \tag{4.4}$$

The deviation of the paths from a pure sinusoid, which is indicated by this geometry for the current design is shown in Figure 4.7 for a peak angular ampli-
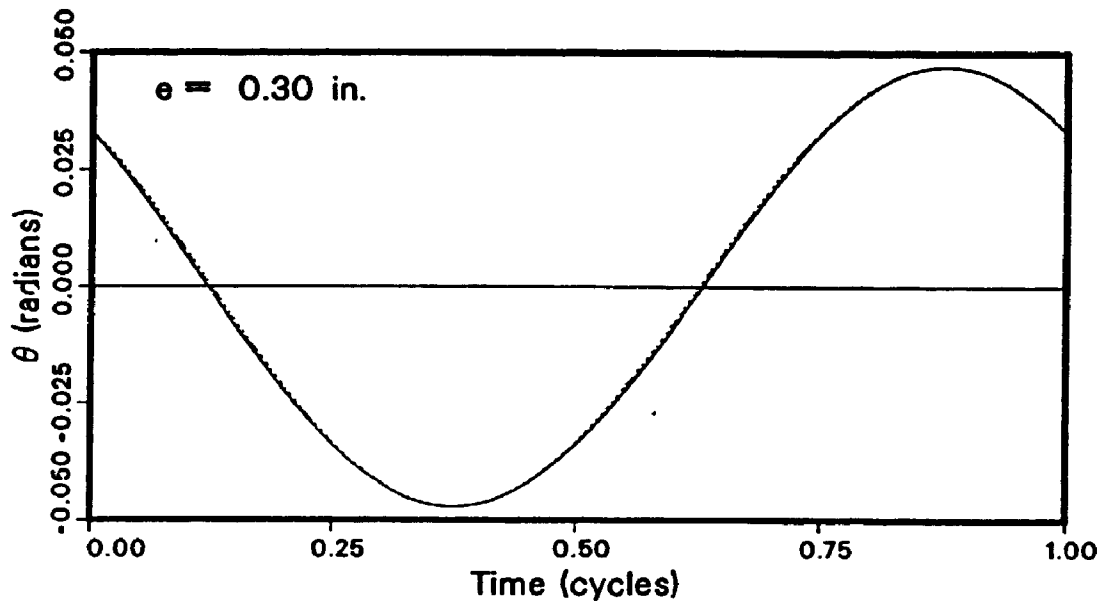
Figure 4.7: Deviation of Forced Motion from a Pure Sinusoid

tude of about 2.7°. Even at this rather extreme amplitude, the deviation is barely noticeable in the figure. It is small enough to neglect for practical amplitudes.

4.2.6 Motor Drive and Controller

The motor used to drive the oscillator and its controller unit can be seen in the photographs of Figure 4.1. It is a 3 HP variable speed DC motor. The motor can be run at any speed from about 1 Hz to well above 50 Hz oscillating the model at the corresponding frequency. The activator was designed with the nominal range of 5-25 Hz in mind, however, some system resonances occur just above this range and so operation has been kept to no more than about 22 Hz.

Without the auxiliary oscillating system, the motor drive would experience an unbalanced load from the inertia of the model and pot substructure. The auxiliary system has been designed to balance the inertia of the pot substructure. It operates 90° out of phase with the main system. The 3 HP motor should be sufficient to adequately control the oscillation motion for any small or medium size model. For larger models, a threaded mass has been constructed which can be located anywhere along the auxiliary system shaft shown in Figure 4.2. This is intended to maintain a balanced load on the motor drive.

The speed of the motor can be controlled by manually setting a potentiometer on the front of the controller. This was the method used in the intial developmental tests; however, the controller was then modified so that the speed can be controlled by a DC voltage level fed into the controller unit. In this way the D/A unit of the data acquisition computer can be used to automatically set or slowly vary the speed of the motor during the data aquisition. The swept frequency method to be described in the next chapter is based on this automatic control. The controller can be switched between manual and automatic modes.

4.2.7 Design Analysis

Dynamic analysis during the design of the activator device was limited to the structural subsystem of the pot substructure, model mounting unit, model, and their interconnections. It therefore included the load links and the two passive pivots for which effective stiffness values were taken from manufacturer's data. The analysis was carried out using a structural analysis program, STRESS, which was available

at the time. This program provides static load analysis; however, it was used iteratively to perform a dynamic analysis. This was done by converging on the inertial loads which balanced corresponding elastic loads, from which an estimate of the fundamental vibration frequency and mode shape could be made. Higher vibration modes could be successively estimated by seeking load shapes orthogonal to the previous ones. A more elaborate dynamic analysis was not performed because it was recognised that the the most flexible parts of the structure, namely the active elastic pivots, were not included – their properties were not adequately known. This analysis was used simply to check that the natural frequencies of the considered subsystem were well out of any operating range.

Structural analysis software, (STRESS), was also used to assist in designing the load paths of the system and to check that overloads would not readily occur. It was ensured that cross loading of the load cells was kept less than a few percent. This cross loading occurs, for example, due to distribution of horizontal shear resistance or of vertical lift resistance between the load links and the passive pivots. These cross loads are further diminished in practice by the pairing of load cells as previously discussed.

The activator can be operated over a wide range of oscillation amplitude and frequency. Signal levels will increase for larger amplitudes and for higher frequencies; however, greater fatigue effects will also result on the elastic pivots. Excessive increases in these variables can also take the load cells outside of their operating range or buckle the load links. These bounds of operation are also a function of the model mass being oscillated. In order to indicate the safe operating zones, a "typical large model" has been defined as a square prism 24 in. high with cross-
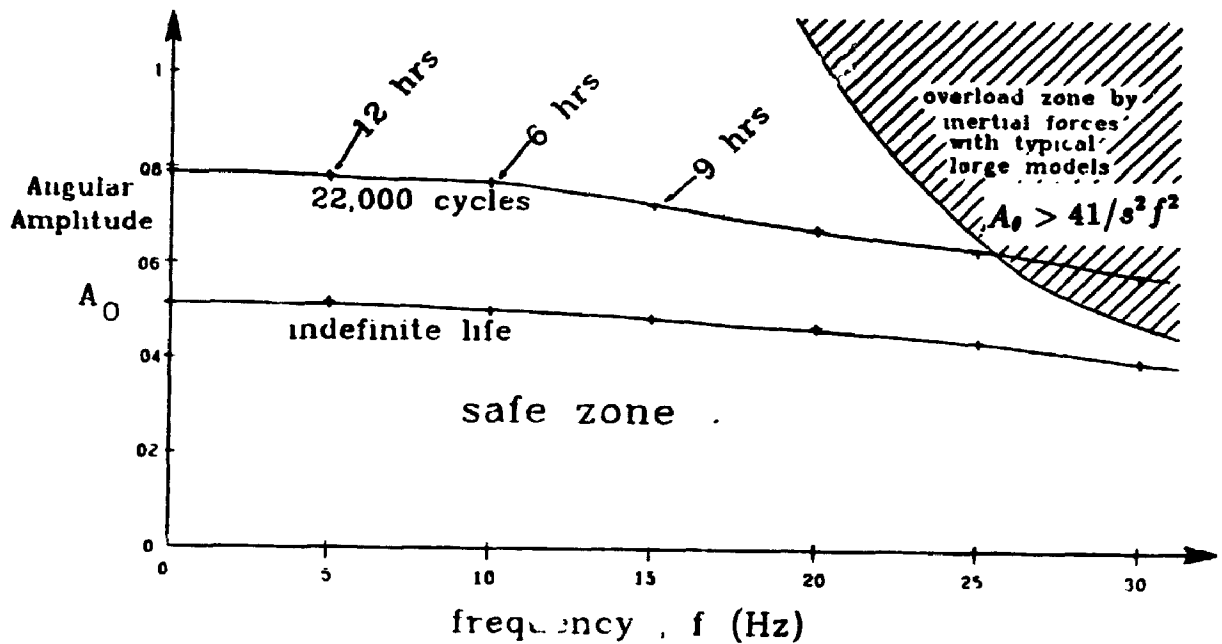
Figure 4.8: Safe Operating Zones for a Typical Large Model

section of 3 in. × 3 in. and a density of about 70 kg/m^3. For this model, Figure 4.8 shows the safe operating zones with respect to inertially induced loads resulting on load cells 1 or 2 as a function of amplitude and frequency of oscillation. Also shown are lifetime limit curves for the active elastic pivots based on manufacturer's data. Figure 4.9 shows the range of reduced velocities which can be achieved without overloading the load cells. A reference velocity of 8 fps is assumed for this graph.

4.3 The Pivot Mode Activator Signal Processor

In principle the processing of the raw signals from the load cell amplifiers, could be carried out digitally by a computer, however,if the A/D conversion is done at this early stage, then there is some loss in signal resolution which becomes more

overload zone by
inertial forces
typical large model
V = 8 fps   B = .25 ft

$$A_\Theta > 41 \, s^{-2} \frac{B^2}{V^2} V_r$$

Angular Amplitude A_Θ

V_r (reference to gradient)
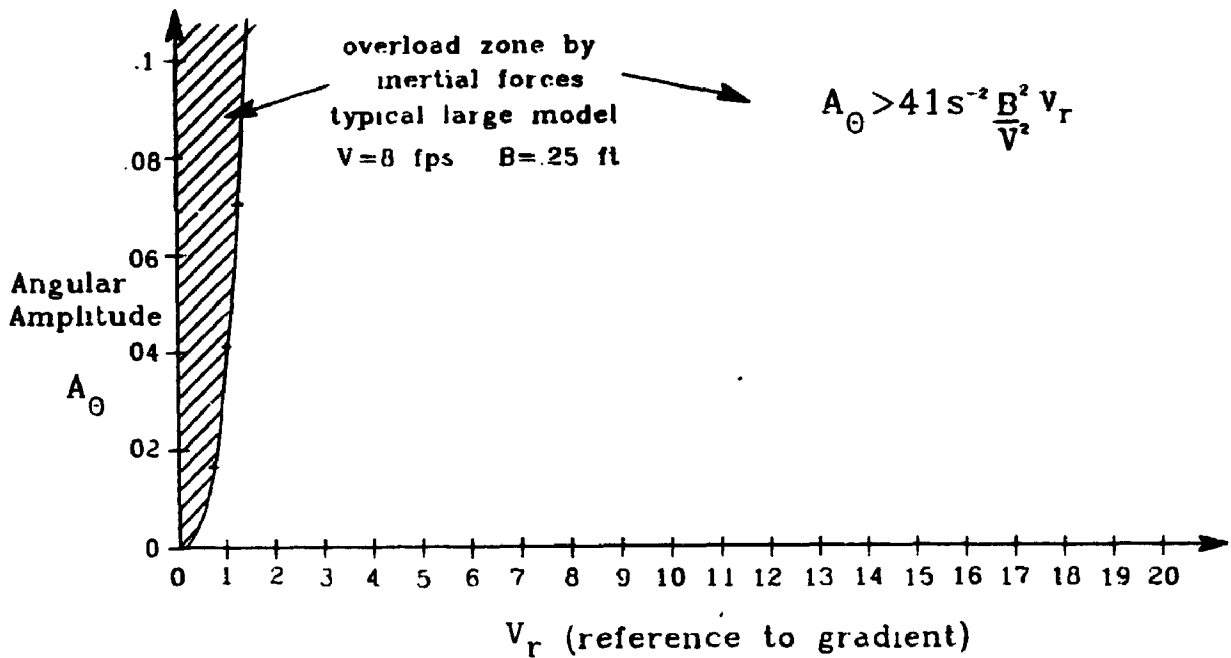
Figure 4.9: Ranges of Achievable Velocity and Amplitude for a Typical Large Model

significant later. It is more profitable to perform the necessary amplifying and combining of signals by an analog signal processor first. This approach also allows more ready access to the signals of interest for calibrations and for monitoring an experiment.

A photograph of the PMA Signal Processor is included in Figure 4.1. A schematic diagram is shown in Figure 4.10.

The gain amplifiers in Stage 1 are provided to balance the calibrations between partner cells. Although the calibration factors of the load cells are all nominally the same, with expected variations of a few percent at most, it was found that once installed they differed by as much as forty percent between partner cells. The

CHAPTER 4. HARDWARE
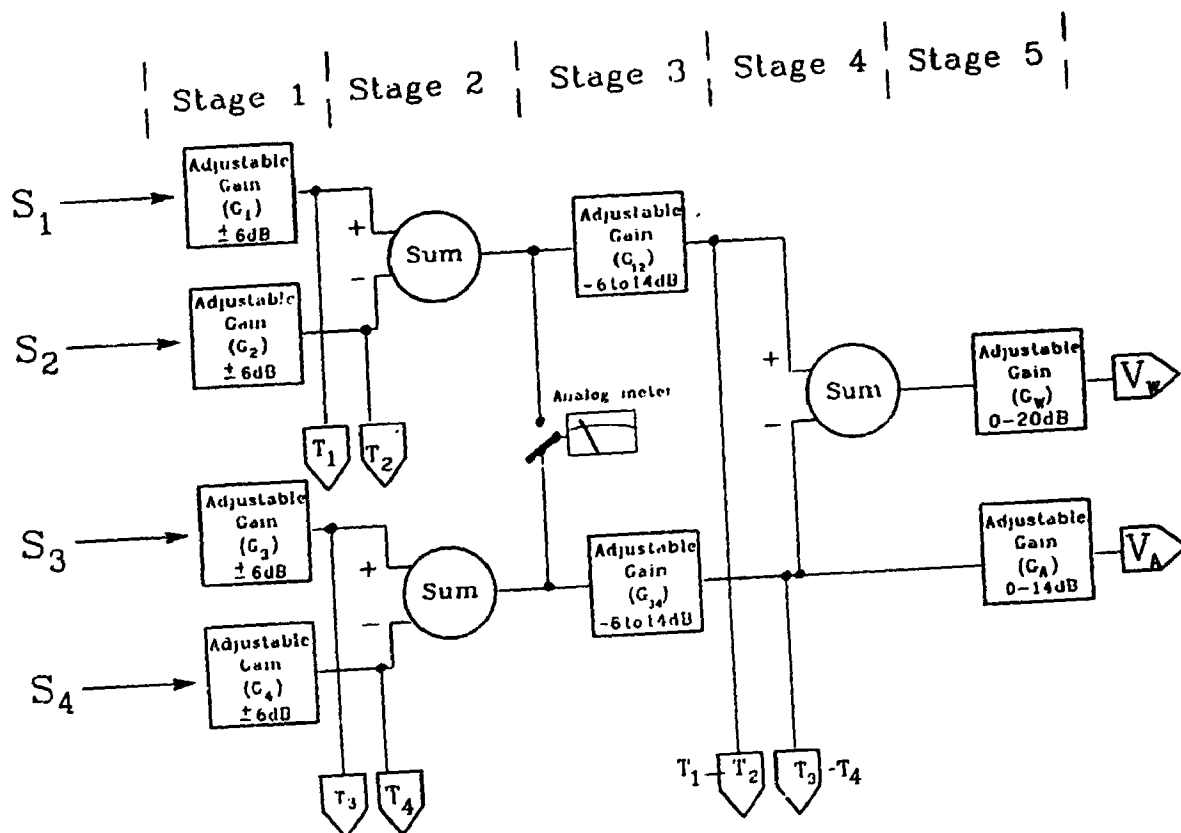
Figure 4.10: Schematic Diagram of the Pivot Mode Activator System Signal Processor

calibration factors were found to be sensitive to the particular static compressions on the cells exerted by the mounting screws. To accommodate this, the variable gain ranges of Stage 1 were modified from an originally designed range of ± 1 dB to the final range of ± 6 dB as shown. Stage 2 combines signals from partner cells. This, as mentioned earlier, takes advantage of the symmetry of the physical system to diminish sensitivity to loads such as vertical lift, while augmenting the sensitivity to the loads of interest, such as moment in the case of the first pair of cells and horizontal inertia in the case of the second pair of cells. In Stage 3, the balancing of the signal representing overturning moment and that representing acceleration of the system is performed. A wider range of gain factor is provided here because, in general, the acceleration signal which is due to the inertia of the dummy masses, is much smaller than the overturning moment which is due mostly to the inertia of the model. The final differencing of signals is performed in Stage 4, resulting in a signal which represents, under ideal conditions, the wind force or other externally applied force on the model. Stage 5 provides for final amplifications to provide signals suitable for on-line digital data aquisition. Output buffers are included at various nodes of the circuit. Direct access to these were of considerable use during the developmental diagnostics.

A specific subsystem, including an analog meter display, was included to assist the balancing procedure. It was found, however, that in certain ranges of oscillation frequency, the reference signal contained a significant contamination due to the non-ideal dynamics of the activator device. Balancing of the signals could still be sufficiently performed but it was more easily done by directly viewing the intermediate signals on an oscilloscope.

The two main outputs have been labelled on the hardware as *W* for the wind force signal and *A* for the system acceleration signal. Throughout this text they will be denoted as V_W, and V_A respectively, to emphasize that they are at this stage, *voltage* signals.

The load cell dedicated amplifier and power drive units contain high pass filters, however, there remains some drifts in their outputs. Although they are small, these drifts are significantly amplified through the signal processor. It was found useful in practice to at times include high pass filters after the signal processor so the peaks of the output signals were not carried out of range of the A/D converter by the small input drift signal. When used, these filters were set to a cutoff frequency well below 1 Hz. Low pass filters were also included at this stage to remove high frequency noise. **It is recommended for any future design that at least the high pass filtering be included within the signal processor at appropriate points so as to ensure that the intermediate signals cannot drift outside the operating range of the operational amplifiers.** There is no indication that this has occurred in any of the data collected to date, however, the potential exists.

During the developmental diagnostics, it was sometimes necessary to check the individual amplifier gain settings within the signal processor. To assist in this, program PMACAL was written which uses the D/A unit to provide known DC inputs to the signal processor. It then checks the outputs. In this way, the gain settings of each of the amplifiers is systematically determined by the program. For the current design, with no internal high pass filtering, the program remains useful for providing a record of the gain settings. PMACAL outputs are shown in
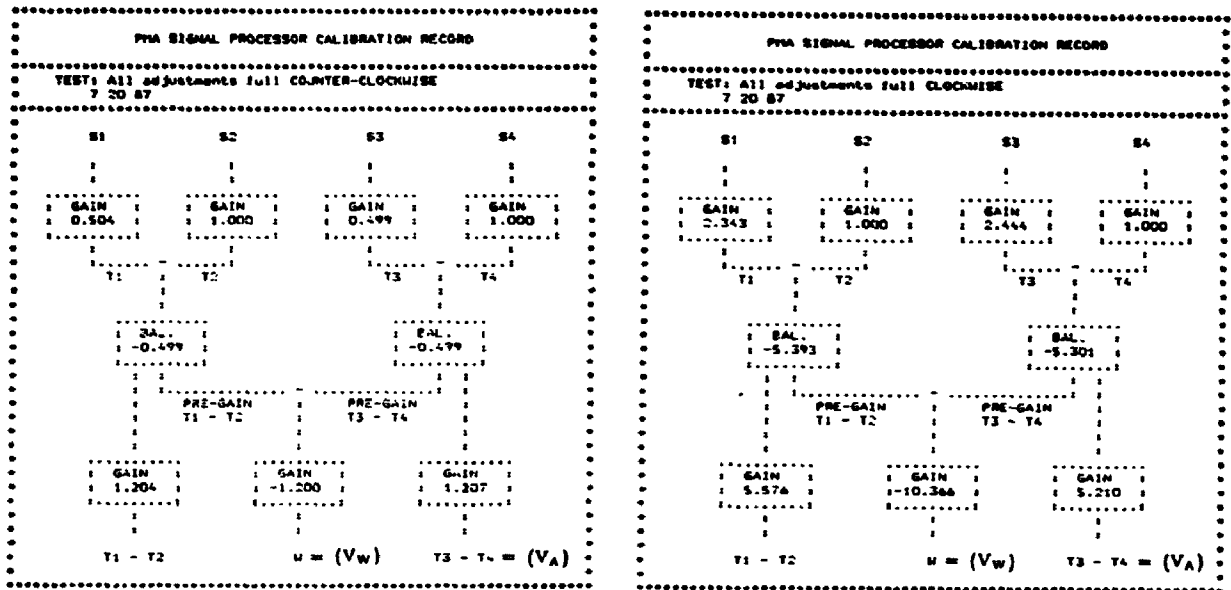
Figure 4.11: Gains Associated with Extreme Settings of the PMASP Adjustments

Figure 4.11 which record the gains associated with extreme clockwise and extreme counter-clockwise settings of the signal processor adjustment screws.

Chapter 5

Calibration and Experimental Procedures

5.1 Introduction

Due to the sensitivity of the system to internal dynamical effects, specific calibration and experimental procedures have been found necessary. These effects and procedures will now be described in detail.

5.2 Calibration

The first step in the calibration process consists of activating the model at a particular amplitude and frequency with no wind on the model and "balancing" the system by adjusting the signal processor amplifiers so that output V_W is essentially zeroed out. Any additional forces applied to the oscillating model when the wind is turned on will then be represented in this output[1]. Ideally this representation would

---

[1] In principle, this procedure will also balance out a small amount of aerodynamic force which occurs as the model moves through still air; however, the contribution that this neglected force is

persist if the amplitude or the frequency of oscillation were changed. In practice, however, the dynamic properties of the activator system as well as the turntable on which it is mounted cause the output to deviate from its balanced state if one moves to conditions different from those under which the initial balancing was carried out. As a result the direct representation of wind force degenerates. As will be seen these effects do not present a difficulty for the practical measurements although they must be precisely dealt with. The second step of the calibration process consists of determining the appropriate conversion factor to relate the V_W voltage signal to actual units of overturning moment. The following discussion first deals with some important aspects which influence the calibration and the testing itself. After that, the calibration procedures which have been found effective are detailed.

5.2.1   Dynamical Effects

It is illustrative to consider the turntable effect in more detail. The BLWT II[23] turntable on which experiments with the PMA system have been performed, has a natural across tunnel sway mode of vibration at approximately 3 Hz. This is shown schematically in Figure 5.1. Under rigid turntable conditions, load cells 3 and 4 produce a signal directly proportional to the acceleration of the dummy masses which are in essentially harmonic horizontal translation for the small oscillation amplitudes which concern us. Consequently, the signal is proportional to the acceleration in an inertial frame of any reference point on the model. This is usually chosen to be the tip of the model. As the dummy masses accelerate to the left, the model tip accelerates to the right and vice versa. The acceleration of the dummy

---

expected to make to the final motion induced forces of interest is negligible.
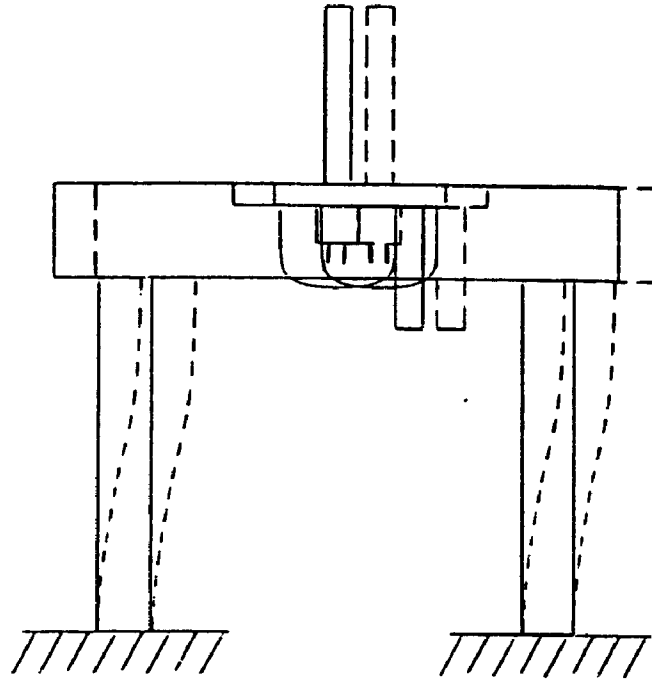
Figure 5.1: Horizontal Mode of Wind Tunnel Turntable

masses is therefore 180° out of phase with the tip acceleration and proportional in magnitude. When the activator is operated near 3 Hz, however, it excites the natural vibration mode of the turntable. This motion, although relatively small, adds to the acceleration of the dummy masses at the same time that it subtracts from the model acceleration. The result is that the magnitude and phase relation between the accelerations of the dummy masses and the model tip is modified by the dynamic characteristics of the turntable. Assuming that those characteristics are constant and linear, the signal V_A can still be used to determine the model tip acceleration, providing the modifying function is taken into account.

The same holds true for any other mechanical admittances which result from the characteristics of the activator itself.

The elastic pivots exhibit some properties of non-linear springs. The natural frequencies of vibrations of the activator have been kept safely out of the design operating range, however, the pivots still appear to present some problems. In particular there is a natural vertical vibration mode of the activator somewhere above 50 Hz; the exact value depends on the mass of the model. Operating the activator near one-fifth of this frequency excites this vibration mode and a relatively strong influence is seen in the V_W signal. This does not appear to present a problem for frequency domain analysis and in fact much of the data collected so far has been done operating the activator quite near that subharmonic value. For time domain analysis, however, these effects must be avoided. This will be discussed more in Chapter 6.

5.2.2 Signal Balancing

Due to the dynamical effects of the turntable and those inherent in the activator device, accurate calibration balancing of the signals can only be carried out at a single oscillation frequency. If one then changes oscillation frequency or amplitude, there will be small deviations from the balanced state. Procedures for accommodating this are described later. A systematic method of signal balancing is here outlined.

> 1) The model is mounted on the activator at the desired orientation and the device located in the tunnel turntable.

2) An oscillation frequency is chosen which will allow the range of reduced velocity of interest to be covered with appropriate tunnel wind speeds. Signal levels due to inertial forces will increase as the oscillation amplitude and as the oscillation frequency squared. This is undesirable for the moment sensing load cells since it is the wind load which is of interest. Lower frequencies are therefore favorable so long as the inertial load signals of the dummy masses remain adequately strong. However, a lower wind speed will be necessary for a given reduced velocity, and this decreases the level of wind forces. So there is some compromise required between these options. Other aspects of concern are that the signal levels do not exceed the operating ranges of the electronic devices and that mechanical resonances be avoided if time domain analysis is attempted. In general, it is best to check the signals visually on an oscilloscope and choose the frequency most suitable for the particular model. If *swept* frequency[2] forced oscillation for the whole operating range of 5-25 Hz is to be performed, a mid range oscillation frequency of between 10 and 15 Hz is appropriate for calibration balancing.

3) The activator is operated at the chosen frequency with no wind. The matching of output levels for load cells 1 and 2 and for 3 and 4 should each be checked. This is easily done by monitoring the difference of outputs $T1$ and $T2$ and minimising the result by adjusting the gain of $S1$ on the front panel of the signal

---

[2]This technique will be described in the next chapter.

processor. This adjusts the gain applied to the signal from load cell 1 so that its output matches that of load cell 2. The gain on load cell 2 is internally set. A similar check is performed on load cells 3 and 4 using outputs $T3$ and $T4$ and adjusting the $S3$ gain. The difference of signals can be monitored either on an oscilloscope using the output BNC connections or via the analog meter. The analog meter can be switched between either pair and the sensitivity level can be chosen high or low.

4) The difference of signals from load cells 1 and 2 is then balanced with the difference from load cells 3 and 4. This is done by monitoring the outputs $T1 - T2$ and $T3 - T4$ on an oscilloscope and setting the balance adjustments on the front panel, or by simply minimising the output from the W BNC connector. The 0, 10, or 20 dB gain options on the load cell dedicated amplifiers can also be adjusted at this time, but they must be set in pairs. That is channels 1 and 2 must be set identically and 3 and 4 set identically. If resonant frequencies are avoided, one should be able to adjust output W to a very low level. Additional force applied to the moving model is then represented in the output signal W.

5) Finally the gains for outputs $T3 - T4 (= V_A)$ and W can be adjusted to produce signal levels appropriate for the A/D conversion. These adjustments only alter the output signal gains and do not affect the previous balancing.

Accurate calibration balancing is not actually necessary. It is only necessary that the component of the moment representing the inertial loads is sufficiently removed that the component of wind loading dominates the remaining signal. One then performs an experiment with the model oscillating and with no wind. The results of this test are then used as a reference for the tests performed with the wind on. This is a relatively convenient approach, particularly for frequency domain analysis.

5.2.3 Determination of Conversion Factors

An absolute conversion factor is required to convert the voltage signal to units of moment. The load cells are dynamic devices and do not pass DC, and so a static loading calibration is not possible. It is possible to load the model with a known moment which is rapidly applied and then rapidly removed and recording the step output of the electronic system. This essentially determines the high frequency conversion factor. In fact the conversion factor will be frequency dependent due to and to the extent of the non-idealities in the mechanical system.

Figure 5.2 shows the results of a dynamic calibration at three different frequencies and two different oscillation amplitudes. To achieve these a specially constructed rig was used. It was mounted on the activator and a mass was attached at various locations so that a set of different inertial loadings were produced. The values of these moments of inertia were determined in separate experiments. As can be seen in the figure, the curves do not collapse onto a single curve. The conversion factor is a frequency dependent function and is also apparently sensitive to the mass
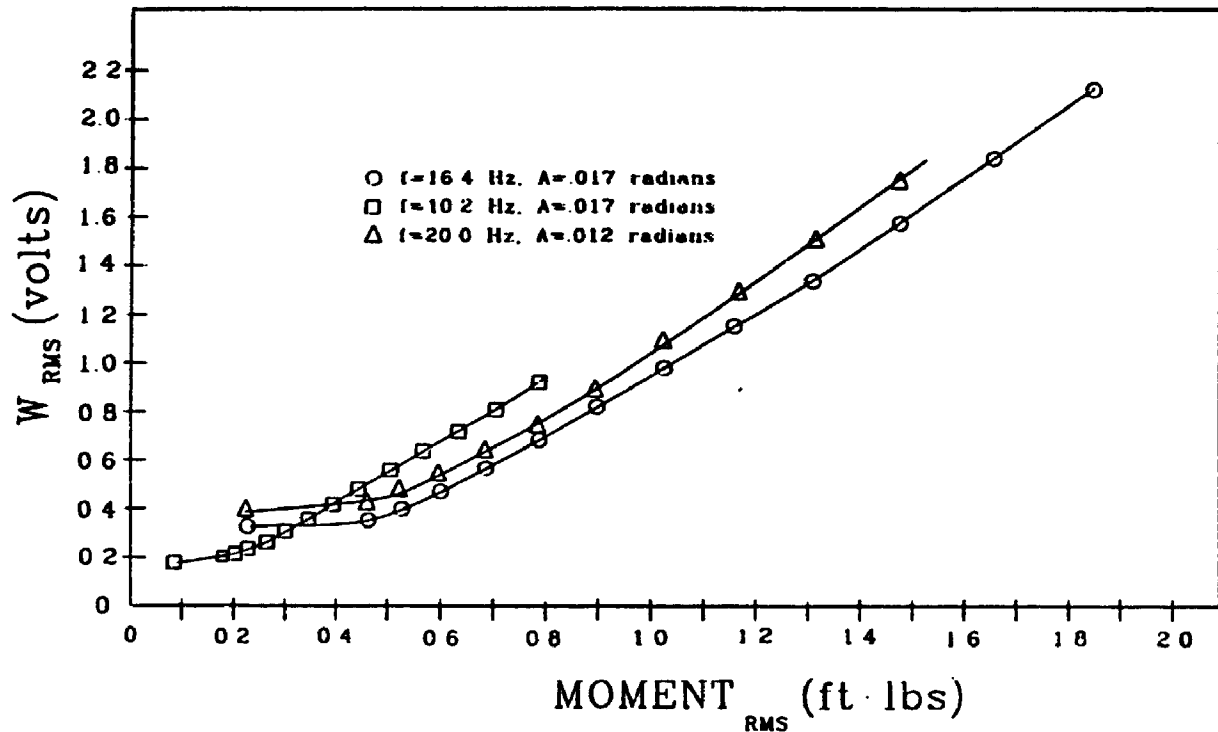
Figure 5.2: Dynamic Calibrations of the Pivot Mode Activator

of the particular model as this modifies the dynamics of the mechanical system.

Where the intent is to obtain a rough measure of the motion-induced forces and particularly to check for negative aerodynamic damping effects, then one may determine the high frequency conversion factor, or some effective factor from these curves. Assuming that it applies at all frequencies should suffice. Where more accurate measurements are desired a frequency dependent conversion function is necessary.

This function has been quite successfully obtained by securely attaching a known mass to the test model after calibration balancing and then oscillating the model at all frequencies of interest. The key assumption here is that the mass is
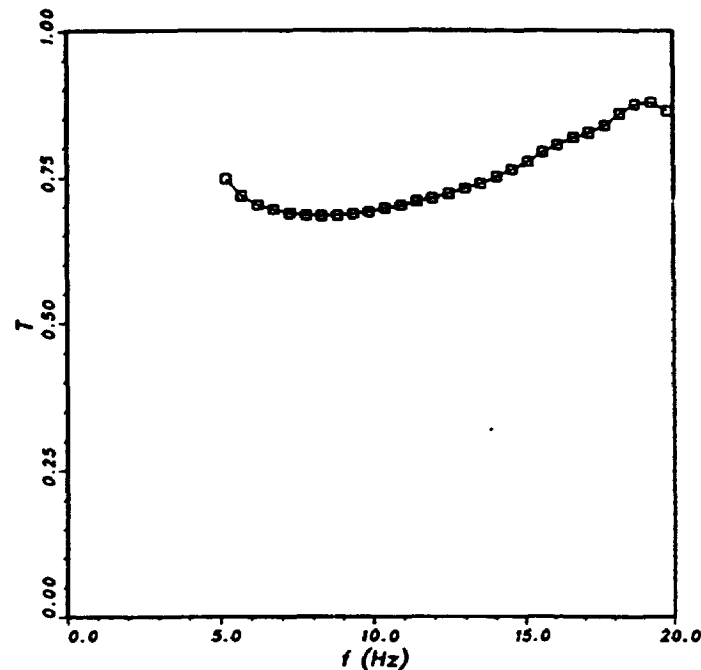
Figure 5.3: Frequency Dependent Calibration Curve

firmly attached so as to apply to the model an additional force which is exactly in phase with the reference acceleration – the model tip acceleration for example. The absolute conversion will still require an accurate estimate of the mass moment of inertia of the added mass about the pivot axis. With this known, as well as the frequency and amplitude of the motion, the extra inertial load applied by the added mass can be calculated and compared with the output signal W. An example of this result is shown in Figure 5.3. It is clearly frequency dependent and the influence of the turntable dynamics can be identified at the low end, as well as another influence toward the high end. This function allows an effectively complete account to be taken for any linear dynamic amplification effects inherent in the mechanical system. In practice, it is not required in this explicit form. An efficient method of taking it into account is described in the next chapter.

5.3 Experimental Method

As mentioned previously, it was found useful at times to high pass filter the output signals of the signal processor before A/D conversion to prevent drift effects, which are amplified by the signal processor, from carrying the signals out of the A/D voltage range. They have also been low pass filtered at 60 Hz as a matter of practice to remove the high frequency noise. This may be a higher than sufficient cutoff depending on the intent of the experiments. The frequency domain analysis in this work considers only first harmonic effects and so could have used cutoff frequencies as low as 20 or 25 Hz.

For routine use, software could be developed for efficient on-line signal analysis by the data aquisition computer. Most of the software currently written was for developmental purposes, however, and performs post experiment analysis on digital time series records on a mainframe computer.

With good calibration balancing, the activator system provides a signal representing the acceleration of the oscillating model and a signal representing the overturning moment directly due to wind forces acting on the model with little or no contamination from dynamic amplification effects. Direct real time analysis of these signals is a potential possibility and this may in fact lead to an understanding of the nonlinear nature of motion-induced forces.[3] Even if the calibration balancing is less than perfect, the reference experiment approach allows frequency domain analysis.

---

[3]The difficulties associated with time domain analysis will be elaborated upon in Chapter 6.

The experimental methods developed so far, consist of recording time series and then analysing them digitally. Three digital time records of sufficient duration are required. Each consists of simultaneous time series of the outputs V_W and V_A. The first is the "reference" record. This is carried out for the system balanced or near balanced, the wind off condition, and the forced oscillation occurring at the frequency of interest. The second is the "conversion" record carried out with the same setup but with the known calibration mass firmly attached to the model. The third is the "primary data" record carried out without the calibration mass and with the model oscillating subjected to a wind at a mean velocity of interest. The first two records are calibration records and are required once for any particular experimental setting of the drive amplitude and signal processor amplifiers. A primary data record is required for each flow condition to be considered.

It is also convenient to include two additional time series in each record in order to monitor the mean wind speed at a reference location and to monitor the amplitude and frequency of the oscillating model by a displacement transducer as shown in Figure 4.2. The latter information can also be determined from the V_A signal, but, in experiments to date, a displacement transducer has been used as an independent measure. Figure 5.4 shows a short section of a four channel time record from a typical experiment.
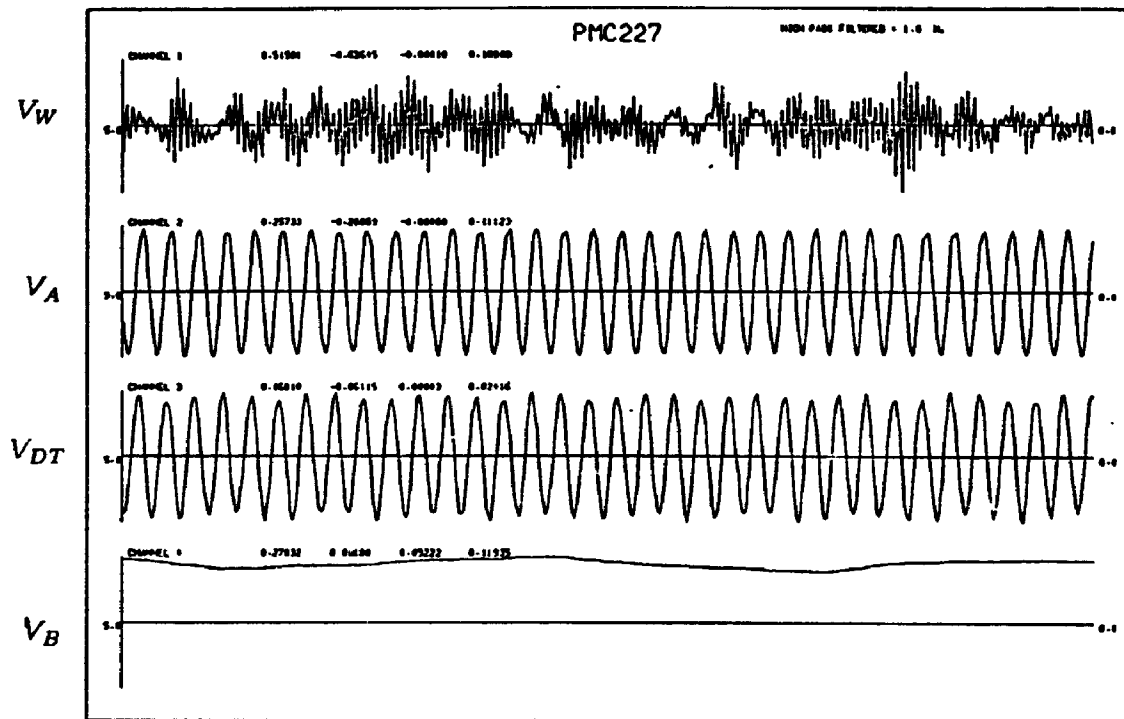
Figure 5.4: Short Section of a Typical Four Channel Time Record

Chapter 6

Analysis Procedures

6.1   Introduction

In view of the irresolute state of current descriptive models of the vortex-induced aeroelastic phenomena, the most meaningful representation of the motion-induced forces is not apparent.

It would be most desirable to develop a deterministic model, that is specific equations, relating the motion-induced forces directly to the motion of the structure. Such a model would have to include the interaction of these forces with the wind forces due to turbulence and then the whole process might then be simplified as a stochastic problem. This is the approach which would naturally follow from a successful oscillator model of the types discussed in Chapter 3. While these types of models may hold some promise, their rational development can only be taken so far, beyond which their success is somewhat a matter of chance and acceptable approximation. Experimental development of such models is further complicated by the fact that under forced oscillation, conditions are realised that will never occur under free oscillation. Nevertheless, time domain analysis of forced oscillation experiments may assist in choosing mathematical forms for such models. Some comments have

therefore been made regarding the potential for time domain analysis of the PMA experimental data and this is discussed in this chapter.

A more practical approach, particularly for situations in which the motions are relatively small, such as they are for tall civil engineering structures, is the linearisation of the motion-induced effects; that is the reduction of the nonlinear phenomenon to a linear model. It is from this approach that the concepts of aerodynamic damping, and aerodynamic stiffness or "added mass" have grown. Under linear assumptions, frequency domain analysis is a more suitable means of reducing the experimental data. Linearisation has been adopted in the current work, and the majority of it has therefore been devoted to frequency domain analysis.

Previous researchers have expressed motion-induced forces is different ways and, to some extent, the different expressions reflect different basic approaches to the problem. In some cases the form of expression reflects an expectation of how these forces arise and act. For example, Bearman and his associates[4,3] focus on a coefficient of fluctuating lift at the frequency of the motion, and on its phase relative to the motion. In other cases, the form is intended more to suggest how one might best manipulate the expressions in application. Along this line, Scruton[68] discusses a linearised version of the forces as two real quantities, representing a part in phase with the displacement of the structure and a part in phase with the velocity of the structure. This latter example is probably the more similar approach to that which will be developed here.

The following section develops the basic notation used in this work. The section after that describes the frequency domain analysis which has been used and

the last section of this chapter discusses time domain analysis.

6.2 Linearised Quantities for Forced Oscillation Results

In the current work, the motion-induced aerodynamic loading has been expressed as a " complex stiffness" or "impedance"[1] in linearised and dimensionless form. This follows the approach taken in the field of soil-structure interactions where foundation effects are considered using a complex stiffness. There, the real part results from the soil stiffness, and the imaginary part results from soil hysteresis and radiation damping. The approach departs somewhat from that generally taken in fluids, where the concept of an "added mass" rather than a "stiffness" is considered. That idea has some justification in fluids, however, since the added mass is identifiably related to the inertial effects of the fluid which are in phase with the motion of the body. In the current situation, fluid inertia rather than displacement is indeed likely to play a larger role; however, there is clearly an additional physical mechanism affecting the phasing of those inertial forces with respect to the motion of the body. As this is by no means clearly understood yet, the choice seems somewhat arbitrary at this time. The main difference is simply a factor of $-\omega^2$ in the real component of the complex quantity.

---

[1]It should be noted that impedance is more properly defined by what might be termed a complex damping rather than a complex stiffness, that is with real component proportionality to velocity rather than displacement[38]. The stiffness definition is not uncommon, however, and since it has certain advantages in the notational developments of the current application, it will be adopted here.

To start, assume that the measured wind moment is composed of a random component due to turbulence and unsteady wake effects in the surrounding flow, and an added component induced by the motion of the model. That is,

$$W(t) = W_i(t) + W_m(t) = pBH^2(C_i(t) + C_m(t)) \tag{6.1}$$

where $C_i(t)$ and $C_m(t)$ are the dimensionless coefficients of instantaneous random wind moment and instantaneous motion-induced wind moment respectively. The former is by definition random and so only the latter will be correlated with the motion. The factor pBH^2 is the dimensionalising factor defined as

$$pBH^2 = \frac{1}{2}\rho_a V^2 BH^2 \tag{6.2}$$

H and B are the model normalising height and width, ρ_a is the air density, and V is the reference wind speed. The corresponding effective force acting at the tip of the model can be related in correspondence to equation 6.1 above as:

$$F(t) = F_i(t) + F_m(t) = pBH(C_i(t) + C_m(t)) \tag{6.3}$$

A complex aerodynamic impedance, K_a is defined such that,

$$K_a y = -pBHC_m \tag{6.4}$$

where y is the tip displacement and is assumed to be of the harmonic form $y = \hat{y}e^{i\omega t}$. Note that the phase shift by which y lags C_m is accounted for by the complex factor, K_a.

A more rigorous definition of K_a would go as follows. It is hypothesised that there exists a deterministic relation between the motion of the structure and the induced force, and that it may be expressed by an impulse response function

$k_a(\tau)$. It is defined as the output —the negative of the induced moment F_m on the structure or, in other words, the resisting moment— at any time due to a unit impulse input —the displacement y— occurring at a time τ before. Note that the displacement alone is an adequate time dependent function to define the motion in the case of forced sinusoidal motion. Of course, this is not true for general motion. The hypothesis may be expressed:

$$F_m(t) = - \int_0^\infty k_a(\tau)\dot{y}(t - \tau)d\tau \qquad (6.5)$$

Consider the products of that force at two times t and $t + \tau$:

$$F_m(t)F_m(t + \tau) = \int \int_0^\infty k_a(\xi)k_a(\eta)y(t - \xi)y(t + \tau - \eta)d\xi d\eta \qquad (6.6)$$

This quantity has an expected value given by the autocorrelation function:

$$R_{F_m F_m}(\tau) = \int \int_0^\infty k_a(\xi)k_a(\eta)R_{yy}(\tau + \xi - \eta)d\xi d\eta \qquad (6.7)$$

Also consider the corresponding product of the displacement and the force:

$$y(t)F_m(t + \tau) = - \int_0^\infty k_a(\xi)y(t)y(t + \tau - \xi)d\xi \qquad (6.8)$$

which has an expected value given by:

$$R_{yF_m}(\tau) = - \int_0^\infty k_a(\xi)R_{yy}(\tau - \xi)d\xi \qquad (6.9)$$

By taking Fourier transforms of these expected values and employing the convolution theorem, one arrives at the relation between the spectral quantities in the complex frequency domain:

$$K_a(f)S_{yy}(f) = -S_{yF_m}(f) \qquad (6.10)$$

or re-expressing in terms of the dimensionless coefficient, C_m:

$$K_a(f)S_{yy}(f) = -pBHS_{yC_m}(f) \qquad (6.11)$$

Equation 6.4 follows as a specific case of this at a single harmonic.

A dimensionless form of impedance may also be defined as

$$G_a = \frac{K_a}{2\omega^2 M_s \eta} \tag{6.12}$$

Here the quantity $M_s \eta$ represents the generalised mass of the structure scaled by the density ratio of air to the structure, and ω is the natural frequency of the structure. Assuming a pivot mode as used in the forced oscillation experiments, one finds:

$$M_s \eta = \frac{\rho_a H B^2}{3} \tag{6.13}$$

Also noting that in these experiments, displacement is related to acceleration by $y = -\ddot{y}/\omega^2$, then:

$$G_a = \frac{3(pBH S_{AG_m})}{2\rho_a H B^2 S_{AA}} \tag{6.14}$$

The explicit dependence of f has been dropped for brevity and the subscript A has been adopted for acceleration $\ddot{y}$. The above can be rewritten in terms of the overturning moment:

$$G_a = \{\alpha + i\beta\} = \left(\frac{3}{2\rho_a H^2 B^2}\right) \left(\frac{S_{AW_m}}{S_{AA}}\right) \tag{6.15}$$

The real and imaginary parts, α and β, of the complex impedance then correspond to an aerodynamic stiffness coefficient and an aerodynamic damping coefficient, respectively.

The ratio of the spectra in the above equation is the so called transfer function or, more precisely, the frequency response function between the acceleration and the motion correlated moment which will be denoted T_{AW_m}. One can substitute W in place of W_m without any change. Recall that $W_m(t)$ was *defined* to be that

part of $W(t)$ which is correlated with the motion or in other words, such that the expected values given by equations 6.7 and 6.9 are maintained. Equation 6.15 then becomes:

$$G_a = \{\alpha + i\beta\} = \left(\frac{3}{2\rho_a H^2 B^2}\right) T_{AW} \tag{6.16}$$

The real quantities α and β are dimensionless coefficients, and are dependent only on the geometry of the structure. A structurally dependent aerodynamic damping, ς_a, would be given by,

$$\varsigma_a = \eta\beta \tag{6.17}$$

The total damping, ς_t, is usually taken to be,

$$\varsigma_t = \varsigma_s + \varsigma_a \tag{6.18}$$

where ς_s is the equivalent viscous structural damping as a fraction of critical. The appropriate use of such results will be dealt with in more detail in the following chapters.

Note that equation 6.4 was defined with a complex stiffness in mind so that the equation of motion for a single degree of freedom structure could be written,

$$M_s \ddot{y} + C_s \dot{y} + (K_s + K_a)y = pBHC_l \tag{6.19}$$

Although, both α and β are of comparable magnitude, attention is sometimes restricted to the aerodynamic damping term alone because it has the dominant effect on the structural response. Nevertheless, equal attention has been given to

both in the data analysis of this thesis, because it is apparent that both will play a significant part in any descriptive model of the underlying physical mechanisms.

6.3   Frequency Domain Analysis

.

Determined from a forced oscillation experiment, α and β depend on the flow conditions, (described by the profile of mean wind speed, the scale of turbulence intensity, and the Reynolds number), and on the reduced velocity or equivalently its inverse, the reduced frequency. Assuming Reynolds number independence, then, for a given flow structure, they are obtained as functions of reduced velocity by considering the complex transfer function between the forced acceleration and the wind-induced moment. It is required to extract this transfer function from the voltage signals of the reference, the conversion, and the primary data records.

6.3.1   Transfer Function Expressions

Some mathematical rigour is required to describe the complex dynamics inherent in the experiments. Consider first a general test case. The expressions will be later reduced for the three specific cases: the reference (r), the conversion (c), and the primary (p) tests. Assuming linear dynamics, the four load cell voltage outputs may be expressed as the sum of impulse responses to real physical quantities plus

electrical noise. That is:

$$V_1 = c_1 \left[\int_0^\infty d_{M_1}(\tau) M(t-\tau) d\tau + \int_0^\infty d_{m_1}(\tau) m(t-\tau) d\tau \right.$$
$$\left. + \int_0^\infty d_{W_1}(\tau) W(t-\tau) d\tau \right] + N_1(t) \tag{6.20}$$

$$V_2 = c_2 \left[\int_0^\infty d_{M_2}(\tau) M(t-\tau) d\tau + \int_0^\infty d_{m_2}(\tau) m(t-\tau) d\tau \right.$$
$$\left. + \int_0^\infty d_{W_2}(\tau) W(t-\tau) d\tau \right] + N_2(t) \tag{6.21}$$

$$V_3 = c_3 w_3 \int_0^\infty d_{A_3}(\tau) A(t-\tau) d\tau + N_3(t) \tag{6.22}$$

$$V_4 = c_4 w_4 \int_0^\infty d_{A_4}(\tau) A(t-\tau) d\tau + N_4(t) \tag{6.23}$$

where:

c_i — conversions in [volts/force] for each cell
M — moment due to model mass
m — moment due to calibration mass
A — acceleration (forced motion) at reference (model tip)
W — external load (wind)

$\left. \begin{array}{l} d_{M_i} \\ d_{m_i} \\ d_{A_i} \\ d_{W_i} \end{array} \right\}$ dynamical influence functions (due to M, m, A, or W) on cell i

$\left. \begin{array}{l} w_3 \\ w_4 \end{array} \right\}$ dummy masses, $w_3 = w_4 = w/2$

$\left. \begin{array}{l} N_1 \\ N_2 \\ N_3 \\ N_4 \end{array} \right\}$ independent (electrical) noise signals at each cell

During the balancing procedure described in § 5.2.2, $m(t) = W(t) = 0$. The PMA Signal Processor gains for cells 2 and 4 (see Figure 4.10) are adjusted so that:

$$G_2 = c_1/c_2 \tag{6.24}$$

$$G_4 = c_3/c_4 \tag{6.25}$$

and G_1 and G_3 are defined to be set to 1. At stage 2 of the Signal Processor:

$$V_{1-2} = V_1 - G_2 V_2 \;=\; c_1 \left[\int_0^\infty d_M(\tau) M(t-\tau)\, d\tau + \int_0^\infty d_m(\tau)\, m(t-\tau)\, d\tau \right.$$
$$\left. + \int_0^\infty d_W(\tau) W(t-\tau)\, d\tau \right]$$
$$+ N_1(t) - N_2(t) + N_{1-2}(t) \tag{6.26}$$

$$V_{3-4} = V_3 - G_4 V_4 \;=\; c_3 w \int_0^\infty d_A(\tau) A(t-\tau)\, d\tau$$
$$+ N_3(t) - N_4(t) + N_{3-4}(t) \tag{6.27}$$

where new dynamical influence functions have been implied:

$$d_M \;=\; d_{M_1} - d_{M_2} \tag{6.28}$$

$$d_m \;=\; d_{m_1} - d_{m_2} \tag{6.29}$$

$$d_A \;=\; d_{A_3} - d_{A_4} \tag{6.30}$$

$$d_W \;=\; d_{W_1} - d_{W_2} \tag{6.31}$$

After the remaining stages, the PMA Signal Processor outputs are:

$$V_W \;=\; G_W \left[G_{12} V_{1-2} - G_{34} V_{3-4} \right] \tag{6.32}$$

$$V_A \;=\; G_A \left[G_{34} V_{3-4} \right] \tag{6.33}$$

where G_W, G_A, G_{12}, G_{34} are the remaining gains of the Signal Processor.

With these expressions, the spectral quantities can now be derived.

$$S_{V_W V_W} \;=\; G_W^2 \left\{ G_{12}^2 c_1^2 \left[|D_M|^2 S_{MM} + |D_m|^2 S_{mm} + |D_W|^2 S_{WW} \right] \right.$$
$$\left. + G_{12}^2 S_{N_W N_W} - G_{34}^2 c_3^2 \left[w^2 |D_A|^2 S_{AA} + S_{N_A N_A} \right] \right\} \tag{6.34}$$

$$S_{V_A V_A} \;=\; G_A^2 G_{34}^2 \left[c_3^2 w^2 |D_A|^2 S_{AA} + S_{N_A N_A} \right] \tag{6.35}$$

$$S_{V_A V_W} \;=\; G_W G_A \left\{ G_{12} G_{34} c_1 c_3 w \left[S_{AM} D_M^* + S_{Am} D_m^* + S_{AW} D_W^* \right] \right.$$
$$\left. - G_{34}^2 \left[c_3^2 w^2 |D_A|^2 S_{AA} + S_{N_A N_A} \right] \right\} \tag{6.36}$$

The spectral contributions from the noise components occurring in the expanded forms of Equations 6.32 and 6.33 have been summed together in $S_{N_W N_W}$ and $S_{N_A N_A}$ respectively. The cross-spectra of noise components are not included since the noises are assumed to be independent. The functions, D_M, D_m, D_W, and D_A represent the fourier transforms of the corresponding dynamical influence functions. They describe the relations in the frequency domain between the physical quantities and the forces occurring at the relevant load cells. The transfer function between signals V_A and V_W is given by

$$T_{V_A V_W} = \frac{S_{V_A V_W}}{S_{V_A V_A}} = \frac{G_W}{G_A} \left[\frac{G_{12} c_1}{G_{34} c_3} \frac{[S_{AM} D_M^* + S_{Am} D_m^* + S_{AW} D_W^*]}{w \left[|D_A|^2 S_{AA} + c_3^{-2} w^{-2} S_{N_A N_A}\right]} - 1 \right] \qquad (6.37)$$

Now for the three tests, reference (r), conversion (c), and primary (p), the transfer functions become:

$$T_{V_A V_W}^r = \frac{G_W}{G_A} \left[\frac{G_{12} c_1}{G_{34} c_3} \frac{[S_{AM} D_M^*]}{w \left[|D_A|^2 S_{AA} + c_3^{-2} w^{-2} S_{N_A N_A}\right]} - 1 \right] \qquad (6.38)$$

$$T_{V_A V_W}^c = \frac{G_W}{G_A} \left[\frac{G_{12} c_1}{G_{34} c_3} \frac{[S_{AM} D_M^* + S_{Am} D_m^*]}{w \left[|D_A|^2 S_{AA} + c_3^{-2} w^{-2} S_{N_A N_A}\right]} - 1 \right] \qquad (6.39)$$

$$T_{V_A V_W}^p = \frac{G_W}{G_A} \left[\frac{G_{12} c_1}{G_{34} c_3} \frac{[S_{AM} D_M^* + S_{AW} D_W^*]}{w \left[|D_A|^2 S_{AA} + c_3^{-2} w^{-2} S_{N_A N_A}\right]} - 1 \right] \qquad (6.40)$$

6.3.2   Some System Sensitivities

At this point a short digression will be taken to analyse the equations developed in the previous section. This exercise will be helpful in understanding some of the sensitivities of the system to the internal dynamical properties. In particular, it will

illustrate why the conversion factor is frequency dependent. It will suffice for this purpose to neglect the noise terms as their influence is not of concern here. Some use will be made of the following expressions:

$$S_{AA}(f) = (2\pi f)^4 S_{vv}(f) \tag{6.41}$$

$$S_{MM}(f) = (\frac{I_M}{H})^2 (2\pi f)^4 S_{vv}(f) \tag{6.42}$$

$$S_{AM}(f) = (\frac{I_M}{H})(2\pi f)^4 S_{vv}(f) \tag{6.43}$$

$$S_{mm}(f) = (\frac{I_m}{H})^2 (2\pi f)^4 S_{vv}(f) \tag{6.44}$$

$$S_{Am}(f) = (\frac{I_m}{H})(2\pi f)^4 S_{vv}(f) \tag{6.45}$$

where I_M and I_m refer respectively to the mass moments of inertia of the model and the calibration mass about the pivot point. Implicit in these relations are the assumptions that the model is very rigid and the calibration mass is firmly attached. These simplifications will allow us to focus on the dynamical effects of the system.

First, consider the situation under which balancing of the system is carried out. There is no calibration mass and no wind so, $S_{mm} = S_{WW} = 0$. During balancing, the gains are adjusted so that $S_{V_W V_W} = 0$. Thus Equation 6.34 implies, after dropping the noise terms,:

$$G_{12}^2 c_1^2 |D_M|^2 S_{MM} - G_{34}^2 c_3^2 w^2 |D_A|^2 S_{AA} = 0 \tag{6.46}$$

$$\Longrightarrow G_{34} = \frac{G_{12} c_1}{w c_3} \frac{|D_M|}{|D_A|} \sqrt{\frac{S_{MM}}{S_{AA}}} \tag{6.47}$$

$$\Longrightarrow G_{34} = \frac{G_{12} c_1}{w c_3} \frac{|D_M|}{|D_A|} \frac{I_M}{H} \tag{6.48}$$

Under ideal conditions both $|D_M|$ and $|D_A|$ are frequency independent and so the gain factor, G_{34} is a constant factor for all frequencies. Unfortunately, things are not ideal and the gain factor required is particularly sensitive to the frequency dependency of the dynamic modifier functions.

Suppose the balancing is carried out at a frequency, f_b. The gain, $G_{34}(f_b)$, is set according to the above condition. If one then considers the transfer function resulting from the reference test it is found that, (showing the frequency dependencies explicitly but dropping the transfer function subscripts for brevity):

$$T^r(f) = \frac{G_W}{G_A} \left[\frac{|D_A(f_b)|D_M(f)}{|D_M(f_b)|D_A(f)} \sqrt{\frac{S_{AA}(f_b)}{S_{MM}(f_b)} \frac{S_{AM}(f)}{S_{AA}(f)}} - 1 \right] \qquad (6.49)$$

or using the assumed relations:

$$T^r(f) = \frac{G_W}{G_A} \left[\frac{|D_A(f_b)|D_M(f)}{|D_M(f_b)|D_A(f)} - 1 \right] \qquad (6.50)$$

Providing that the system is close to ideal – specifically, that the dynamic modifiers have negligible imaginary parts– then it can be shown that, for $f = f_b$, this function is very nearly zero. However, for frequencies other than f_b it grows directly with the non-ideal phase of the dynamic modifier functions. Note that this is a mechanical property of the system and occurs even for an ideal absence of electrical noise.

Now consider the transfer function of the conversion test for a particular balancing at frequency f_b. Making use of the reference function found above, one finds for this case:

$$T^c(f) = T^r(f) + \frac{G_W}{G_A} \left[\frac{|D_A(f_b)|D_m(f)}{|D_m(f_b)|D_A(f)} \frac{I_m}{I_M} \right] \qquad (6.51)$$

Here also, there is a strong sensitivity to the dynamic modifiers, for frequencies other than that at which balancing is carried out. The second term is in effect measured as shown in Figure 5.3.

Similarly, for the primary test transfer function one may derive:

$$T^p(f) = T^r(f) + \frac{G_W}{G_A} \left[\frac{|D_A(f_b)||D_W(f)|}{|D_W(f_b)||D_A(f)|} \sqrt{\frac{S_{AA}(f_b)}{S_{MM}(f_b)} \frac{S_{AW}(f)}{S_{AA}(f)}} \right] \tag{6.52}$$

$$T^p(f) = T^r(f) + \frac{G_W}{G_A} \left[\frac{|D_A(f_b)||D_W(f)|}{|D_W(f_b)||D_A(f)|} \left(\frac{H}{I_M}\right) \left(\frac{S_{AW}(f)}{S_{AA}(f)}\right) \right] \tag{6.53}$$

In each of the cases above, there is a strong sensitivity to the dynamic modifier functions.

Suppose the system is ideal so that all of the modifier functions are frequency independent. The above results may then be reduced to:

$$T^r = 0 \tag{6.54}$$

$$T^c = \left(\frac{G_W}{G_A}\right) \left(\frac{I_m}{I_M}\right) \tag{6.55}$$

$$T^p(f) = \left(\frac{G_W}{G_A}\right) \left(\frac{H}{I_M}\right) \left(\frac{S_{AW}(f)}{S_{AA}(f)}\right) \tag{6.56}$$

From this, the transfer function between wind moment and the tip acceleration may be expressed as:

$$T_{AW}(f) = \frac{S_{AW}(f)}{S_{AA}(f)} = \left(\frac{I_m}{H}\right) \frac{T^p(f)}{T^c} \tag{6.57}$$

In this ideal case, the factor $I_m/(HT^c) = G_A/G_W$ simply represents a real conversion factor between T^p and T_{AW}.

Unfortunately, a less than ideal situation must be accepted in reality. There is, in fact, some electrical noise present in the signals, as well as internal dynamical influences These influences can actually be accounted for in a relatively straightforward manner, despite the seemingly discouraging results derived in this section.

Before describing how that may be done, note one further relation which may be derived.

Consider a primary test situation, wherein $S_{mm} = 0$, and again assume little noise. If one substitutes the expression for the G_{34} for the system balanced at frequency f_b, into the expression for $S_{V_W V_W}$, the following expression can be derived after simplification:

$$S_{V_W V_W}(f) = |D_W(f)|^2 S_{WW}(f) + \left[|D_M(f)|^2 - \frac{|D_A(f)|^2}{|D_A(f_b)|^2}|D_M(f_b)|^2\right] S_{MM}(f) \quad (6.58)$$

This indicates that, even for a noiseless system, the spectrum of the signal V_W does not directly represent the wind-induced moment, but will show a component from the model inertia at frequencies other than f_b. This is not so if $|D_A(f)| = |D_M(f)|$, that is, if the tip acceleration of the model is related to the loads sensed at load cells 3 and 4 in the same way that the model inertial load is related to the loads sensed at load cells 1 and 2. Although some effort was spent to make the system independent of these effects, it is not perfect. The horizontal modes of the turntable in particular will cause some differences in the functions D_A and D_M. Moreover, these differences do not need to be very great since the model inertial load is generally much larger than the wind load, and so the contamination of the signal may be significant. Therefore, one cannot measure a complete spectrum of moment using the device, unless the dynamical influence functions are determined and the model mass is very well defined.

6.3.3   Extraction of Relevant Transfer Function

Three assumptions regarding the system will now be made.

1. While there may be some contaminating dynamical effects in the system, there are no nonlinear dynamic properties that are relevant. That is, the linear analytical approach of the previous sections applies.

2. The inertial load of the calibration mass is transmitted to the moment sensing load cells in the same way, that is according to the same dynamical influence function, as the external wind load. Thus $D_W = D_m$.

3. The calibration mass is attached firmly to the model. Hence the following relations are valid:

$$m = \frac{-I_m}{H} A \tag{6.59}$$

$$S_{Am} = -\left(\frac{I_m}{H}\right) S_{AA} \tag{6.60}$$

With these assumptions, the desired frequency response function between W and A can be simply extracted by considering the following combination of the three test transfer functions:

$$\frac{T^p_{V_A V_W} - T^r_{V_A V_W}}{T^c_{V_A V_W} - T^r_{V_A V_W}} = \frac{S_{AW}}{S_{Am}} = \frac{-H}{I_m} \frac{S_{AW}}{S_{AA}} \tag{6.61}$$

The desired frequency response function is thus given by:

$$T_{AW} = \frac{S_{AW}}{S_{AA}} = -\left(\frac{I_m}{H}\right) \frac{T^p - T^r}{T^c - T^r} \tag{6.62}$$

This expression can be substituted into equation 6.16 giving:

$$G_a = \{\alpha + i\beta\} = \left(\frac{-3I_m}{2\rho_a H^3 B^2}\right)\left(\frac{T^p - T^r}{T^c - T^r}\right)$$

(6.63)

Equation 6.63 expresses the complex impedance K_a in terms of known quantities and transfer functions which can be calculated from the three experimental records.

Note that no assumptions about the noise levels, nor about the dynamical modifier functions D_A or D_M have been made. The derived expression accounts for these contaminants.

Having justified Equation 6.63 through the preceding mathematical developments, one may now re-express it in a form which is more compatible with a direct intuitive approach.

$$G_a = \frac{G_a^p - G_a^r}{G_a^c - G_a^r}$$

(6.64)

Here G_a^r represents a reference or background impedance due to the measuring system as a whole. It is independent of the actual aerodynamic impedance. And G_a^c represents an impedance associated with a known situation, namely a purely real impedance of magnitude determined by the calibration mass and its location, and as seen through the measuring system and its background impedance. Finally, G_a^p

represents the aerodynamic impedance as seen through the measuring system. The combination simply amounts to removing the background impedance from each of the latter two, and scaling the primary impedance with the known impedance resulting from the inertial loading of the calibration mass.

One may in fact treat each experimental record as if the signals V_A and V_W represented direct measures of the acceleration and the moment. The impedance resulting from each may then be combined as above to derive the actual aerodynamic impedance of interest. This approach is helpful for the discussion of the methods in the following sections. There, for simpler presentation, reference to the three experimental records will be dropped, with the understanding that the results of each record are combined according to Equation 6.64 or where more appropriate, Equation 6.63.

6.3.4   Steady Frequency Data Analysis

Method of Direct Integration

As prefaced in the preceding discussion, one may treat each PMA experimental record as if it provided a time history of the overturning moment due to wind force on the oscillating model. The task of data reduction is essentially to linearise this force or, more correctly, that component of it correlated to the motion. In the present context, linearisation means expressing the motion-induced force as a function of displacement and velocity. In other words it is assumed that the effective

wind force at the tip of the model can be expressed as,

$$F(t) = pBHC_l(t) + \left(2\omega^2 M_s \eta\right) \{\alpha y + \frac{\beta}{\omega}\dot{y}\} \qquad (6.65)$$

or:

$$W(t) = pBH^2 C_l(t) - H\left(2\omega^2 M_s \eta\right)\{\alpha y + \frac{\beta}{\omega}\dot{y}\} \qquad (6.66)$$

In consideration of the pivoting mode, this can be re-expressed as:

$$W(t) = pBH^2 \left(C_l(t) - \frac{4}{3}B\{\alpha\omega^2 y + \beta\omega\dot{y}\}\right) \qquad (6.67)$$

Consider the quantities,

$$I_1 = \lim_{T\to\infty} \frac{1}{T}\int_0^T W(t)cos(\omega t)dt \qquad (6.68)$$

and

$$I_2 = \lim_{T\to\infty} \frac{1}{T}\int_0^T W(t)sin(\omega t)dt \qquad (6.69)$$

By substituting into the expression for $W(t)$, the forced oscillation condition of

$$y = \hat{y}cos(\omega t) \qquad (6.70)$$

it can be easily shown that,

$$\alpha = \frac{-3}{\rho_a \omega^2 B^2 H^2 \hat{y}}I_1 \qquad (6.71)$$

and

$$\beta = \frac{3}{\rho_a \omega^2 B^2 H^2 \hat{y}}I_2 \qquad (6.72)$$

These quantities can then be estimated by the direct numerical integration of the experimental data. The necessary reference functions, $cos(\omega t)$ defined to be in phase with the displacement y, and $sin(\omega t)$ defined to be out of phase, can be estimated from the digital time series of the V_A signal. The first can be estimated

by normalising the signal itself and the second can be estimated by numerically integrating the signal and removing the mean of the resulting series. The mean is, in effect, an estimate of the integration constant. The integrated series must be then normalised as well. The correct normalisations can be estimated by taking $\sqrt{2}$ times the rms of each series since both are, ideally, sinusoids.

This method is relatively straightforward conceptually. It amounts to a direct calculation of the active and reactive powers. It is also relatively easy to program, however, it is not particularly efficient. It is sensitive to numerical errors in the estimates of the reference functions and requires longer data records than are actually necessary before stable limit values of I_1 and I_2 are produced by numerically integrating.

Slightly shorter time records may be used by assuming that these integrations approach their limiting values asymptotically according to some model. Then, by numerically estimating the series $I_1(T)$ and $I_2(T)$, and using a least squares fitting technique to the assumed model, an estimate of limiting value may be determined. This has been tried with some success, however, the direct integration remains inefficient relative to other methods of analysis.

Figure 6.1 shows some early raw results obtained using the direct integration method. Each data point is the result of 30 seconds or more of accumulated data at 200 samples per second. The calibration system had not been developed at this time so the vertical scale is of no significance. These results demonstrated that the system worked in principle. The direct integration method was subsequently abandoned in favour of the methods discussed in the following sections.
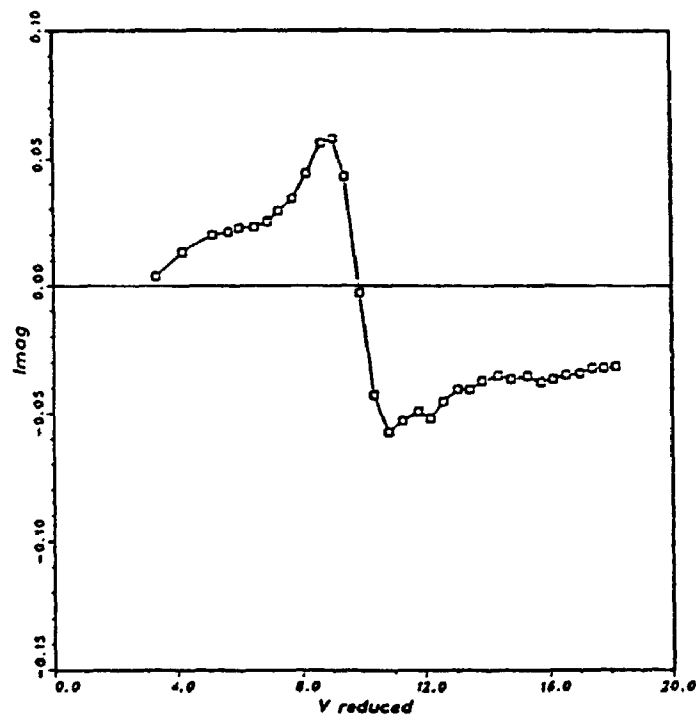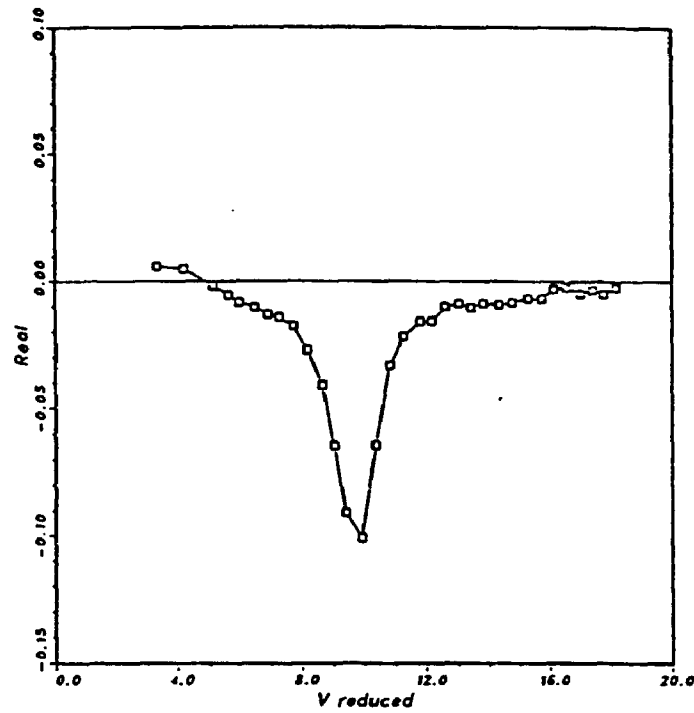
Figure 6.1: Raw Results Obtained From Early Developmental Test Using the Direct Integration Method

Linear Fitting of the Cross Correlation

Since it is assumed that the motion-induced forcing is a stationary ergodic process, linearisation can be expedited by making use of the cross correlation functions between the motion and the force. Consider the expression for the overturning moment due to the wind, as in the previous section:

$$W(t) = pBH^2 \left(C_l(t) + \frac{4}{3} B\{\alpha\omega^2 y + \beta\omega\dot{y}\} \right) \tag{6.73}$$

With the assumed sinusoidal motion for the forced oscillation, this becomes:

$$W(t) = pBH^2 \left(C_l(t) + \frac{4}{3} Ba\omega^2\{\alpha cos(\omega t) - \beta sin(\omega t)\} \right) \tag{6.74}$$

and the acceleration of the model becomes:

$$A(t) = \ddot{y} = -\omega^2 \hat{y} cos(\omega t) \tag{6.75}$$

The cross correlation of these functions is defined as,

$$R_{AW}(\tau) = \lim_{T\to\infty} \frac{1}{T} \int_0^T A(t)W(t + \tau)dt \tag{6.76}$$

Expanding this and recalling that $C_l(t)$ is a random function with zero mean, the cross correlation becomes:

$$R_{AW}(\tau) = \frac{1}{3}\rho_a B^2 H^2 \omega^4 \hat{y}^2 \{\alpha cos(\omega\tau) - \beta sin(\omega\tau)\} \tag{6.77}$$

This function can be estimated numerically for any desired number of discrete lags from the experimental data either by direct calculation or indirectly using FFT algorithms. It remains to extract from this function, the sine and cosine parts and to numerically estimate their relative contributions without accumulating numerical error and without requiring estimates at an excessive number of lags.

One could simply fit the function to an ideal sinusoid using a nonlinear fitting routine. Such routines, however, are not very robust when it comes to fitting periodic functions nor are they particularly efficient. Alternatively, one could estimate the magnitude of the sinusoidal function from its peak values and its phase from its intercepts with the horizontal axis. The corresponding values of α and β could then be determined. This is a poor approach as the estimates in both the magnitude and phase contain significant uncertainty unless a large number of lags is considered, most lags would not contribute to the estimates, and the magnitude estimates would be biased toward the low side. Since the final estimates of α and β would be derived from estimates of phase, their errors can be significant, particularly when one is much smaller than the other.

A simple and efficient method of estimating the two contributions is illustrated in Figure 6.2. The first stage of the figure shows small portions of experimentally measured discrete time series of the wind moment and the model acceleration. Below that is an estimate of the cross correlation function. The next step in the method requires separating the even and odd parts of that estimate. This is easily done according to the relations:

$$R_{AW}(-\tau) + R_{AW}(\tau) = \frac{-2}{3}\rho_a B^2 H^2 \omega^4 \hat{y}^2 \alpha cos(\omega\tau) \tag{6.78}$$

$$R_{AW}(-\tau) - R_{AW}(\tau) = \frac{-2}{3}\rho_a B^2 H^2 \omega^4 \hat{y}^2 \beta sin(\omega\tau) \tag{6.79}$$

Plotting the even part versus the odd part produces, ideally, an ellipse whose intercepts with the axes are proportional to α and β. Fitting this curve would still be quite difficult. If one squares both parts, however, and replots them as shown, the data then follow a straight line with negative slope. This can be easily fitted using linear regression and the intercepts represent direct measures of the desired quantities. The reliability of the estimates, particularly for cases where one quantity
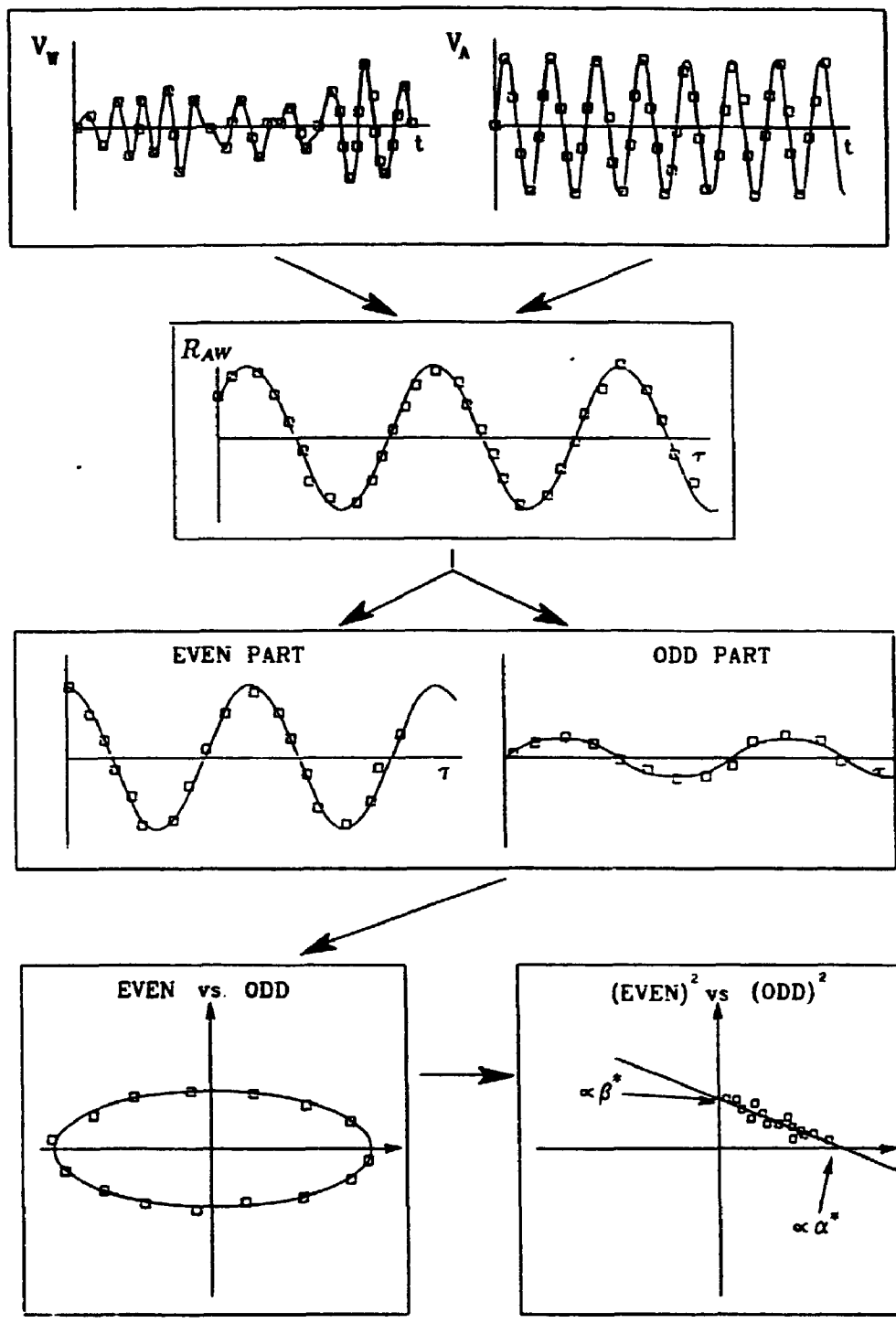
Figure 6.2: Schematic Diagram of the Cross Correlation Linear Fit Method

is much smaller than the other, is improved at little cost by performing the linear regression twice. The vertical axis intercept is estimated by minimising the sum of the squares of the vertical deviations. The horizontal axis intercept is estimated by considering in the same way, the horizontal deviations. The sign information, which is lost in the squaring process, may be restored by examination of the even part and the slope of the odd part, both at $\tau = 0$.

Frequency Estimation of a Discrete Sine Series

The estimation of the steady frequency of the model motion from a discrete time series of either the acceleration or the displacement of the model is not particularly difficult but it does deserve some note. It is first necessary to filter out any high frequency noise and any significant low frequency contributions as well. The most direct method is then to simply estimate the number of cycles occurring in a long time series by counting the number of sign changes. For a rough estimate this is an adequate approach.

A more refined estimate can be made by interpolating to determine estimates of the times at which sign changes occur and then estimating from these the average period per half cycle.

Spectral analysis may of course be used and the peak frequency value determined. Unless attempts are made to actually fit the peak in some way, the uncertainty in this approach will be directly related to the record length. For ex-

ample, if an accuracy of .1% is desired and the frequency is approximately $10Hz$, then a record length of 200 seconds would be required. There is no problem in this, but it may not be the most efficient approach if it is desired to program efficient on line data analysis.

Another method which works surprisingly well on filtered data, and which takes little computing effort. is to take advantage of the ratio of a sinusoid to its curvature, namely $-\omega^2$. Every three consecutive samples in the time series can be used to contribute an estimate towards ω according to the following:

$$e_i = \left(2\Delta\omega^2\right)_i = \frac{s_{i-1} - s_{i+1}}{s_i} \tag{6.80}$$

where Δ is the sampling interval. Of course, the odd wild contribution occurs near cross over points when s_i is very small and cases of $s_i = 0$ must be omitted, nevertheless, so long as there is several samples per cycle, a quite good estimate can be obtained within a couple hundred cycles, or about 10 seconds of data.

The most stable estimates of frequency were found by using this method with the refinement of throwing out all estimates, e_i which lay outside of a standard deviation or so of the mean.

6.3.5   Swept Frequency Data Analysis

An efficient method of accumulating test data is to slowly sweep the forced motion through a range of oscillation frequency while maintaining a steady wind speed. A

complete sweep must be much longer than a steady frequency record since data are being accumulated over a whole range rather than just one frequency. In terms of acquiring information for a given range of reduced velocity, however, a great savings is made in the manual overhead of running the tests. This method also lends itself well to standard Fourier analysis techniques as will be described.

Frequency Variation for Sweep Experiments

In order to give an equal weighting to the amount of information gathered at each frequency in a sweep, it is necessary to consider the time scaling during the sweep. A linear sweep, wherein the instantaneous value of frequency is a linear function of time and varying from the minimum to the maximum frequency, is a poor method since the final resolution in the data will also vary with the frequency; a greater number of oscillation cycles are included in the accumulated data at lower frequencies than at higher ones.

An exponential sweep, however, maintains equal weighting since the number of cycles per unit frequency during the sweep is kept constant. The form of the sweep follows directly from that requirement:

$$\frac{n}{df} = \frac{f dt}{df} = constant \tag{6.81}$$

$$\implies f = c_1 e^{c_2 t}$$

where n is the number of cycles, and c_1, c_2 are constants. In terms of sweeping over a range, $[f_{min}, f_{max}]$ in time T, the solution is simply:

$$f = f_{min} e^{ln\left[\frac{f_{max}}{f_{min}}\right] \frac{t}{T}} \tag{6.82}$$

This equation describes an appropriate control frequency as a function of time. The experimental implementation of this has already been described in Chapter 4.

In fact, as will be seen by the results presented in a later section, the resolution of the results decreases at lower frequencies due to lower signal levels. This can be compensated for by defining a sweep function which provides more cycles of data at the low end of the sweep than at the high end. Such a function can easily be defined in a similar way to the one above. In the experiments to date, however, the function defined above has been used.

Direct FFT Method

Calculation of the complex frequency response function between the acceleration and the moment can be efficiently carried out using FFT algorithms which are well established, see Brigham[14] for example. Smooth spectral estimates of the cross-spectrum between these quantities, $S_{AW}(f)$, and the auto-spectrum of the acceleration, $S_{AA}(f)$, are first required. The estimate of the complex frequency response function is then given by:

$$T_{AW}(f) = \frac{S_{AW}(f)}{S_{AA}(f)} \tag{6.83}$$

A Parzen window function is the recommended window for these calculations. Beyond that, the procedure is relatively straightforward and detailed procedures can be found in many references[6,63].

Blackman-Tukey Method

Although the computational efficiency of the FFT has made the previous approach much more popular for basic spectral analysis, the "standard" or "Blackman-Tukey" method based on taking the Fourier transform of the correlation functions is still sometimes used. When the complete spectral density matrix is required for two channels, the speed ratio of the FFT method to the Blackman-Tukey method is $\frac{m}{p}$ where m is the number of spectral estimates and the number of data points in the time series is 2^p.

Generally, for spectral analysis, and particularly when power spectral densities of narrow band processes are the main purpose, a reasonably high frequency resolution is desired. In that case, m is usually much higher than p and the FFT method is far superior. In the current application, 30 or so estimates over the frequency range may be more than sufficient, and p of typically 17 or 18 has been found to provide quite good data. Hence, depending on the quality of the results required, the speeds of the two methods can be more comparable than in typical applications. For this reason, the standard methods were also programmed.

As with the direct FFT method, the specific procedures are well established and details can also be found elsewhere[6,63].

6.4   Comparison of Results from Steady and Swept Frequency Methods

Overlaid in Figure 6.3 are the results of many different experiments carried out on a square prism, including both steady frequency and swept frequency experiments. These experiments will be discussed in more detail in the next chapter. The emphasis here is on the different experimental methods used to obtain these results. The upper plot shows the real part of the aerodynamic impedance, α, or the aerodynamic stiffness, and the lower one shows the imaginary part, β, or the aerodynamic damping.[2]

The unshaded points are from tests in which the forced oscillation frequency was swept continuously from 5 Hz to 20 Hz while the mean wind speed was kept at a constant value thus obtaining results for various reduced velocities, defined by $V_r = V_H/fB$. Three such sweeps are included in the figure and are differentiated by different shaped plotting symbols. Each sweep shows results over a different range of reduced velocity. The shaded points in the figure represent results of tests carried out with a single forced oscillation frequency[3] of about 11 Hz and with the hardware system well balanced as described in § 5.2.2. The mean wind speed was varied discretely to obtain the result for each point.

---

[2] This form of presentation is used for most plots of aerodynamic impedance discussed in the body of this thesis. In some cases. it is useful to consider the alternative representation of magnitude, $|G_a|$, and phase, Θ. Therefore, wherever such a complementary figure is not included in the body, it can be found in Appendix A.

[3] The convention of shaded and unshaded points representing steady and swept frequency data respectively, has been used in all figures except where otherwise noted.
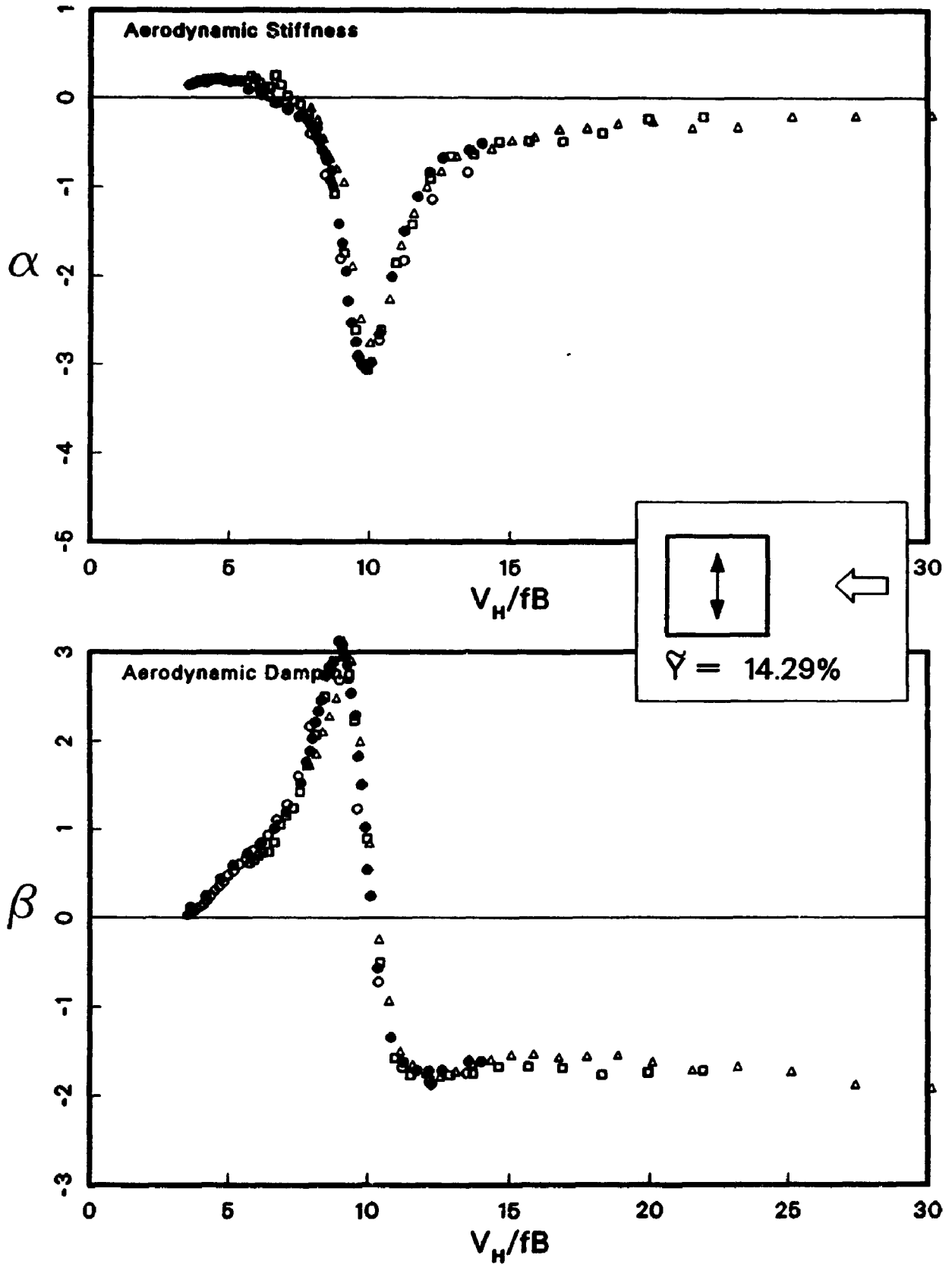
Figure 6.3: Comparison of Results from Disparate Experimental Techniques and Analysis Methods, Large Amplitude

Similar data are shown in Figure 6.4 and Figure 6.5 for two other forced oscillation amplitudes. The three figures span a range of dimensionless rms tip amplitude, $\tilde{Y} = \tilde{y}/B$, from 1.6% to 14% which represents the range af amplitudes investigated to date.

The effect of decreased signal strength can be seen in the case of the lower amplitude plots as well as in the low frequency (high reduced velocity) end of each sweep. The latter two figures include connecting lines to aid in this observation. Under either of these conditions, lower amplitude or lower frequency, the signal to noise ratio of the acceleration mesurement becomes smaller. The steady frequency data, of course, do not suffer from changing signal strengths with respect to frequency, but only with amplitude variations. All of these results are for data records of 1500 seconds in the case of the swept frequency data and 360 seconds in the case of the steady frequency data.

For the lower noise conditions, the data in the figures overlay very well. This is quite significant because the two types of tests from which they were derived are distinctly different. The swept frequency experiments are directly influenced by the internal dynamics of the activator system at all frequencies in the sweep, both in the primary data record as well as in the calibration records. The single frequency experiments, on the other hand, are influenced only by the internal dynamics as they manifest themselves at that oscillation frequency. In addition the analysis procedures to derive the final data are quite different. The first uses direct FFT routines to process the raw data while the second performs the linearised fitting of the cross correlations. Both are discussed in the previous section.
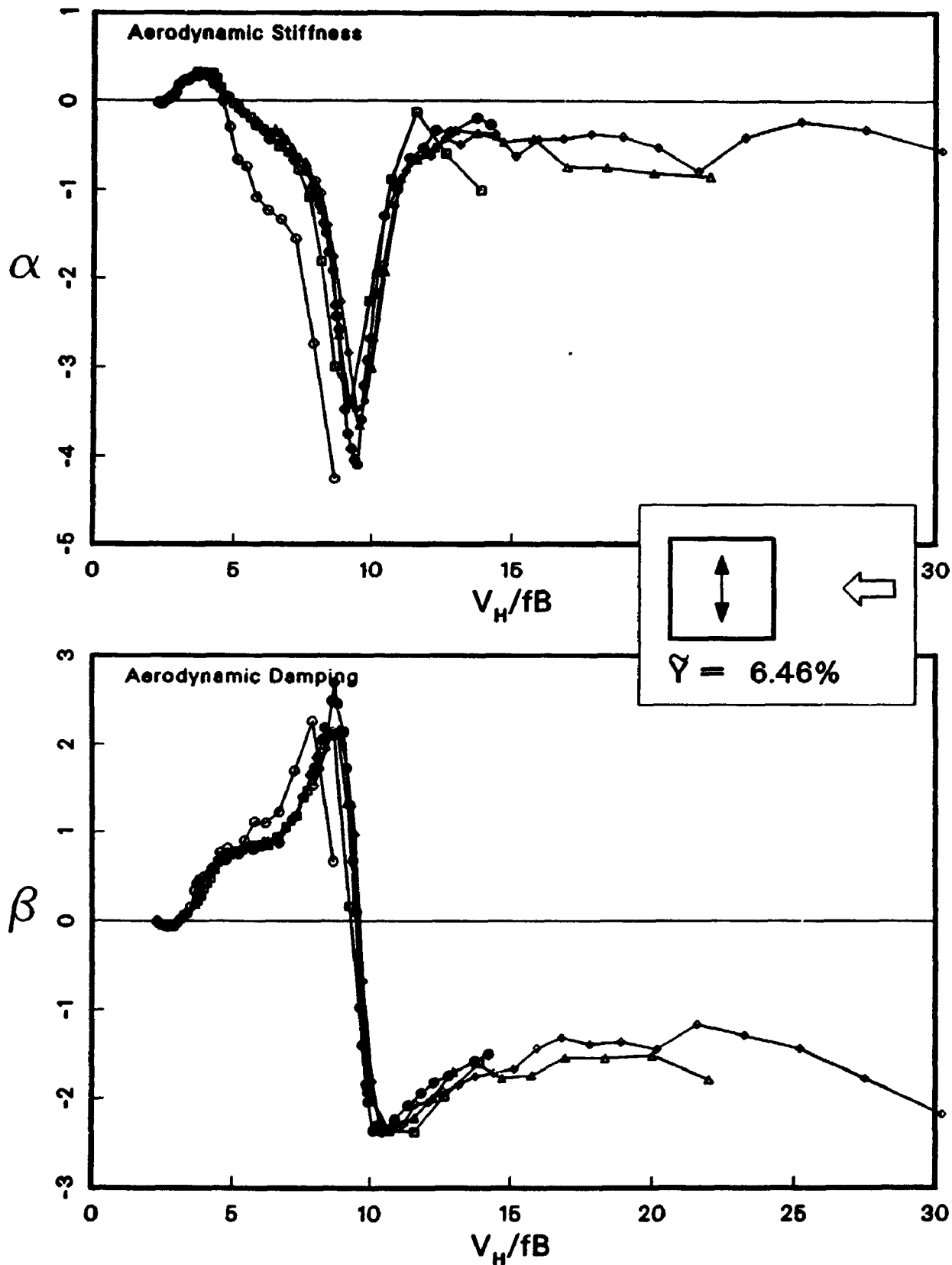
Figure 6.4: Comparison of Results from Disparate Experimental Techniques and Analysis Methods, Medium Amplitude
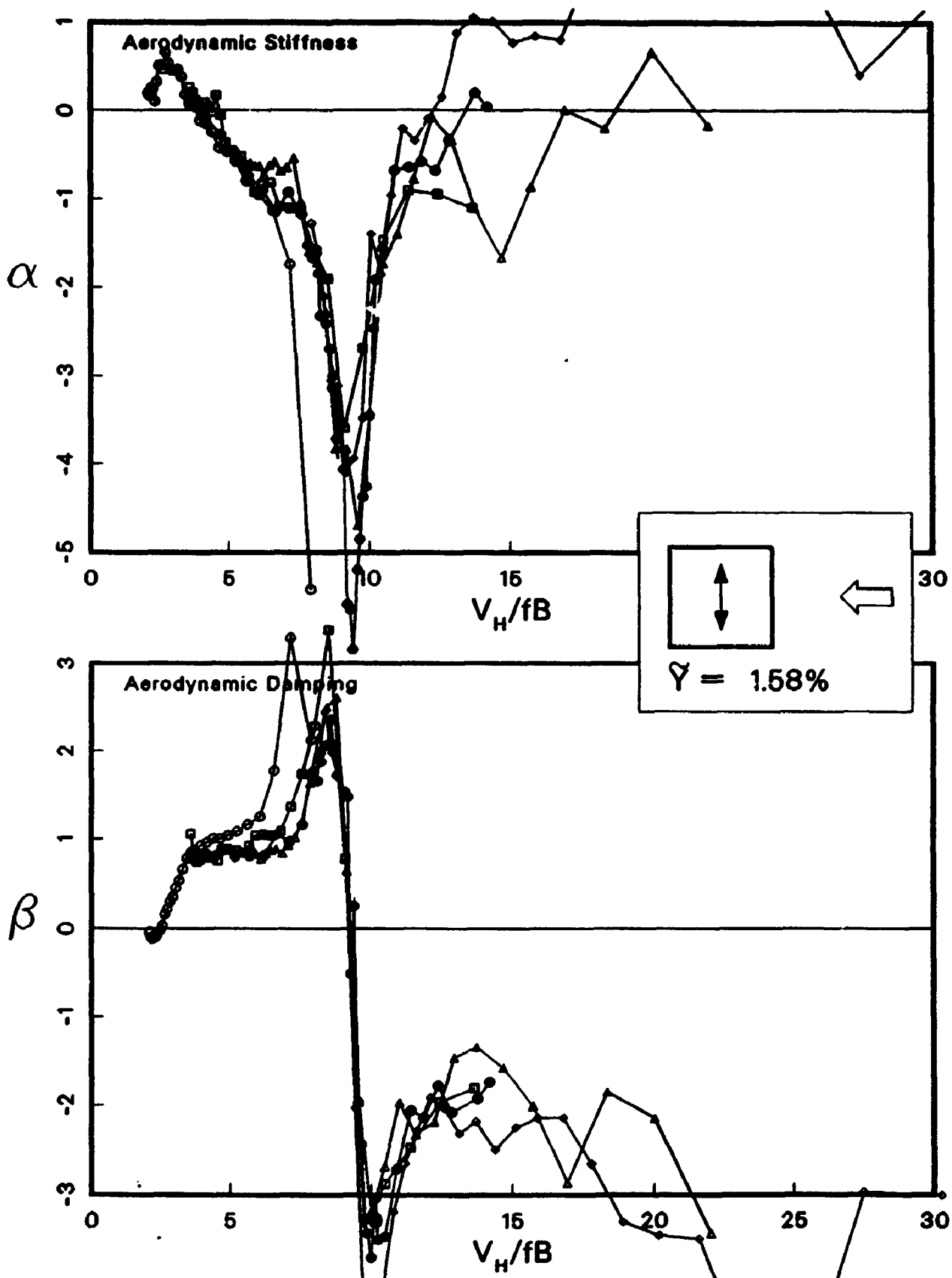
Figure 6.5: Comparison of Results from Disparate Experimental Techniques and Analysis Methods, Small Amplitude

The disparate techniques provide a convenient method of checking that the results produced are in fact phenomenological and not flawed by experimental method nor by systematic errors in analysis. The agreement in the results indicates that the calibration procedures and their inherent assumptions are quite adequate and that the system can in fact measure the motion-induced forces with a high degree of resolution and reliability.

It may also be noted that in the same way in which the swept frequency experiments are affected by the dynamics of the hardware, the complementary experiments would be affected by any anomalies in the structure of the wind as the mean flow speed were varied. Any strong Reynolds number influences would also be revealed.

The quality of the data can be improved by increasing the length of data accumulation for the lower amplitude cases. Figure 6.6 shows the variation of the calculated results with the record length at a sampling rate of 200/second for typical estimates of two steady frequency cases, one at an amplitude of $\tilde{Y} = 1.71\%$ and one at 14.0%. This type of quality control check can be used to determine whether a sufficient length of record has been obtained. The choice of 360 seconds for the steady frequency data was made to ensure high quality data for the purposes of the detailed study discussed in Chapter 7. For the swept frequency data, 1500 seconds of exponentially varying frequency sweep was chosen as a reasonable compromise between quality of results and quantity of raw data.
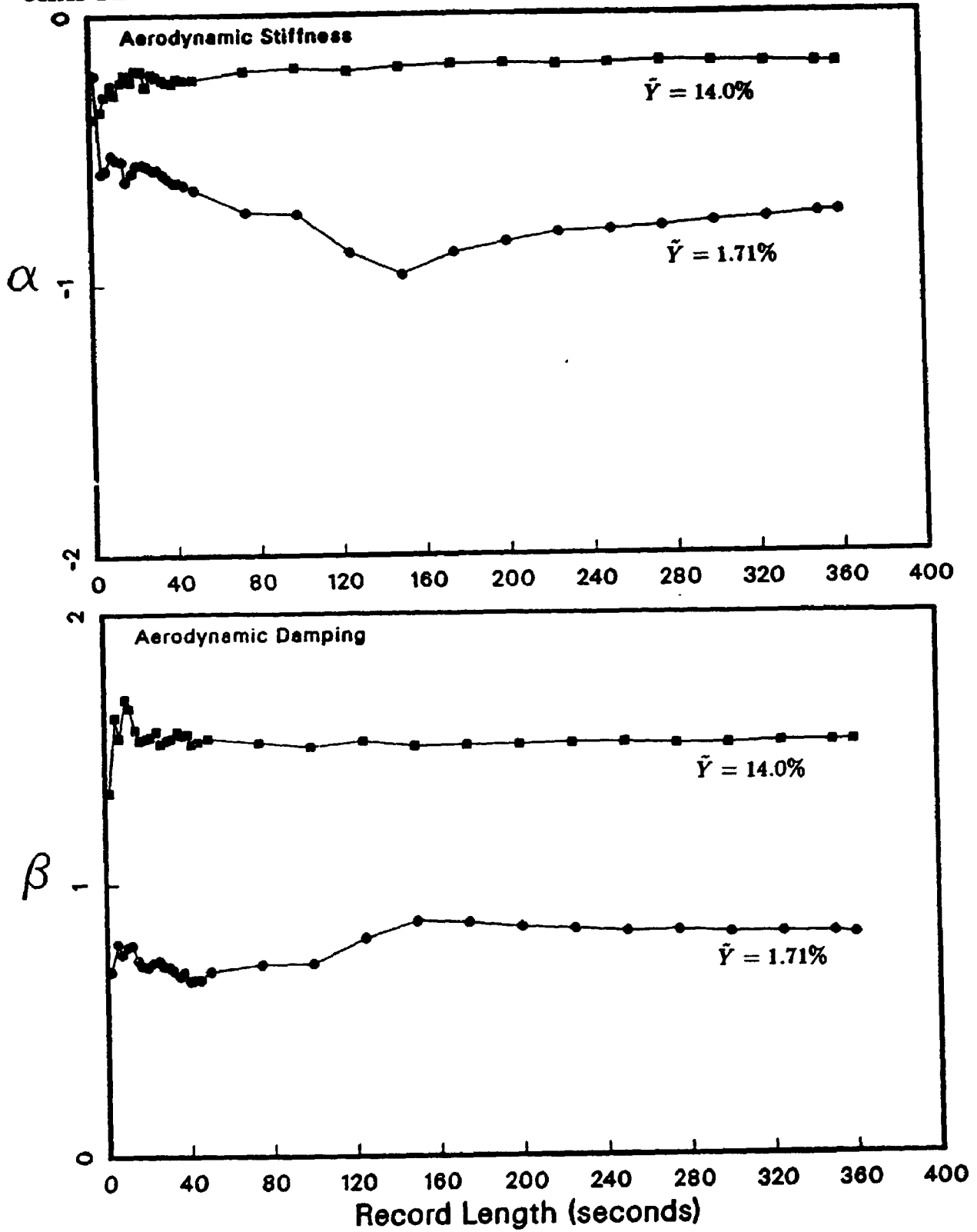
Figure 6.6: Variation of Estimate with Record Length (Steady Frequency)

6.5 Time Domain Analysis

Some references to time domain analysis have been made in the previous sections. While time domain analysis was initially anticipated and attempted during the current research, there are at present some difficulties associated with it. The reasons for this have been shown in § 6.3.2. and in fact the detailed mathematical analyses of that section were initiated by the difficulties which were encountered with time domain analysis. The amplified influence of the non-ideal dynamics of the system makes the conversion factor from volts to moment a frequency dependent function and therefore it is difficult to account for in the time domain.

Partly due to the further developmental work which would be required and mainly because of the success and adequacy of the frequency domain approaches which have been developed, time domain analysis has not been pursued any further in this work. Based on the limited results which were achieved, it is also anticipated that the additional insights into the phenomena gained by time domain analysis would be minimal.

It is worth pointing out, however, that should further improvements in the measuring system be made, some information regarding the nature of the nonlinear interactions between flow and structure may be possible by time domain analysis and it may be worth reconsidering development of it at that time.

Part III

EXPERIMENTAL STUDIES

Chapter 7

Experimental Study of the Square Prism

7.1 Introduction

Primarily as a demonstration of the use and potential of the Pivot Mode Activator System, a detailed study was carried out for a square prism. This shape was chosen because it is one of the most common shapes studied. Therefore, there exists some previous findings with which comparisons, if only qualitative, can be made. Moreover, it is not an uncommon shape for practical situations. Circular cross-sections are perhaps more common for tall chimneys, however, in the case of a square, the sharp corners at the leading edge as seen by winds at normal angles of attack make it less sensitive to Reynolds number effects. This is essentially due to the stability of the flow separation locations at the leading corners. In contrast, for a bluff body with curved surfaces, such as a circular cylinder, the location of flow separation is highly dependent on the relative strength of the inertial and viscous forces within the fluid and hence the Reynolds number. For the first shape studied using the Pivot Mode Activator System, the independence from the Reynolds number modelling parameter was an advantage.

The secondary purpose of this detailed study was to provide a complete and comprehensive set of experimental dat. against which theoretical models of motion-induced forces may be compared. For this reason, great care was taken to ensure that various tests were carried out under known and suitably matched conditions with respect to model properties (mass, stiffness, and damping), geometry (shapes and pivot point locations), and flow conditions (reference speeds, and profiles). The actual development of theoretical models is beyond the scope of the current study.

Several different wind tunnel experiments were performed besides the pivot mode activator experiments. These included base balance experiments, forced oscillation pressure model experiments, and free oscillation aeroelastic model experiments. All of the tests were carried out in BLWT II at the Boundary Layer Wind Tunnel Laboratory at the University of Western Ontario[23]. Each of the experiments will be described in this chapter along with their results. A combined analysis of the results from the various experiments will also be presented.

The major portion of the study was restricted to a single case of aspect ratio and roughness exposure and for a mean wind direction normal to one side of the prism. The model was 1.5 in. × 1.5 in. × 20 in. giving a nominal aspect ratio of 13.3. All automatic roughness elements of BLWT II were lowered to floor level to achieve a relatively smooth exposure and this exposure was used for most tests in the study. Figure 7.1 shows the velocity profile for the resulting turbulent shear flow. The mean velocity and local turbulence intensity as functions of height are both shown. Spectra of the longitudinal component of the wind at four heights are included in Appendix B. The scale of turbulence was $L_m = \frac{\lambda_m}{2\pi} \approx 1.6$ ft. where λ_m is the wavelength at which $fS(f)$ is maximum.
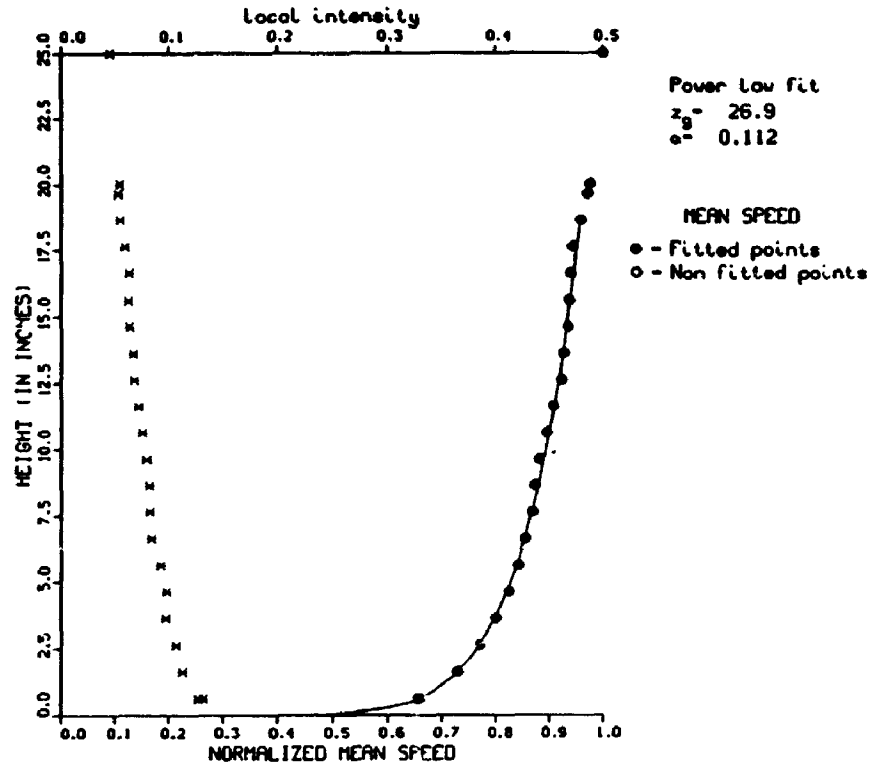
Figure 7.1: Velocity Profile And Turbulence Intensity for Main Tests

The reference velocity for all tests was taken as the mean velocity at the model height of 20 in. denoted V_H and measured by a pitot tube situated approximately midway between the model and the tunnel wall. The Reynolds numbers for all tests were on the order of 10^4.

Additional tests were also carried out to investigate the effects of varying roughness exposure and of varying aspect ratio. Further details regarding model dimensions and velocity profiles particular to those tests are described in the appropriate sections.

Figure 7.2: Photograph of the PMA Square Prism Model

7.2   PMA Balance Model Experiments

7.2.1   Experiments

The model used for the PMA experiments was of typical base balance model construction and is shown in Figure 7.2. Rohacel styrofoam with a density of about 70 kg/m^3 was used. Since this was a particularly slender model, it included a central aluminum tube for added rigidity.

The test series included forced oscillation tests for several different oscillation amplitudes ranging from normalised rms values, $\tilde{Y} = \tilde{y}/B$, of 1.5% to 14% and a range of reduced velocity from about 2 to 30. Forced oscillations were performed in the lift direction for all cases and in the drag direction for one case of amplitude. The latter was used only to compare with quasi-steady theory and so its results are included in a later section. The experiment and analysis procedures have been discussed in detail in previous chapters. Frequency domain data reduction was used to obtain measures of the complex impedance of the motion-induced forces using both steady frequency and swept frequency approaches.

7.2.2   Results

The bank of data accumulated was examined as a whole to verify the resolution quality and the agreement between steady frequency and swept frequency results. The data sets for each amplitude were then collected and edited to provide best estimate data sets spanning a range of reduced velocity from about 2 to 30. This generally involved using the long record steady frequency data where available and the low reduced velocity ends of the frequency sweeps for other ranges. The resulting set of data is shown for each amplitude in Appendices C and D.

7.2.3 Four-Dimensional Interpolated Manifold

In order to conveniently use the data in further analyses, cubic spline interpolations were made on both the real and imaginary functions first along the reduced velocity dimension and then in the amplitude dimension. In this way a four dimensional grid manifold was created in the space $\{V_r, \tilde{Y}, \alpha, \beta\}$. This manifold is plotted from two viewpoints in Figures 7.3 and Figure 7.4. The first figure shows the aerodynamic stiffness parameter α, and the aerodynamic damping parameter β. Figure 7.4 shows the complementary representation of magnitude defined here as:

$$|G_a| = \sqrt{\alpha^2 + \beta^2} \tag{7.1}$$

and phase defined as:

$$\Theta = arctan\left[\frac{\beta}{\alpha}\right] \tag{7.2}$$

Either of these figures, then summarises the entire set of experiments on the square prism for forced oscillation in the lift direction.

Figure 7.5 shows α and β curves interpolated from the manifold for amplitudes from $\tilde{Y} = 2\%$ to 14% at increments of 2%. The vertical line indicates the vortex shedding velocity as suggested by the peak in the spectrum of moment measured on a stationary model.

Recall that α and β are dimensionless quantities dependent only on the geometry of the model structure. Full scale dimensioned quantities are obtained by scaling these values according to Equation 6.12:

$$K_a = \left(2\eta M_s \omega^2\right) G_a \tag{7.3}$$
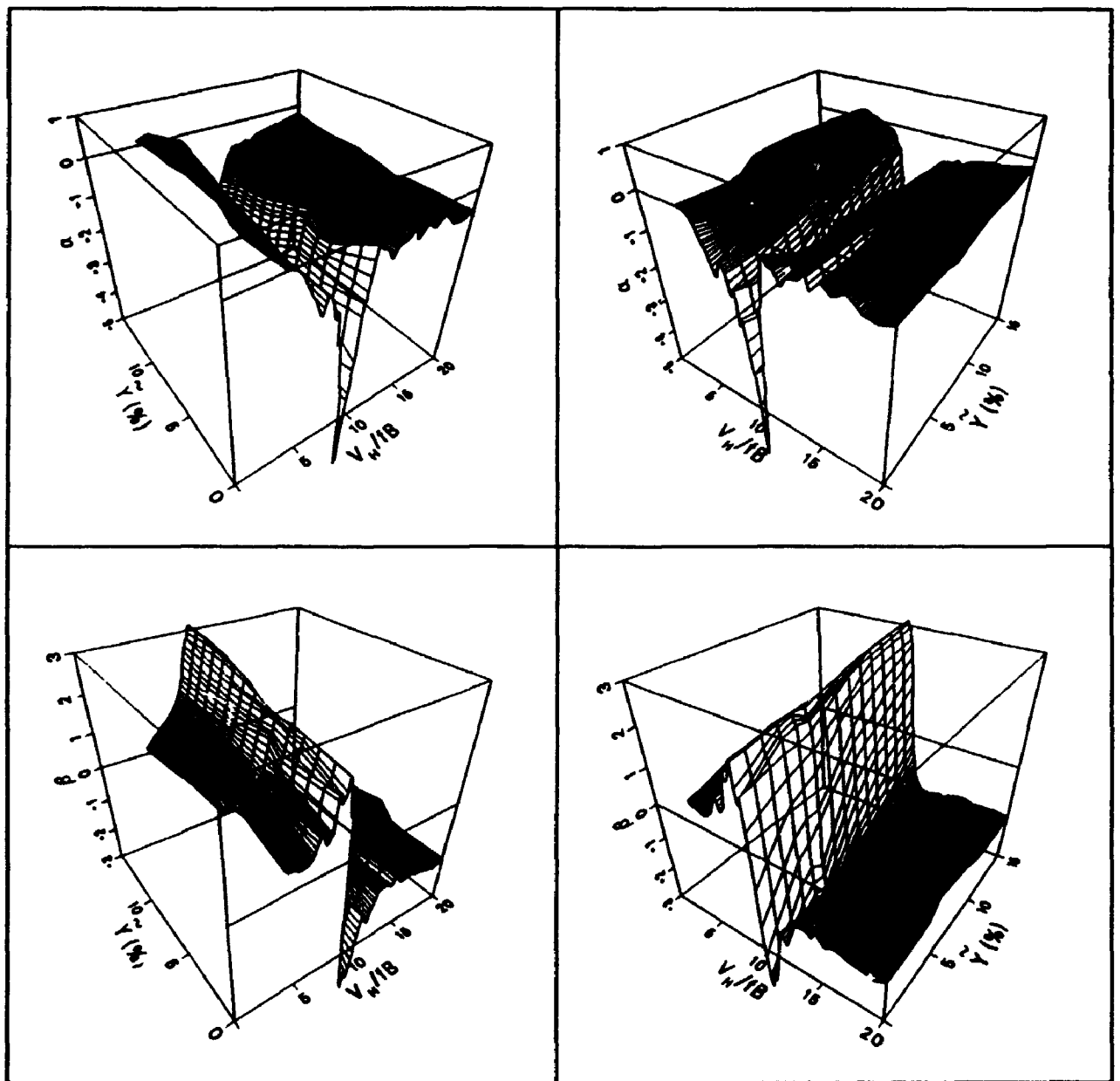
Figure 7.3: Four-Dimensional Interpolated Manifold (α, β Representation)
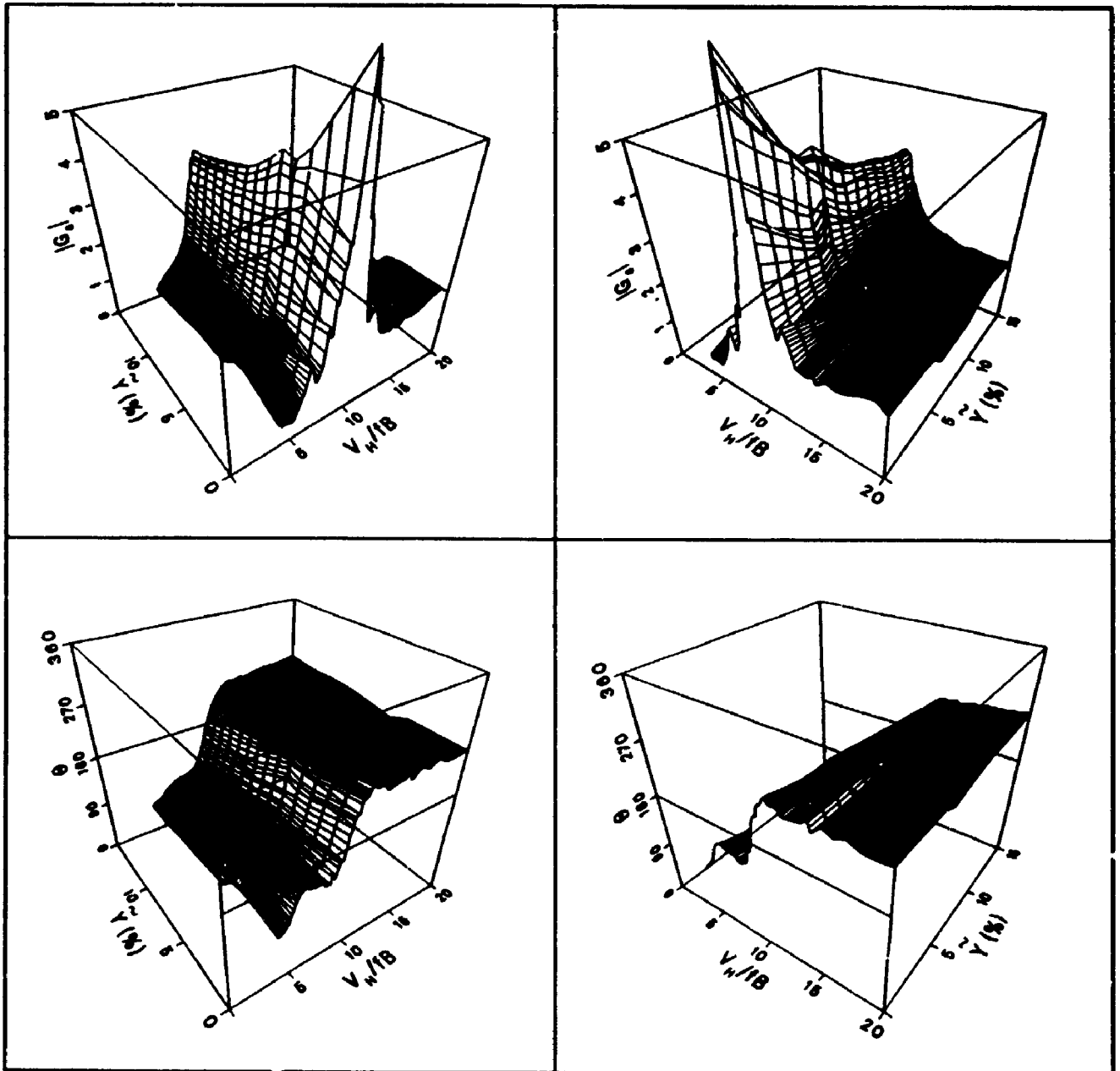
Figure 7.4: Four-Dimensional Interpolated Manifold ($|G_a|$, Θ Representation)
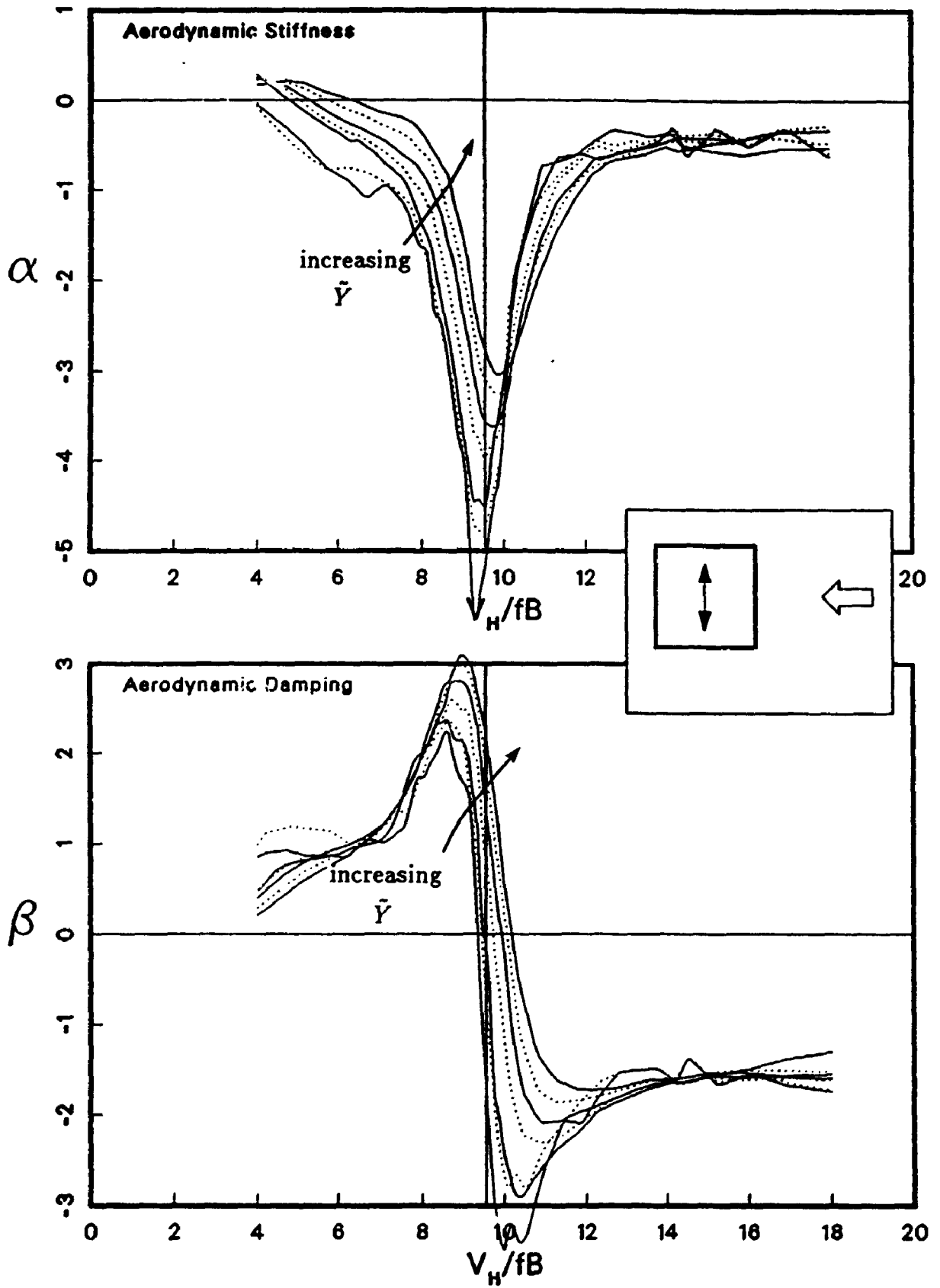
Figure 7.5: Interpolated Curves Showing Variation of Aerodynamic Impedance with Amplitude ($\tilde{Y}$ = 2% to 14% at 2% intervals)

The gross features of these results are in agreement with the findings of previous research[53,54,55][1]. The aerodynamic stiffness peaks in the region of vortex shedding. The aerodynamic damping undergoes a rapid sign change in the same region. Below the critical speed the damping is positive. Therefore, neglecting it in the regular base balance technique for predicting response would be a conservative approach. Above the critical speed, however, the damping becomes negative thereby reducing the total damping available to the structure and producing the potential for instability.

There are distinct trends which occur as the oscillation amplitude is increased indicating a highly nonlinear aspect of the motion-induced forces. This will be elaborated on in later discussions. The complicating influence of these trends on practical predictions using these data are also discussed in a later section.

7.2.4 Effect of Roughness Exposure on Motion-Induced Forces

In order to investigate the effect of varying the roughness exposure on the motion-induced forces, six tests were carried out with the model oscillated at a dimensionless amplitude of approximately 3.2%. The velocity profiles corresponding to each of the tests are shown in Figure 7.6. Nominal turbulence intensities have been associated with each one based on the local intensities occurring over the upper portion of the model. These range from 6% to 22%.

---

[1]Direct comparisons with the current study are not appropriate because the experiments are still quite different; these researchers studied square prisms in two dimensional flow and forced to oscillate in a heaving mode.
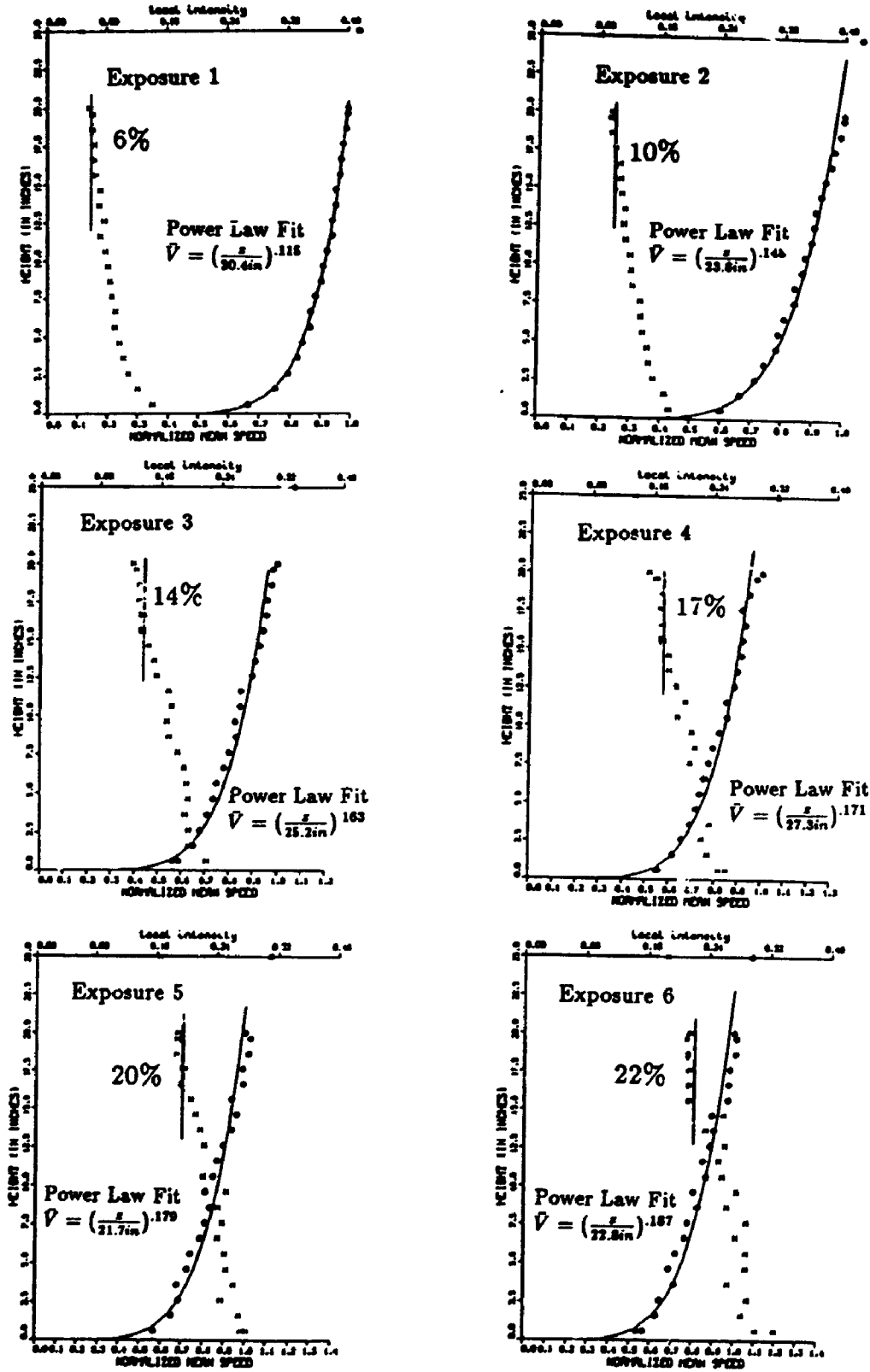
Figure 7.6: Six Velocity Profiles Used in the Effect of Turbulence Tests

All six tests were carried out using the swept frequency method. **Figure 7.7** shows the corresponding aerodynamic impedance curves for α and β respectively. Clearly, the increased level of turbulence in the latter exposures has a significant effect. **Higher turbulence not only decreases the magnitude of the aerodynamic damping, whether it be positive or negative, but it also increases the velocity at which it becomes negative.** Over the range of turbulence level shown, that critical reduced velocity increases from about 9 to about 13. There is possibly a rapid change in critical velocity commencing at a nominal turbulence intensity of between 17% and 20%, however, any conclusions regarding this observation would require verification with data of higher resolution.

7.2.5 Effect of Aspect Ratio on Motion-Induced Forces

Three tests were carried out to investigate the effect of varying aspect ratio. These tests also were carried out using the swept frequency method. The standard roughness exposure was used. The three models were of heights 20 in. (the standard model), 15 in., and 10 in. The cross-sections were 1.5 in. × 1.5 in. in all cases. These provided aspect ratios of 13.3, 10.0, and 6.67. In each case the reduced velocities were referenced to the mean wind speed at the height of the respective model. The angular oscillation amplitude was changed so that a dimensionless tip amplitude of 3.2% was achieved in each case. Figure 7.8 shows the aerodynamic impedance curves for the three tests described.

For the lower aspect ratios, the peaks in the functions are diminished and broadened. This is due, at least in part, to the different effective
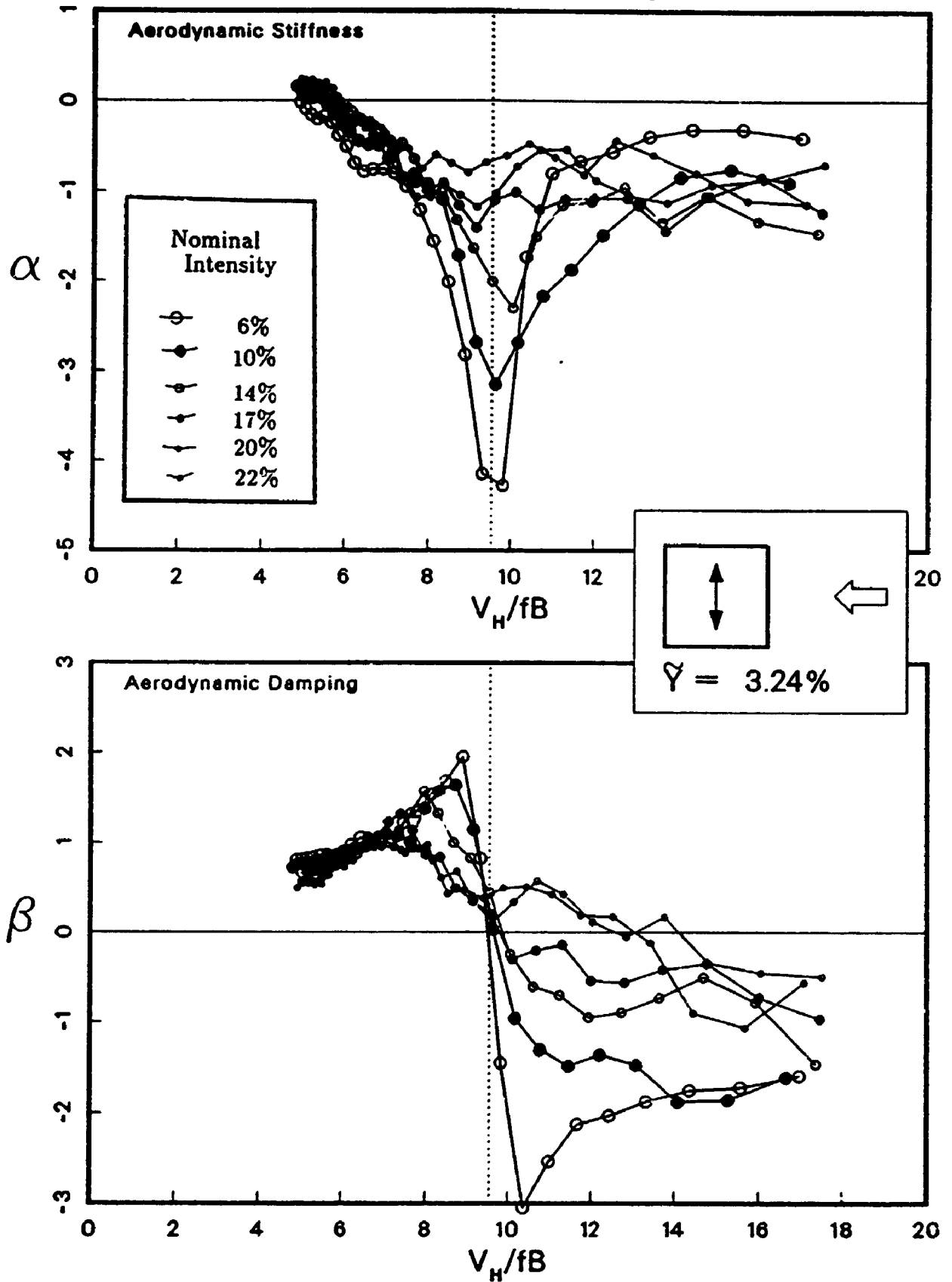
Figure 7.7: Aerodynamic Impedance for Various Turbulent Shear Flows
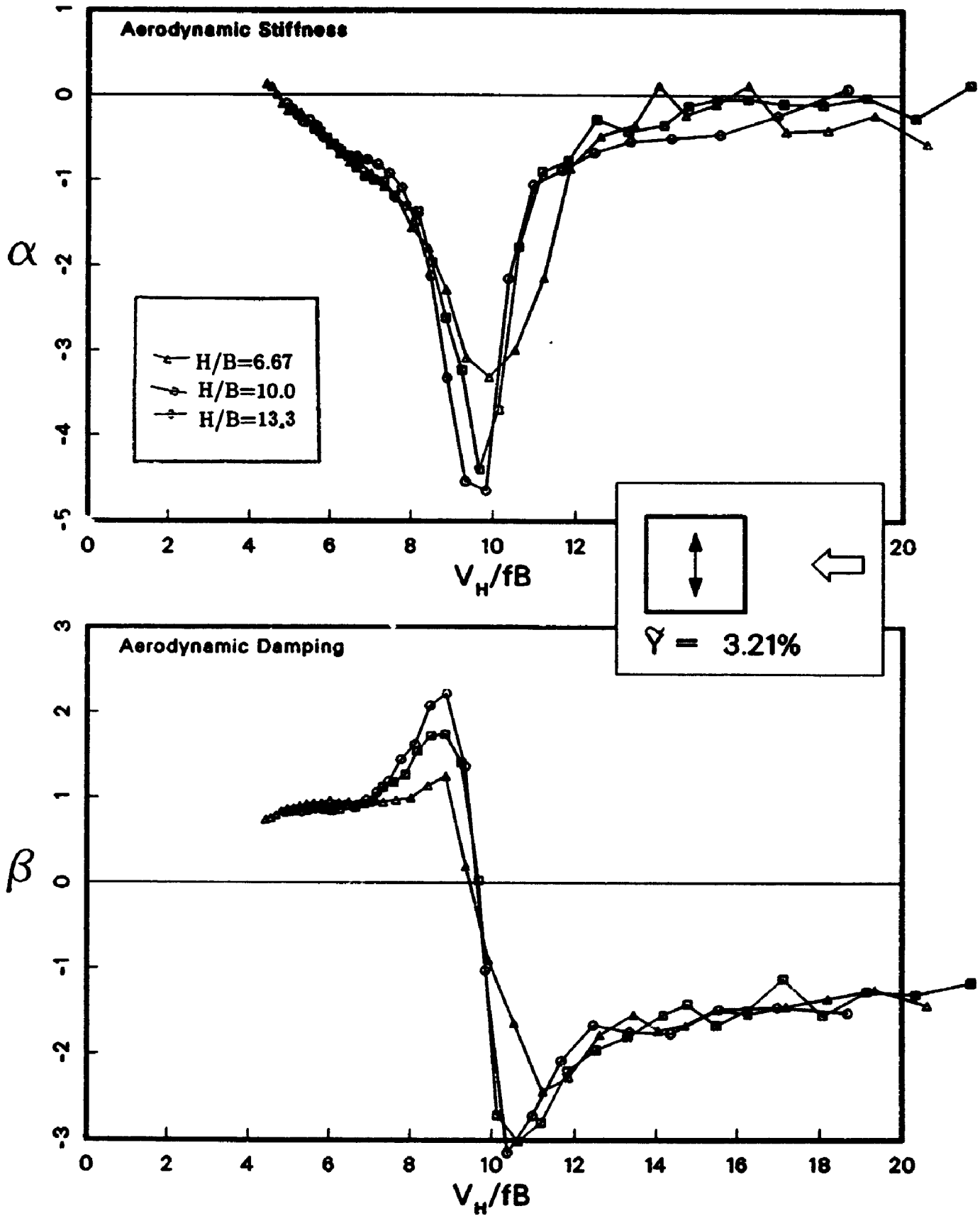
Figure 7.8: Aerodynamic Impedance for Three Different Aspect Ratios (13.3:1, 10:1, 6.7:1)

turbulence intensities present over the height of each model. The lowest aspect ratio sees a turbulence intensity over its upper portion which is around 9% in the standard exposure. This corresponds roughly to the intensity seen by the tallest model in Exposure 2 of the tests previously described. It can be seen that the second curve of Figure 7.7 is indeed similar to that of the lowest aspect ratio in the current figure.

7.3 Base Balance Experiments

The base balance experiments were performed to obtain the loads acting on a stationary model. The same model as in the main test series was used ($H/B = 13.3$). The spectral density function of overturning moment was measured for the wind normal to side of the model and is shown in normalised form in Figure 7.9. The rms value is given as a dimensionless coefficient of moment. The mean loads in perpendicular directions were also measured for varying angles of attack. These are shown in moment coefficient form in Figure 7.10. These results will be used in later analyses.

7.4 Pressure Model Experiments

The base balance tests provide information concerning the total overturning moments acting on the structure and the pivot mode activator provides information
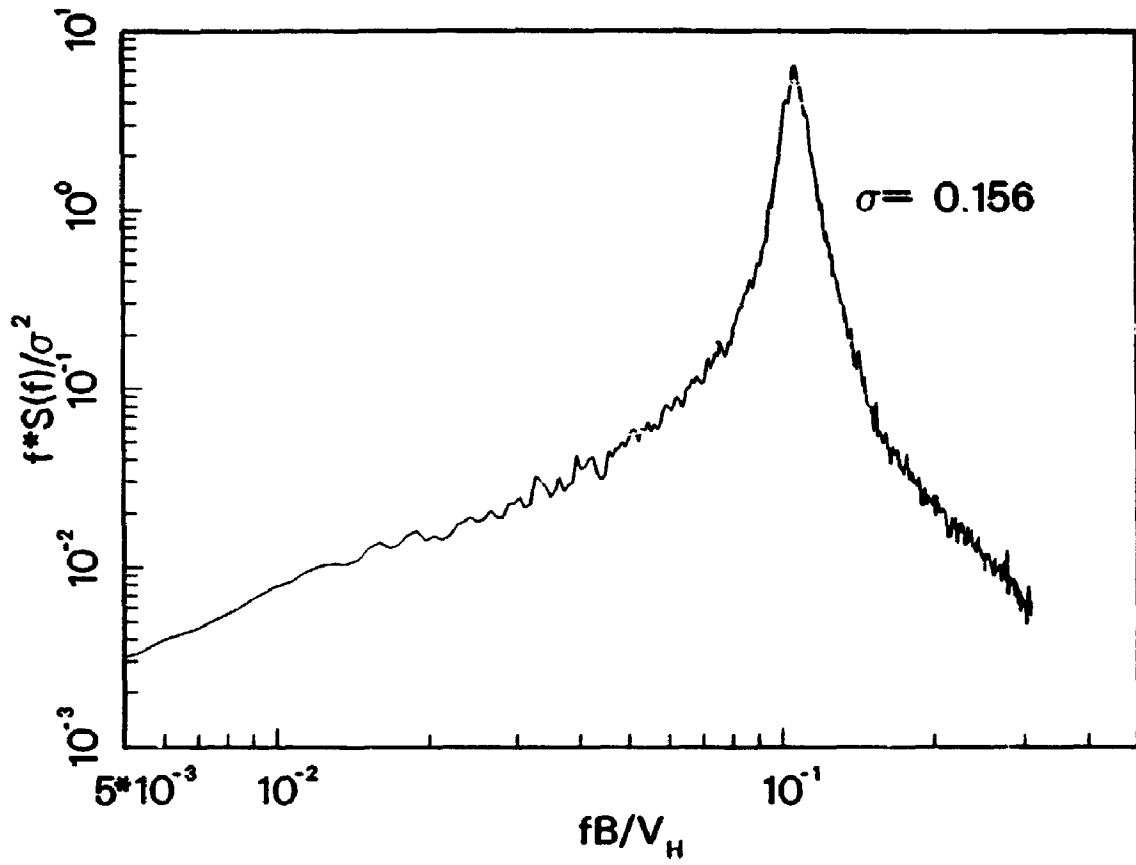
Figure 7.9: Normalised Spectrum of Lift Overturning Moment from Base Balance
Tests
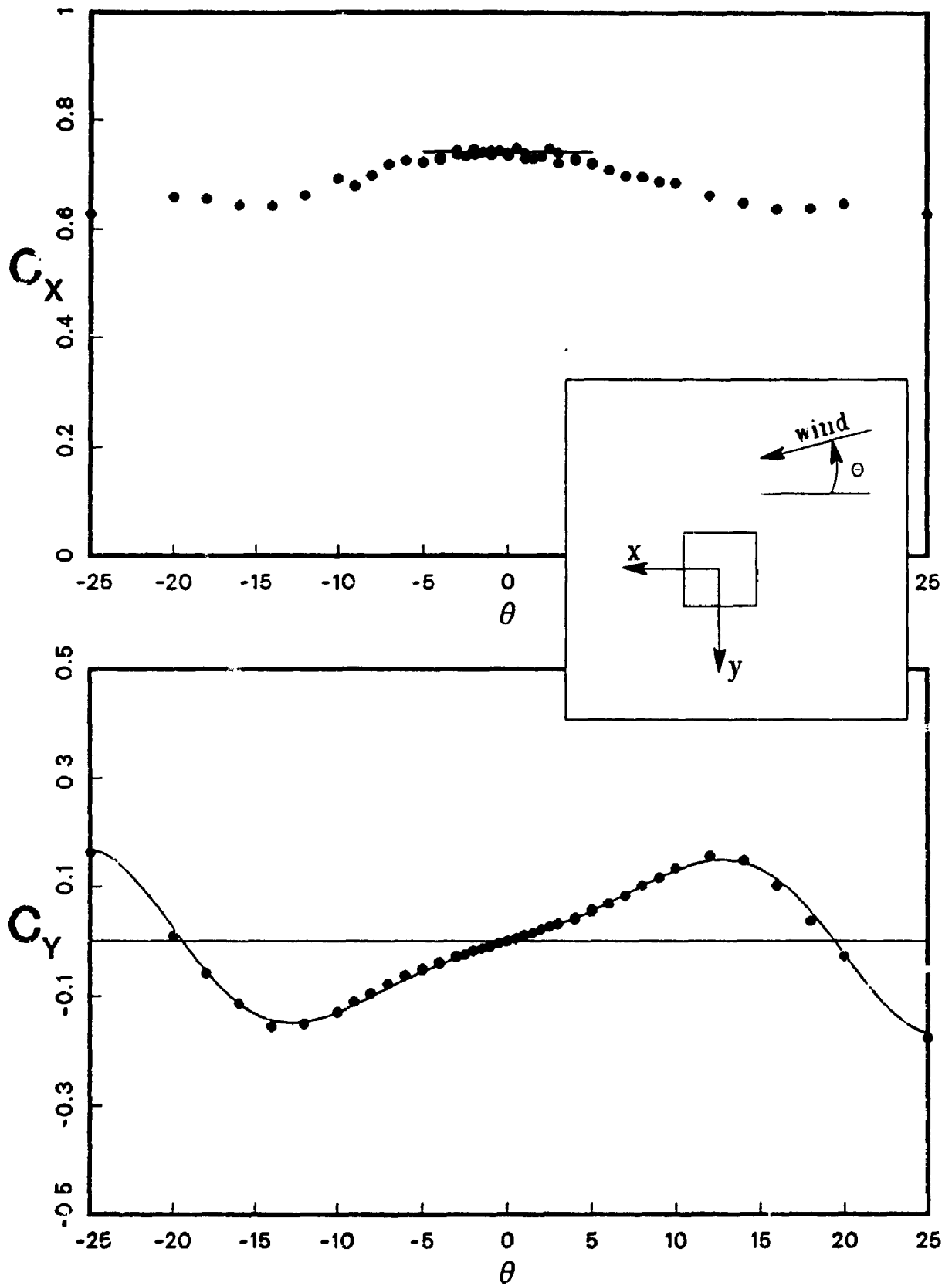
Figure 7.10: Variation of Moment Coefficients with Wind Angle

on the motion correlated forces. No information, however, regarding the spatial distribution of these loads is acquired, nor is there any information on how the motion affects the spectral distribution of forces. In order to obtain some fundamental understanding of these effects and, in particular, how load distribution is affected by the motion, a pressure model subjected to forced oscillation was used.

7.4.1   The Porous Polyethylene Pressure Model

The pressure model, shown in Figure 7.11, was constructed with identical exterior geometry to the previous model. A relatively new pressure measuring system was used which takes advantage of the porous properties of a certain polyethylene material. The suitability of porous polyethylene for measuring spatially averaged loads has been verified [64] and the technique has been used by the author in previous research[73,88]. Therefore, only a brief description of the technique will be included here.

Thin elements of porous polyethylene, mounted with their surface flush to the exterior of the model, are used to transmit wind-induced pressures to interior cavities of the model. Each cavity pressure is then measured by a single interior pressure tap constructed in the common way. Figure 7.12 shows a schematic diagram of one such cavity. It has been shown that, providing certain design conditions are followed, the cavity pressure represents the spatially averaged pressure acting on the exterior surface of the polyethylene. Porous polyethylene pressure cavities were built into the model along two opposite sides centered at one inch intervals along the height of the model. Each cavity was approximately $\frac{1}{4}$ in. high and extended
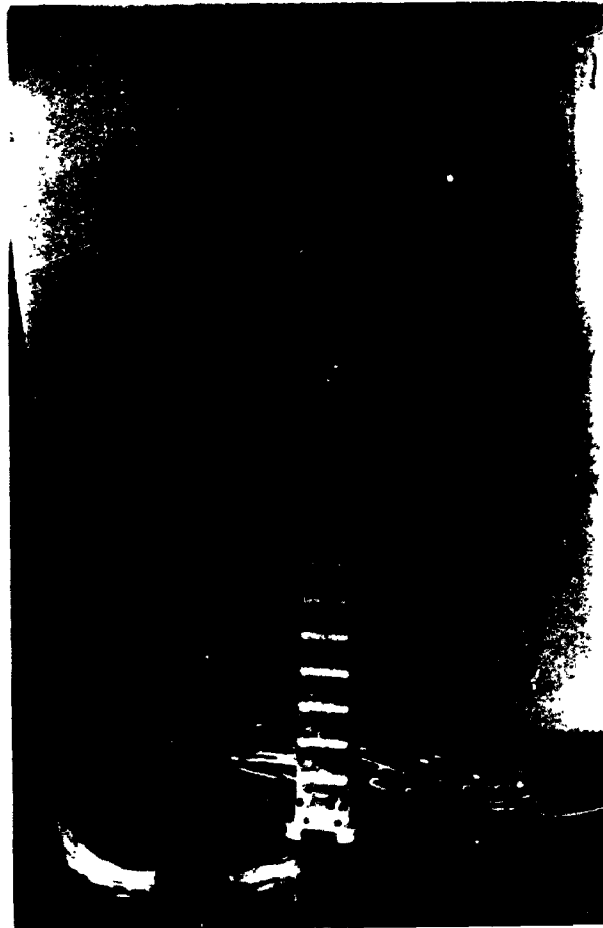
Figure 7.11: Photograph of the Porous Polyethylene Pressure Model
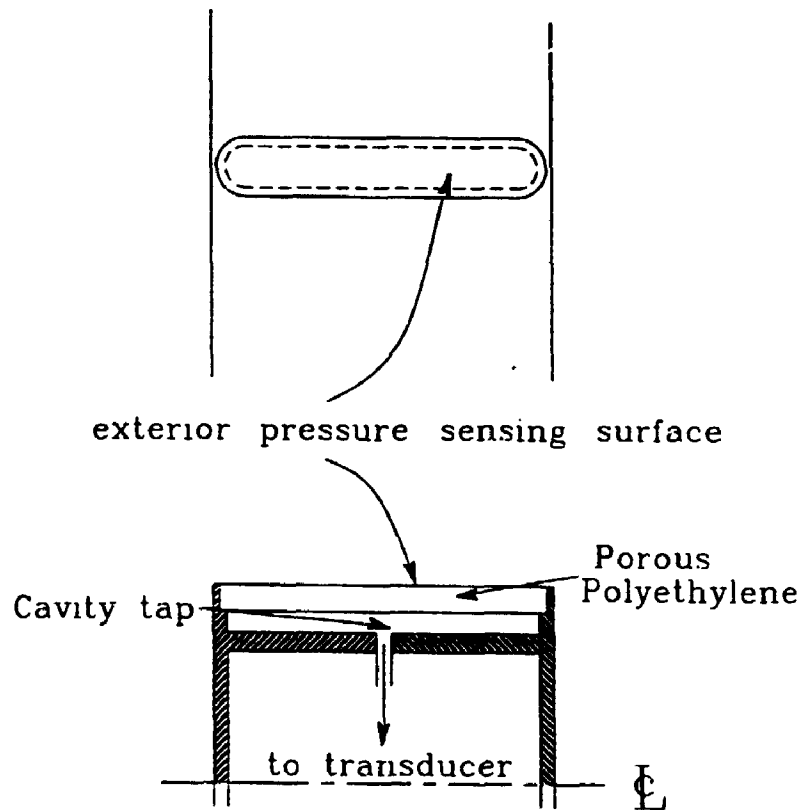
Figure 7.12: A Porous Polyethylene Pressure Cavity

to within $\frac{1}{16}$ in. of each corner of the model.

The polyethylene material acts as a low pass filter to the dynamic pressures, as does a sealed pressure tap system. Figure 7.13 shows the frequency response function for the complete pressure measuring system used with this model, including the porous polyethylene cavity and the pressure tap and tube system. It rises to a resonant peak somewhere above 100 Hz. This transfer function was obtained using a spatially coherent white noise pressure input, however, the averaging properties for spatially random pressures has also been verified[73]. The corresponding phase,
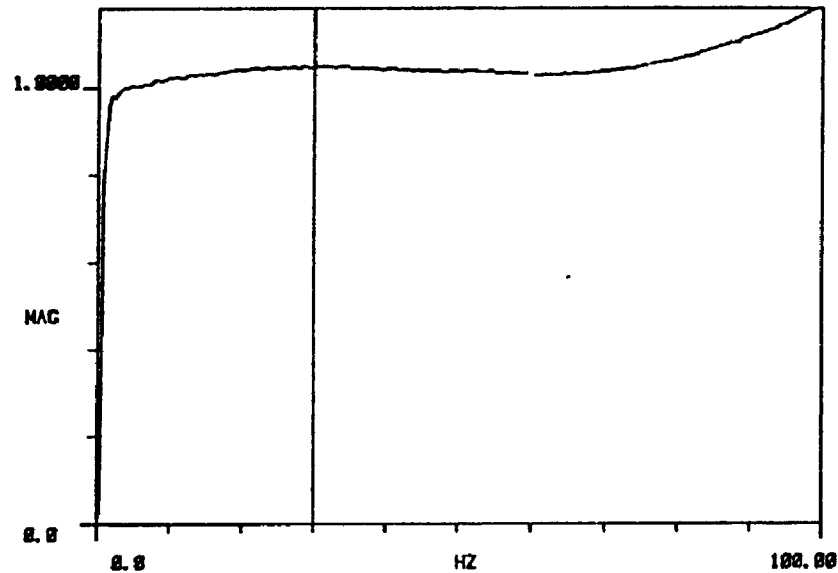
Figure 7.13: Frequency Response Function for a Porous Polyethylene Pressure Transducer System

not shown here, is a very nearly linear function of frequency which is the required condition for undistorted signal transmission.

7.4.2 Experiments

The pressure model was mounted on the pivot mode activator. The mechanical activator was used simply to provide the forced oscillation and a signal representing the notion; no measurements of wind loads were made using the PMA system itself.

There were sixteen measurement channels available in the data acquisition system so measurements were limited to simultaneous measurements of net force acting at seven levels on the model. This results from fourteen channels being used to measure pressures from pairs of opposing cavities, one channel measuring the motion of the model, and one channel left unused. Two sets of seven levels were designated and each test was carried out accumulating simultaneous data for each set. The first set consisted of the top seven levels of the model and the second set consisted of the seven levels below this. These two sets covered the top two-thirds of the model and therefore comprise the most important contributions to the total overturning moment.

Digital time series of the fifteen channels used, were accumulated for the same set of oscillation amplitudes used in the PMA experiments. For each amplitude a test was carried out at three different reduced velocities; one below, one above, and one very near the vortex shedding velocity. A fourth test with the wind off was also performed for each amplitude case. Four additional reduced speeds were tested for one amplitude of $\tilde{Y} = 6.8\%$. Each time series was 12.5 minutes and included 200 samples per second per channel. These series comprised a formidable amount of data to be analysed.

7.4.3 Results

The data analysis consisted of first calculating spectral density matrices. To do this, the fifteen channel raw time times series were converted to eight channel time series as follows. To each pressure channel was applied the appropriate calibration

factor for the pressure transducer of that channel and a tributary area weighting factor. Long term drift trends were removed and corresponding pairs of channels, now representing forces acting on opposite faces and at a particular level, were differenced. The motion signal was carried along in raw voltage form. This resulted in seven channels representing net dynamic lift forces acting at different levels and one channel representing the motion of the model. The eight by eight spectral density function matrix was then calculated using FFT techniques. Each complete matrix was stored as a processed file.

From the spectral density matrices, various functions could be calculated. These included coherence functions, coincident and quadrature spectra in normalised or coefficient form, as well as magnitude and phase of cross-spectra.

Even in processed form, the results of these experiments comprise a tremendous amount of data and so the bulk of it has not been presented here. Only some of the more illustrative examples, which are directly related to the current study and its findings, have been included. The data set in its entirety has been compiled as a separate report entitled, "Forced Oscillation Experiments on a Pressure Model of A Square Prism", BLWTL-SS17-89 and is available from the Boundary Layer Wind Tunnel Laboratory.

Spectra of Lift Force

Figures 7.14 and 7.15 show some examples of the spectral density matrix plots. The first is for a negligible amplitude or an essentially stationary model and the second is for a large amplitude of $\bar{Y} \approx 13.9\%$. The partial diagram of the model in each figure represents the upper two thirds of the model only. Along the left hand side of the model diagram are the auto-spectra of net lift force corresponding to each of the fourteen levels. On the right side of the model are the normalised cross-spectra arranged in relation to their tributary levels. Each plot follows the scaling of the blank sample located at middle right. The horizontal axis is frequency normalised by the forced oscillation frequency which will be denoted f_r. It is in log scale and runs from .5 to 2. The location $f/f_r = 1$ is indicated by the vertical slash on each of the smaller plots. The functions plotted are actually normalised auto-spectra multiplied by frequency so the areas under the curves represent the associated energies. In each case a large spike which occurs at the oscillation frequency has been removed for presentation purposes and replaced by a linear interpolation across about 8 data points. The variances in lb^2 associated with the removed spike and with the remaining portion of the spectrum are shown on each plot scaled by a factor of 10^6 for presentation. The spike may be considered to indicate the motion-induced forces while the remaining portion, representing the fluctuations at other frequencies, indicates the non-correlated or random part of the forces.

Figures 7.16, 7.17, and 7.18 show a complete set of auto-spectra of pressures at fourteen levels, for three speeds and for nine amplitudes including $\bar{Y} \approx 0$. Each column of plots represent the auto-spectra for the forced oscillation amplitude indicated. Each row represents the corresponding level on the model from the top
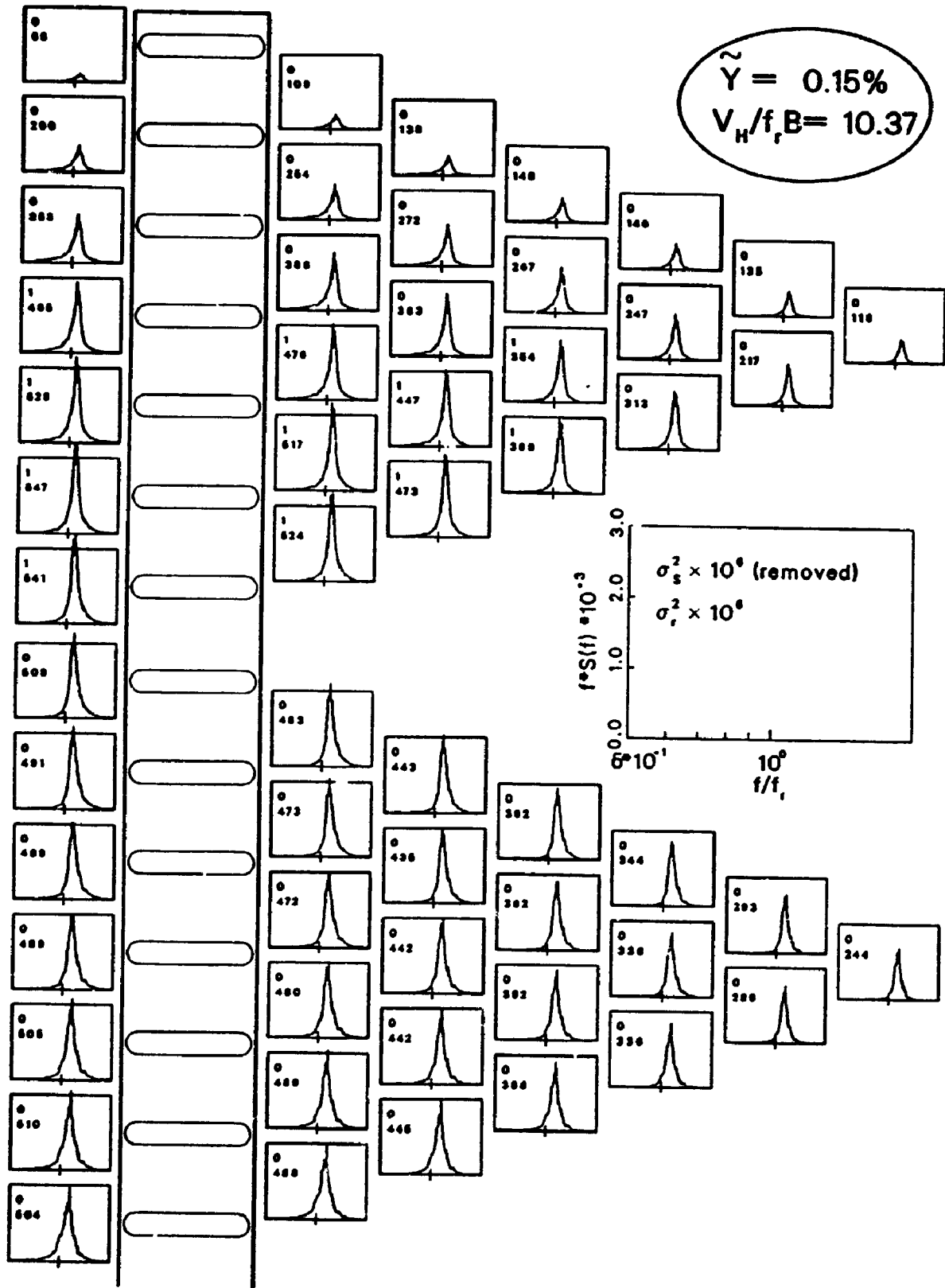
Figure 7.14: Example of Spectral Density Matrix of Forces on Upper Portion of an Essentially Stationary Square Prism
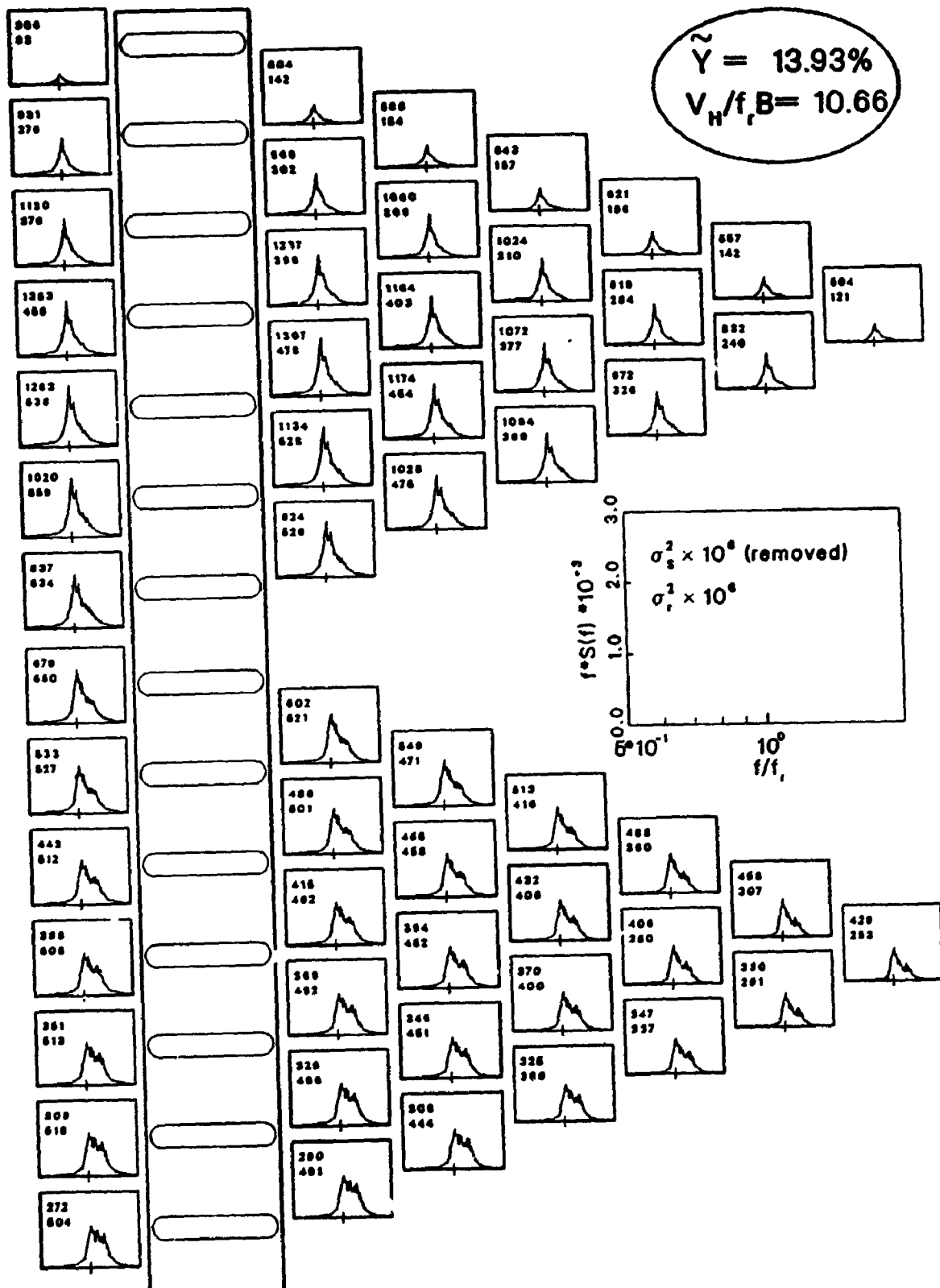
Figure 7.15: Example of Spectral Density Matrix of Forces on Upper Portion of a Square Prism Forced to Oscillate

down. All vertical axes within each figure are at the same scale previously indicated. The power associated with the removed spike is indicated by the top number in the upper left hand corner of each plot. The number below it represents the power associated with the remaining spectrum. As before, each is scaled by 10^6.

The spectra in the first column are for an essentially stationary model. As is common with lift force spectra, almost all of the energy is due to the narrow band peak associated with the vortex shedding process. This peak shifts to higher frequency as the mean velocity is increased.

In the lower velocity case, where the vortex shedding frequency is just below the forced oscillation frequency, there are some variations of the spectral shapes as the amplitude increases, that is as one moves right across the figure. This can also be noticed in the vertical direction as one moves upward, since the pivoting mode implies an increase of amplitude up the model. This, however, will be complicated by changing mean speed as well. In the second figure where the vortex shedding frequency closely coincides with the frequency of the motion, one can see the minor variations occurring at the larger amplitudes – the upper right hand portion of the figure.

The variations in the spectral distribution for these cases remain relatively minor; however, once the vortex shedding frequency becomes higher than the frequency of the motion the variations become considerably more significant. The variations, occur not just at the frequency of the forced oscillation, but at nearby frequencies as well. It appears that at a certain amplitude, $\tilde{Y} \approx 5\%$, vortex shedding is disrupted by the motion and becomes more so as the amplitude increases. The
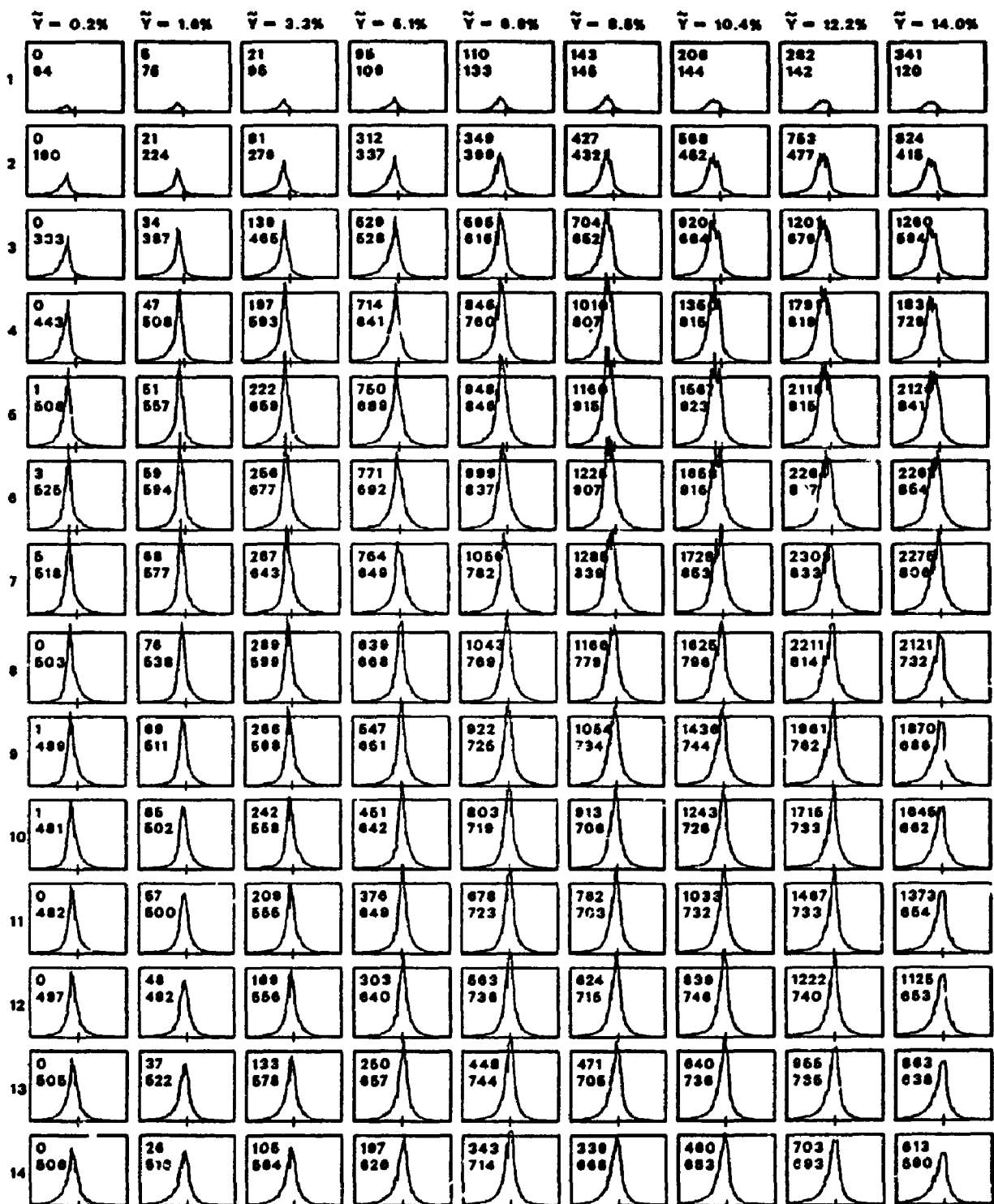
Figure 7.16: Auto-Spectra of Forces for Various Amplitudes of Forced Oscillation and for $f_v < f_r$
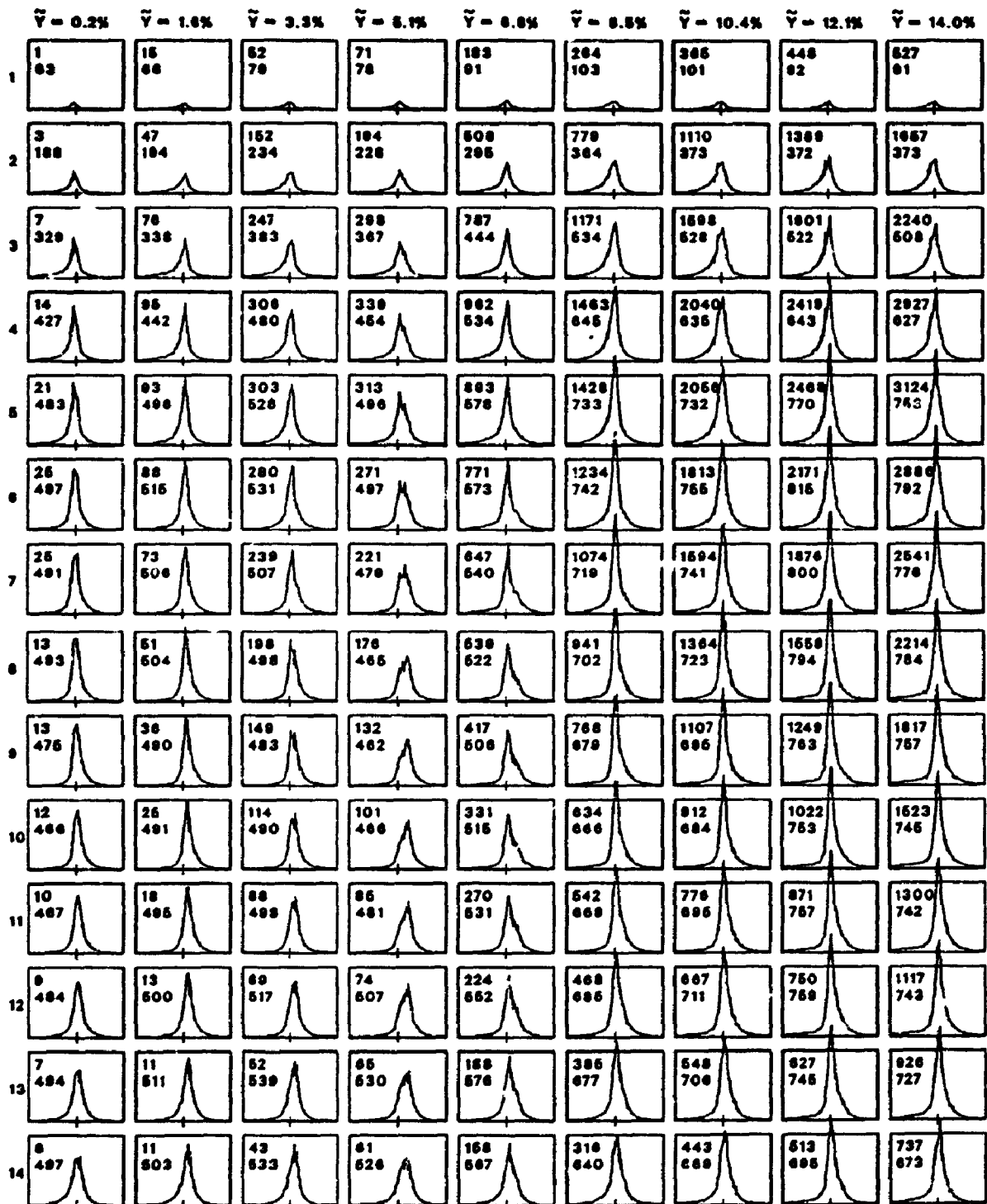
Figure 7.17: Auto-Spectra of Forces for Various Amplitudes of Forced Oscillation and for $f_v \approx f_r$
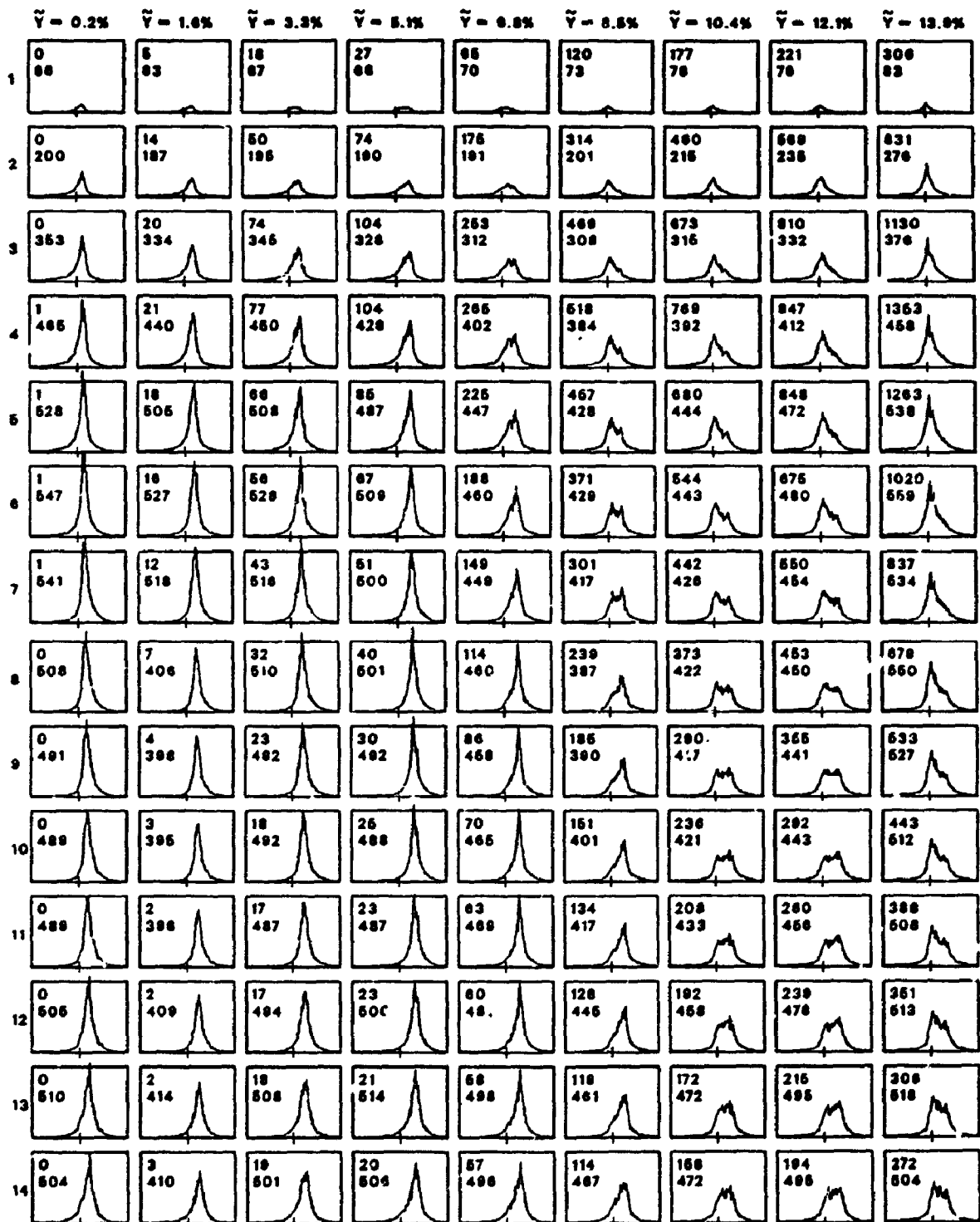
Figure 7.18: Auto-Spectra of Forces for Various Amplitudes of Forced Oscillation and for $f_v > f_r$
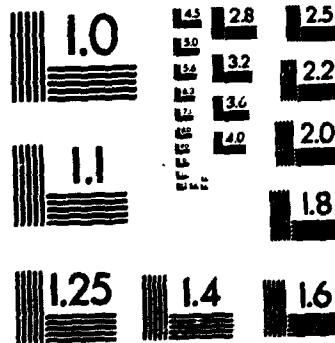
3

energy then begins to reorganise around the frequency of the motion. This pattern is particularly noticeable as one scans say the fourth or fifth level for example.

Some of these effects, particularly the tip effect, can be more clearly seen in Figures 7.19, 7.20, and 7.21, These figures show the corresponding rms values from both the spike and the remaining parts of the spectra for each amplitude plotted over the height of the model. The increase of the rms of the spike, or in other words, of the motion-induced forces, with amplitude is apparent. The amplitude effect, however, can also be seen in the rms values associated with the remaining parts of the spectra. In that case, there is also a distinct change occurring in the rms at all heights for an amplitude of about 7% for the case of $f_v \approx f_r$.

The vertical extent of the tip effect on the motion-induced forces decreases somewhat with speed, but is noticeably greater at the lower speed when $f_v < f_r$, where it extends for about four model diameters from the top. Below that level, the rms value is approximately linear with height for the cases of $f_v < f_r$ and $f_v \approx f_r$. The character of the vertical variation appears distinctly different when $f_v > f_r$.

The vertical extent of the tip effect on the rms values associated with the remaining parts of the spectra does not vary as distinctly with speed, and appears to be about three model diameters from the top in each case. Below that level, the rms is roughly constant with height.
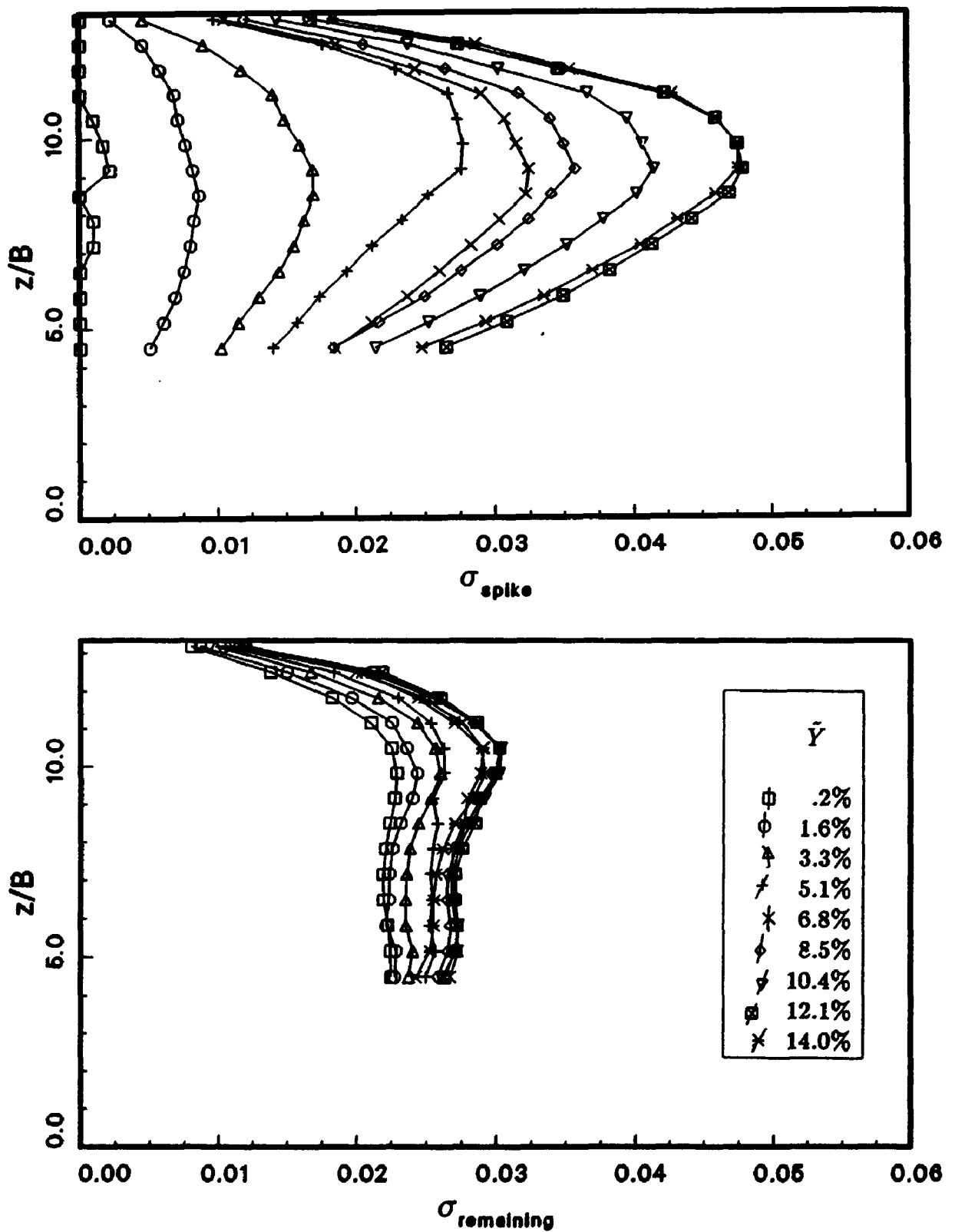
Figure 7.19: Rms Values Associated with Spikes and with Remaining Portions, $f_v < f_r$
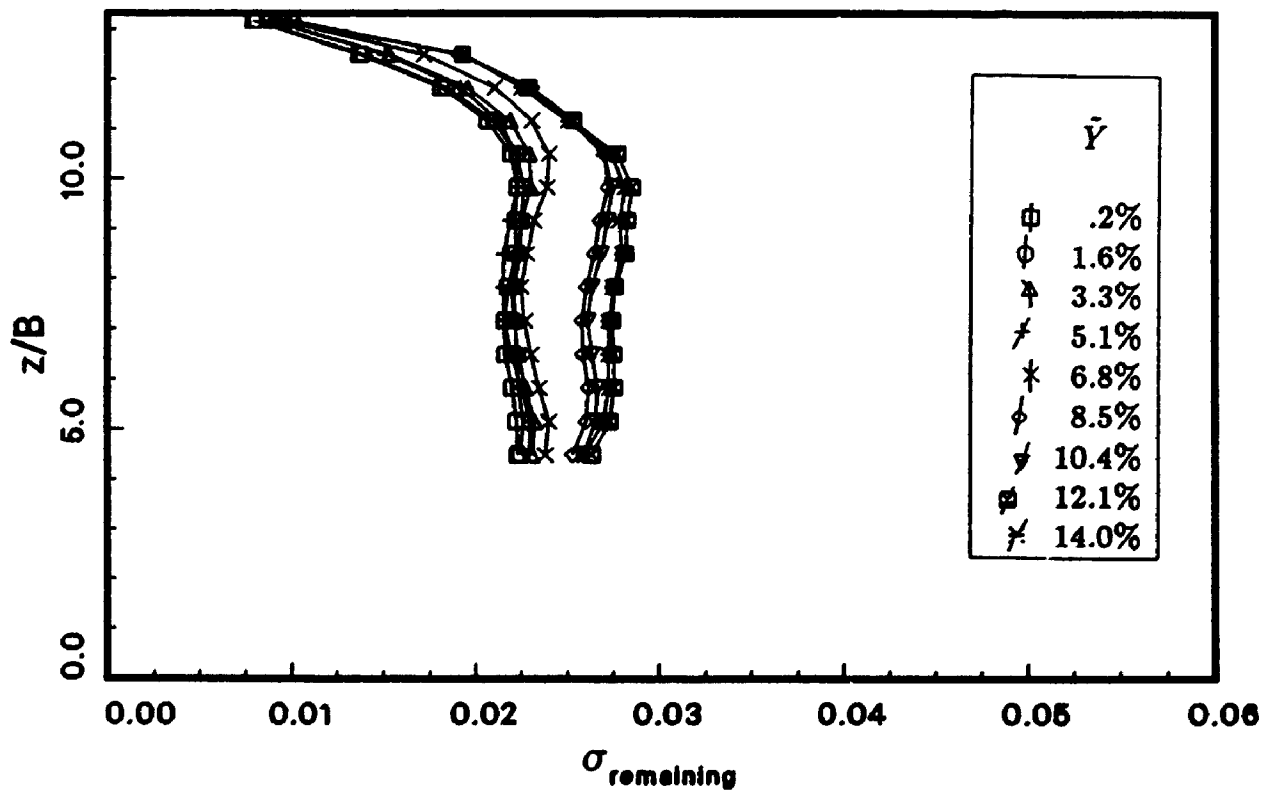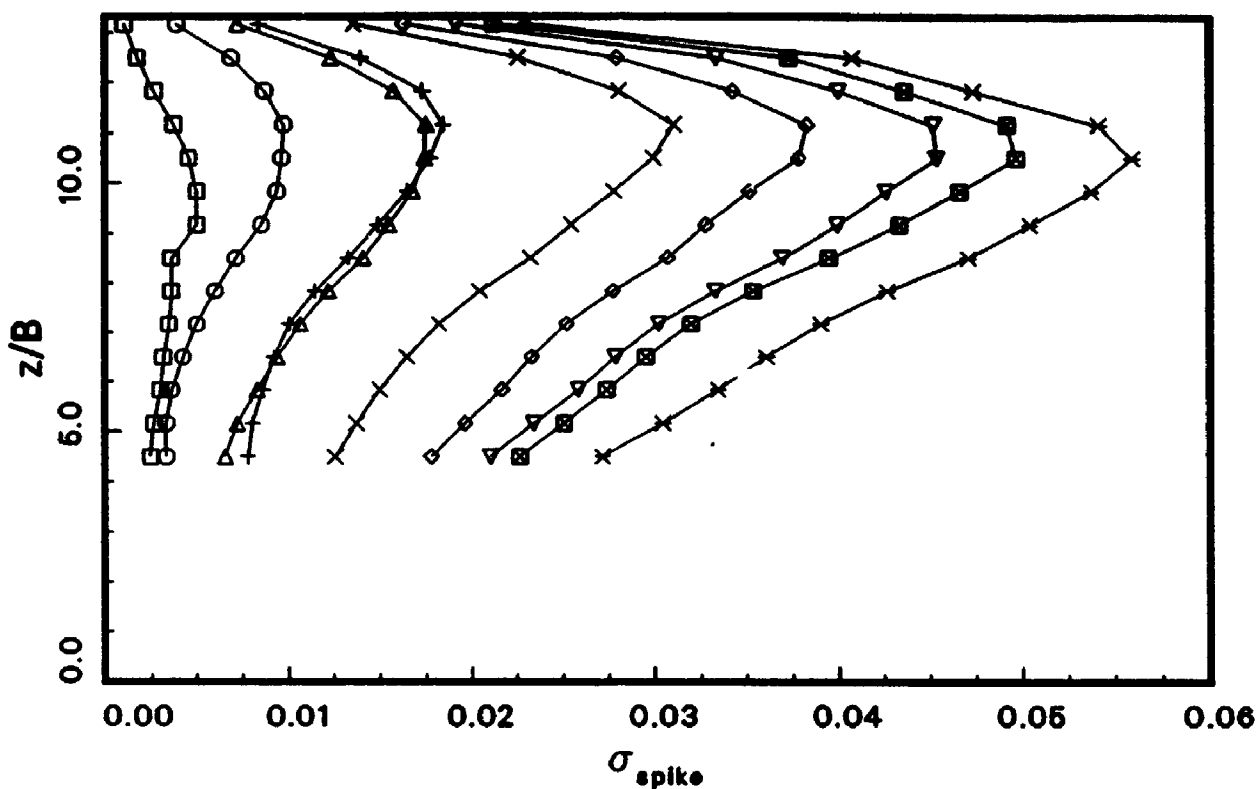
Figure 7.20: Rms Values Associated with Spikes and with Remaining Portions, $f_v \approx f_r$
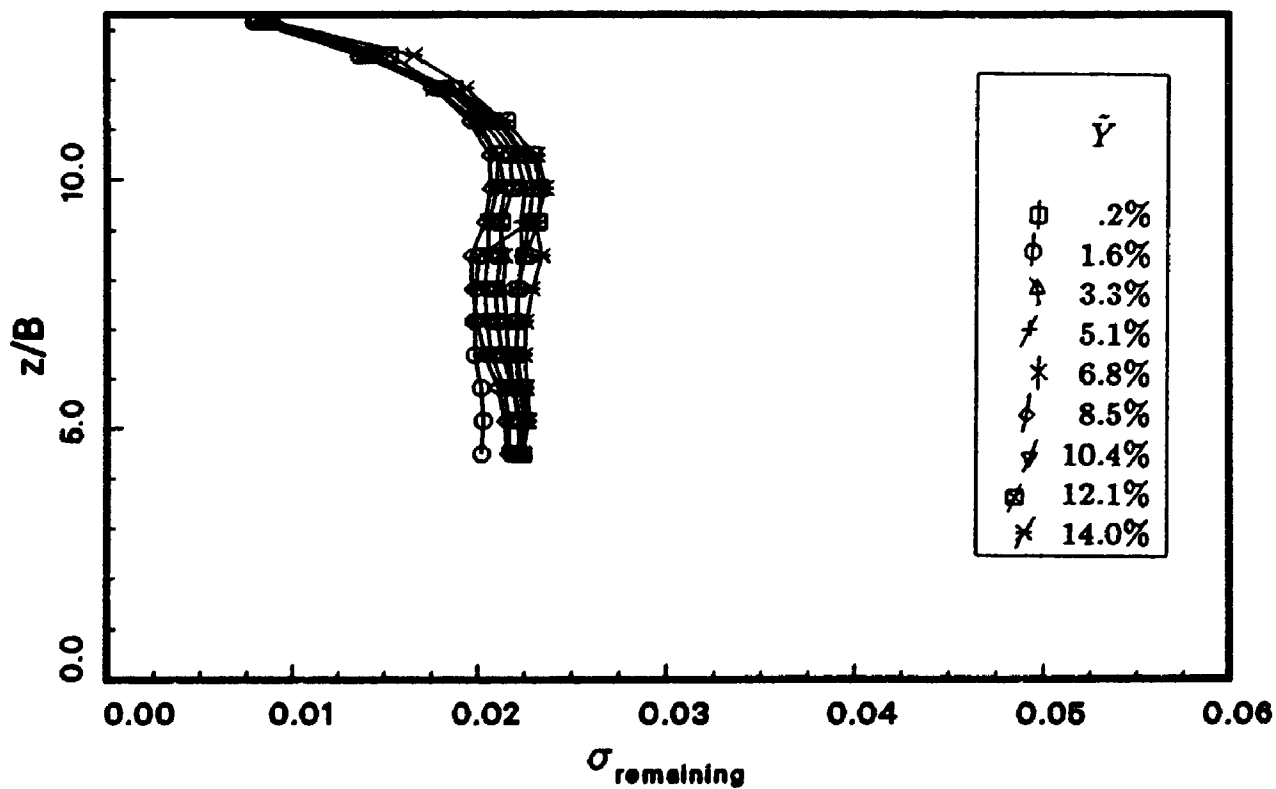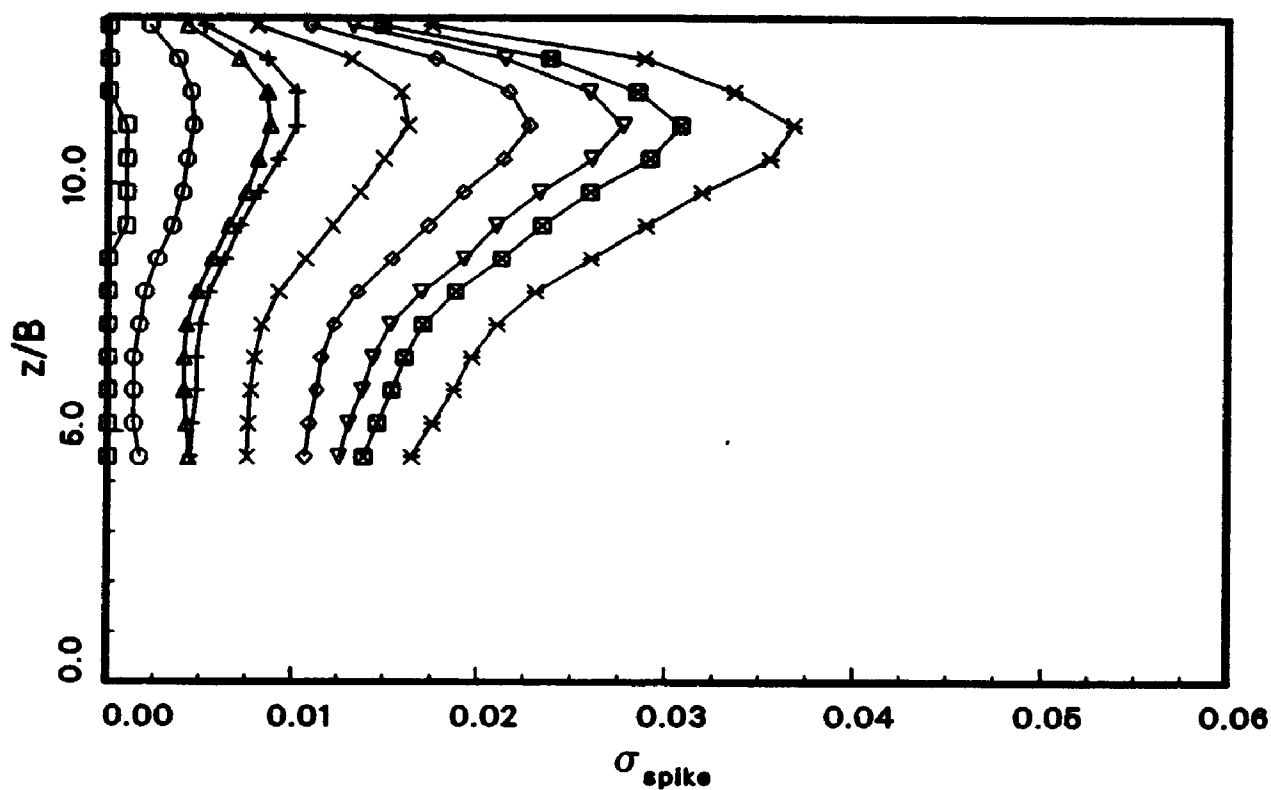
Figure 7.21: Rms Values Associated with Spikes and with Remaining Portions, $f_v > f_r$

Coherence Functions

Figures 7.22 and 7.23 show coherence functions which correspond to the amplitude cases shown in Figures 7.14 and 7.15, but for different velocities. These confirm the observations. The motion clearly has an effect on frequencies other than the motion frequency. The fluctuations occurring at lower frequencies become more organised.

Correlation Coefficients

Correlation coefficient matrices were calculated by integration of the coincident spectra for all pairs of forces. These were done considering the total spectra and then considering the spectra with the spikes removed. The latter therefore indicated the degree of correlation associated with frequencies other than that of the motion. Coefficients corresponding to common separation distances were averaged together to reduce the data and are shown plotted in Figures 7.24 and 7.25 for all amplitudes and for each of the three speeds.

In both cases the body motion increases the effective correlation length. It is more apparent in the first figure indicating the significant contribution from the motion frequency, however there are significant increases seen in the second figure also. It is interesting that for the higher velocity, that is when the vortex shedding frequency is higher than the motion frequency, the effect of the motion on the
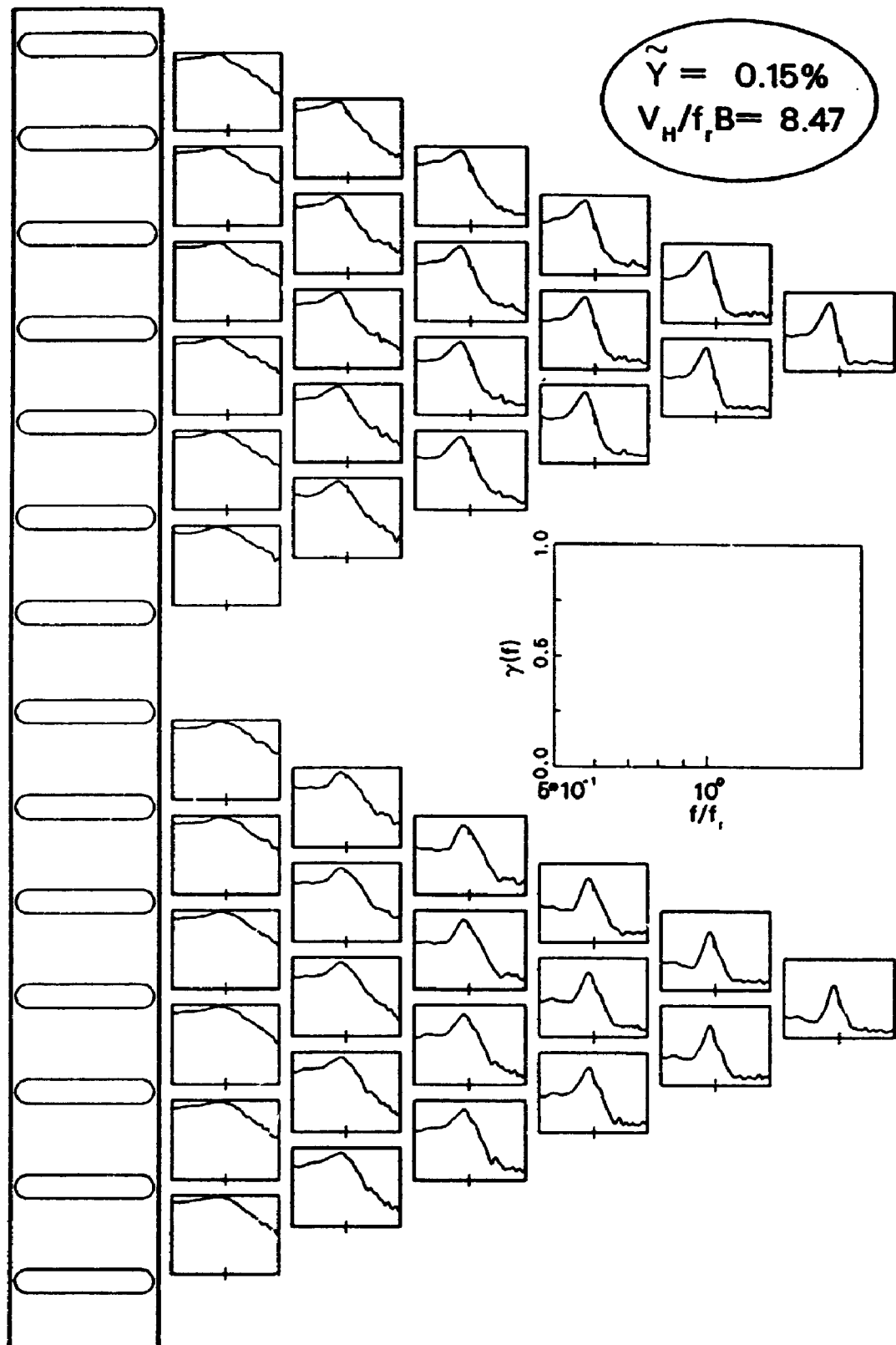
Figure 7.22: Example of Root Coherence Functions for Forces on Upper Portion of an Essentially Stationary Square Prism
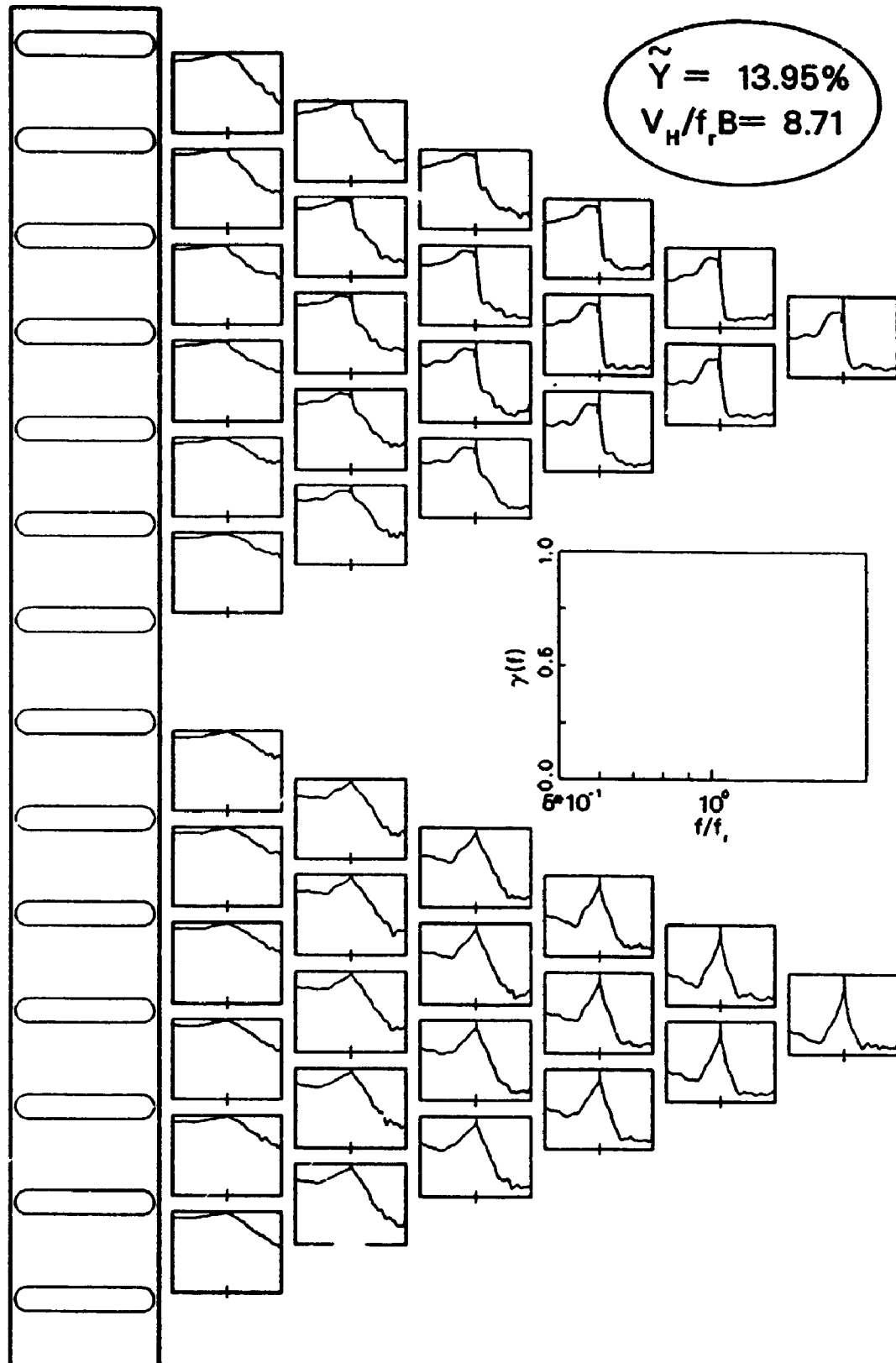
Figure 7.23: Example of Root Coherence Functions for Forces on Upper Portion of a Square Prism Forced to Oscillate
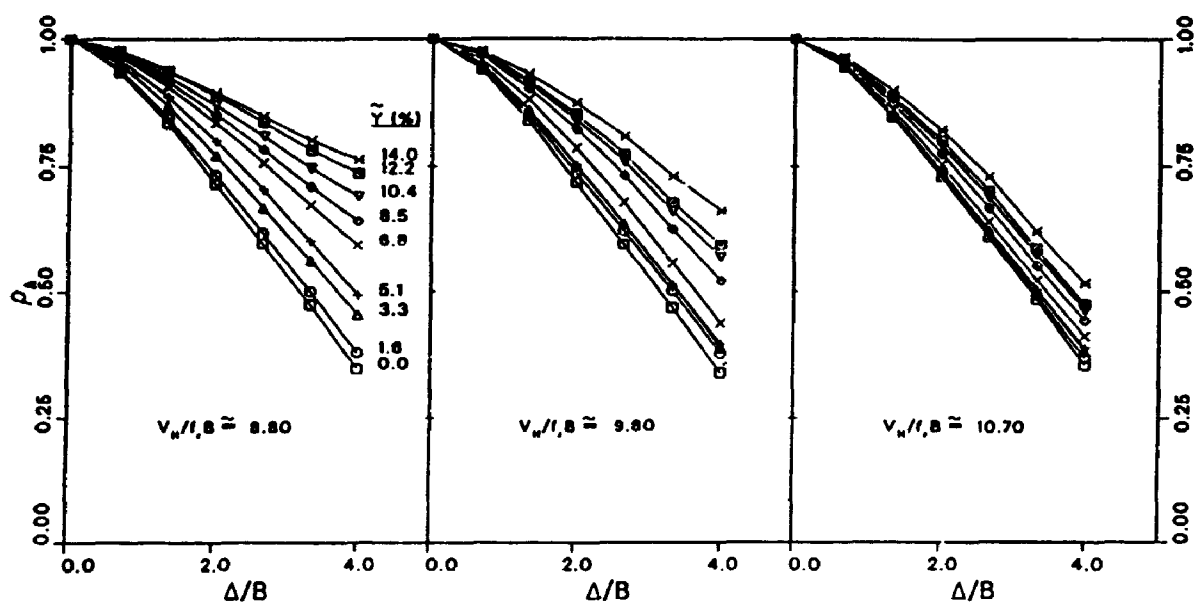
Figure 7.24: Average Correlation Coefficient versus Separation Distance Determined from Complete Coincident Spectra

correlation is much less. Moreover it is almost negligible until a certain amplitude is reached. Recall that this is the situation where the most significant alterations of spectral distributions occurred. It would appear from these results and those previously discussed that the motion tends to organise the fluctuations occurring at lower frequencies than the motion. This effect begins immediately for small motions and increases with amplitude. The organisation occurs in such a way as to increase the correlation length for these fluctuations. The motion does not organise those fluctuations occurring at higher frequencies. However, if the motion is large enough, it redistributes the energy of the higher frequency fluctuations to those frequencies closer to that of the motion and causes an increase in their organisation in the process.
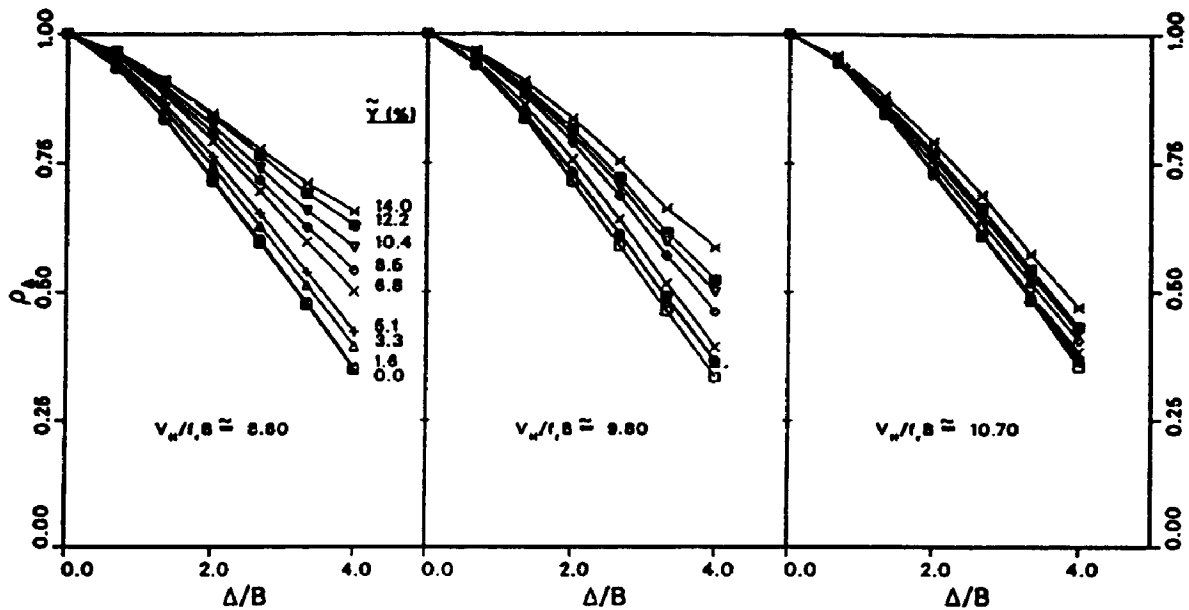
Figure 7.25: Average Correlation Coefficient versus Separation Distance Determined from Coincident Spectra with Spikes Removed

Presumably, the energy of the forcing at the frequency of motion is highly organised, even for very small amplitudes.

Spectra of Overturning Moment

In order to obtain a clearer picture of these effects on the total structure, the spectra of total loads on the structure were required. It was necessary to estimate these since the complete spectral density matrix for the structure was not measured. In particular, the cross-spectra relating the top set of simultaneously measured pressures to the middle set were not known. Also not known, but less consequential

to the total overturning moment, were the pressures acting on the bottom third of the model. It was assumed first that estimates of the total overturning moment spectra due to loads acting only on the upper two-thirds of the model would be adequately indicative of the complete moment spectra. The contribution to the total moment due to loads acting on each of these thirds was first calculated by summing the entire spectral density matrix of the corresponding third. That is:

$$S_{TT}(f) = \sum_{i=1}^{7} \sum_{j=1}^{7} h_i h_j S_{ij}(f) \qquad (7.4)$$

$$S_{MM}(f) = \sum_{i=8}^{14} \sum_{j=8}^{14} h_i h_j S_{ij}(f) \qquad (7.5)$$

where the subscripts T and M denote top and middle third respectively and h_i is the height of the ith level of pressure cells. Two estimates of the total spectrum were then made; a lower bound, and an upper bound estimate. These two estimates still provided a fair range of uncertainty and so a more refined intermediate or "best" estimate was also made.

Figure 7.26 illustrates schematically the spectral density matrix associated with the entire model. The check marks indicate those elements for which experimentally measured functions were available.

For any two levels within the top third or the middle third, a coherence function relating the loads can be calculated according to:

$$\gamma_{ij}(f) = \frac{|S_{ij}(f)|}{\sqrt{S_{ii}(f)S_{jj}(f)}} \qquad (7.6)$$

This function is bounded between 0 and 1 and indicates the degree of correlation, in the frequency domain, of loads acting at levels i and j. Similarly a coherence
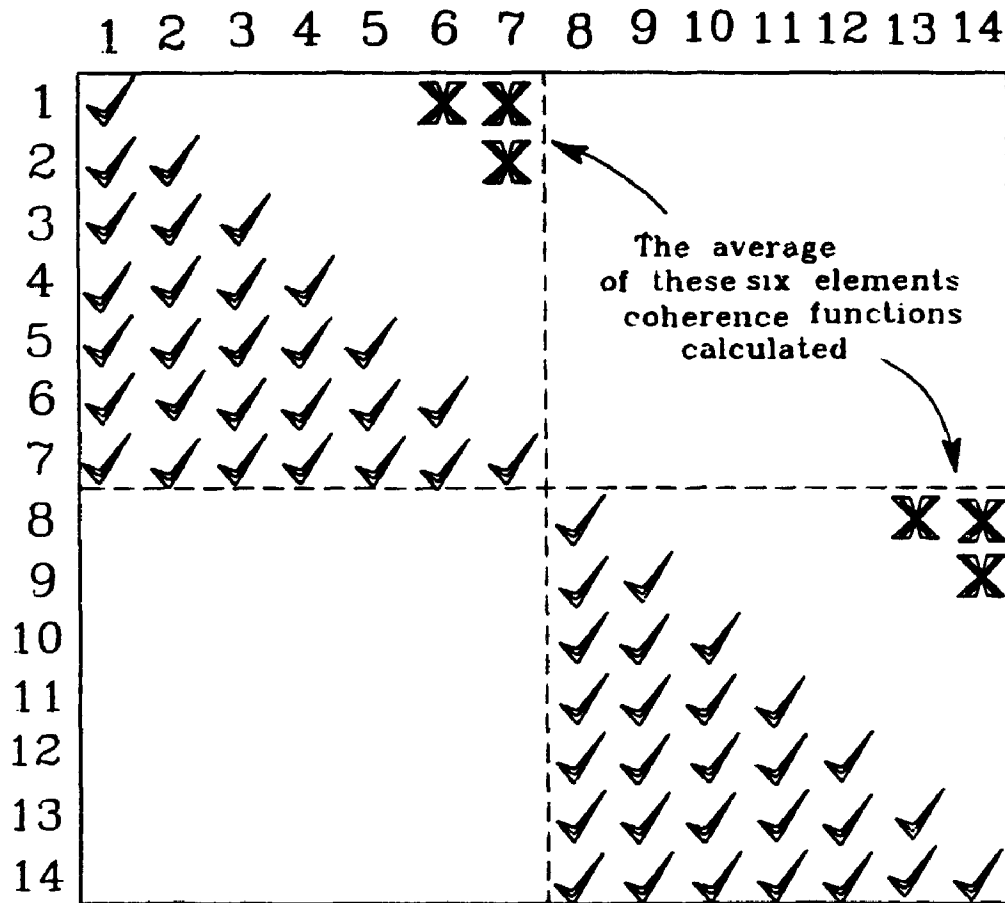
Figure 7.26: Schematic of the Spectral Density Matrix from Fourteen Load Levels

function relating the top third moment contribution spectrum to the middle third one could be defined:

$$\gamma_{TM}(f) = \frac{|S_{TM}(f)|}{\sqrt{S_{TT}(f)S_{MM}(f)}} \tag{7.7}$$

An approximation of the total spectrum of moment due to loads on the top two thirds can then be written in terms of this function as:

$$S(f) = S_{TT}(f) + S_{MM}(f) + 2\gamma_{TM}\sqrt{S_{TT}(f)S_{MM}(f)} \tag{7.8}$$

It is assumed in this that the imaginary part of the cross-spectra are relatively small. Some estimation of the missing cross-spectrum, $S_{TM}(f)$, or of the coherence function, $\gamma_{TM}(f)$, is necessary.

For the lower bound estimate it was assumed that the net load acting on the top third was completely uncorrelated to the net load acting on the middle third, that is: $\gamma_{TM} = 0$. This amounted to neglecting the unknown cross-spectra and calculating the total spectrum according to:

$$S_u(f) = S_{TT}(f) + S_{MM}(f) \tag{7.9}$$

For the upper bound estimate, it was assumed that these two contributions were fully correlated: $\gamma_{TM} = 1$. The total spectrum was then estimated according to:

$$S_{uu}(f) = S_{TT}(f) + S_{MM}(f) + 2\sqrt{S_{TT}(f)S_{MM}(f)} \tag{7.10}$$

The third term in Equation 7.10 represents an upper bound estimate of the unknown cross-spectral contributions.

For the intermediate estimate, the unknown coherence function was estimated as:

$$\gamma_{TM}(f) = \frac{\gamma_{1,6}(f) + \gamma_{1,7}(f) + \gamma_{2,7}(f) + \gamma_{8,13}(f) + \gamma_{8,14}(f) + \gamma_{9,14}(f)}{6} \qquad (7.11)$$

and substituted in Equation 7.8. These six coherence functions are indicated in Figure 7.26. They were chosen for the estimate because they represent coherence between loads acting at vertical distances most likely representative of the effective distance between the net forces acting on each third of the model.

Two examples of the spectral estimates are shown in Figures 7.27 and 7.28, each showing the three estimates. The variances are given in dimensionless coefficient form scaled by 10^3. The similarity of the estimates for each case lends confidence that the estimates adequately illustrate the variations between different cases, particularly with respect to their shape. The first example corresponds to an essentially stationary model and the rms value of the intermediate estimate is within a few percent of that obtained in the base balance experiments ($\sqrt{23.5 \times 10^{-3}} = .153$). In view of these similarities, the intermediate estimate was adopted for data presentation.

Figure 7.29 shows all of the intermediate spectral estimates for each of the three velocity cases. Note that the three velocities are nominal. The actual velocity corresponding to each plot is shown in parentheses. Only the first and fourth rows deviate notably from the nominal. They have been retained here for presentation, however.

Figure 7.30 shows the estimates for the particular case of $\tilde{Y} = 6.81\%$ for
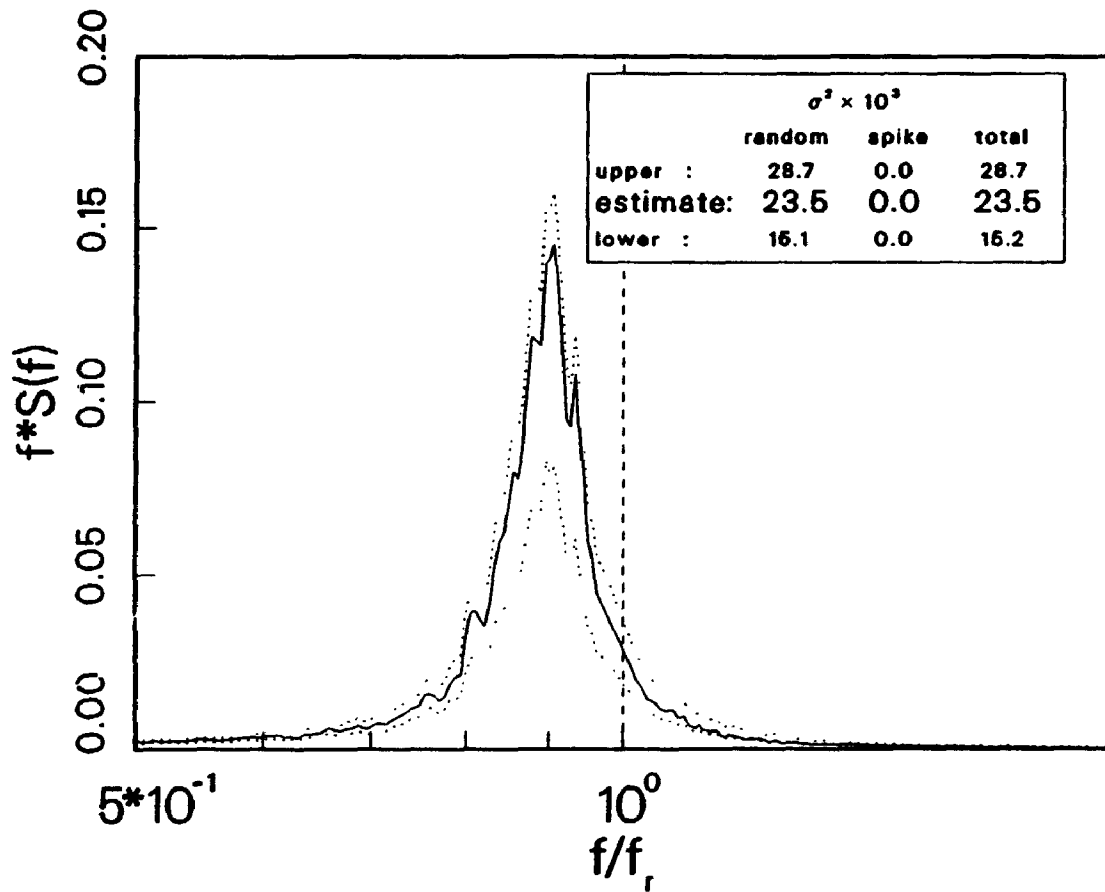
Figure 7.27: Example of Three Total Moment Spectrum Estimates on an Essentially Stationary Square Prism
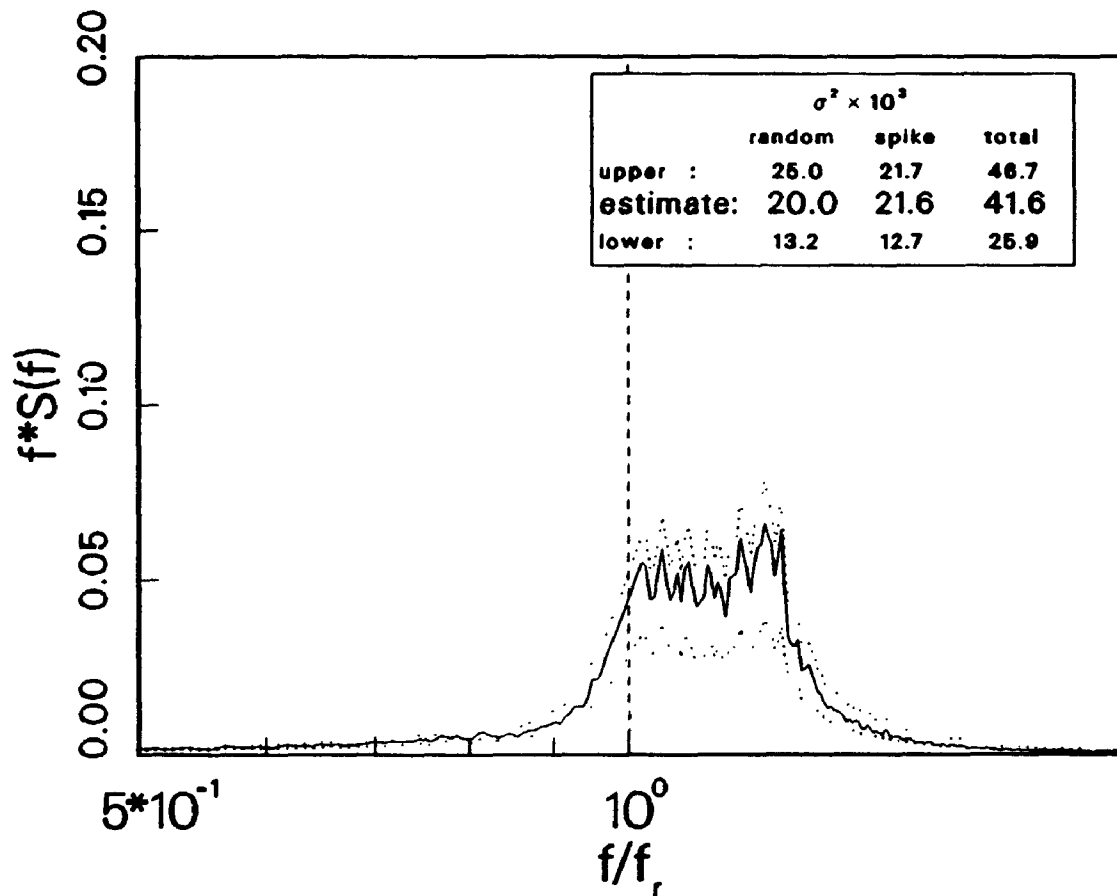
Figure 7.28: Example of Three Total Moment Spectrum Estimates on a Square Prism Forced to Oscillate
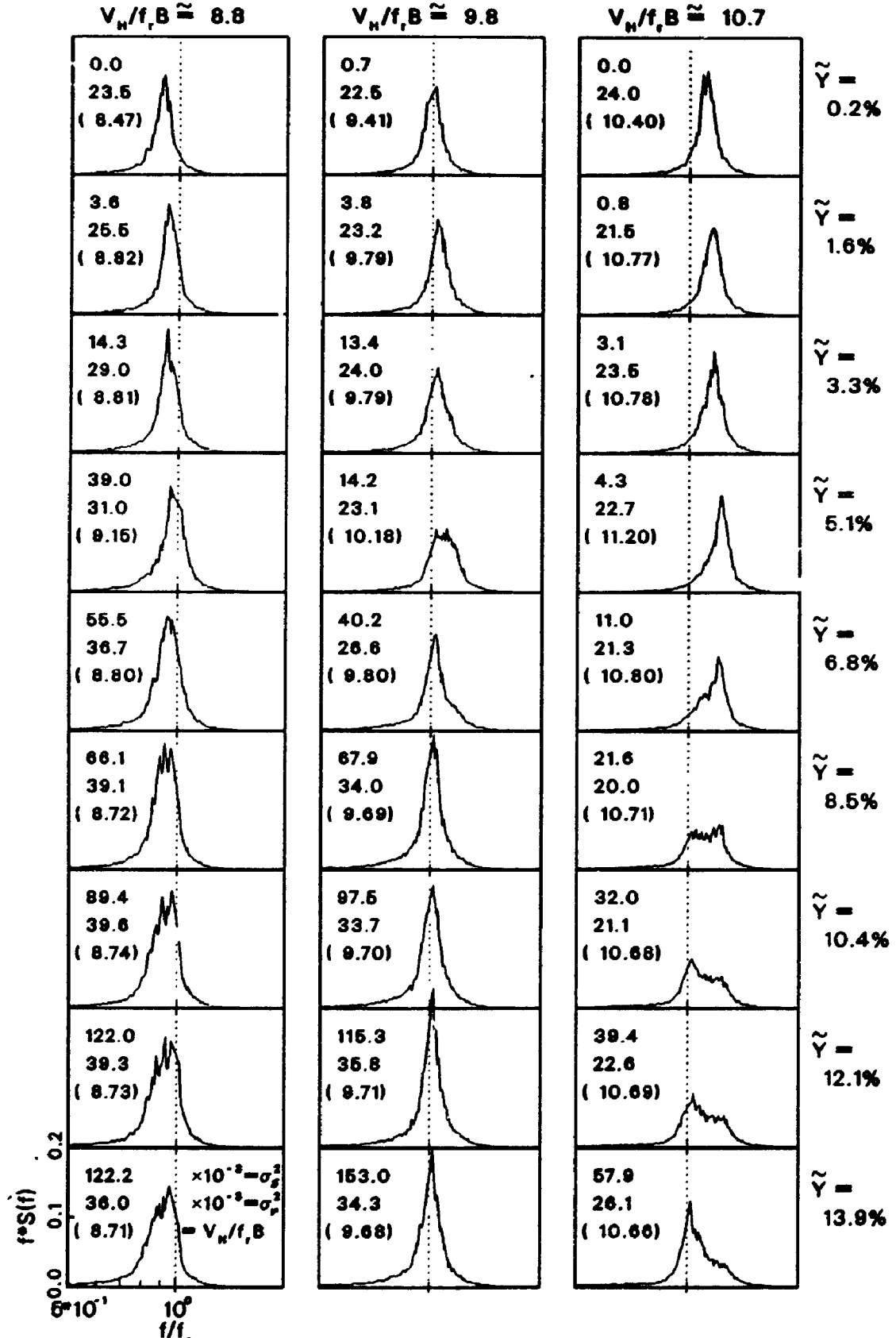
Figure 7.29: Estimates of Total Moment Spectra for Various Amplitudes and Nominal Velocities

which four additional velocities were considered. In this case the vertical direction varies the velocity rather than the amplitude. The corresponding reduced velocity for each plot is shown to the left below the variances.

These total spectrum estimates support the observations noted in examining the component spectra. The most dramatic variations occur when the velocity is such that the frequency of vortex shedding is just above the frequency of forced oscillation. In this case, for oscillation amplitudes above about $Y \approx 7\%$, the spectral energy of the vortex shedding peak is redistributed to the nearby frequencies. For a certain range of amplitude during the peak relocation, the redistribution appears to be such that the vortex shedding becomes a random process within a finite bandwidth which does not differ much from the bandwidth of the original narrow band shedding occurring on a stationary model.

Considering the changes in spectral shape, the total energy remains remarkably stable. This is shown in Figure 7.31, where the coefficients of rms moment associated with the spectrum excluding the spike are plotted. Figure 7.32 s.10ws the variation of the rms contained in the removed spike at the oscillation frequency. The value increases approximately linearly with the oscillation amplitude, although the rate of increase depends on the mean wind speed. A small component of the energy in the spike is due to inertially induced pressures within the pneumatic measuring system. This effect has been referred to by Bearman [3]. This component is relatively small and independent of the wind flow. It has been removed from these data by evaluating it in each case from a test case carried out with the wind off condition. The spike variances shown in the previous figures do not include this correction. The correction amounts to about 5% in the worst case.
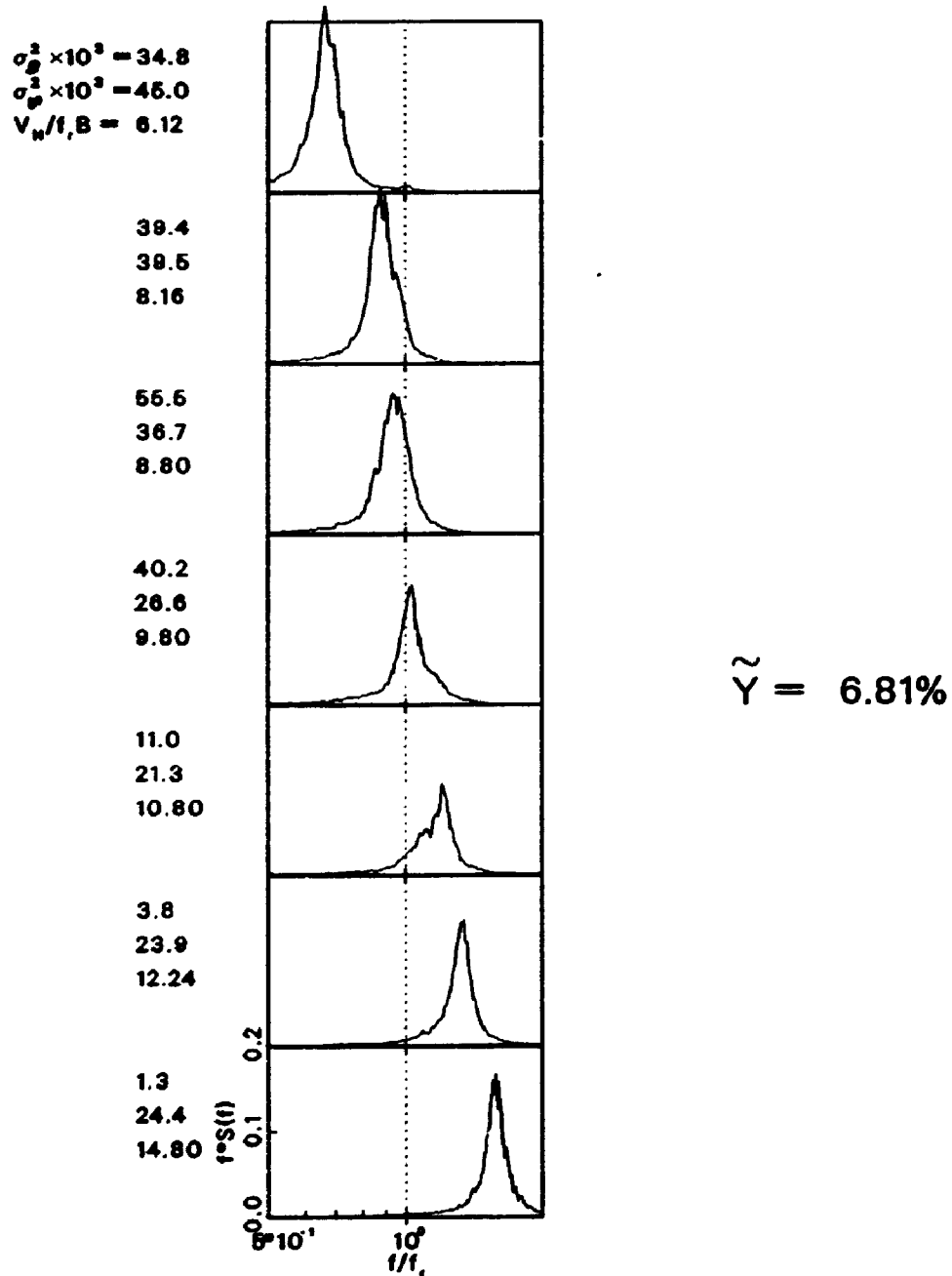
Figure 7.30: Estimates of Total Moment Spectra for Various Velocities and $\tilde{Y} = 6.81\%$
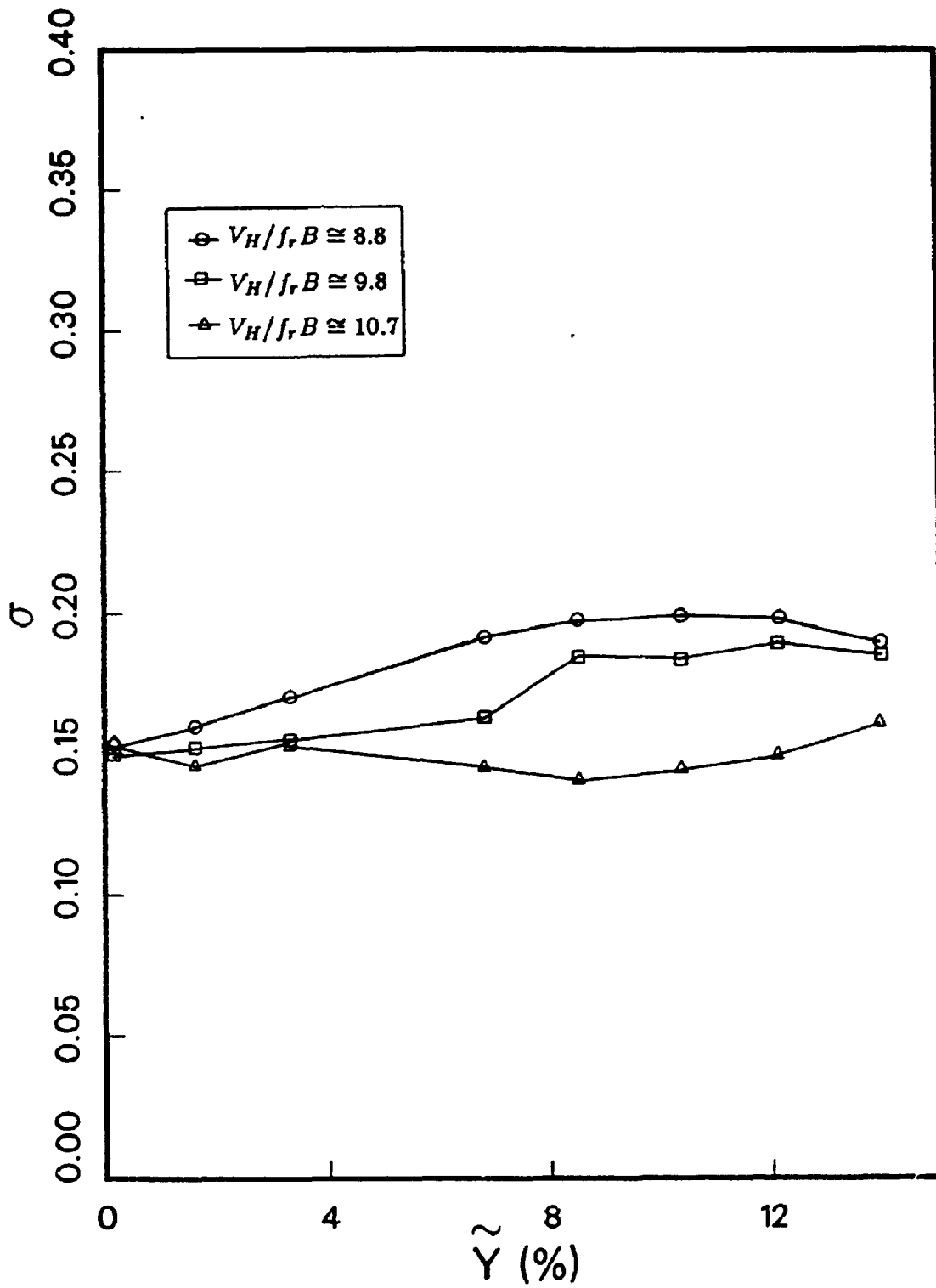
Figure 7.31: Variation with Amplitude of Rms Moment Coefficient Corresponding to Spectrum with Spike Removed
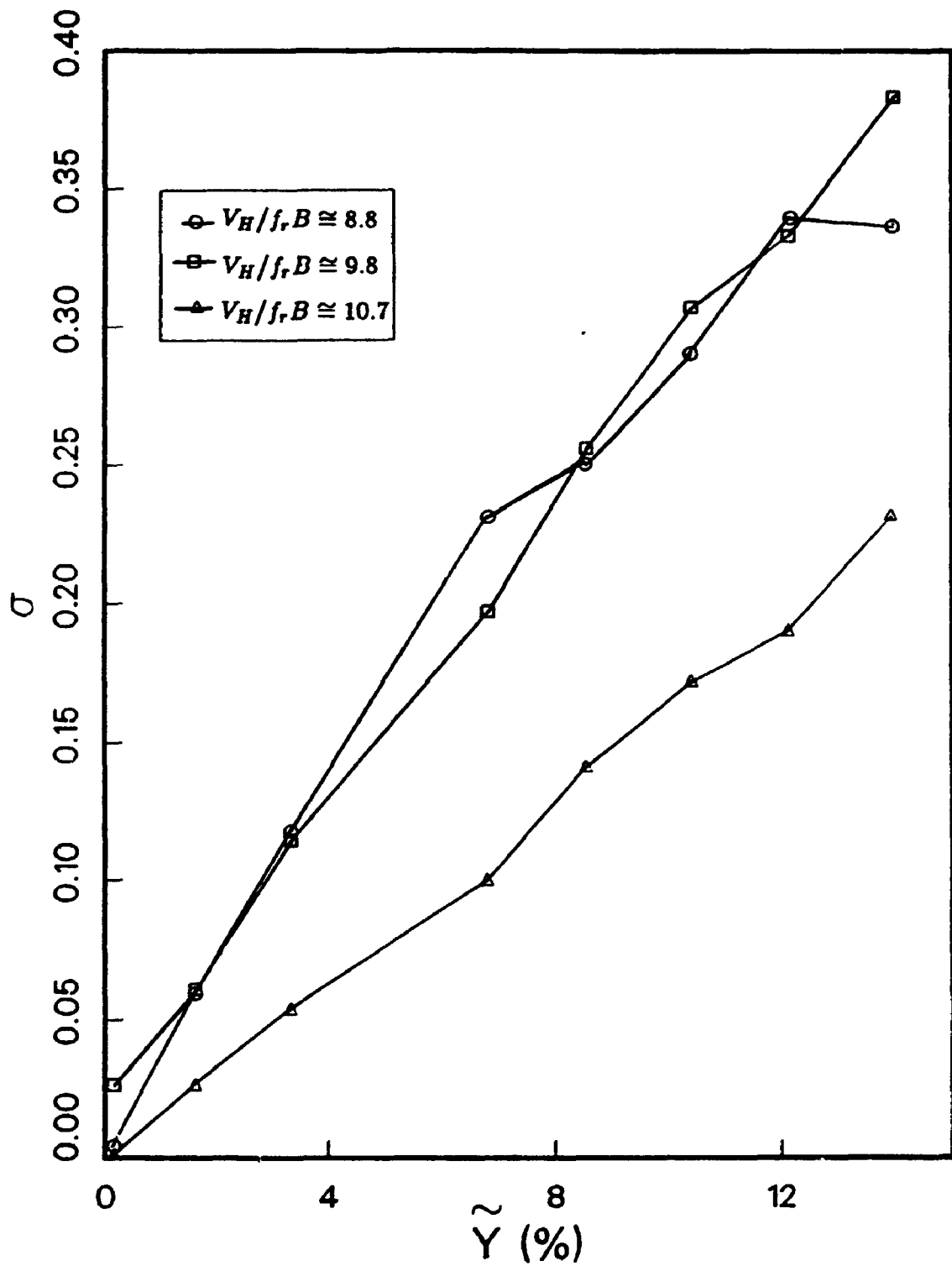
Figure 7.32: Variation with Amplitude of Rms Moment Coefficient Corresponding to the Spike in the Spectrum

7.5 Aeroelastic Model Experiments

7.5.1 The Aeroelastic Model Structures

It was important to, in effect, close the loop and compare the experimental and analytical results of the previous tests with results from corresponding free oscillation experiments. Several such experiments were carried out using an aeroelastic model of identical geometry as the previous models. A one degree of freedom "stick" aeroelastic setup was use. While the restriction to a single degree of freedom is less representative of practical structural cases, it was maintained for this stage of the research in order to reduce the potential parameters and in order to keep the experiments appropriately matched.

A schematic of the aeroelastic stick model is shown in Figure 7.33. The model pivoted about the axis shown. It was constructed of Rohacel foam with a central aluminum tube to half height for rigidity. Springs located on the lower portion of the model shaft provided the main elastic support. Effective viscous damping was provided by an eddy current damper located at the bottom of the shaft. A strain gage system provided a measure of the overturning moment acting on the model. Tip displacements could also be inferred from this measure.

Five different structures were tested. These were achieved by varying the DC current through the damper coil and, once, changing the thickness of the damping plate at the bottom of the shaft. This resulted in various combinations of effective
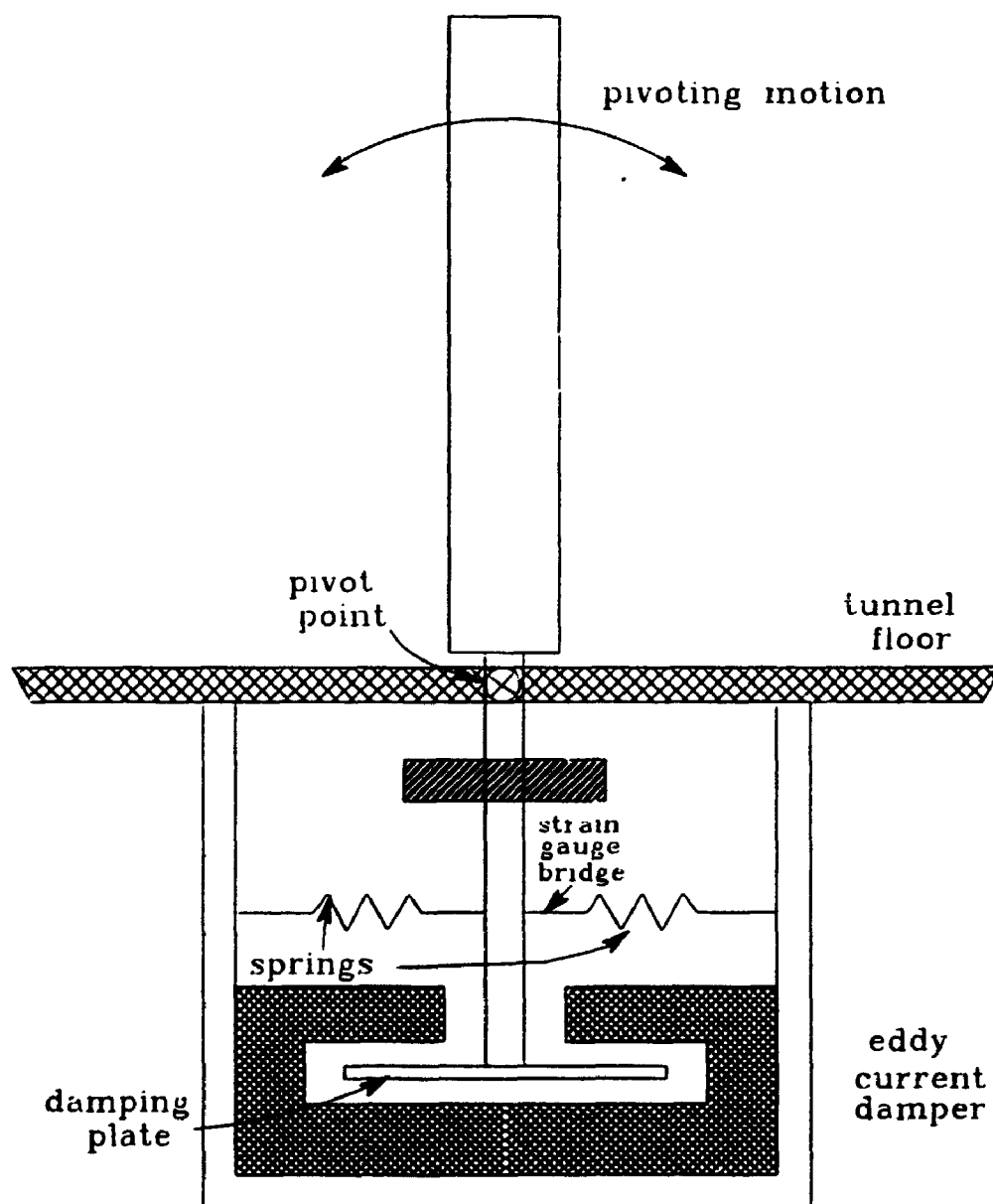
Figure 7.33: Single Degree of Freedom Aeroelastic Stick Model

viscous damping and generalised mass of the structure. Only one set of springs were used for all experiments.

Calibrations were performed in the following ways. The strain gage system was calibrated by statically loading the model with known loads and measuring the resulting strain gage outputs. The linear relationship between the moments and output voltages then provided an appropriate conversion factor.

For each experiment,the value of effective viscous damping was estimated by measuring the logarithmic decay of the model response due to impulse loading. Numerous damping traces were recorded before and after each experiment. These estimates are shown in Figure 7.34. The large amount of scatter seen in these plots illustrates the uncertainty which can be associated with estimates of structural damping, even in a very controlled experiment. Some variation of damping with amplitude can be seen. A linear function of amplitude has been estimated for Structures 1 and 2. For all structures, a nominal value has been estimated as shown.

Estimates of the generalised mass and stiffness of the structures were determined by adding a small incremental mass to various locations along the lower shaft. In each case the resulting free vibration frequency was accurately recorded. With these results a linear relationship can be plotted, the slope and intercept of which give direct estimates of the generalised mass and stiffness of the basic structure. The generalised stiffness was used to convert the measured moments to equivalent tip displacements. It was assumed that the generalised stiffness of each of the five structures was the same. There were, however, two different mass cases associated
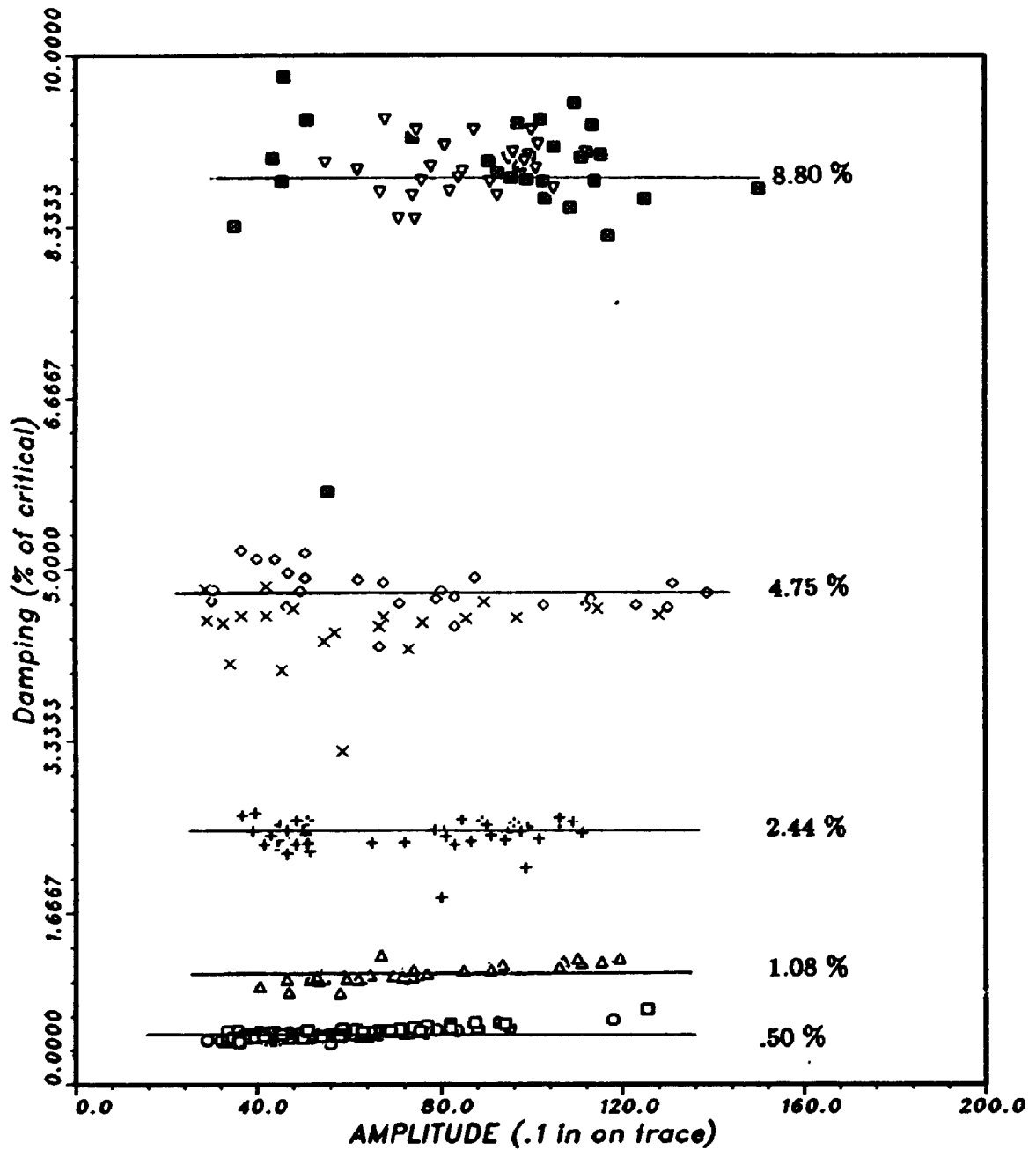
Figure 7.34: Estimates of Damping Determined From Free Decay Damping Traces for the Five Aeroelastic Model Structures

Table 7.1: Aeroelastic Model Structures

Struct.	Gen. Mass M_s $(\times 10^{-3}$ slugs$)$	Gen. Stiffness K_s (lbs/ft)	Struct. Damping ζ_s (% crit.)	Density Ratio η	Natural Freq. f_s (Hz)	Mass-Damping Parameter ζ_s/η
1	3.549	41.63	.50	1/172	17.24	0.86
2	3.549	41.63	1.08	1/172	17.24	1.86
3	5.860	41.63	2.44	1/281	13.42	4.20
4	5.860	41.63	4.75	1/284	13.42	13.49
5	5.860	41.63	8.80	1/284	13.42	24.99

$\rho_a \doteq 0.00238$ slugs/ft^3

with two different damping plates used. The incremental mass calibration was carried out for each of the two cases, and then a best fit estimate of the three unknown quantities, one generalised stiffness and two generalised masses, was determined.

Table 7.1 summarises the estimated structural properties for each of the five structures. Nominal values of damping are indicated in the table and these will be quoted for data presentations, however, the degree of uncertainty associated with these values and shown in Figure 7.34, should be noted.

7.5.2   Experiments

Each model structure was tested in the wind flow described in Section 7.1. Measures of the maximum, minimum, and rms lift response for seventy second intervals were recorded for a number of mean wind speeds varying from about $V_H = 7$ to 43 ft/sec. The speed was increased in small increments through this range and then decreased as well in order to catch any hysteresis. There were none apparent.

7.5.3   Results

Rms Tip Deflections and Peak Factors

Figure 7.35 shows the rms normalised tip deflection for each of the five structures as a function of reduced velocity. However, not only the energy of the response changes over the velocity range, but also the distribution. This is illustrated better by considering the peak factor, g, defined in general as the ratio of the peak response to the rms response. It can be shown[22] that for a purely random response of Gaussian distribution, the expected value of peak factor is given by:

$$g = \frac{E[\hat{y}]}{\tilde{y}} = \sqrt{2ln|\nu T|} + \frac{.5772}{\sqrt{2ln|\nu T|}} \tag{7.12}$$

where ν is the effective cycling frequency:

$$\nu = \sqrt{\frac{\int_0^\infty f^2 S_{rr}(f)df}{\int_0^\infty S_{rr}(f)df}} \tag{7.13}$$

which for the current case implies that $g \approx 4$. For a purely sinusoidal response case g approaches $\sqrt{2}$.

To reduce the number of points and the scatter, the peak factor is here calculated from the experiments in each case as:

$$g = \frac{\hat{y} - \check{y}}{2\tilde{y}} \quad . \tag{7.14}$$

The peak factor for each case is shown in Figures 7.36 to 7.40. The solid line shows the lower limit associated with purely sinusoidal motion and the dashed line shows that given by Equation 7.12

During the data acquisition, some samples occurred at the extreme bounds of the A/D range and these were flagged. Cases where overbounds occurred have been indicated by the portion of dashed line and the unshaded points in Figures 7.35 to 7.37. These overbound samples were rare occurrences, however, and so the data has not been disqualified.

7.5.4   Spectra

For each of the aeroelastic model structures, auto-spectra of the tip displacement were calculated at five velocity cases. These are shown in Figure 7.41 for Structure 1. Similar plots for the other four structures are included in Appendix E. The expected locations of the vortex shedding peaks based on the stationary model Strouhal number is shown as well as the location of the natural frequency as measured in still air.
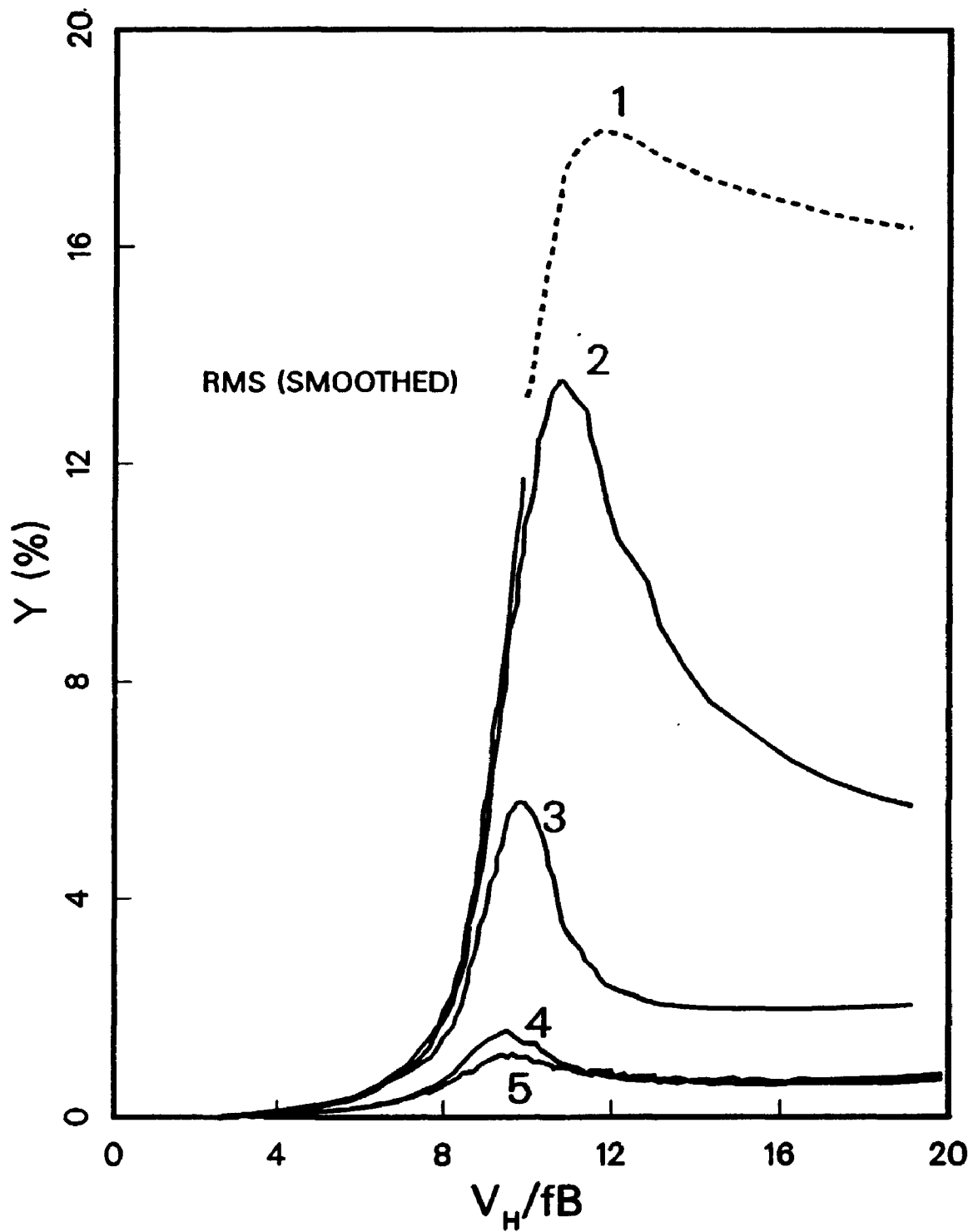
Figure 7.35: Variation of Rms Tip Displacement with Wind Speed for the Five Aeroelastic Model Structures
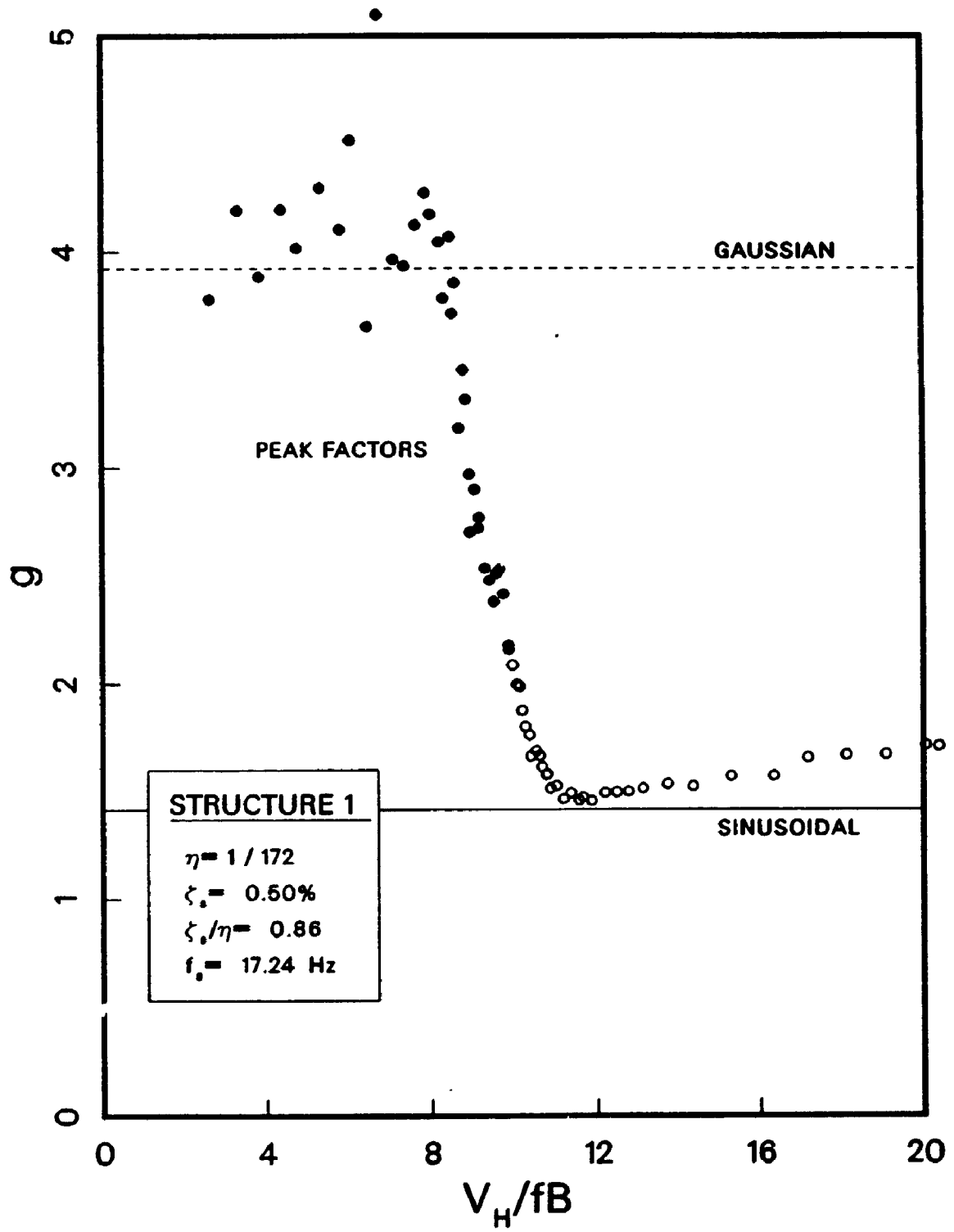
Figure 7.36: Peak Factors from Tests on Aeroelastic Model Structure 1
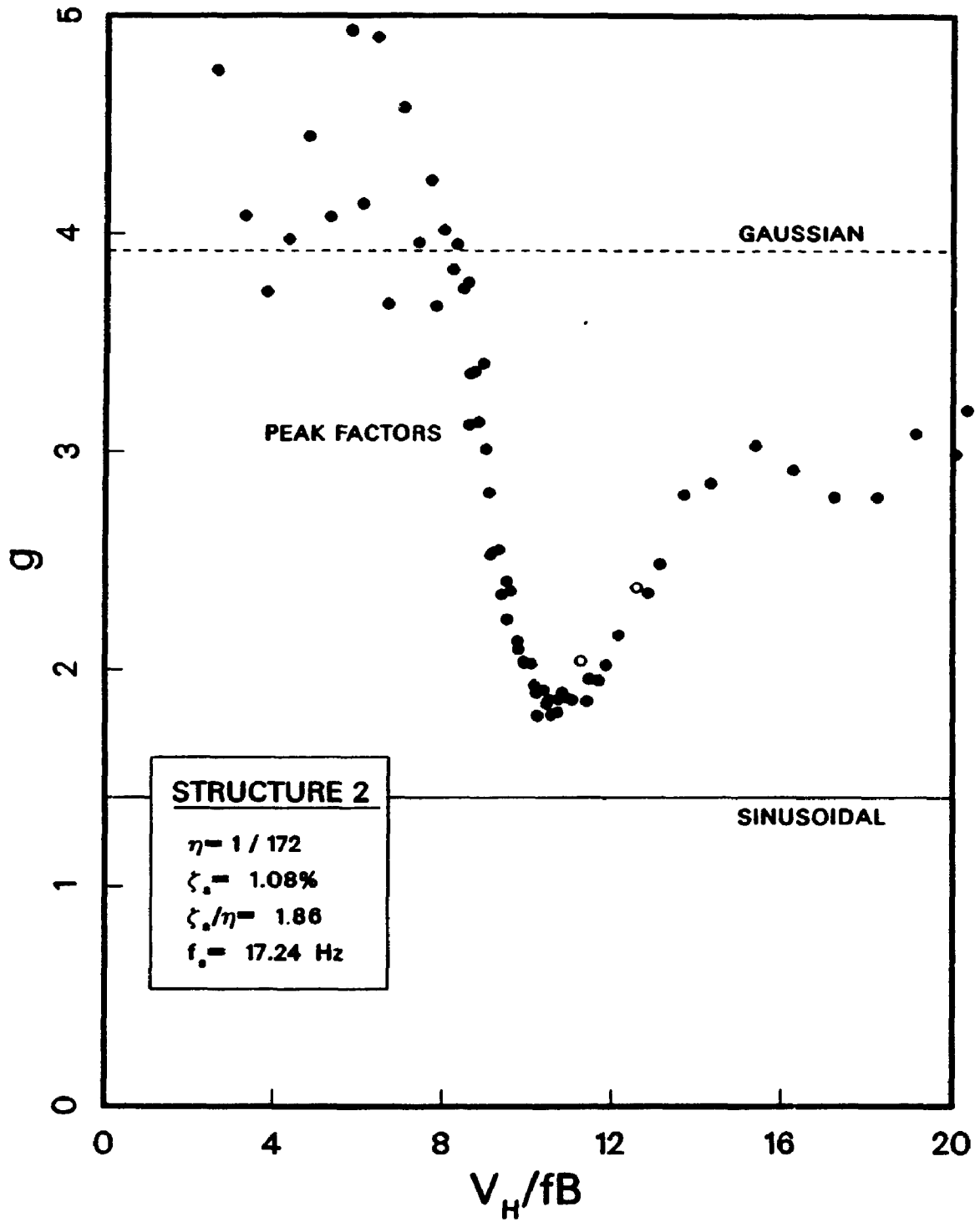
Figure 7.37: Peak Factors from Tests on Aeroelastic Model Structure 2
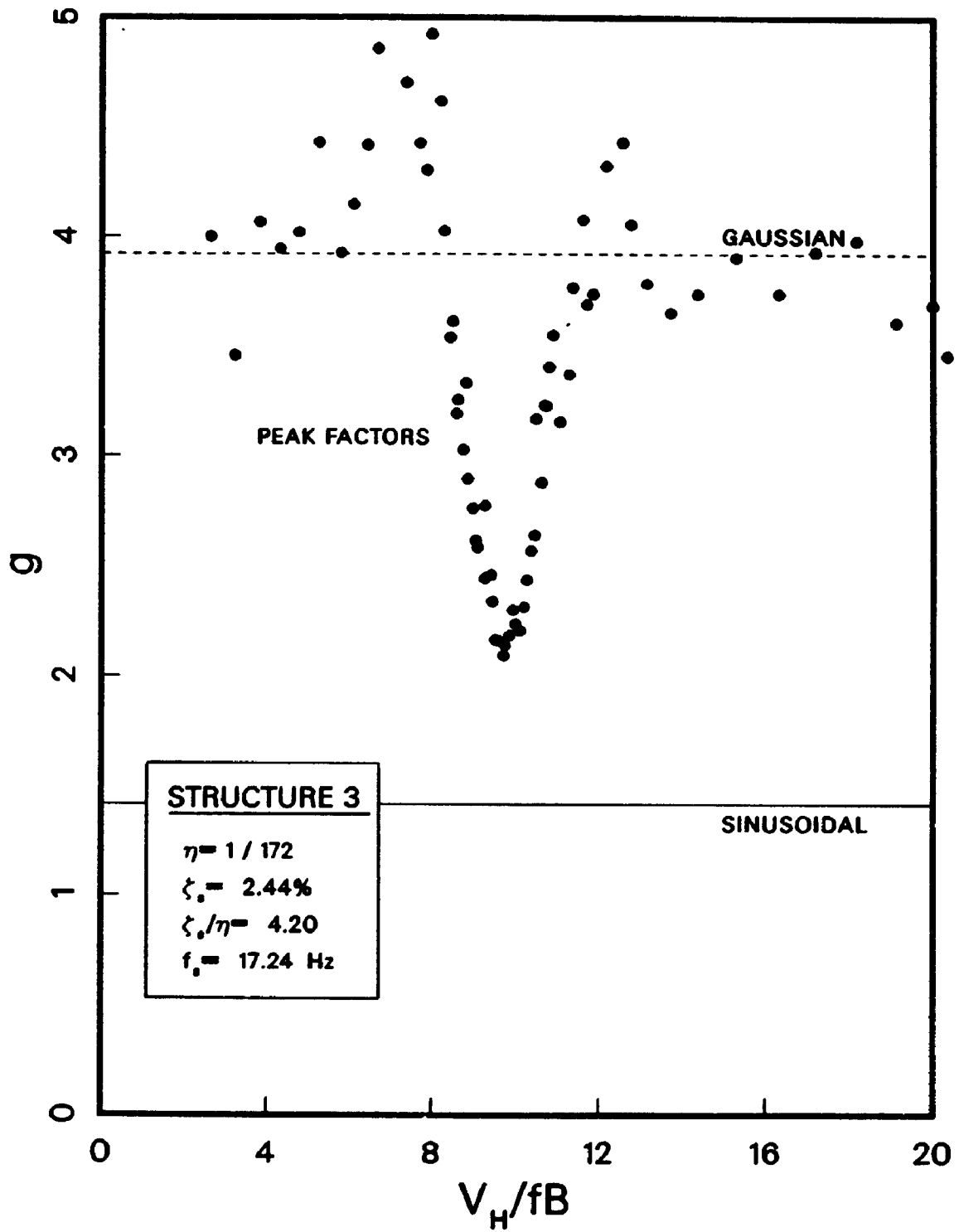
Figure 7.38: Peak Factors from Tests on Aeroelastic Model Structure 3
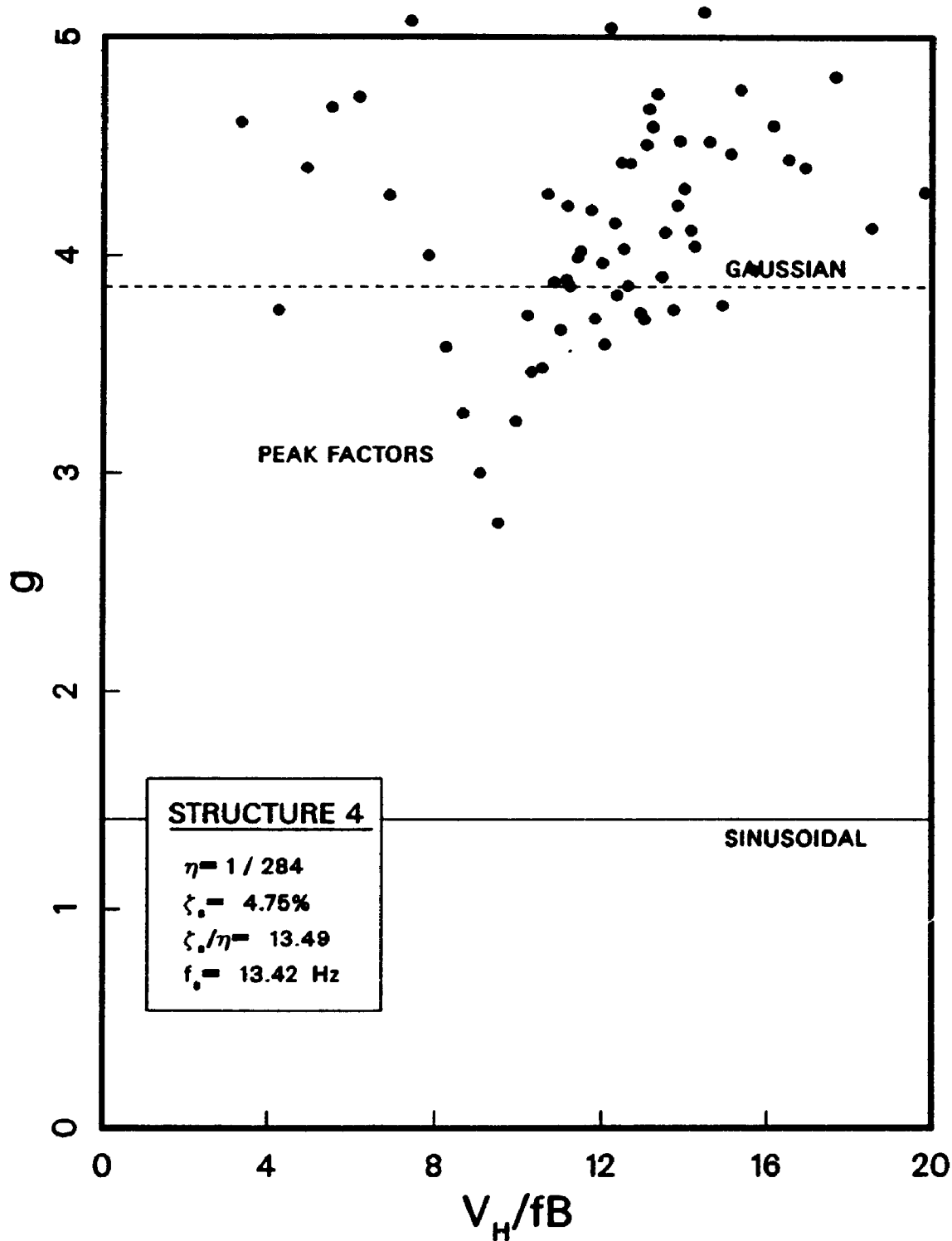
Figure 7.39: Peak Factors from Tests on Aeroelastic Model Structure 4
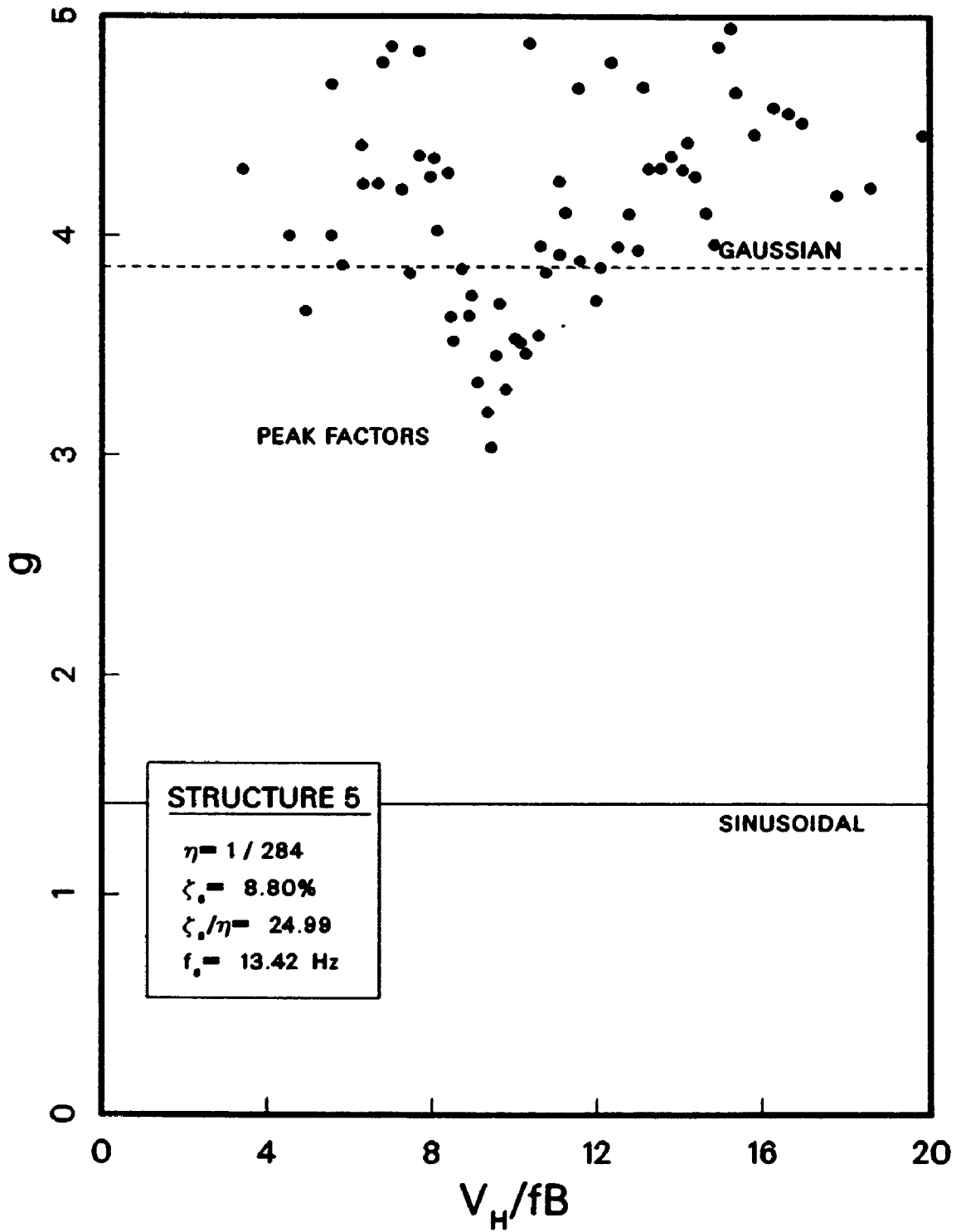
Figure 7.40: Peak Factors from Tests on Aeroelastic Model Structure 5
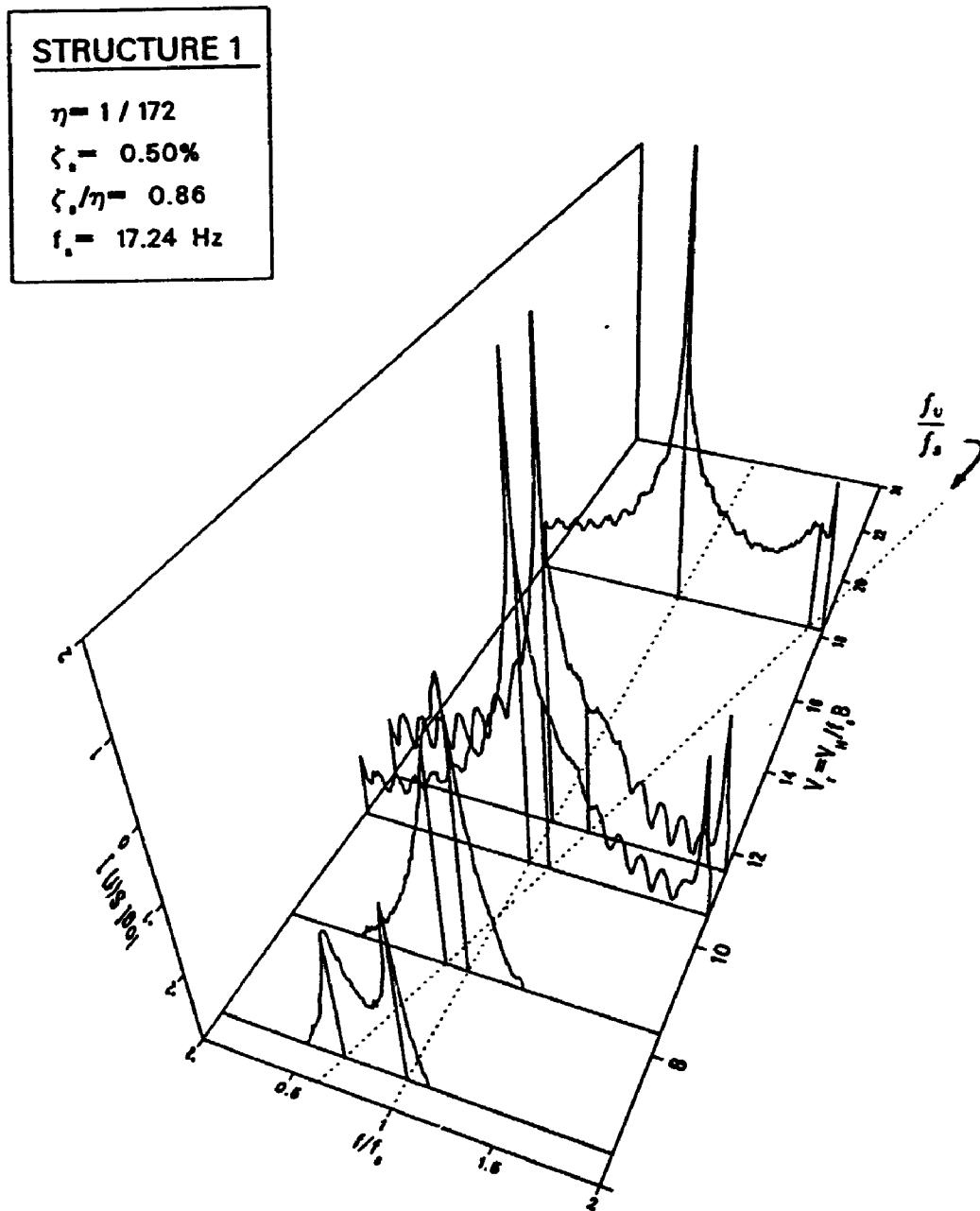
Figure 7.41: Auto-Spectra of Tip Displacement for Aeroelastic Model Structure 1

There is a distinct downward shift in the natural frequency of the structure which can be seen in the spectra. The shift is greatest in the range where the two peaks coincide; examination of the actual data values confirms this. These observations are in qualitative agreement with the measurements of aerodynamic stiffness obtained in the PMA experiments. The negative aerodynamic stiffness in the vortex shedding range would be expected to slightly reduce the natural frequency of the structure. Unfortunately, the frequency resolution is not such that these observations could be adequately quantified for further comparisons.

7.6   Analysis of the Combined Results

7.6.1   Comparisons of PMA results with Quasi-Steady Approach

Theoretical estimates of the motion-induced forces may be made based on assumptions of quasi-steady aerodynamics. In this approach it is assumed that for any instant, the aerodynamic force on the moving structure may be replaced by a time averaged force acting on a stationary structure subject to the same *relative* wind velocity. Turbulence and its effects are neglected.

Along Wind Direction

First consider a simple quasi-steady approach for the along wind motion-induced forces. Figure 7.42 shows a coordinate system of lift and drag forces for a square body cross-section. The mean wind speed is V, however, as the structure moves in the along wind direction, the relative wind speed will be:

$$V_R = V - \dot{x} \qquad (7.15)$$

Following the quasi-steady approach we assume that the instantaneous force per unit height may be expressed as:

$$f_D = \frac{1}{2}\rho_a V_R^2 B C_D \qquad (7.16)$$

Expanding this and dropping terms of order $\dot{x}^2$, gives:

$$f_D = \frac{1}{2}\rho_a \left(V^2 - 2V\dot{x}\right) B C_D \qquad (7.17)$$

The two terms in the above equation may be considered a mean and a dynamic component of the force with the dynamic component being proportional to $\dot{x}$. A per unit height damping coefficient may then be expressed as:

$$C_a [z] = -\rho_a V [z] B C_D \qquad (7.18)$$

We wish to consider a whole structure and we will assume that the mean wind profile may be described by,

$$V [z] = \left(\frac{z}{z_g}\right)^a V_g \qquad (7.19)$$
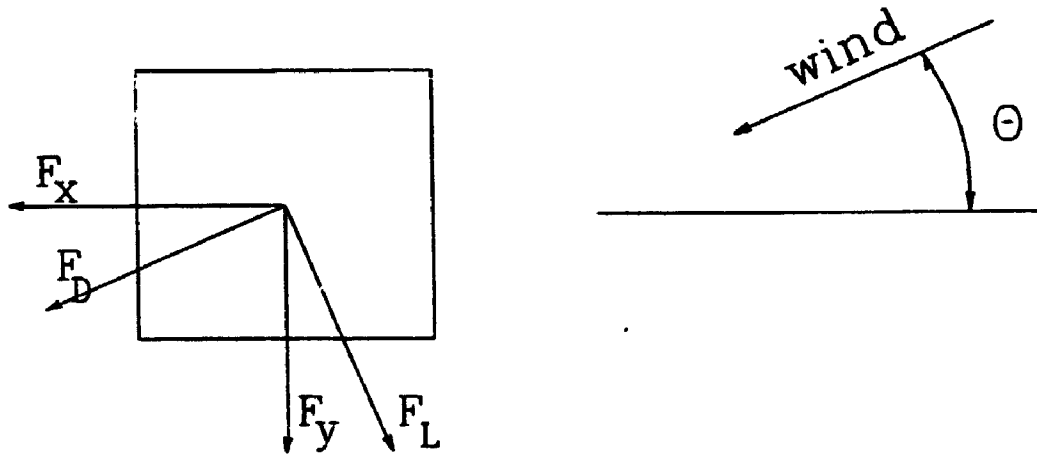
Figure 7.42: Coordinate System for Lift and Drag Forces on Square Body

where z_g, V_g, and a are the gradient height, gradient wind speed, and power law profile parameter respectively. The total generalised force can then be expressed as:

$$F_D = \dot{x}_H \int_0^H C_a \left[z \right] \mu^2 \left[z \right] dz \tag{7.20}$$

$$= -\rho_a \frac{V_g}{z_g^a} B \int_0^H z^a C_D \left[z \right] \mu^2 \left[z \right] dz \dot{x}_H \tag{7.21}$$

Assuming that C_D is independent of height and assuming a pivot mode so that $\mu \left[z \right] = z/H$:

$$F_D = -\rho_a \frac{V_g}{z_g^a} B C_D \frac{H^{1+a}}{3+a} \dot{x}_H \tag{7.22}$$

Consistent with the aerodynamic impedance definitions, we may express the quasi-steady form of β:

$$\beta_{QS} = -\frac{F_D / \dot{x}}{2 M_e \eta \omega^2} \tag{7.23}$$

$$= \frac{3}{4\pi} \left(\frac{C_D}{3+a} \right) V_r \tag{7.24}$$

Finally it would be convenient to express this in terms of the total moment coefficient, C_M, rather than the coefficient of drag per unit height, C_D. The total moment in terms of C_D is:

$$M = \int_0^H \frac{1}{2}\rho_a V^2 |z| BC_D z dz \qquad (7.25)$$

$$= \frac{1}{2}\rho_a V_s^2 BH^2 C_D \left(\frac{H}{z_s}\right)^{2a} \left(\frac{1}{2+2a}\right) \qquad (7.26)$$

Equating this with the expression for the total moment using V_H as a reference:

$$M = \frac{1}{2}\rho_a V_H^2 BH^2 C_M \qquad (7.27)$$

we find that:

$$C_D = (2 + 2a)C_M \qquad (7.28)$$

We can then re-express β_{QS} as:

$$\beta_{QS} = \frac{3}{4\pi}\left(\frac{2+2a}{3+a}\right) C_M V_r \qquad (7.29)$$

The moment coefficient from the base balance results has been taken as .734 and this is shown in Figure 7.10 as the short horizontal line. Combining this with the power law profile fit of Figure 7.1, the quasi-steady estimate was calculated. Figure 7.43 shows this quasi-steady estimate along with the results of a direct measurement using the PMA system. This plot shows an extended range of reduced velocity up to $V_r = 40$.
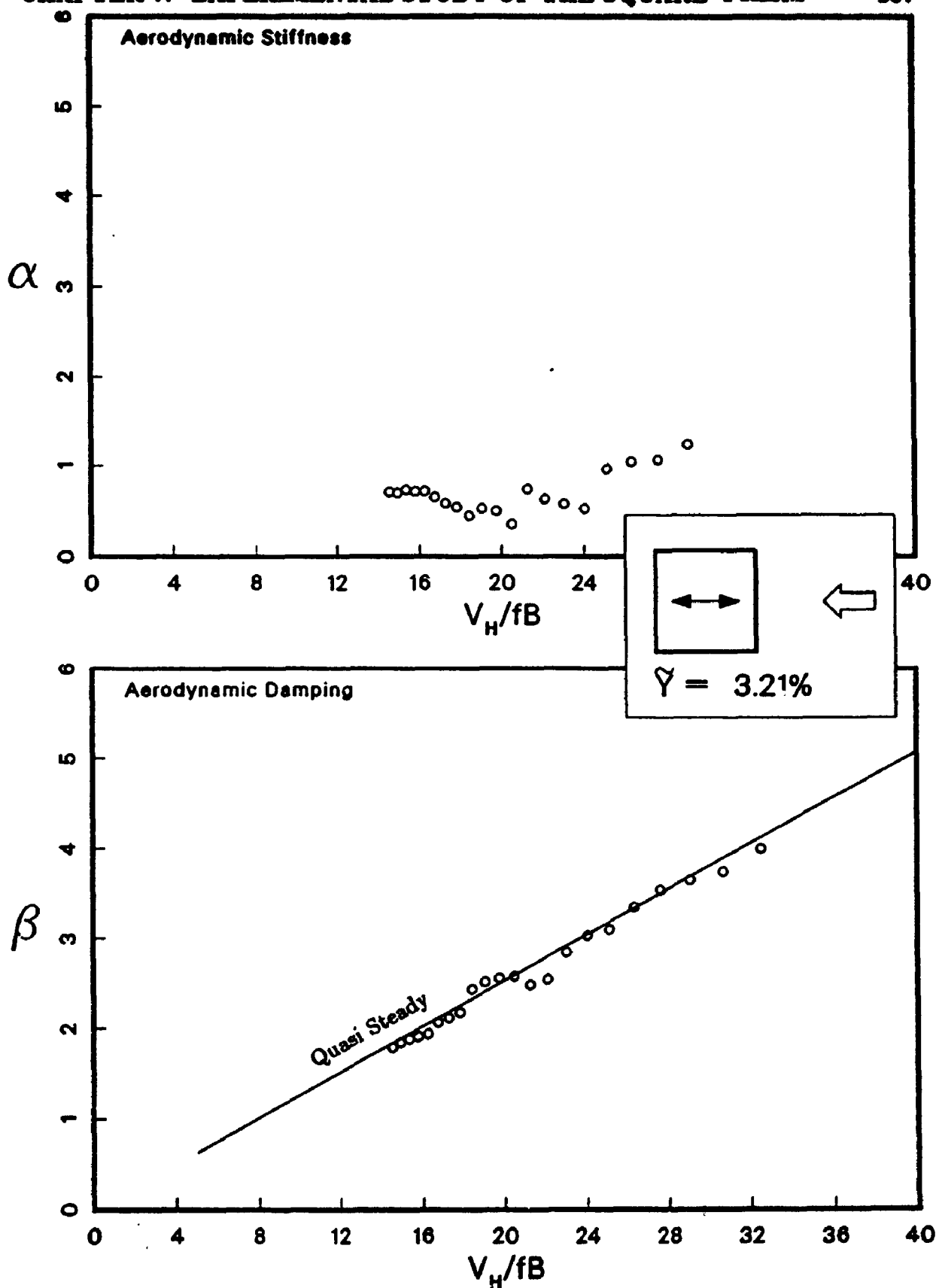
Figure 7.43: Comparison of PMA Results with Quasi-Steady Theory for Along Wind Direction

Across Wind Direction

For the across-wind direction, we take a slightly more detailed approach following the examples of Parkinson[58] and, in particular, Novak[48]. Treating a two dimensional problem first, and using the sign convention shown in Figure 7.42, we express the drag and lift components of the instantaneous force as:

$$F_D = \frac{1}{2}\rho_a BHV_R^2 C_D \qquad (7.30)$$

$$F_L = \frac{1}{2}\rho_a BHV_R^2 C_L \qquad (7.31)$$

The instantaneous across wind force is given by:

$$F_y = -\frac{1}{2}\rho_a BHV^2 sec^2\theta \left(C_D sin\theta + C_L cos\theta\right) \qquad (7.32)$$

$$= \frac{1}{2}\rho_a BHV^2 C_y \qquad (7.33)$$

where

$$C_y = -\left(C_L + C_D tan\theta\right) sec\theta \qquad (7.34)$$

and we note that the effective angle of attack due to across wind motion of the structure is:

$$\theta = arctan\left[\frac{\dot{y}}{V}\right] \qquad (7.35)$$

The coefficient of force, C_y in Equation 7.33 can be approximated by a polynomial in the variable $tan\theta = \dot{y}/V$. A convenient form for the symmetric case of the square prism is:

$$C_v = A_1\left(\frac{\dot{y}}{V}\right) + A_2\left(\frac{\dot{y}}{V}\right)^2\frac{\dot{y}}{|\dot{y}|}$$
$$+ A_3\left(\frac{\dot{y}}{V}\right)^3 + A_4\left(\frac{\dot{y}}{V}\right)^4\frac{\dot{y}}{|\dot{y}|}$$
$$+ A_5\left(\frac{\dot{y}}{V}\right)^5 + A_6\left(\frac{\dot{y}}{V}\right)^6\frac{\dot{y}}{|\dot{y}|}$$
$$+ A_7\left(\frac{\dot{y}}{V}\right)^7 \tag{7.36}$$

The terms of even degree are included to give a better fit and are made into odd functions to match the symmetry condition as do the other terms already. The generalised equation of motion can now be written:

$$\ddot{y} + \omega_s^2 y + 2\left(\varsigma_s\omega_s - \frac{\eta}{4B}VA_1\right)\dot{y} - \frac{\eta}{2B}V^2\left[A_2\left(\frac{\dot{y}}{V}\right)^2\frac{\dot{y}}{|\dot{y}|}\right.$$
$$+ A_3\left(\frac{\dot{y}}{V}\right)^3 + A_4\left(\frac{\dot{y}}{V}\right)^4\frac{\dot{y}}{|\dot{y}|}$$
$$+ A_5\left(\frac{\dot{y}}{V}\right)^5 + A_6\left(\frac{\dot{y}}{V}\right)^6\frac{\dot{y}}{|\dot{y}|}$$
$$\left. + A_7\left(\frac{\dot{y}}{V}\right)^7\right] = 0 \tag{7.37}$$

Steady state solutions to this equation can be estimated using the approximate method of Krylov and Bogoliubov[47]. The first approximation in their successive approach has been found to be quite suitable. In this method, a solution is

assumed to be of the form:

$$y(t) \ = \ a(t)cos(\omega_s t + \phi(t)) \tag{7.38}$$

$$\dot{y}(t) \ = \ -a(t)sin(\omega_s t + \phi(t)) \tag{7.39}$$

where $a(t)$ and $\phi(t)$ are slowly varying functions of time. Substituting these into the equation of motion leads to the following conditions:

$$\dot{a} \ = \ \frac{1}{2\pi\omega_s} \int_0^{2\pi} f(-a\omega_s sin\tau)sin(\tau)d\tau \tag{7.40}$$

$$\dot{\phi} \ = \ \frac{1}{2\pi\omega_s a} \int_0^{2\pi} f(-a\omega_s sin\tau)cos(\tau)d\tau \tag{7.41}$$

where the function $f(\dot{y})$ denotes all but the first two terms on the left hand side of Equation 7.37. Making the substitution and evaluating the integral, one finds that the second equation reduces to:

$$\dot{\phi} = 0 \tag{7.42}$$

implying that the motion-induced force does not cause a change in the frequency ω_s, at least to the first approximation. Evaluation of the first equation gives an expression for time rate of change of the amplitude, $\dot{a}$. Using the expressions for dimensionless amplitude, $Y = a/B$, and reduced velocity, $V_r = V/\omega_s B$, this is:

$$\dot{a} = \eta\omega_s B \left[\frac{-\varsigma_s Y}{\eta} \ + \ \left(\frac{1}{8\pi}\right) A_1 Y V_r + \left(\frac{2}{3\pi}\right) A_2 Y^2 \right.$$
$$+ \ \left(\frac{3\pi}{8}\right) A_3 \frac{Y^3}{V_r} + \left(\frac{64\pi}{15}\right) A_4 \frac{Y^4}{V_r^2}$$
$$+ \ \left(\frac{5\pi^3}{8}\right) A_5 \frac{Y^5}{V_r^3} + \left(\frac{256\pi^3}{35}\right) A_6 \frac{Y^6}{V_r^4}$$
$$\left. + \ \left(\frac{35\pi^5}{8}\right) A_7 \frac{Y^7}{V_r^5} \right] \tag{7.43}$$

By setting this equal to zero, one can determine the steady state solutions. For non-zero amplitudes, the following equation is derived:

$$\left(-\frac{8\pi\varsigma_s}{\eta V_r}\right) + A_1 + \left(\frac{16}{3}\right)A_2\left(\frac{\bar{Y}}{V_r}\right)$$
$$+ \left(3\pi^2\right)A_3\left(\frac{\bar{Y}}{V_r}\right)^2 + \left(\frac{512\pi^2}{15}\right)A_4\left(\frac{\bar{Y}}{V_r}\right)^3$$
$$+ \left(10\pi^4\right)A_5\left(\frac{\bar{Y}}{V_r}\right)^4 + \left(\frac{2048\pi^4}{35}\right)A_6\left(\frac{\bar{Y}}{V_r}\right)^5$$
$$+ \left(35\pi^6\right)A_7\left(\frac{\bar{Y}}{V_r}\right)^6 = 0 \qquad (7.44)$$

Novak has treated this problem in some detail [48,49]. By making use of a strip assumption, he extended the idea from the single degree of freedom case discussed above to continuous systems with general mode shapes and in the presence of a variable mean velocity profile. In that case the above solution is modified slightly in such a way that each of the coefficients, A_i are replaced by modified values, $\underline{A}_i$, where:

$$\underline{A}_i = c_i A_i \qquad (7.45)$$

$$c_i = \frac{\int_0^H \nu^{2-i}[z]\,|\mu[z]|^{1+i}dz}{\int_0^h \mu^2[z]\,dx} \qquad (7.46)$$

and where $\nu[z]$ describes the velocity profile:

$$V[z] = V_H\nu[z] \qquad (7.47)$$

For a power law profile as described by Equation 7.19 and a linear mode shape, these c_i coefficients reduce to:

$$c_i = \frac{3}{(2+i)+(2-i)a} \qquad (7.48)$$

where a is the power law exponent.

The measured moment coefficients shown in Figure 7.10 were used to form C_y taking into account Equation 7.28. A least squares polynomial fit according to Equation 7.36 was determined giving the following values.

$$\left. \begin{array}{rcl} A_1 & = & 1.2596 \\ A_2 & = & -0.20434 \\ A_3 & = & 14.592 \\ A_4 & = & 306.12 \\ A_5 & = & -2788.7 \\ A_6 & = & 6624.6 \\ A_7 & = & -4901.2 \end{array} \right\} \tag{7.49}$$

The fitted curve corresponding to total moment coefficient is shown plotted in Figure 7.10. The fitted values were modified according to Equation 7.48 using the power law profile shown in Figure 7.1.

Using the modified fitted values, Equation 7.44 can be solved iteratively to provide estimates of steady state response versus reduced velocity. This is not necessary for the current purpose and, furthermore, a more refined fitting procedure would be required than was used for the present example. It is useful, however, to estimate the critical onset reduced velocity. This can be done by just considering the first two terms of Equation 7.44 with the modified fitted value, which gives:

$$V_o \left(\frac{\eta}{\varsigma_t} \right) = \frac{8\pi}{A_1 c_1} = 20.7 \tag{7.50}$$

This suggests a critical onset reduced velocity of about 17.8 for the aeroelastic model Structure 1 and higher values for the other cases. Hence all of the aeroelastic results are for cases where the range of vortex shedding falls below the critical onset velocity for galloping.[2]

An expression for the quasi-steady form of G_a for the across-wind direction can be extracted from the previous development as follows using the method of equivalent linearization. This is based on the principle of power balance and the details of the general approach are covered elsewhere[12]. Equations 7.40 and 7.41 can be related to equivalent values of stiffness, K_e, and damping, C_e, as follows:

$$K_e(a) = K_s + 2M_s\omega_s\dot{\phi} \tag{7.51}$$

$$C_e(a) = -2M_s\frac{\dot{a}}{a} \tag{7.52}$$

From this the quasi-steady impedance can then be determined:

$$\alpha_{QS} = \frac{(K_e - K_s)}{2\eta M_s\omega_s^2} = \frac{\dot{\phi}}{\eta\omega_s} \tag{7.53}$$

$$\beta_{QS} = \frac{(C_e - C_s)}{2\eta M_s\omega_s} = -\frac{\dot{a}}{a\eta\omega_s} - \frac{\varsigma_s}{\eta} \tag{7.54}$$

Substituting in Equations 7.42 and 7.43 with modified coefficients, A_i, gives:

$$\alpha_{QS} = 0 \tag{7.55}$$

$$\beta_{QS} = -\left[\left(\frac{1}{8\pi}\right)A_1V_r + \left(\frac{2}{3\pi}\right)A_2Y \right.$$
$$+ \left(\frac{3\pi}{8}\right)A_3\frac{Y^2}{V_r} + \left(\frac{64\pi}{15}\right)A_4\frac{Y^3}{V_r^2}$$
$$+ \left(\frac{5\pi^3}{8}\right)A_5\frac{Y^4}{V_r^3} + \left(\frac{256\pi^3}{35}\right)A_6\frac{Y^5}{V_r^4}$$
$$\left. + \left(\frac{35\pi^5}{8}\right)A_7\frac{Y^6}{V_r^5}\right] \tag{7.56}$$

---

[2]By the extent of the velocity range over which large amplitudes occur, it would appear that Structure 1 and, possibly, Structure 2 demonstrate behavior associated with combined vortex-induced vibration and galloping effects as discussed in Chapter 3.

This quasi-steady estimate using the fitted values is shown in Figure 7.44 along with the results of the PMA tests. The curve shown has been calculated for $\tilde{Y} = 3\%$, however, over the range shown, the curve is almost insensitive to this and essentially depends on the first term of Equation 7.56.

7.6.2 Comparisons of PMA and PP Results

Estimates of the motion-induced forces were calculated from the porous polyethylene pressure model data. This was done according to Equation 6.11. Rearranged it is:

$$K_a = \frac{-pBHS_{yC_m}}{S_{yy}} \tag{7.57}$$

From this, an expression for the aerodynamic impedance may be derived as:

$$G_a = \frac{-3}{16\pi^2} V_r^2 \frac{S_{YC_m}}{S_{YY}} \tag{7.58}$$

To estimate the transfer function, the cross-spectral estimates between the motion and the moment spectrum contribution from the upper third of the model were used. Summations were performed on the appropriate spectra for a few points about the frequency of forced oscillation and then the ratio was taken. That is:

$$\frac{S_{YC_m}}{S_{YY}} \approx \frac{\Sigma S_{YT}}{\Sigma S_{YY}} \tag{7.59}$$

This ratio was determined for each test case of the pressure model experiment series and for the corresponding case which was carried out with forced oscillations but with the wind off. The latter spectra were not significant in magnitude, however, the transfer function estimate contributed a reference phase condition which accounted
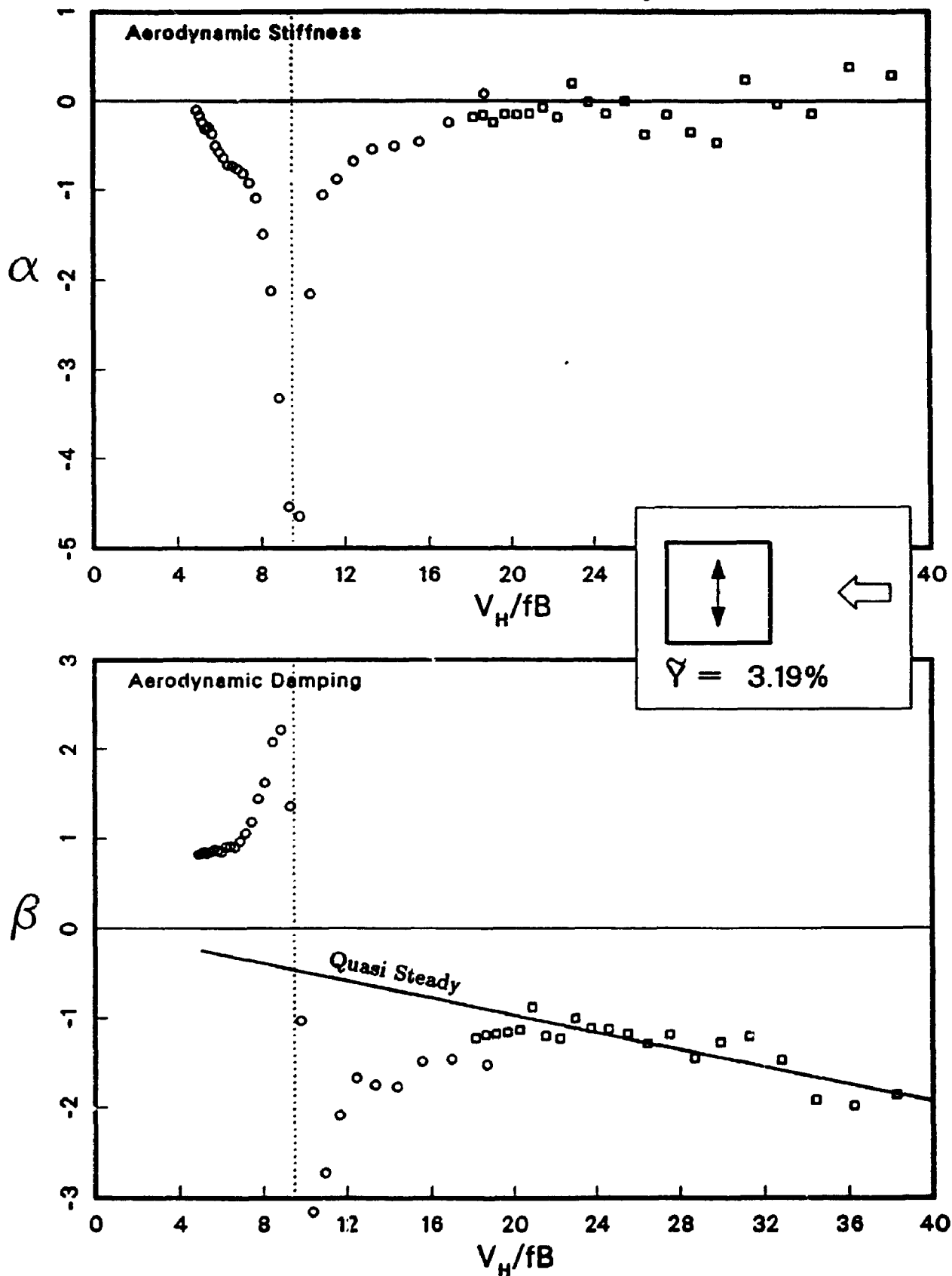
Figure 7.44: Comparison of PMA Results with Quasi-Steady Theory for Across-Wind Direction

for the different instrumentation used to measure pressures and displacements. The phase corrected estimate of the transfer function was then used in Equation 7.58 to estimate G_a.

Figure 7.45 shows most of these results. The aerodynamic impedance estimates have been plotted versus the rms oscillation amplitude. The three nominal velocities are differentiated. The solid lines are interpolated curves from the PMA results. The results from both sources are in good qualitative agreement. It is expected that the PMA results represent the finer measurement as there is greater uncertainties and approximations involved in the estimates from the PP results.

7.6.3 Free Oscillation Predictions from BB Results

The base balance technique was reviewed in some detail in Chapter 2. Response curves using this technique were predicted for each of the five aeroelastic structures. Motion-induced forces are neglected in this approach. The reduced velocity at which the highest response occurs is the same in all cases since the different structural parameters do not affect this in the base balance approach. However, this is not the case for actual free oscillation response as is seen in the aeroelastic experiment results. At and above this velocity range, the base balance technique grossly underestimates the response, indicating the significant role played by the motion-induced forces. The reader is referred ahead to Figures 7.47 to 7.51 where the response curves are plotted. They have not been presented independently in the interests of space.
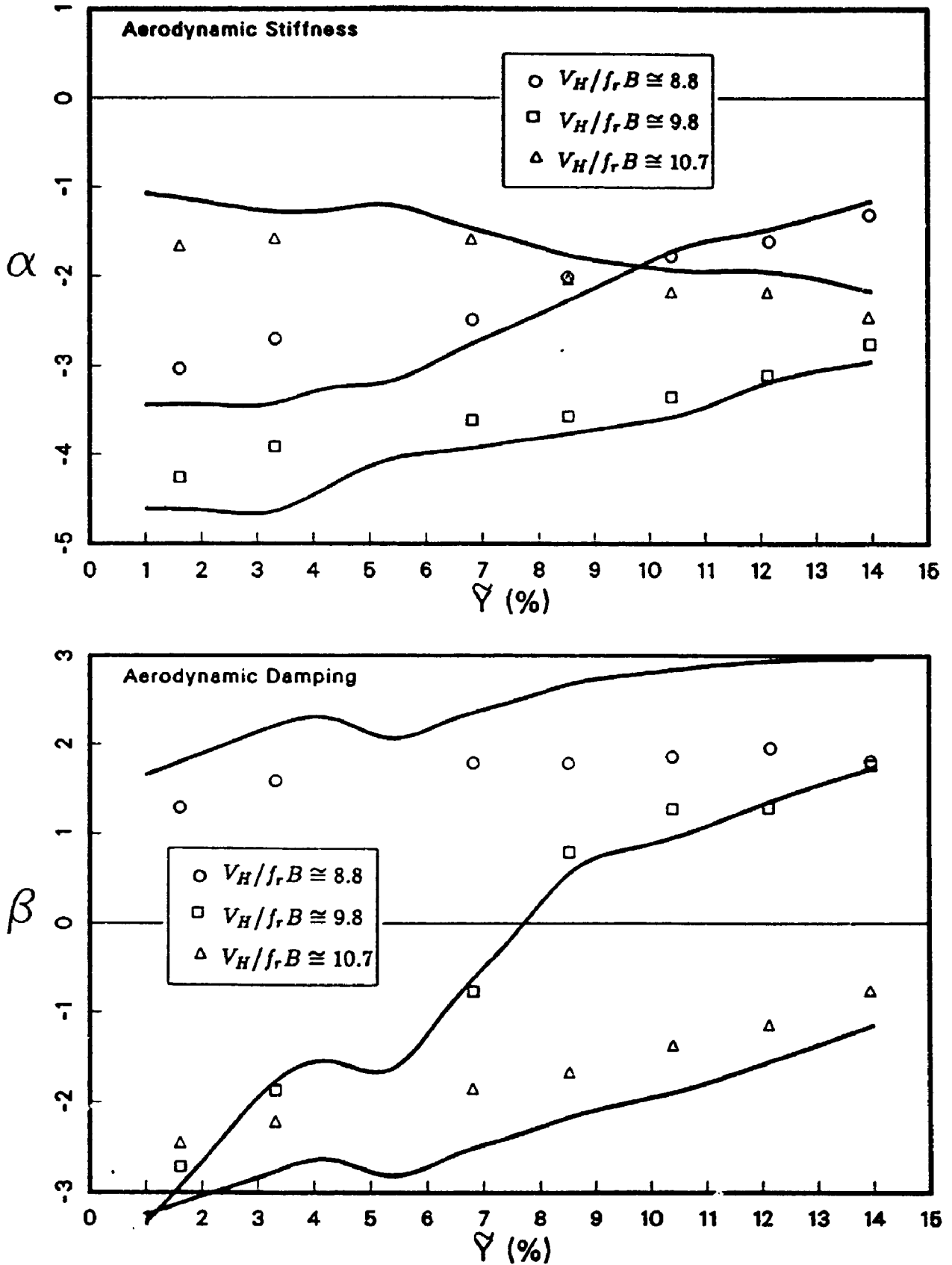
Figure 7.45: Comparison of Aerodynamic Impedance Determined from the PP Experiments with the PMA Results

7.6.4 Free Oscillation Predictions from PMA Results

As a first approach to predicting free oscillation amplitudes using the measured motion-induced forces, we can search for solutions compatible with the measured forces with the assumption that all of the motion is resonant and the random wind force contributes nothing to the response. In other words we assume that $C_l(t) = 0$. We will see that neglecting the random wind force does not provide adequate predictions, although it does provide a lower bound of the potential free oscillation motion. The generalised equation of motion becomes simply:

$$M_s \ddot{y} + C_s \dot{y} + (K_s + K_a)y = 0 \tag{7.60}$$

Assuming finite harmonic motion, that is:

$$y = y_r e^{i\omega t} \tag{7.61}$$

the equation of motion can be expanded as:

$$\left(\left(-M_s\omega^2 + K_s + 2M_s\omega^2\eta\alpha\right) + i\left(C_s\omega + 2M_s\omega^2\eta\beta\right)\right)y_r e^{i\omega t} = 0 \tag{7.62}$$

Recall that $\eta = \rho_a/\rho_s \propto 1/M_s$. Both the real and the imaginary parts must be zero for non trivial solutions, $(y_r \neq 0)$. Therefore, we require:

$$\omega^2 = \frac{\omega_s^2}{1 - 2\eta\alpha\,[\omega]} \tag{7.63}$$

$$\varsigma_s + \left(\frac{\omega}{\omega_s}\right)\eta\beta\,[\omega] = 0 \tag{7.64}$$

Here the structural frequency, ω_s, and damping ς_s are defined as usual:

$$\omega_s^2 = \frac{K_s}{M_s} \tag{7.65}$$

$$\varsigma_s = \frac{C_s}{2M_s\omega} \tag{7.66}$$

Since α is relatively small, the first of these equations is very nearly $\omega \approx \omega_s$. However, recall that $\beta[\omega]$ varies rapidly in the vicinity of $\omega \approx \omega_v$. As a result, the effect when the first equation is substituted into the second, is not negligible. The second equation results from the requirement that the net energy dissipation over many cycles is zero and hence the steady state motion is maintained. In effect, the aerodynamic damping must be negative and just balance the positive structural damping. These equations can be solved iteratively. The results of this process, using the data from this study, and considering both equations, can be seen in Figures 7.47, 7.48, and 7.49 compared with the corresponding aeroelastic experiment results. No solutions are produced from the current data set for the particular parameters of the other two aeroelastic structures. The solutions in the range of $V_r = 12$ to 15 for Structure 2 which show some detailed variations are not likely significant as they are essentially due to the poorer resolution of the interpolated data in this range. As expected the free oscillation response is underpredicted.

7.6.5   Development of a Combined BBPMA Analysis

Consider the SDOF equation of motion modified for the aerodynamic impedance and including the random wind force.

$$M_s\ddot{y} + C_s\dot{y} + (K_s + K_a)y = F(t) \tag{7.67}$$

Our measured K_a is the result of a forced oscillation experiment and is expressed in the form:

$$K_a = \left(2M_s\omega_r^2\eta\right) G_a \tag{7.68}$$

Here, ω_r represents the normalising frequency used for non-dimensionalising in the PMA analysis. It was there appropriately chosen as the oscillation frequency. To determine the appropriate value of K_a for a free oscillation case, some value of ω_r must be used to dimensionally scale G_a. The choice, however, is not as clear as in the forced oscillation case. Maintaining it as simply ω_r for now, Equation 7.67 becomes:

$$M_s\ddot{y} + C_s\dot{y} + \left(K_s + 2M_s\omega_r^2\eta\left(\alpha + i\beta\right)\right)y = F(t) \tag{7.69}$$

Assuming a sinusoidal excitation, that is:

$$F(t) = F_0 e^{i\omega t} \tag{7.70}$$

the steady state solution becomes:

$$y = \frac{F_0}{K_s}H_a(\omega)e^{i\omega t} \tag{7.71}$$

where $H_a(\omega)$ is a complex *aeroelastic admittance function*, which can be expressed:

$$H_a(\omega) = \frac{1}{\left(1 + 2\left(\frac{\omega_r}{\omega_s}\right)^2\eta\alpha\left|\omega_r\right| - \left(\frac{\omega}{\omega_s}\right)^2\right) + i2\left(\frac{\omega}{\omega_s}\right)\left(\varsigma_s + \left(\frac{\omega_r^2}{\omega_s\omega}\right)\eta\beta\left|\omega_r\right|\right)} \tag{7.72}$$

Here the functional dependence of α and β on ω_r has been shown explicitly using square brackets[3]. Taking the squared modulus of this gives the real quantity:

$$|H_a(\omega)|^2 = \frac{1}{\left(1+2\left(\frac{\omega_r}{\omega_s}\right)^2\eta\alpha|\omega_r|-\left(\frac{\omega}{\omega_s}\right)^2\right)^2 + 4\left(\frac{\omega}{\omega_s}\right)^2\left(\varsigma_s+\left(\frac{\omega_r^2}{\omega_s\omega}\right)\eta\beta|\omega_r|\right)^2} \tag{7.73}$$

We must now deal with the crucial fact that forced oscillation and free oscillation are not the same thing. Free oscillation is in general not sinusoidal, but contains significant random motion, particularly far from resonance. To examine

---

[3]Recall, however, that α and β are also functions of the amplitude.

the consequences of this, consider the very general expression of the motion-induced forces in the form:

$$A(y, \dot{y}, \ddot{y}, ...)$$ (7.74)

Expanding this in a Taylor series about $y = 0$ we get an expression of the form:

$$A_1 y + A_2 \dot{y} + A_3 \ddot{y} + A_4 y^2 + A_5 \dot{y}^2 + A_6 \ddot{y}^2 + A_7 y \dot{y} + A_8 y \ddot{y} + A_9 \dot{y} \ddot{y} + ...(higher\ order\ terms)$$ (7.75)

where A_i are unknown coefficients. In the special case that all the coefficients of $i > 3$ are zero, then we would find that for sinusoidal motion as we have in the forced oscillation experiments:

$$\alpha = \frac{-A_1 + \omega_r^2 A_3}{2 M_s \omega_r^2 \eta}$$

$$\beta = \frac{-i A_2}{2 M_s \omega_r \eta}$$ (7.76)

which are both independent of the amplitude y. In this special case the linearised impedance from the forced oscillation experiment in fact offers a complete description of the motion-induced forces. We can then replace ω_r by the excitation frequency ω and Equation 7.72 can be simplified to:

$$H_a(\omega) = \frac{1}{\left(1 - (1 - 2\eta\alpha\,|\omega|)\left(\frac{\omega}{\omega_r}\right)^2\right) + i2\left(\frac{\omega}{\omega_r}\right)\left(\varsigma_s + \left(\frac{\omega}{\omega_r}\right)\eta\beta\,|\omega|\right)}$$ (7.77)

If α and β are independent of y then in accordance with linear random excitation theory, the mean square displacement can be determined by:

$$\bar{y}^2 = \frac{1}{K_s} \int_0^\infty S_{FF}(f) |H_a(f)|^2 df$$ (7.78)

Urfortunately it is quite clear from the test results, for example Figure 7.5 that the aerodynamic impedance does depend on amplitude and certainly does not

follow the simple dependence on frequency demanded by Equations 7.76. Apparently the higher coefficients, A_i, $i > 3$ are significant. At least some of them will contribute to the measured aerodynamic impedance and so the assumptions on which Equation 7.77 rely are not valid.

This leads us to the basic assumption of the forced oscillation approach. It is assumed that despite the unavoidable differences, the forced oscillation experiments, and the forces there measured, are at least representative of free oscillation experiments for ranges where the response is largely resonant. Specifically we assume that the measured aerodynamic impedance at a specific reduced frequency represents an effective value valid for some free oscillation case. Physically, the idea is that periodic motion of the structure sets up or modifies existing fluid field structures which have coherence in both space and time. These fluid field structures in turn supply an aerodynamic impedance to the moving structure. A certain amount of additional random motion may be tolerated without significantly altering the coherent field. Hence the aerodynamic impedance remains effective even in the presence of some random motion. The amount of additional random motion required to foil the structure of the coherent field would depend on the strength and nature of that structure. It is hypothesised that the vortex shedding process, representing a strong coherent fluid field structure, would tolerate a significant amount of random moti n and still maintain a consistent impedance to the total motion.

This physical argument gives some guidance in an appropriate choice of scaling frequency, ω_r for the measured aerodynamic impedance. One immediate choice is the natural frequency of the structure:

$$\omega_s = \sqrt{\frac{K_s}{M_s}} \tag{7.79}$$

Substituting this in Equation 7.72 we get:

$$H_a(\omega) = \frac{1}{\left(1 + 2\eta\alpha\,[\omega_s] - \left(\frac{\omega}{\omega_s}\right)^2\right) + i2\left(\left(\frac{\omega}{\omega_s}\right)\varsigma_s + \eta\beta\,[\omega_s]\right)} \qquad (7.80)$$

Equation 7.80 is not entirely appropriate. The response even when strongly organised does not resonate at exactly ω_s since the real part of the aerodynamic impedance modifies the effective stiffness of the structure. This was seen in the aeroelastic model test results.

For a slightly more refined approach, we assume that the response of the free oscillation case, while containing some random motion, is largely organised and responds most dominantly at a frequency determined by the modified stiffness. The aerodynamic impedance measured in a forced oscillation experiment at that dominant frequency then represents the effective impedance acting on the structure in the free oscillation case. The dominant response frequency is then given by:

$$\omega_r = \sqrt{\frac{K_s + \Re(K_a)}{M_s}} \qquad (7.81)$$

or expanding this and showing the frequency dependence of α explicitly:

$$\omega_r^2 = \frac{K_s + 2M_s\omega_r^2\eta\alpha\,[\omega_r]}{M_s} \qquad (7.82)$$

$$\omega_r = \frac{\omega_s}{\sqrt{1 - 2\eta\alpha\,[\omega_r]}} \qquad (7.83)$$

This is Equation 7.63 again, which can be re-expressed as a scaling condition on the reduced velocity as based on ω_r. This allows one to transform G_a from a function of reduced velocity based on forced oscillation frequency to a function of reduced

velocity based on natural frequency of the structural. That is:

$$(\alpha^* + i\beta^*) = G_a^* [V_H/f_s B] = G_a \left[\frac{V_H/f_s B}{\sqrt{1-2\eta\alpha[\omega_r]}} \right]$$

(7.84)

There is also a functional dependence on the oscillation amplitude in the above, but this is not shown explicitly. Note that G_a is an aerodynamic impedance which is independent of structural properties; it depends only on the geometry of the structure and on the flow conditions. However, G_a^* is a modified *aeroelastic* impedance which incorporates the structural properties, η and f_s.

Substituting this into Equation 7.72 gives:

$$H_a(\omega) = \frac{1}{\left(1+2\frac{\eta\alpha^*}{1-2\eta\alpha^*}-\left(\frac{\omega}{\omega_s}\right)^2\right)+i2\left(\left(\frac{\omega}{\omega_s}\right)\varsigma_s+\frac{\eta\beta^*}{1-2\eta\alpha^*}\right)}$$

(7.85)

where α^* and β^* here refer to the particular values of α and β which satisfy Equation 7.83. The differences between these two assumptions for the effective ω_r is not great, since the modified stiffness is very nearly the same as the structural stiffness; however, the effect on the aerodynamic damping in the vicinity of the vortex shedding is more significant.

With regard to the excitation spectrum $S_{FF}(\omega)$, which occurs in Equation 7.78, it will be assumed as a first approximation that it remains unchanged from that measured on a stationary model. It is known from measurements of the force spectra on moving models, that this is in fact not the case, however, it appears

to be reasonable up to some amplitude. This problem will be returned to in the next section.

As we have seen, G_a is a function of the oscillation amplitude. Therefore when Equation 7.85 is substituted into Equation 7.78, iteration must be used to solve for the response amplitude. Acknowledging some inconsistency, we will assume that the resonant rms amplitude by which α^* and β^* are determined and the total rms amplitude implied on the left hand side of Equation 7.78 are in fact the same.

Since the damping term is squared in this calculation, cases of negative damping which are physically unrealisable will appear as solutions as well. Such conditions must be checked for. More specifically, we must ensure that $H_a(\omega)$ never goes to infinity, since this would mean that the response amplitude would grow without bound as well. We may note that the real part of the aeroelastic admittance denominator becomes zero only when:

$$\frac{\omega}{\omega_s} = \sqrt{1 + \frac{2\eta\alpha^*}{1 - 2\eta\alpha^*}} \qquad (7.86)$$

Ensuring that the imaginary part cannot go to zero at the same time leads to the requirement that:

$$\varsigma_s + \frac{\eta\beta^*}{\sqrt{1 - 2\eta\alpha^*}} \neq 0 \qquad (7.87)$$

This represents the net damping as a fraction of critical for the aeroelastically modified system. In fact, since the structural damping is always positive and the system will vary continuously, we can restate this condition as

$$\varsigma_s + \frac{\eta\beta^*}{\sqrt{1 - 2\eta\alpha^*}} > 0 \qquad (7.88)$$

The lower bound in fact corresponds to the conditions by which the predic-

tions in the previous section were derived. Those predictions, thus form a dividing curve between regions of valid and invalid solutions for the current calculations. That is, they provide a lower bound solution for the response.

Setting α^* and β^* to zero for all amplitudes reduces the above calculations to that of the simple base balance approach described in Chapter 2.

Figure 7.46 shows some results as calculated for Structure 2. The main plot symbols indicate the valid solutions according to Equation 7.88. The invalid solutions are also shown in this figure for illustration. The solutions determined from the PMA results alone, (see Figure 7.48) falls between these sets of solutions and as mentioned indicates a lower bound for the valid solutions.

To illustrate the sensitivities to the estimate of structural damping, two other sets of solutions are also shown, one corresponding to damping slightly greater than the estimated (with a nominal value of 1.19% of critical), and the other corresponding to damping lower than the estimated (with nominal value of .98% of critical). The large degree of scatter and multiple solutions occurring to the right of the peak can be understood by looking at the form of the aerodynamic damping in this range, see Figure 7.5. It becomes almost constant with reduced velocity and amplitude. If the mass-damping parameter, that is ζ_s/η, is such that the total or net damping available is very small, then the aeroelastic admittance function becomes very peaky. In turn the numerical integration, although carried out at very fine increments, becomes extremely sensitive to the value of the forcing spectrum at the peak frequency. The scatter seen in the lower damping case is due largely to the scatter in the unsmoothed spectrum used for the numerical calculations, that
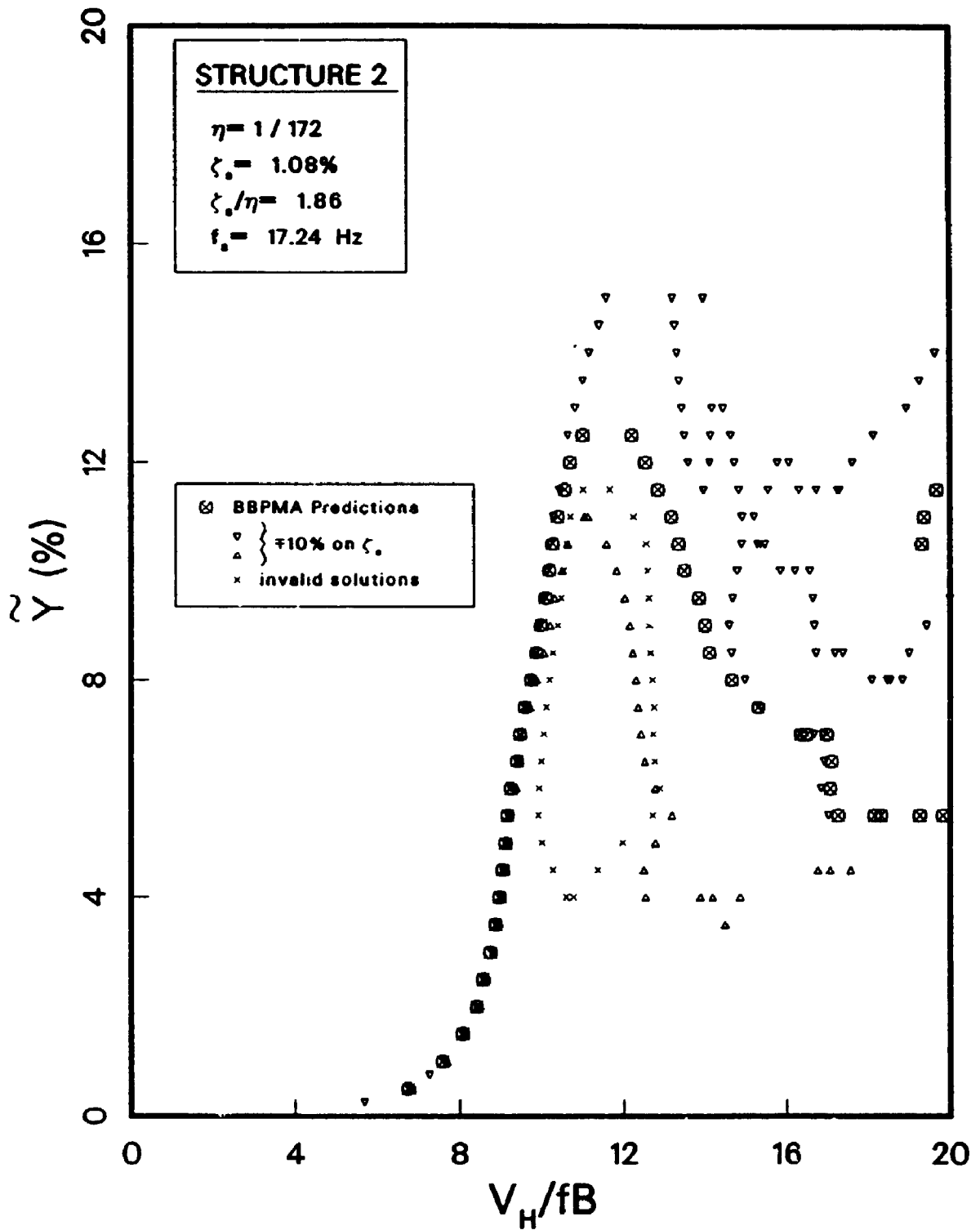
Figure 7.46: Some Comparison of Predictions Using PMA Results

is the spectrum in Figure 7.9. While smoothing the spectrum would improve the numerical stability, the inherent uncertainty of the damping estimates and of the true forcing spectrum acting on the moving structure must be accepted. In fact, these numerical sensitivities are simply indicative of an inherent sensitivity of the phenomenon. **When conditions are such that the net damping available is very small and the aerodynamic impedance is a locally constant function, then the response becomes very sensitive to the random forcing available from the turbulent flow.**

In the following section, the results of the calculations for each of the model structures will be presented for comparison with the aeroelastic results.

7.7   Comparisons of Predictions with Aeroelastic Results

7.7.1   Comparisons of Rms Response

The results from the aeroelastic tests and the predictions resulting from the methods discussed in the previous three sections are presented now in overlaid form in Figures 7.47 to 7.51 for each of the model structures. This figure contains the results from all four sources. For the first two structures, the amplitude dependent structural damping assessed from the aeroelastic damping trace measurements has been included in the calculations. For the other three structures, a constant structural

damping has been assumed. For the combined BBPMA predictions, the calculations for the latter three structures have been repeated for a slightly increased and a slightly decreased value of structural damping. These results are also shown in those cases.

The BB predictions, as noted earlier, grossly underpredict the response at higher velocities, particularly for the lightly damped structures. The prediction is reasonable or even conservative at lower velocities.

The PMA predictions, which neglect the background turbulence, are in good agreement when the response is very large. This is a consequence of the strong aerodynamic damping effects in these ranges.

In each case, the combined BBPMA predictions show very good agreement throughout the velocity range, particularly for the more realistically damped structures. This may be at first surprising, considering the assumptions made in the previous section. Recall that the aerodynamic impedance was chosen in each situation based on the total rms response, whether it arose from the random background motion or from resonant motion. The latter condition would be more consistent with the forced oscillation situation in which the impedance was measured. Also, the form of the forcing spectrum was assumed to be invariant from that measured on a stationary prism, which is known to be not the case at larger amplitudes.

The reason that the combined BBPMA prediction method performs as well as it does appears to arise from the fact that the situations where these assumptions
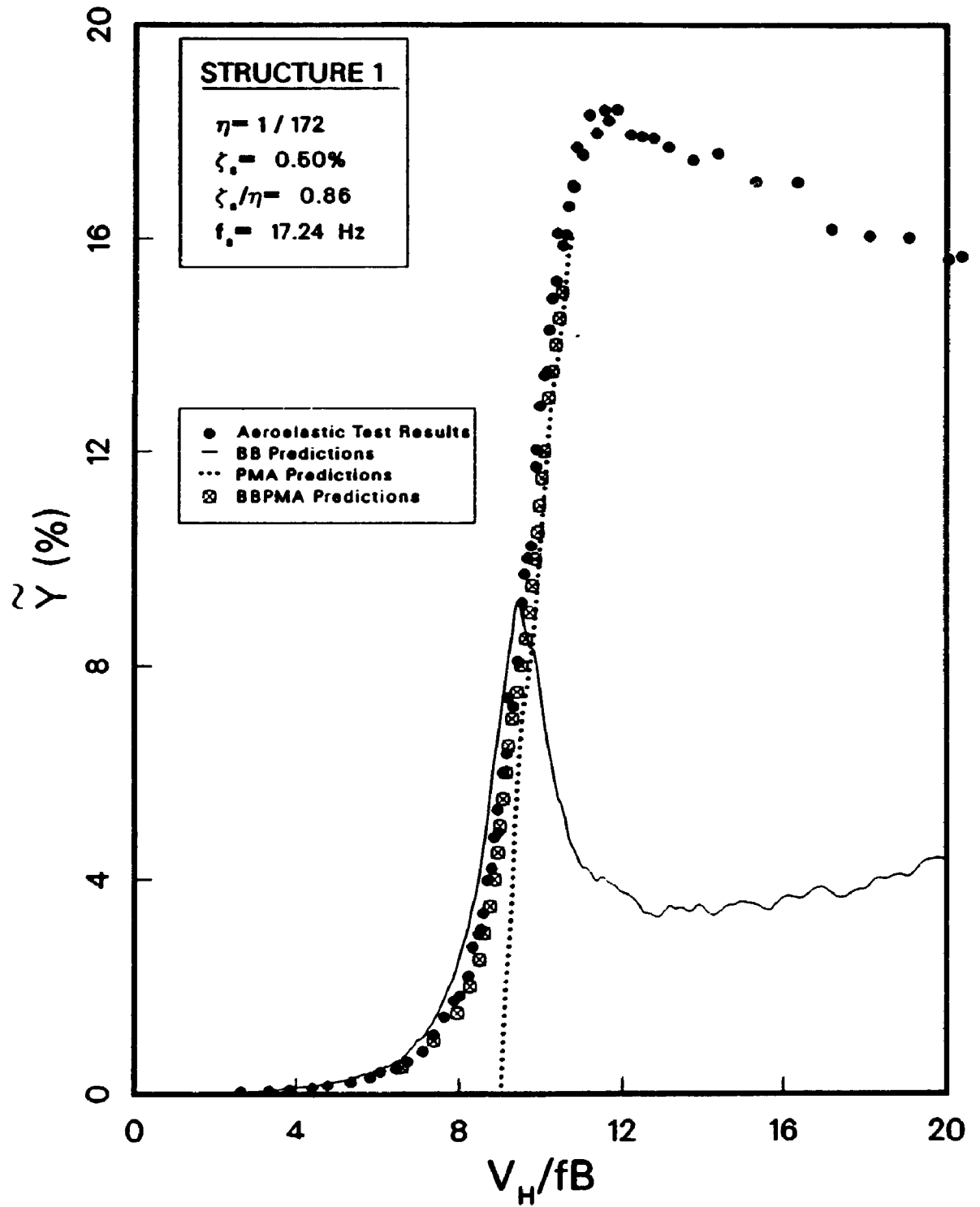
Figure 7.47: Overlaid Predictions and Aeroelastic Results for Structure 1
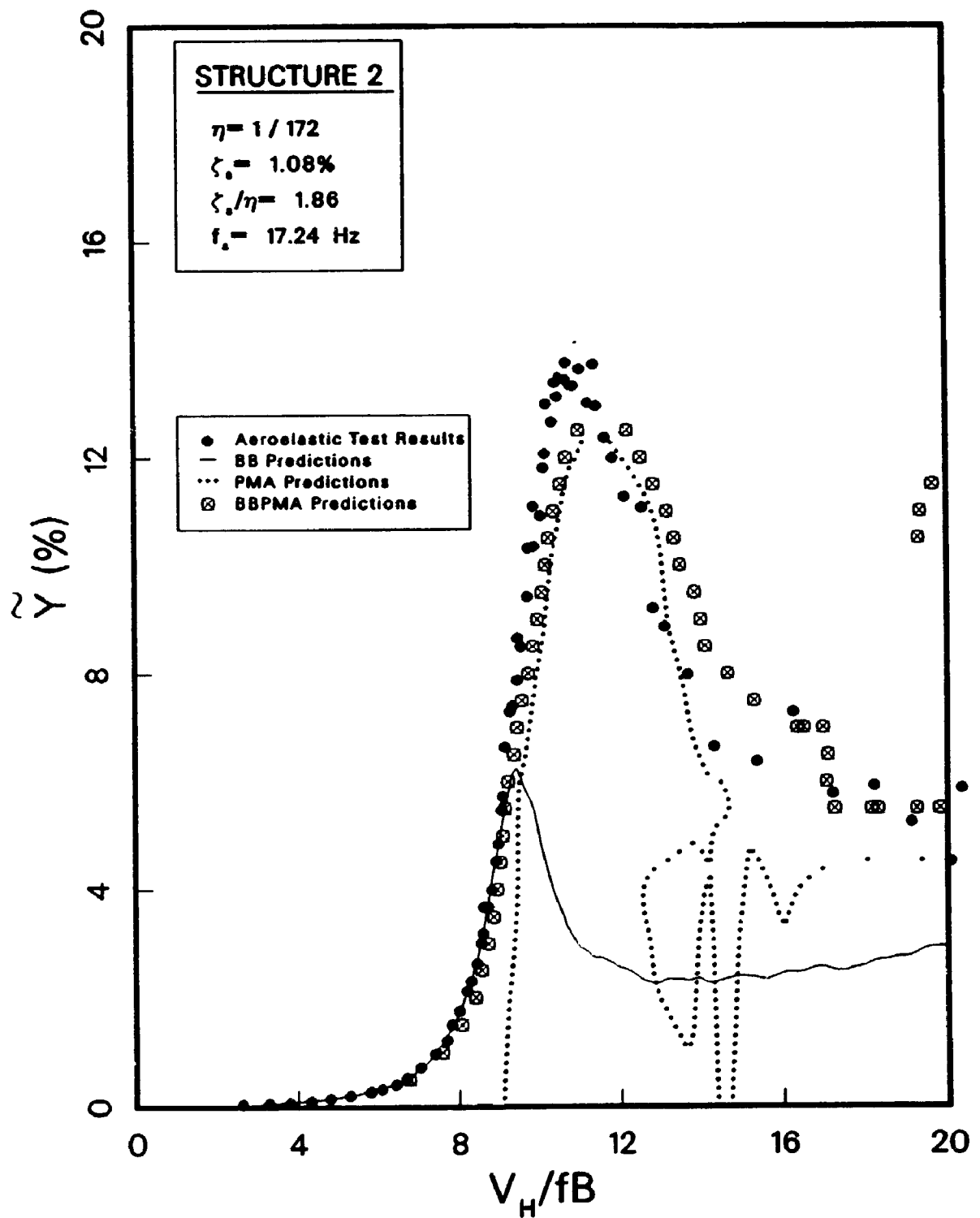
Figure 7.48: Overlaid Predictions and Aeroelastic Results for Structure 2
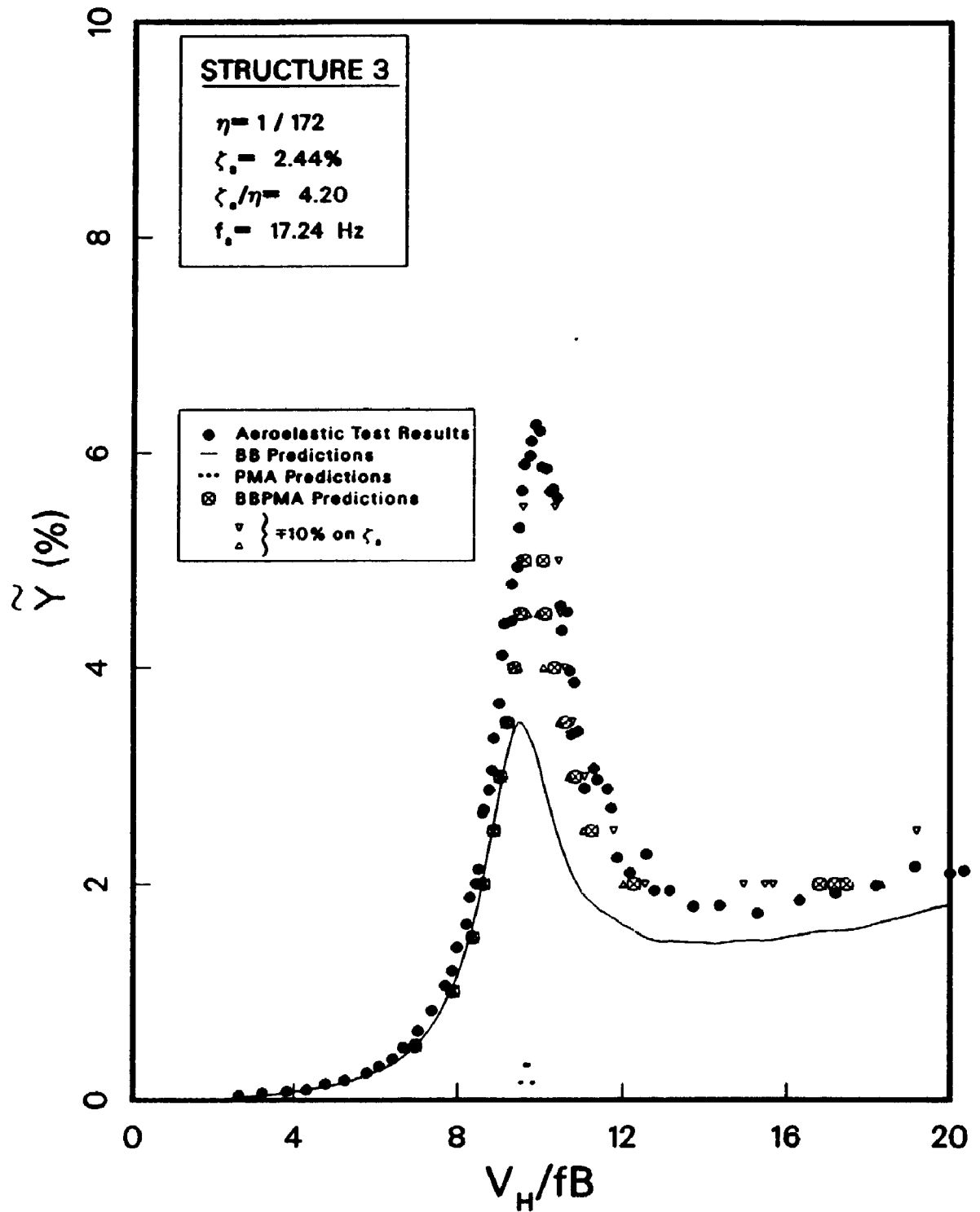
Figure 7.49: Overlaid Predictions and Aeroelastic Results for Structure 3
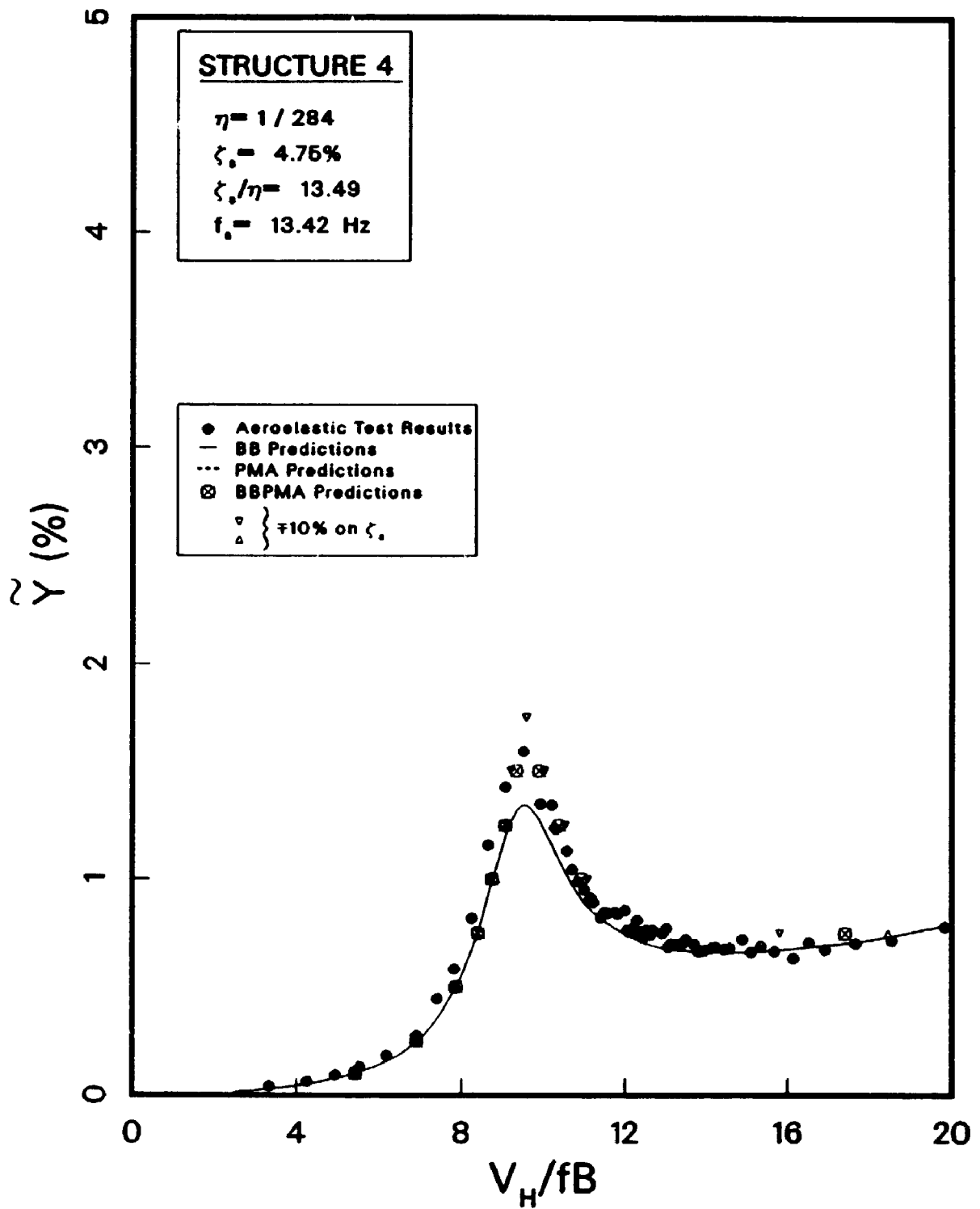
Figure 7.50: Overlaid Predictions and Aeroelastic Results for Structure 4

STRUCTURE 5

$\eta = 1 / 284$

$\zeta_a = 8.80\%$

$\zeta_a/\eta = 24.99$

$f_a = 13.42$ Hz

- ● Aeroelastic Test Results
- — BB Predictions
- ••• PMA Predictions
- ⊗ BBPMA Predictions
- ∇ ⎱ ∓10% on ζ_a
- △ ⎰

$\tilde{Y}$ (%)

V_H/fB
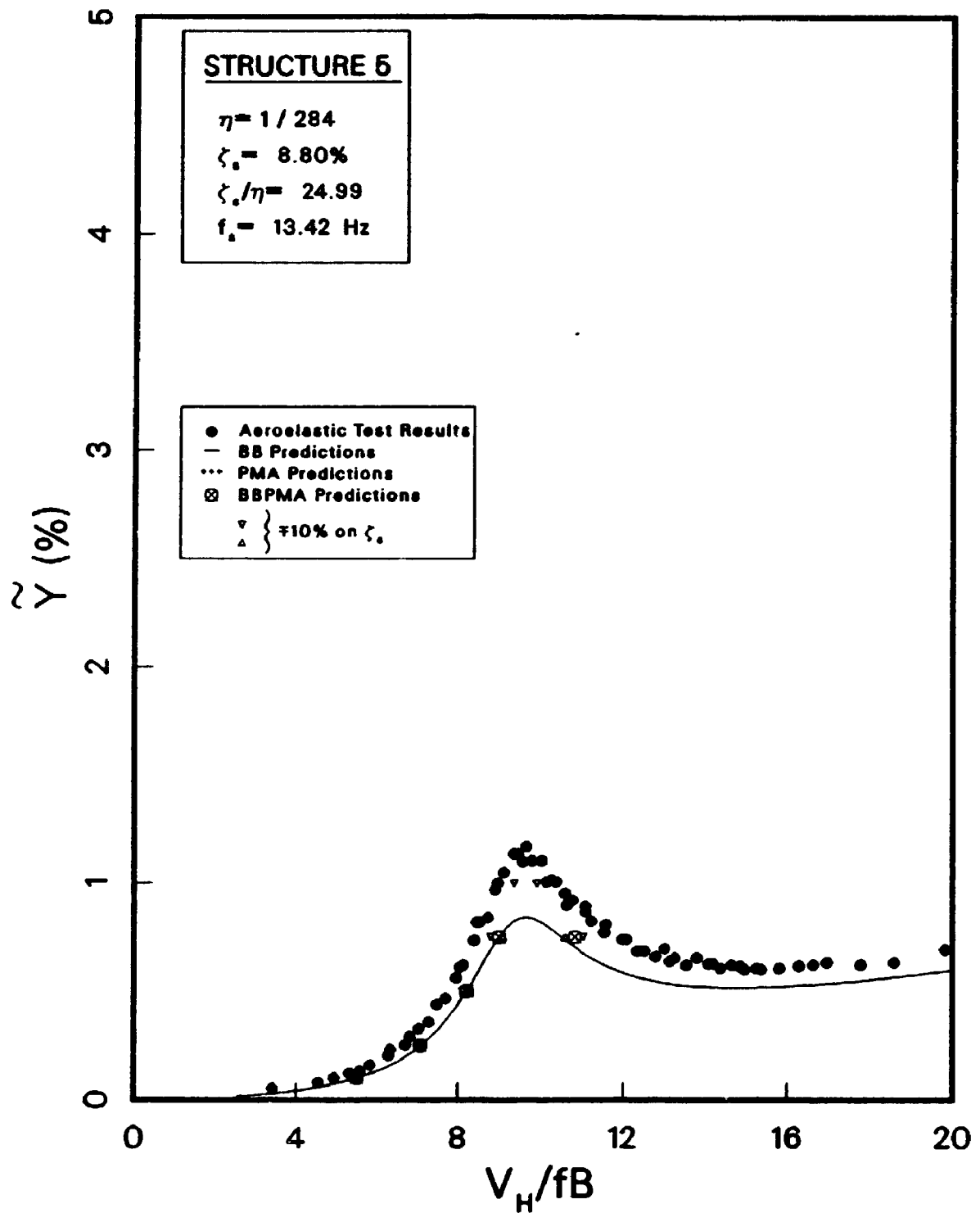
Figure 7.51: Overlaid Predictions and Aeroelastic Results for Structure 5

are important also happen to be the situations where they are most valid. At lower velocities, below the vortex shedding range, there is sufficient damping available that the response is relatively small and therefore, as assumed, the forcing spectrum has not varied much from that which would act on a stationary structure. Even if the aerodynamic damping value used is not entirely applicable, due to the presence of random non-resonant response, the errors are not significant in this range. At higher velocities, at and above the vortex shedding range, the aerodynamic damping reduces the total damping available. The response grows, becomes more highly resonant, and the aerodynamic damping effects begin to dominate the response. At these higher amplitudes, the background spectrum plays a smaller role, and so the validity of the assumption regarding its form is less important.

The combined BBPMA analysis, then, appears to provide a generally applicable method of predicting the rms response of a free aeroelastic structure, based on forced oscillation data and data obtained using a stationary model.

7.7.2 Further Comparisons with Consideration of Peak Response

While the ability to predict rms response is an important and progressive step in the development of the predictive techniques, estimates of the peak responses expected in a structure are very important for practical design purposes. While this has not been attempted in the current work, it is expected that with some further research, methods of predicting peak response using the the experimental

data from BB and PMA tests, may be developed. This has been considered to be outside the present scope. Some comments regarding the peak response levels are, nevertheless, appropriate.

For this purpose the results of the aeroelastic tests have been compared with predictions obtained from the base balance results, assuming that the response is entirely random. In other words, a peak factor based on a Gaussian response and defined by Equation 7.12 has been applied to the BB predictions of rms response to determine peak responses. This would be a typical practice in the absence of any information about the motion-induced forces. Figure 7.52 shows smoothed curves representing the ratio of response levels from the BB and AERO plotted against reduced velocity as determined from three of the model structures. The ratio of peak response is shown in the upper plot and the ratio of rms response is shown in the lower figure. Values greater than 1 suggest that a conservative estimate results from the BB approach assuming Gaussian response. Recall that the structural damping associated with the third structure, $\zeta_s \approx 2.5\%$, is less certain.

This figure further illustrates the importance of motion-induced forces near and above the vortex shedding range. While design situations for most buildings fall safely below this range, the design of other tall structures such as stacks and chimneys may be largely dictated by the motion-induced effects.

The base balance technique provides quite adequate or even conservative results for velocities below about 80% of the Strouhal velocity. Just above that range, however, the magnitude of the motion-induced forces increases significantly as can be seen in Figure A.5. The response also becomes more
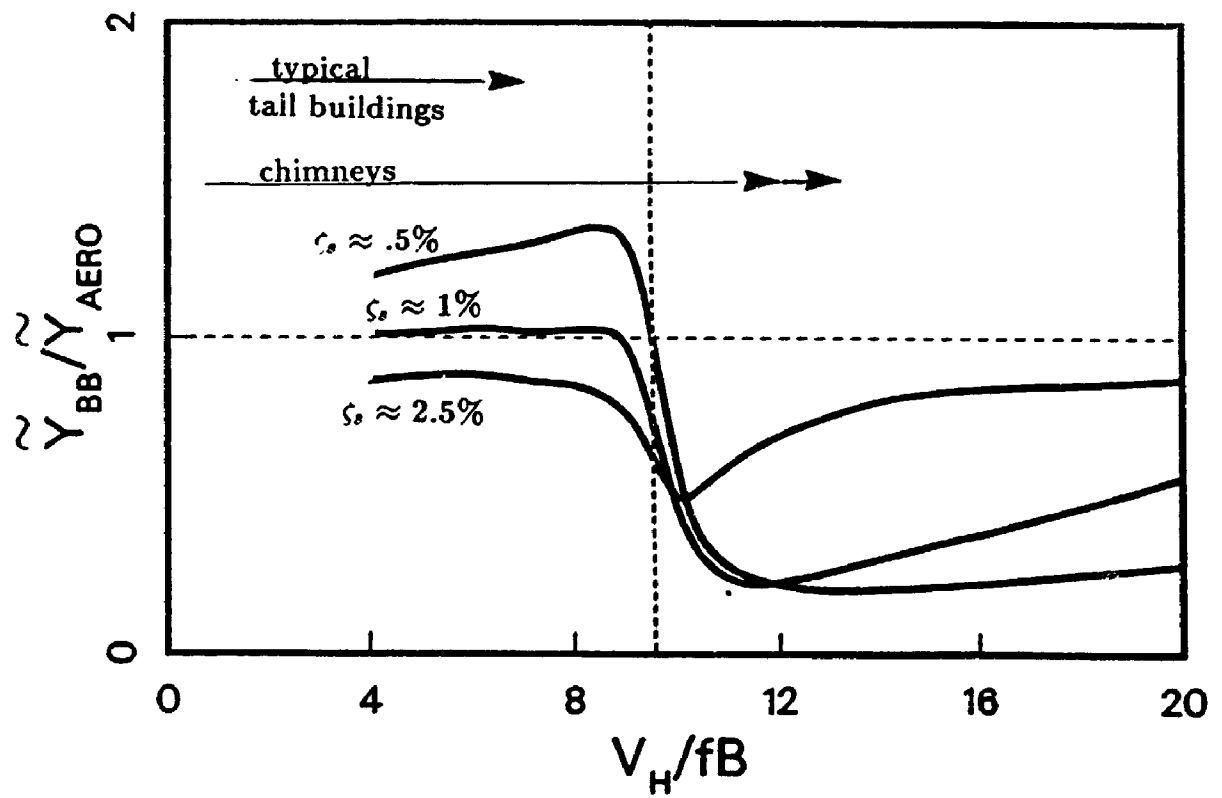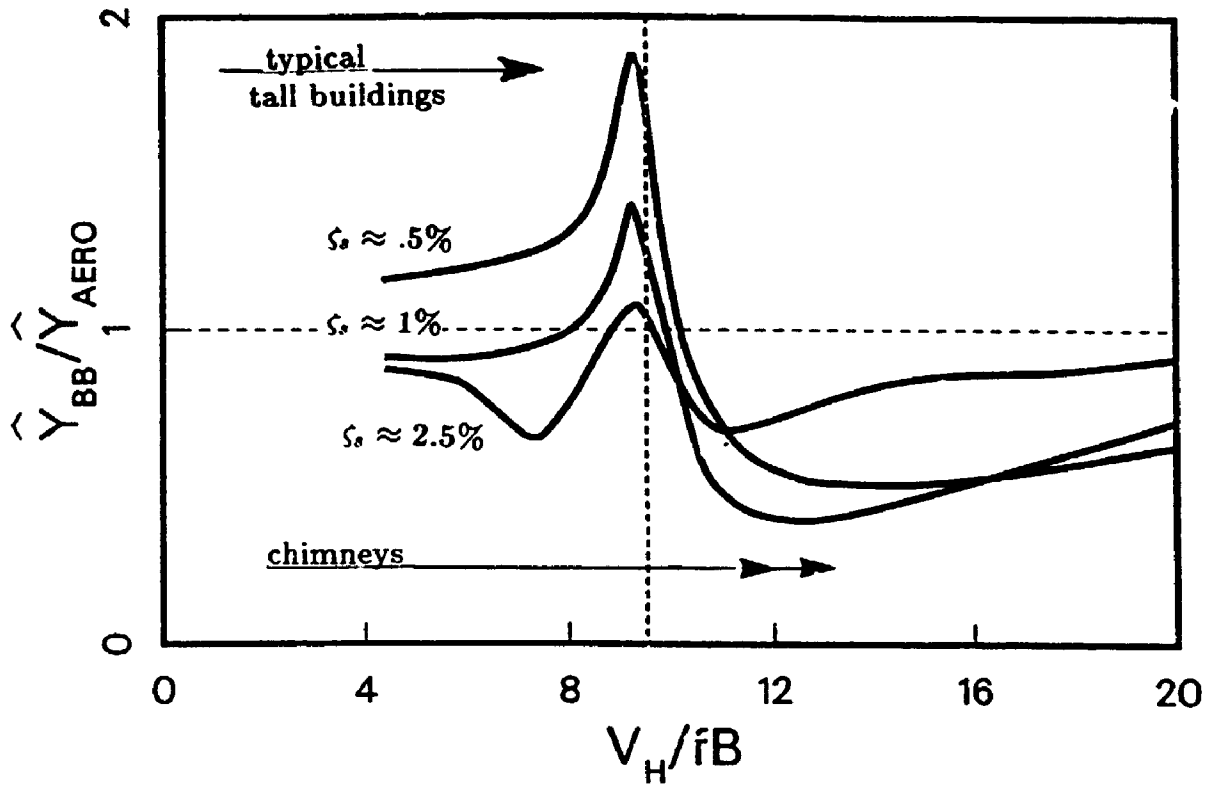
Figure 7.52: Ratio of AERO results and BB Predictions for Rms and Peak Responses

regular and the the peak factor falls sharply. This can be seen in Figure 7.36 for example. The aerodynamic damping at these velocities is still positive and in fact becomes more so just before the Strouhal velocity. Therefore, the base balance technique, assuming a Gaussian response, overestimates the response in this range, as seen in the upper plot of Figure 7.52. Recall that the base balance procedure has neglected both the aerodynamic damping and aerodynamic stiffness effects.

As the velocity increases through the Strouhal velocity, the motion-induced forces undergo a rapid change in phase relative to the motion. As a consequence the aerodynamic damping becomes negative and significantly reduces the total damping available to the structure. The response remains very regular but increases sharply in magnitude. The base balance technique then *underestimates* the rms response. The larger peak factor used is not enough to compensate for the increased level of the response and so the peak response is also significantly underestimated.

At higher velocities, there is some decrease in the magnitude of the motion-induced forces, as well as in the degree of organisation of the response, depending on the conditions considered. The base balance technique persists in underestimating the response for velocities above the Strouhal velocity, however.

Results from the tests investigating the effects of higher turbulence intensities and lower aspect ratio indicated marked reductions in the motion-induced forces. **This would suggest that the errors in the base balance predictions might be much less for typical buildings ($H/B < 10$) situated in a built up environment with local intensities higher than those considered.**

Further research and analysis is required in this area, however, these results would suggest that a promising potential exists for developing a theoretical approach to predicting the degree of organisation and thereby the peak responses.

Chapter 8

Experimental Study of Various Shapes

8.1 Introduction

The circular cross-section is perhaps the most common shape used in the design of tall chimneys. Most aerodynamic data available are for this shape or the square cross-section. For simplicity of design and construction, these shapes have some clear advantages. There does exist demand for other shapes as well, generally arising out of aesthetic considerations. However, with the deficiency of information regarding other shapes, the extent of the possible benefits and costs from a wind loading viewpoint has not been fully assessed.

As a second demonstration of the use of the Pivot Mode Activator System, a more routine study was carried out involving several different cross-sectional shapes. This study contrasts somewhat with the previous study in that the experimental series, while quite extensive, was less detailed and more systematic.

The main purpose of this portion of the overall study is to provide a data base

240

which can assist in the basic design process of tall chimneys or slender buildings. Together with some judicious interpolation, these data should allow the designer to obtain wind load estimates suitable at least to the preliminary design stages.

8.2   Test Models

Eight different cross-sectional shapes were considered. These were chosen to represent the most common shapes used in chimney design as well as slight variations thereof. These are referred to as shapes A - H. They are shown in Figure 8.1. For each of these shapes stiff geometric models were constructed for use on the high frequency sensitive base balance and on the pivot mode activator. There was only one 2:1 rectangle tested, but it has been treated in the presentation as two separate cases differing by a rotation of 90°. These are shapes H and I in Figure 8.1.

Models were constructed at three different aspect ratios, however, not all combinations of shape and aspect ratios have been tested. The three model heights used were 10 in., 15 in. and 20 in. For each cross-section considered, models were designed so that the nominal width, B, was 1.5 inches, hence the three nominal aspect ratios were 6.67, 10.0, and 13.3.

The BB test series was carried out in two phases. In the first phase, one cross-sectional shape of particularly common occurrence, shape C which is a square cross-section with chamfered corners, was tested in four different roughness exposures, representing a range of nominal turbulence intensities from 8 - 13%, and for three
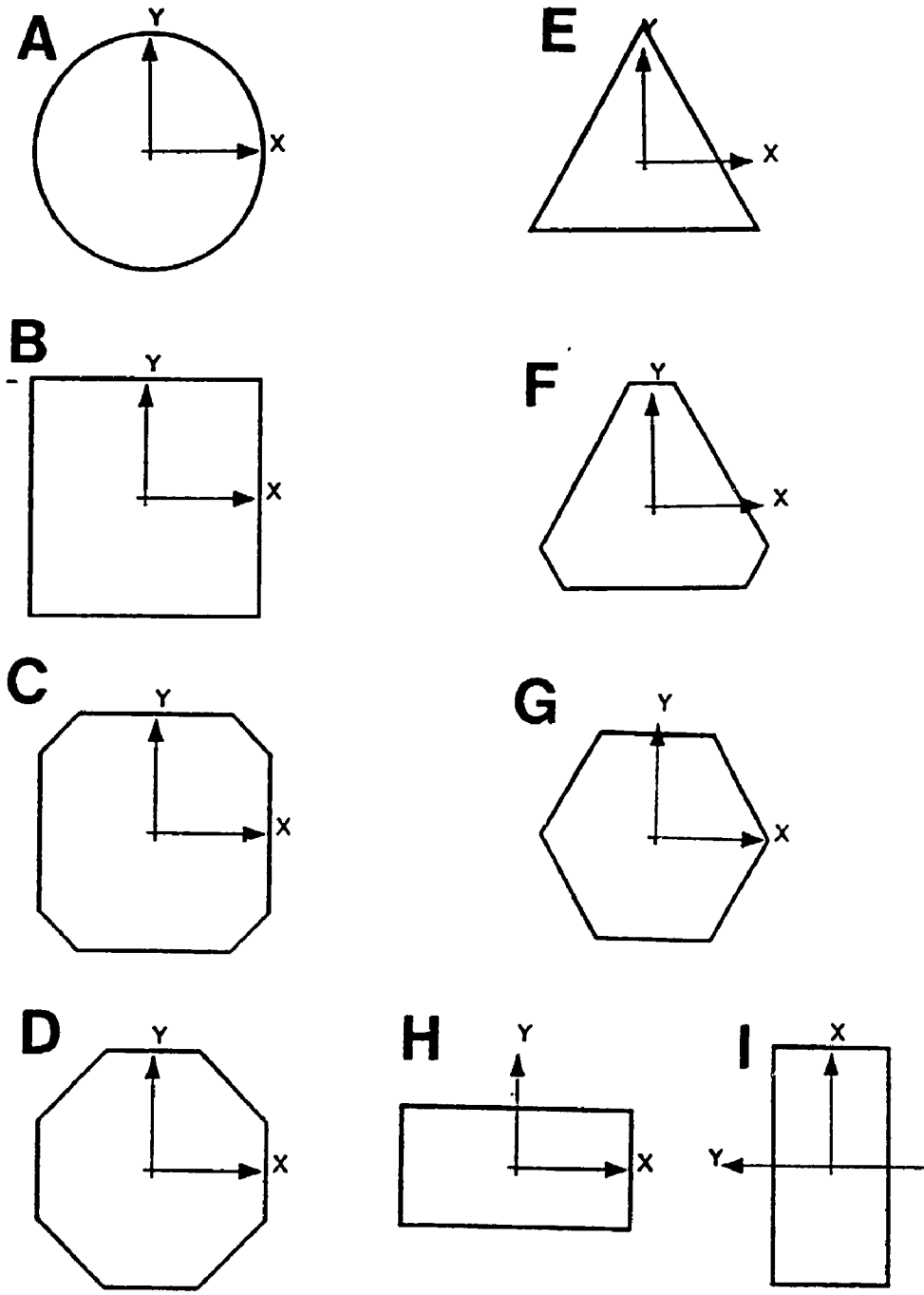
Figure 8.1: Various Cross-Sectional Shapes Tested

different aspect ratios. On the basis of the results from this phase, a test series for the second phase was defined. This comprised testing each of the shapes for the tallest aspect ratio, 13.3, and for one exposure.

8.3 Flow Conditions

All BB tests were carried out in BLWT I; the 24-meter long open circuit wind tunnel of the Boundary Layer Wind Tunnel Laboratory at the University of Western Ontario. The PMA experiments were carried out in BLWT II[23].

Four different turbulent shear flows were used. During the second phase of testing, only one of these exposures, Exposure 2 was used. For practical reasons, the exposure was in actuality a slightly different one than was used in the first phase of testing, however, they are both referred to as Exposure 2, the latter only being distinguished by the fact that it is associated with the second phase of testing. The mean profile and turbulence intensities of each of these exposures is shown in Figure 8.2. For completeness, the profile measured with the second phase, Exposure 2, is also included. Only the lower portion below 25 inches is shown in these plots as this describes the flow up to five inches above the tallest model. The reference wind speed height was approximately 48 inches.

Table 8.1 displays summary information for each of the exposures including the ratio of mean wind speed at reference height to that of model heights. Nominal values of turbulence intensities have been defined for each exposure and these are
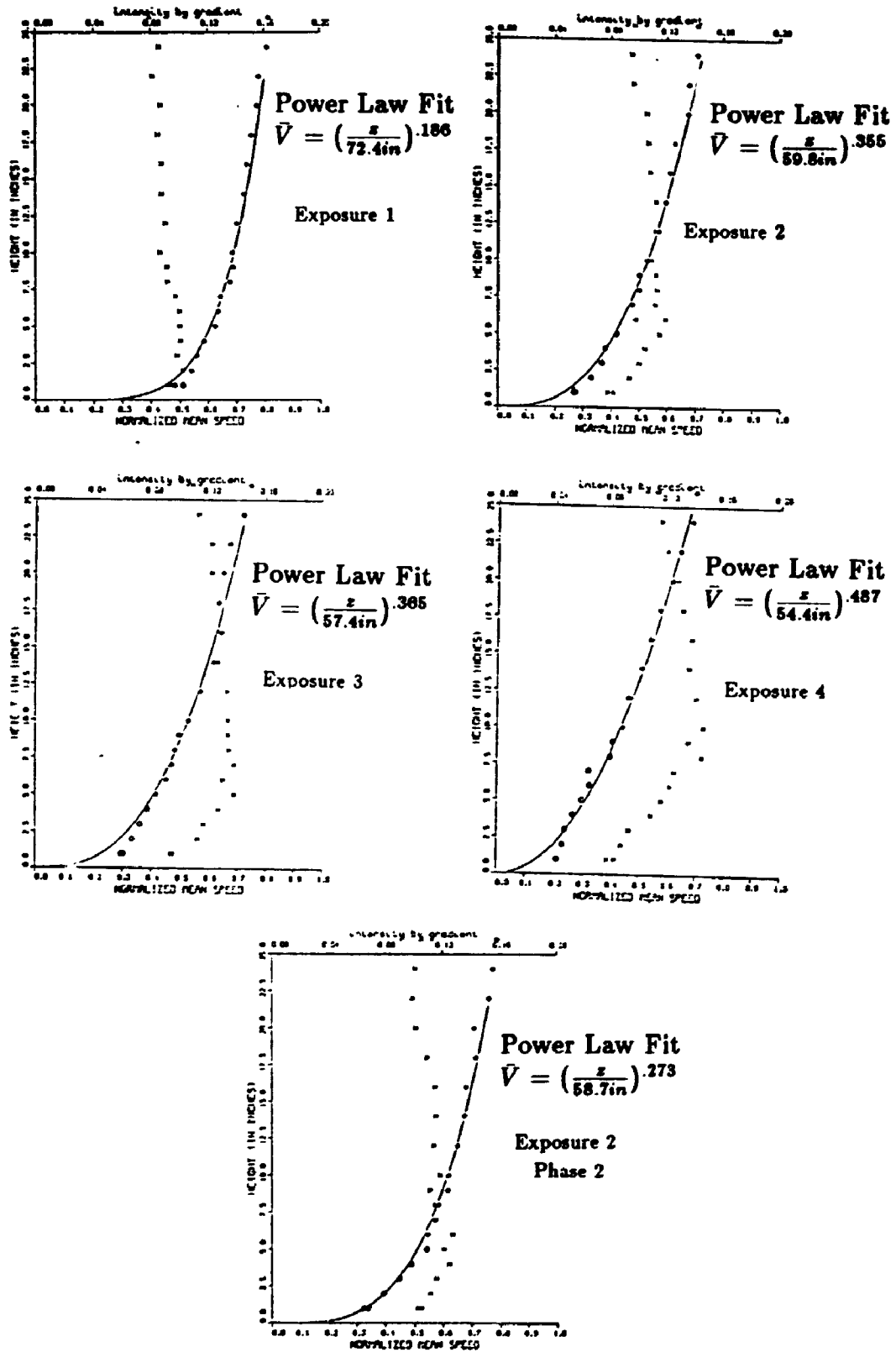
Figure 8.2: Velocity Profiles Used in th Study of Various Shaped Prisms

Table 8.1: Summary of Exposures Used in the Study

Exposure	Intensity (% of Gradient)		Mean Velocity as Percentage of Gradient		
	Range	Nominal	H_1	H_2	H_3
1	7 - 9	8	64.2	68.5	72.2
2	8.5-11.5	10	54.8	62.6	69.9
3	10.5-13.5	12	48.6	58.0	61.1
4	11-14	13	43.8	51.8	61.2

given in the third column of Table 8.1.

Auto-spectral measurements of the longitudinal component of velocity were madι at various heights. These have been included in the separate report[78] but are not necessary here.

8.4   BB Experiments

The models were tested on a high frequency base balance. The natural frequencies of the model-balance systems were determined by impulse excitation and power

spectral measurements were made of the resulting outputs. The fundamental frequency occurred at about 41 Hz in the case of the softest model. Therefore during testing, the outputs were low pass filtered at a cutoff frequency of 38 Hz in order to reduce aliasing effects on FFT spectral estimates. The filter response functions were also recorded for later use in data correction. In some cases the low pass filters were not included and post measurement corrections were made to the data.

The tests were conducted with mean reference velocities of 15, 20,25,30 or 35 fps depending on the particular exposure and model height. In all cases, test speeds were chosen to maximise both signal strength and dimensionless frequency range. Measurements of the mean and the rms base moments about two orthogonal axes were made as well as power spectral estimates. For each case considered, several wind directions were tested which, after symmetry was taken into account, provided data for the full azimuth.

In the first phase of testing, cross-sectional Shape C was tested in all four exposures, and all three available aspect ratios. In the second phase of testing, all cross-sectional shapes were tested but only for the highest aspect ratio, 13.3:1, and only for Exposure 2 which represents approximately an open country terrain. Table 8.2 summarises all test parameters in both phases indicating amongst other things the wind directions tested in each particular case.

Table 8.2: Summary of Test Cases Considered in the Study

Shape	Aspect Ratio			Exposures				Wind Angles
	6.67	10	13.3	1	2	3	4	
C	√	√	√	√	√	√	√	0°, 2°, 5°, 10, 15, 30, 45
A			√		√			0
B			√		√			-2, 0, 2, 5, 10, 15, 30, 45
C			√		√			-2, 0, 2, 5, 10, 15, 30, 45
D			√		√			-2, 0, 2, 5, 10, 15, 30, 45
E			√		√			-30, -20, -10, -5, -2, 0 2, 5, 10, 20, 30
F			√		√			-30, -20, -10, -5, -2, 0 2, 5, 10, 20, 30
G			√		√			-30, -20, -10, -5, -2, 0 2, 5, 10, 20, 30
H			√		√			-2, 0, 2, 5, 10, 20, 30 60, 70, 80, 85, 88, 90, 92

8.5   BB Results for Various Shapes

8.5.1   Moment Coefficients

The moment coefficients are expressed in the dimensionless form:

$$C_M = \frac{M}{\frac{1}{2}\rho_a V^2 B H^2} \tag{8.1}$$

The mean or time averaged values of lift and drag coefficient for Shape C are shown plotted against wind angle in Appendix F as derived from the first phase of the study. Also shown there are similar plots for each shape including again Shape C, as derived from the second phase of the study for Exposure 2 and aspect ratio of 13.3:1. Shape A is not included here as it is axially symmetric. The mean moment coefficient in its case was .353 for the drag direction and of course 0.0 for the lift direction.

8.5.2   Moment Spectra

The spectra as measured were corrected for the 38 Hz cutoff filter response function and for the dynamic amplification of the balance-model systems. In the latter case, both fundamental sway frequencies were corrected for. Attempts were then made to fit the spectra according to a theoretical model. The model will now be described in more detail.

Spectral Fitting Procedure

The theoretical model is defined as:

$$\frac{fS(f)}{\sigma^2} = \overbrace{\frac{C_1 C_2 f_r}{[1 + (C_2 f_r)^{C_3}]^{\frac{5}{3C_5}}}}^{Background} \cdot \overbrace{\frac{1}{[1 + (C_4 f_r)^{C_5}]}}^{Admittance} + \overbrace{\frac{A}{b\sqrt{\pi}}\left(\frac{f_r}{f_s}\right) exp\left[-\left(\frac{1 - \frac{f_r}{f_s}}{b}\right)^2\right]}^{Shedding\ Peak} \quad (8.2)$$

where

$$f_r = \frac{fB}{V_H} \quad (8.3)$$

As indicated the three components of the model correspond to a background wind spectrum (C_1, C_2, C_3), a modifying aerodynamic admittance function (C_4, C_5), and a narrow band peak which corresponds to the vortex shedding peak (f_s, b, A). The last three parameters correspond to the vortex shedding frequency or Strouhal number, S, the width of the shedding peak and the area of the peak respectively. A fitting program was written which made use of Marquardt's method for nonlinear parameter estimation which is described in detail elsewhere[62]. This was a lengthy program involving a systematic analysis of the data to fit, first, the separate components of the model and then, ultimately, the composite version. Although, the fitting was not successful for all of the spectra, excellent fits were obtained for the vast majority. For the remaining ones, hand calculated estimates completed the data set. Due to the large amount of data, all of the spectra are not included here. They have been compiled in a separate report entitled "Design Data for Tall Chimneys of Various Cross-Sectional Shape", BLWTL-SS18-89[78] which is available from the Boundary Layer Wind Tunnel Laboratory. This report includes all of the measured spectra along with the theoretical model fits. Only the most important spectra for design purposes are included here as described in the next section.

8.5.3 Worst Cases for Various Shapes

The data set accumulated from this portion of the study comprises a formidable amount of data. Attention is therefore focused on the worst cases which are anticipated to govern design situations. Figures 8.3 to 8.10 show spectra for the worst direction for each shape as determined from the second phase of testing. These figures include mean coefficient information as well as the best fit theoretical model parameters obtained from the fitting program previously referred to. There are three fitted curves shown, although they cannot be each distinguished in all plots. These correspond to different components of Equation 8.2; the dashed line shows the fitted "background", the thin solid line shows the product of fitted "background" and "admittance", and the thick solid line shows the complete fit including the fitted "shedding peak".

This information is further summarised for easy reference in Table 8.3. This table was originally published in [86], and includes information on two additional shapes which were tested in previous studies.

8.6 PMA Results for Various Shapes

The Pivot Mode Activator System was used to supply some information regarding the motion-induced forces for each of the various shapes. Tests were carried out for a single RMS oscillation amplitude of approximately $\tilde{Y} = 3\%$ for all shapes
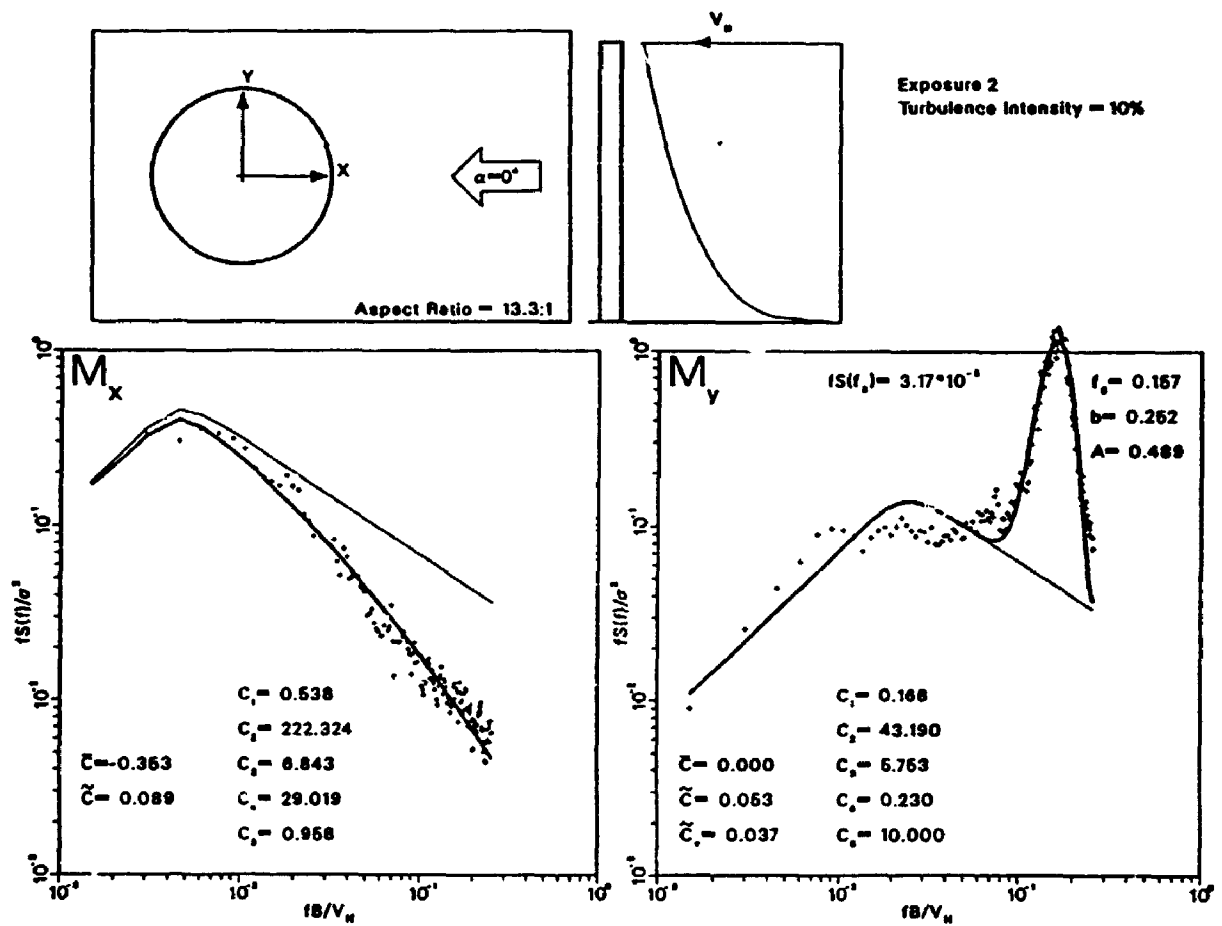
Figure 8.3: Moment Spectra for the Worst Wind Direction for Shape A
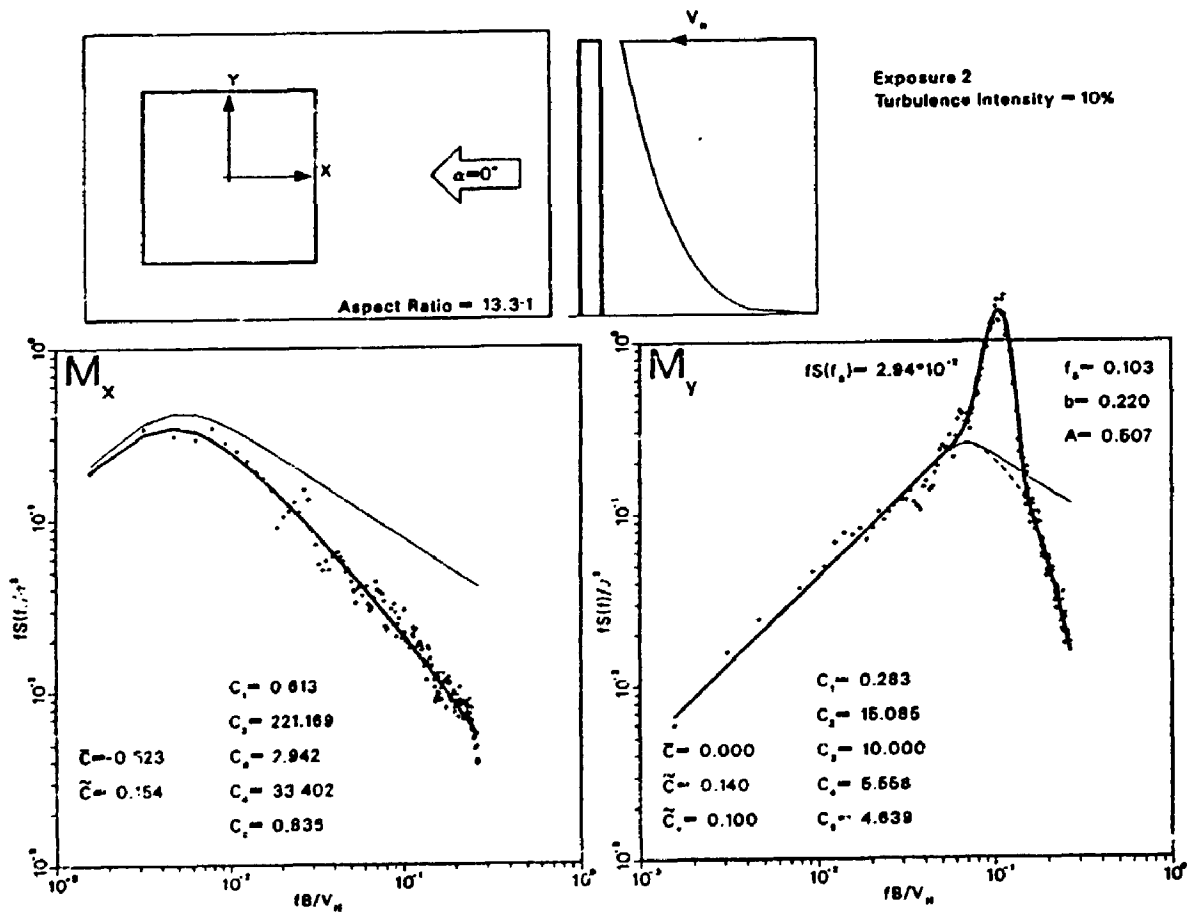
Figure 8.4: Moment Spectra for the Worst Wind Direction for Shape B
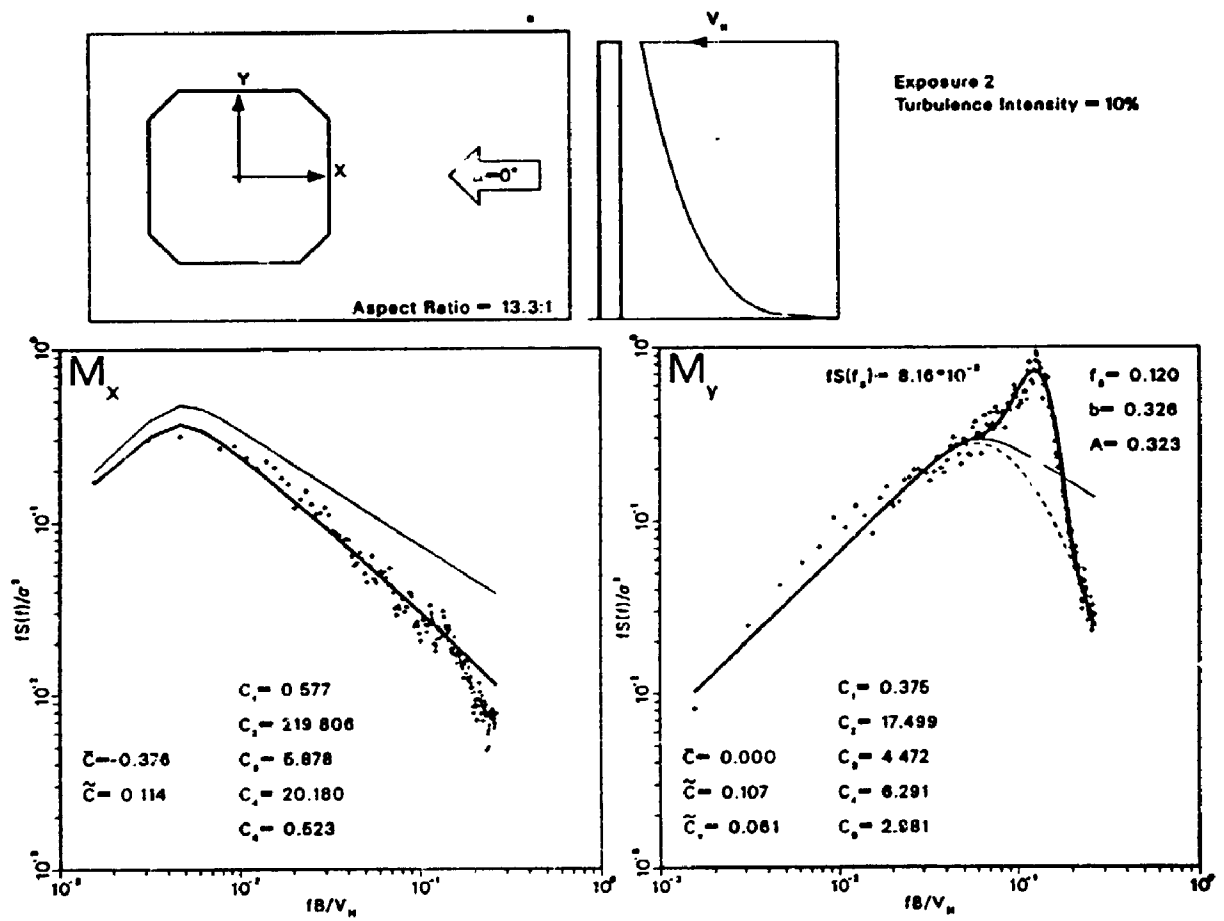
Figure 8.5: Moment Spectra for the Worst Wind Direction for Shape C
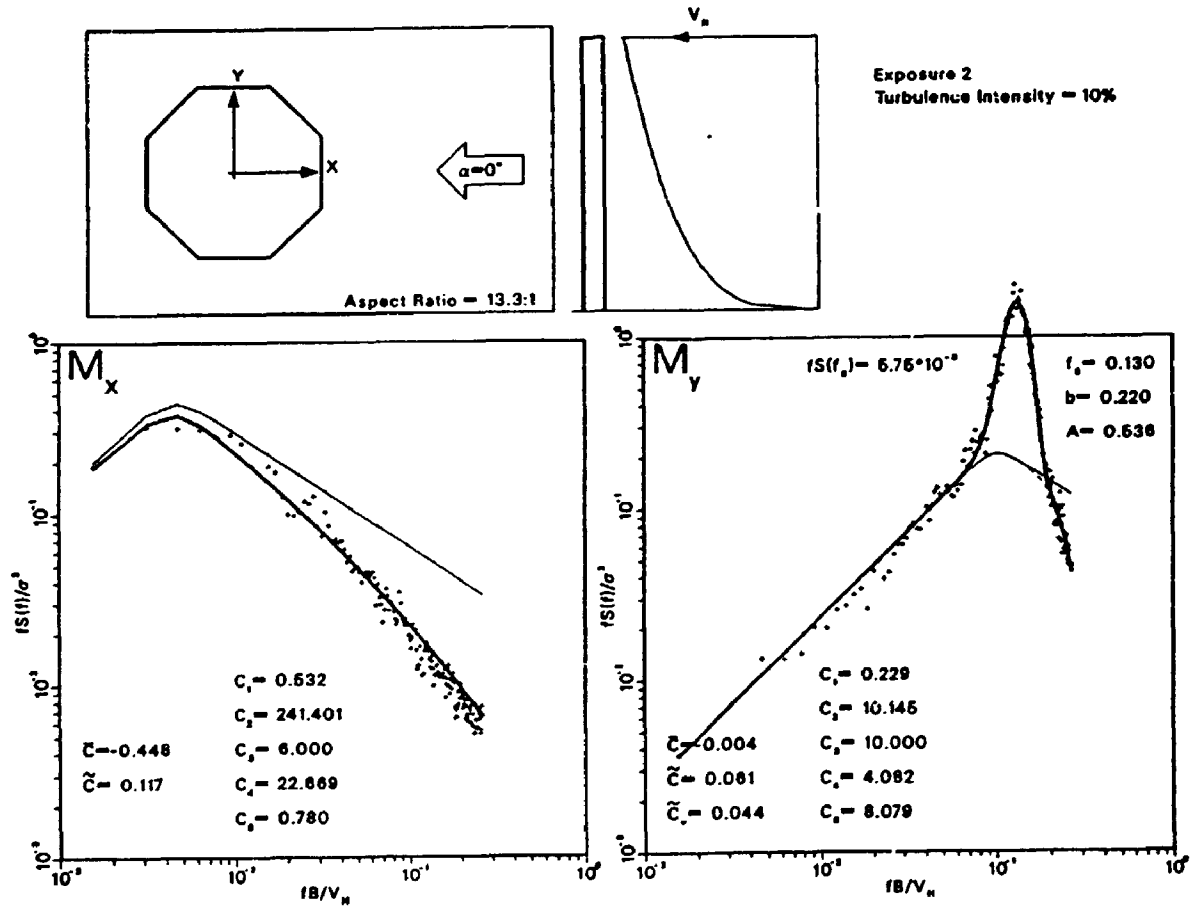
Figure 8.6: Moment Spectra for the Worst Wind Direction for Shape D
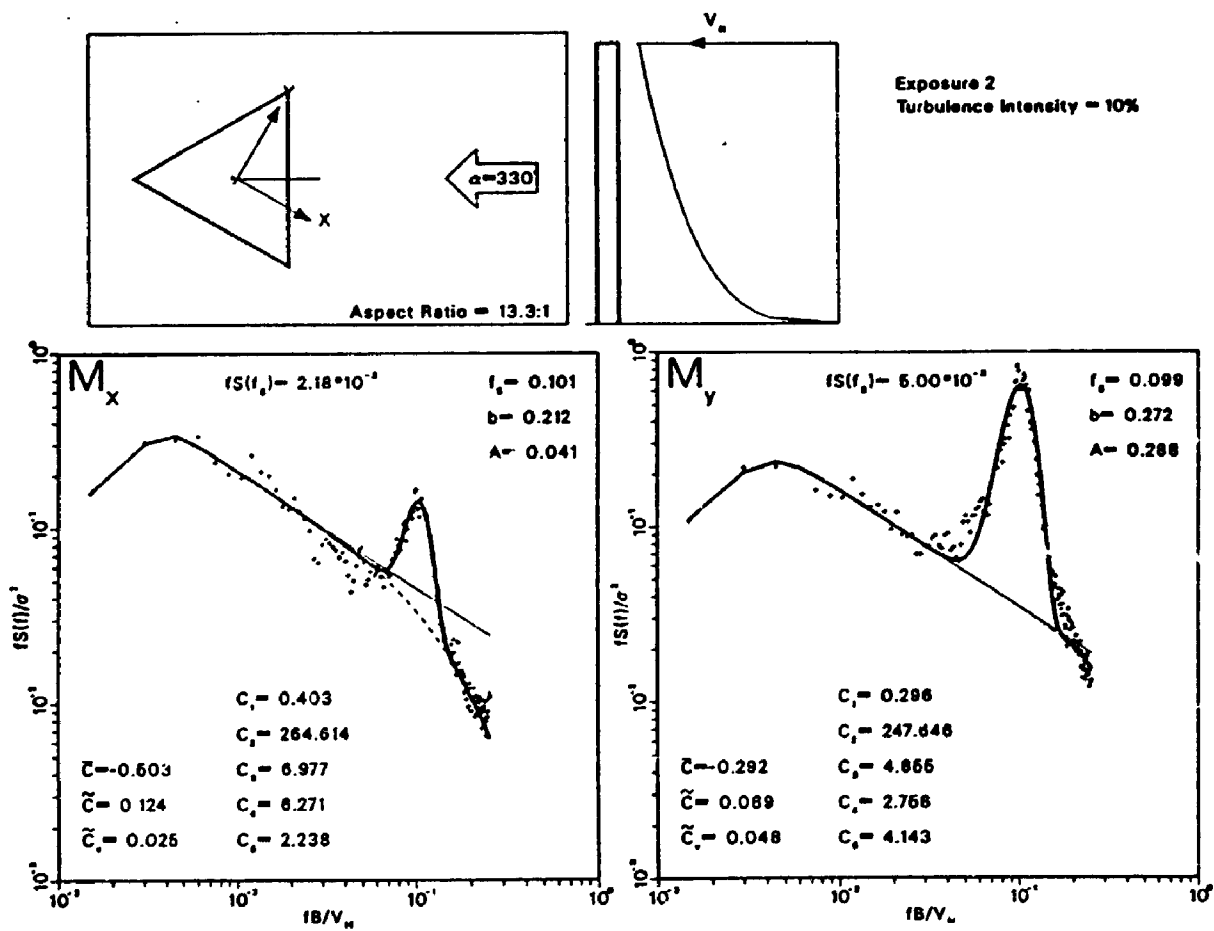
Figure 8.7: Moment Spectra for the Worst Wind Direction for Shape E
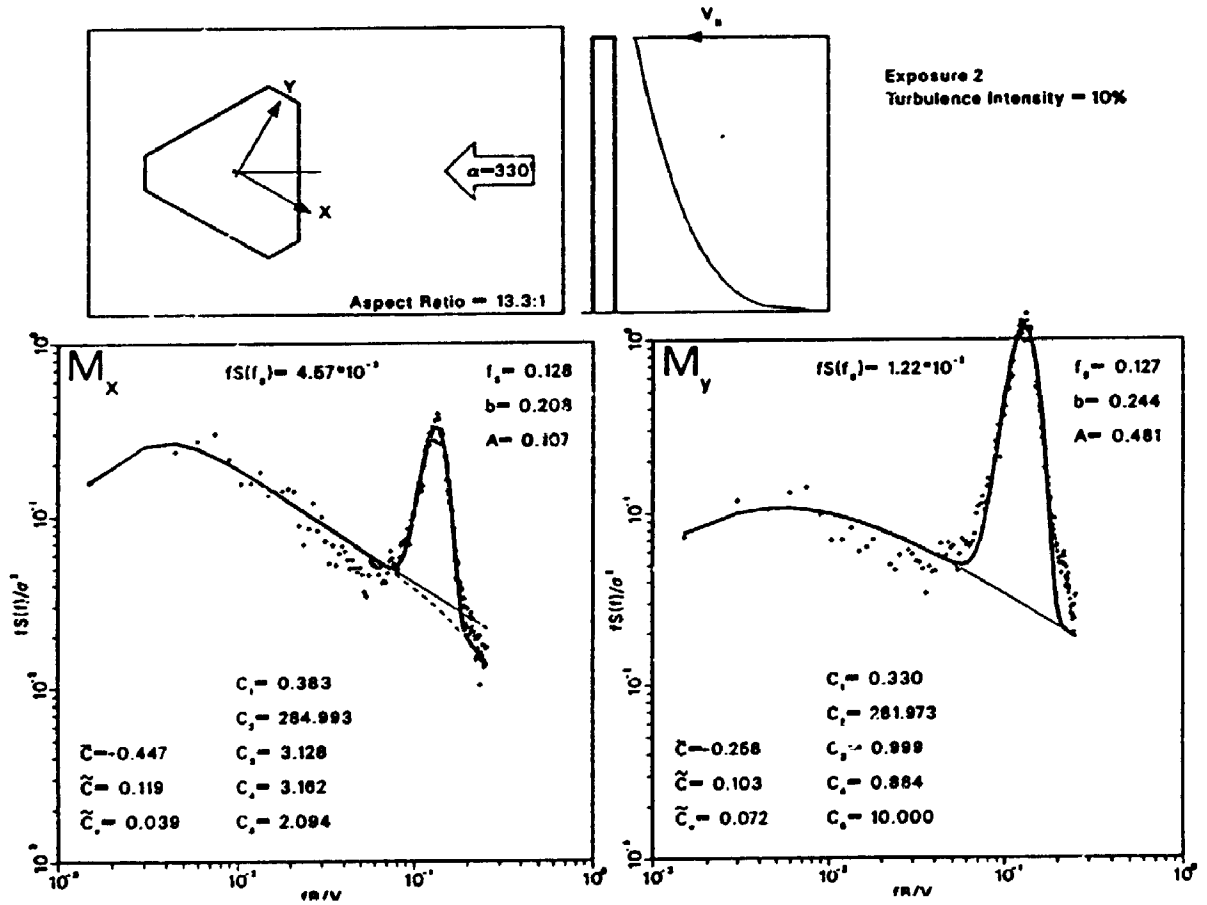
Figure 8.8: Moment Spectra for the Worst Wind Direction for Shape F
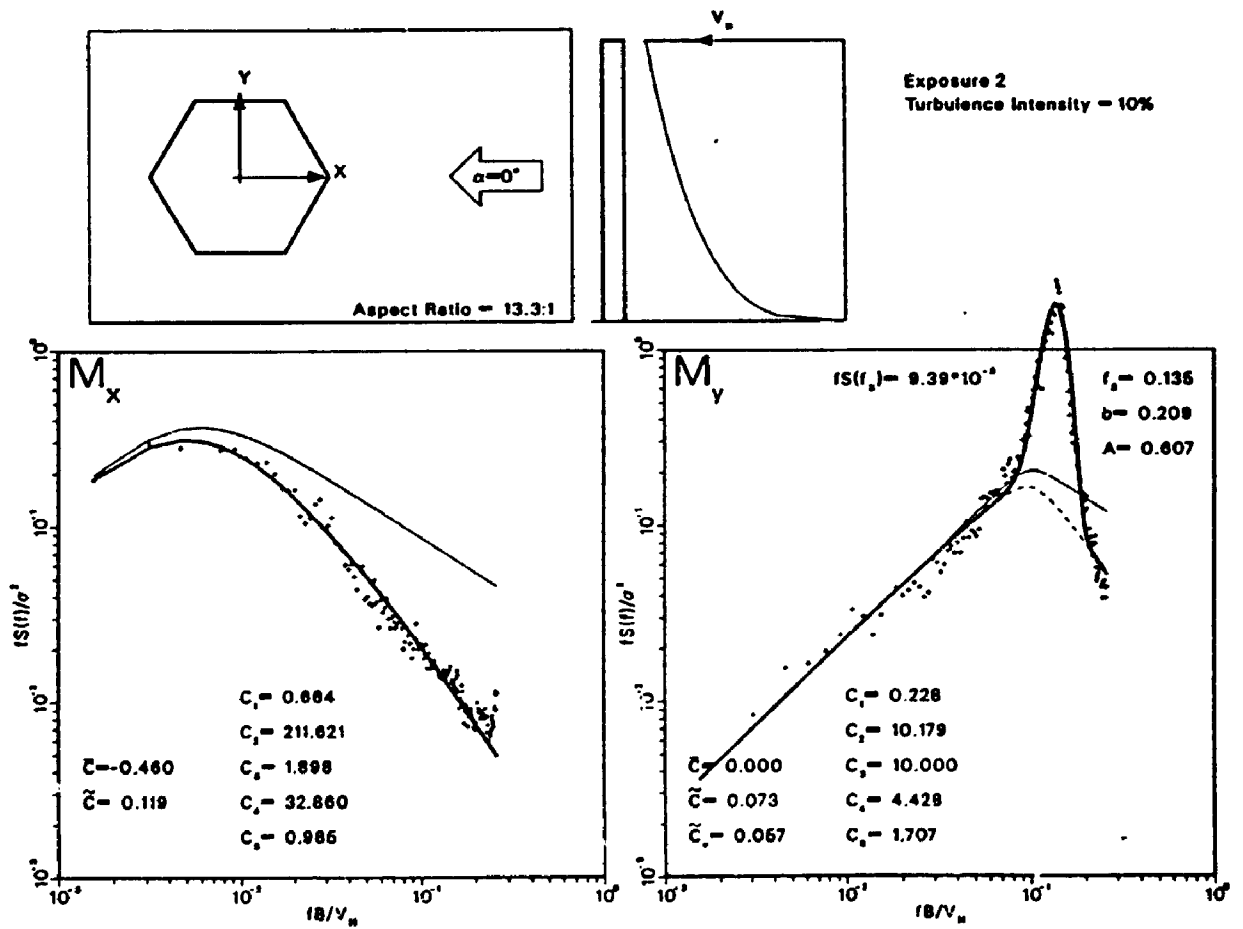
Figure 8.9: Moment Spectra for the Worst Wind Direction for Shape G
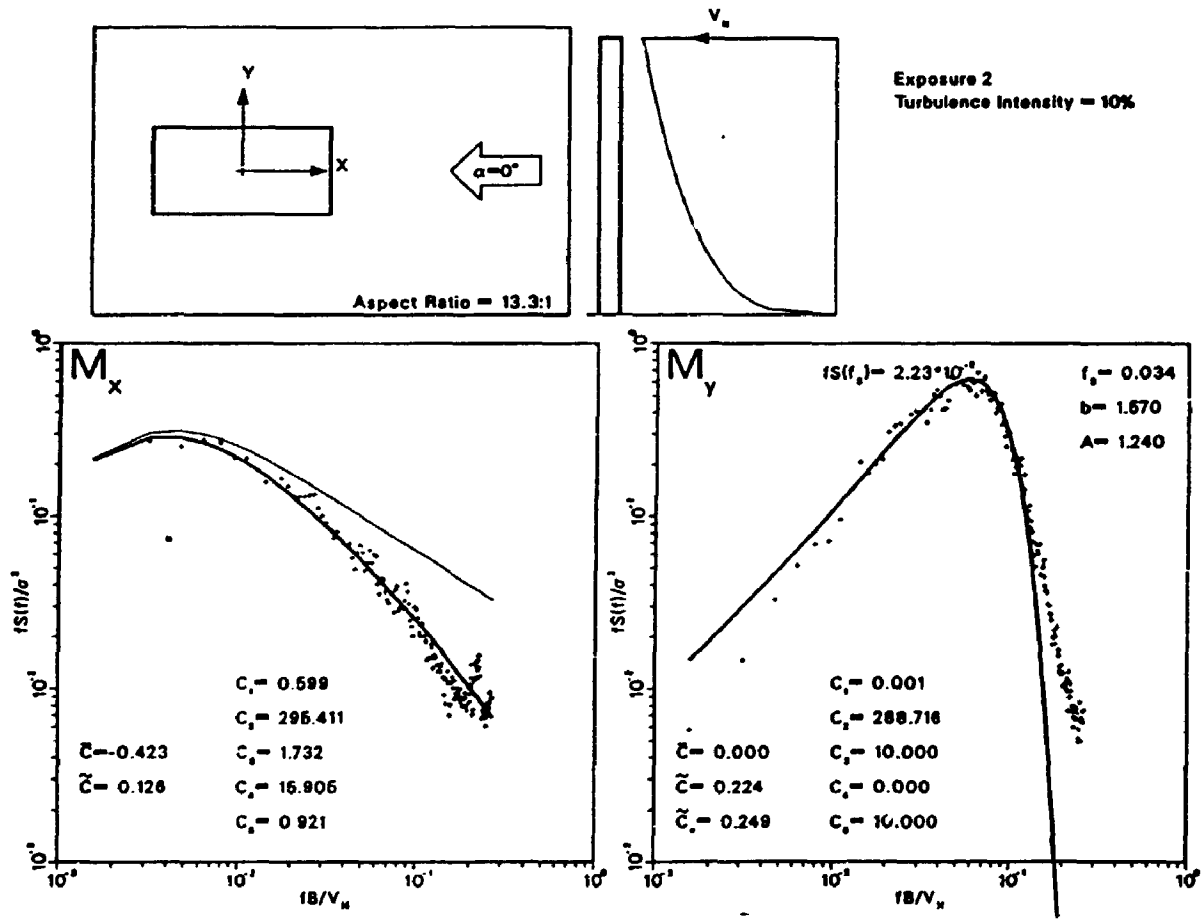
Figure 8.10: Moment Spectra for the Worst Wind Direction for Shape H
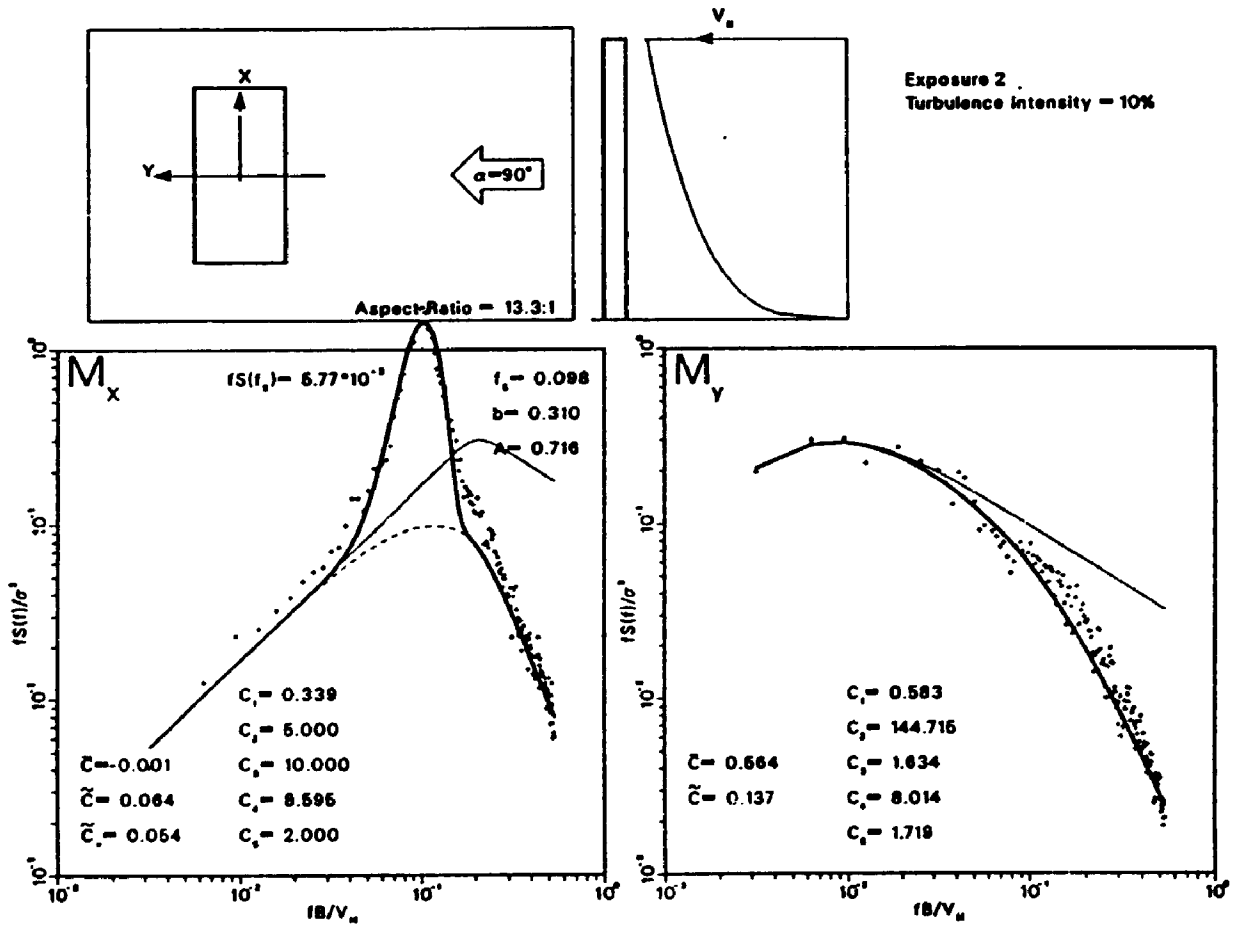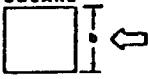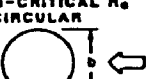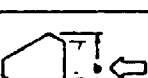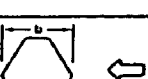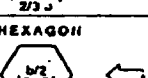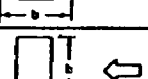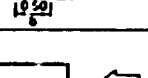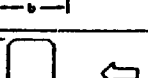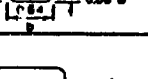
Figure 8.11: Moment Spectra for the Worst Wind Direction for Shape I

Table 8.3: Aerodynamic Characteristics of Various Shapes[86]

Shape and Critical Wind Direction	Drag Properties	Lift Properties
SQUARE	$\bar{C}_{MD}$ = 0.52 σC_{MD} = 0.154 R_{OS} = 0.021	$\bar{C}_{ML}$ = 0 σC_{ML} = 0.140 θ = 0.22 S = 0.103 a_f = 0.51
(square with cut corners)	$\bar{C}_{MD}$ = 0.38 σC_{MD} = 0.114 R_{OS} = 0.029	$\bar{C}_{ML}$ = 0 σC_{ML} = 0.107 θ = 0.33 S = 0.120 a_f = 0.54
OCTAGON	$\bar{C}_{MD}$ = 0.45 σC_{MD} = 0.117 R_{OS} = 0.018	$\bar{C}_{ML}$ = 0 σC_{ML} = 0.061 θ = 0.22 S = 0.130 a_f = 0.32
SUB-CRITICAL R_e CIRCULAR	$\bar{C}_{MD}$ = 0.35 σC_{MD} = 0.089 R_{OS} = 0.01	$\bar{C}_{ML}$ = 0 σC_{ML} = 0.053 θ = 0.25 S = 0.157 a_f = 0.49
EQUI. TRIANGLE	$\bar{C}_{MD}$ = 0.58 σC_{MD} = 0.143 R_{OS} = 0.022	$\bar{C}_{ML}$ = 0 σC_{ML} = 0.12 θ = 0.26 S = 0.100 a_f = 0.56
(pentagon shape)	$\bar{C}_{MD}$ = 0.52 σC_{MD} = 0.137 R_{OS} = 0.032	$\bar{C}_{ML}$ = 0 σC_{ML} = 0.086 θ = 0.24 S = 0.127 a_f = 0.90
(hexagon shape 2/3 b)	$\bar{C}_{MD}$ = 0.54 σC_{MD} = 0.133 R_{OS} = 0.025	$\bar{C}_{ML}$ = -0.16 σC_{ML} = 0.090 θ = 0.25 S = 0.140 a_f = 0.94
HEXAGON	$\bar{C}_{MD}$ = 0.46 σC_{MD} = 0.119 R_{OS} = 0.013	$\bar{C}_{ML}$ = 0 σC_{ML} = 0.073 θ = 0.21 S = 0.135 a_f = 0.61
(vertical rectangle)	$\bar{C}_{MD}$ = 0.56 σC_{MD} = 0.137 R_{OS} = 0.056	$\bar{C}_{ML}$ = 0 σC_{ML} = 0.064 θ = 0.31 S = 0.098 a_f = 0.72
(horizontal rectangle)	$\bar{C}_{MD}$ = 0.21 σC_{MD} = 0.063 R_{OS} = 0.008	$\bar{C}_{ML}$ = 0 σC_{ML} = 0.112 θ = 1.57 S = 0.068 a_f = 1.0
(rectangle with fillet)	$\bar{C}_{MD}$ = 0.52 σC_{MD} = 0.130 R_{OS} = 0.025	$\bar{C}_{ML}$ = 0 σC_{ML} = 0.080 θ = 0.31 S = 0.124 a_f = 0.85
(rounded rectangle)	$\bar{C}_{MD}$ = 0.23 σC_{MD} = 0.064 R_{OS} = 0.06	$\bar{C}_{ML}$ = 0 σC_{ML} = 0.102 θ = 1.6 S = 0.054 a_f = 1.0

except Shape I for which the amplitude was about half this value. This resulted from keeping the actual tip displacement the same and normalising by the larger width dimension.

The standard roughness exposure used for the extensive study of the square prism was used for the present tests. The profile is shown in Figure 7.1 and was described in Chapter 7.

For each shape, PMA tests were carried out for lift action corresponding to the worst case wind angles previously identified. The aerodynamic impedance functions are shown in Figures 8.12 to 8.20. In each case the critical reduced velocity suggested by the Strouhal frequencies shown in Table 8.3 and obtained from the fitting program is indicated by a vertical dotted line.

All of the shapes considered exhibit ranges of velocity over which the aerodynamic damping is negative. Although there are some uncertainties associated with the Strouhal values shown, due to the broadness of some of the spectral peaks from which they were derived, and the slightly different flow conditions between the BB and PMA tests, nevertheless, it appears that there is not a clear cut relation between the ranges of negative aerodynamic damping and the Strouhal velocities inferred from moment spectra measured on a stationary model. In some cases, for example shapes E or I, the damping parameter has become negative at velocities significantly below the Strouhal velocity shown.

One final comment regarding Strouhal velocities is worth making. Previous
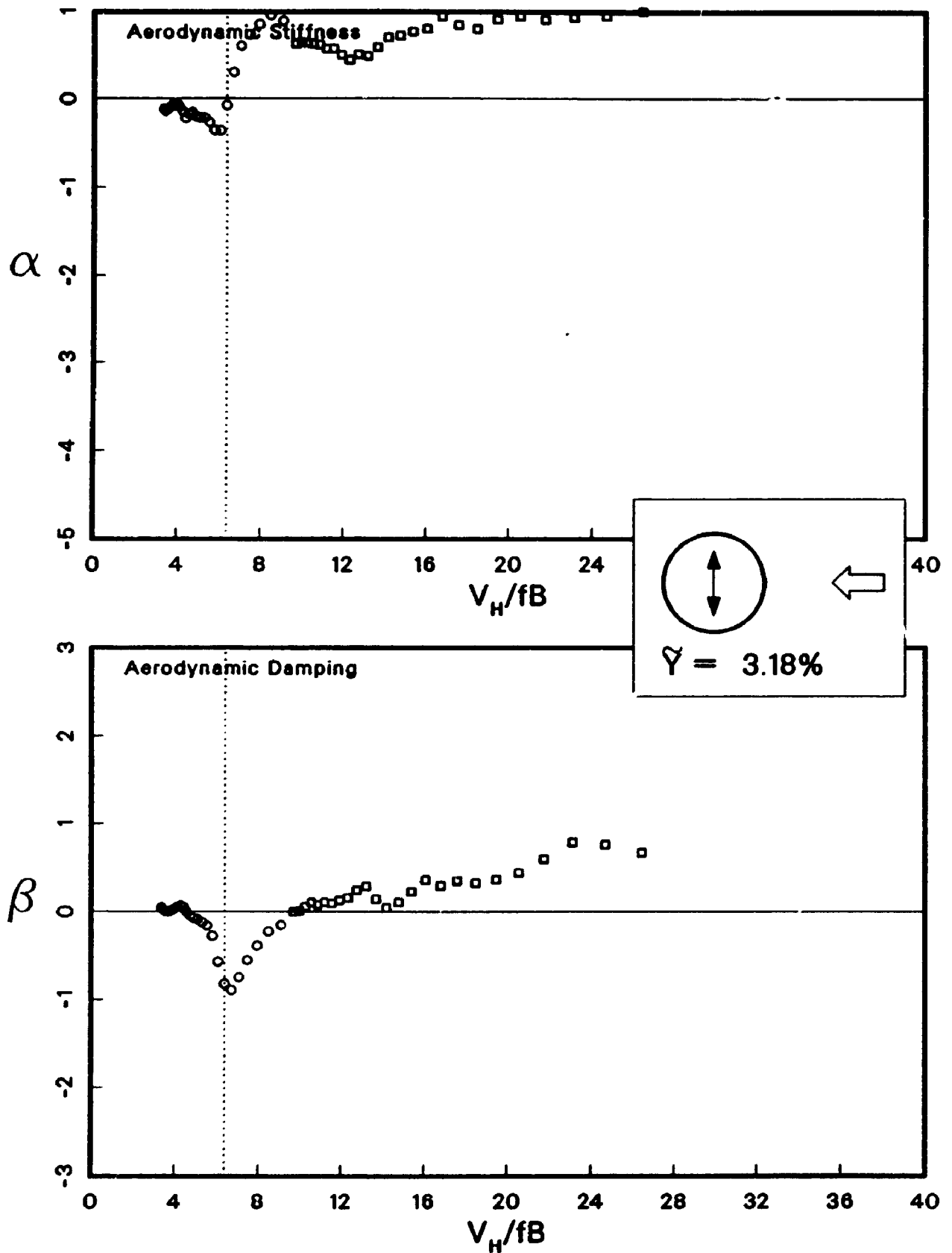
Figure 8.12: Aerodynamic Impedance for Worst Wind Direction For Shape A
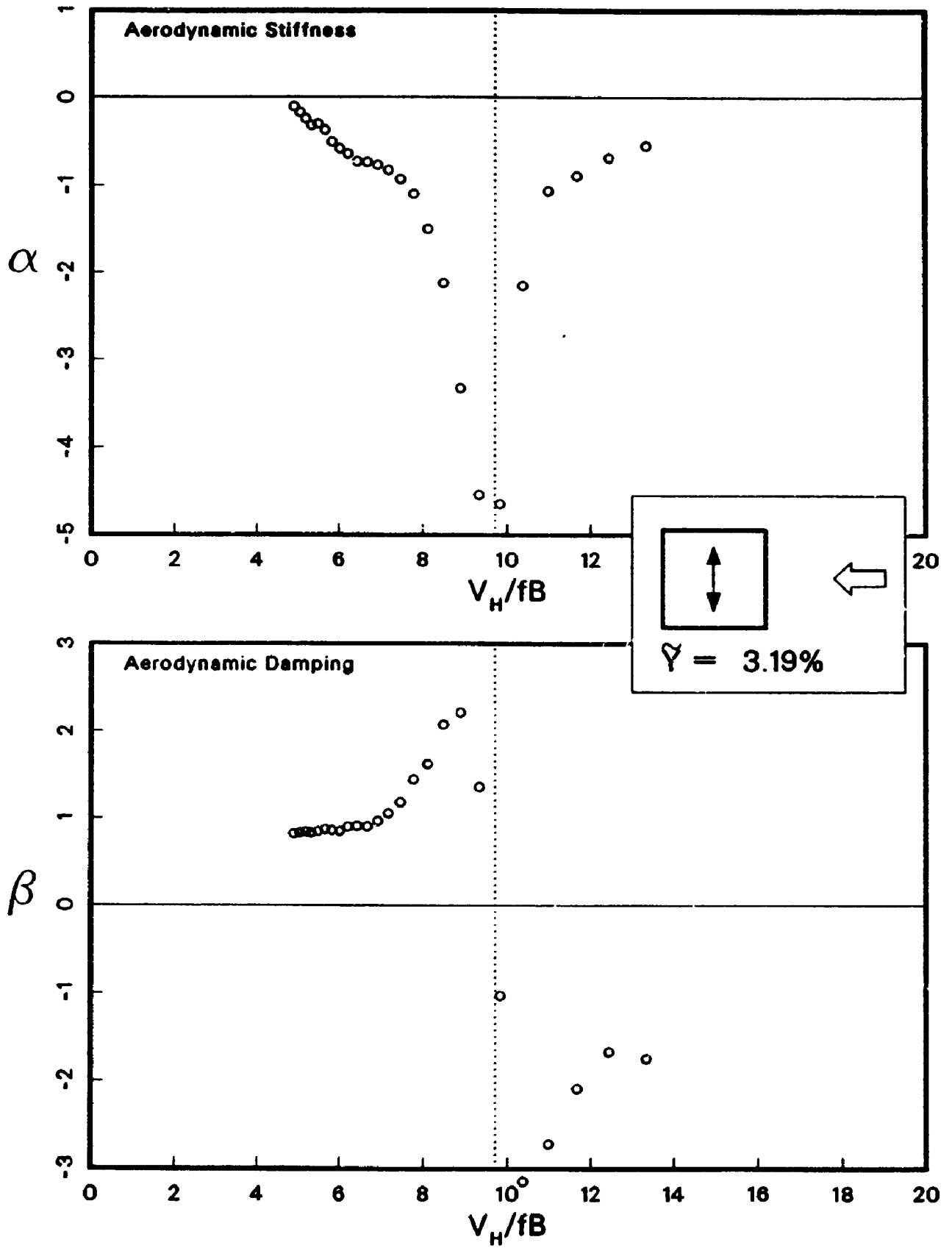
Figure 8.13: Aerodynamic Impedance for Worst Wind Direction For Shape B
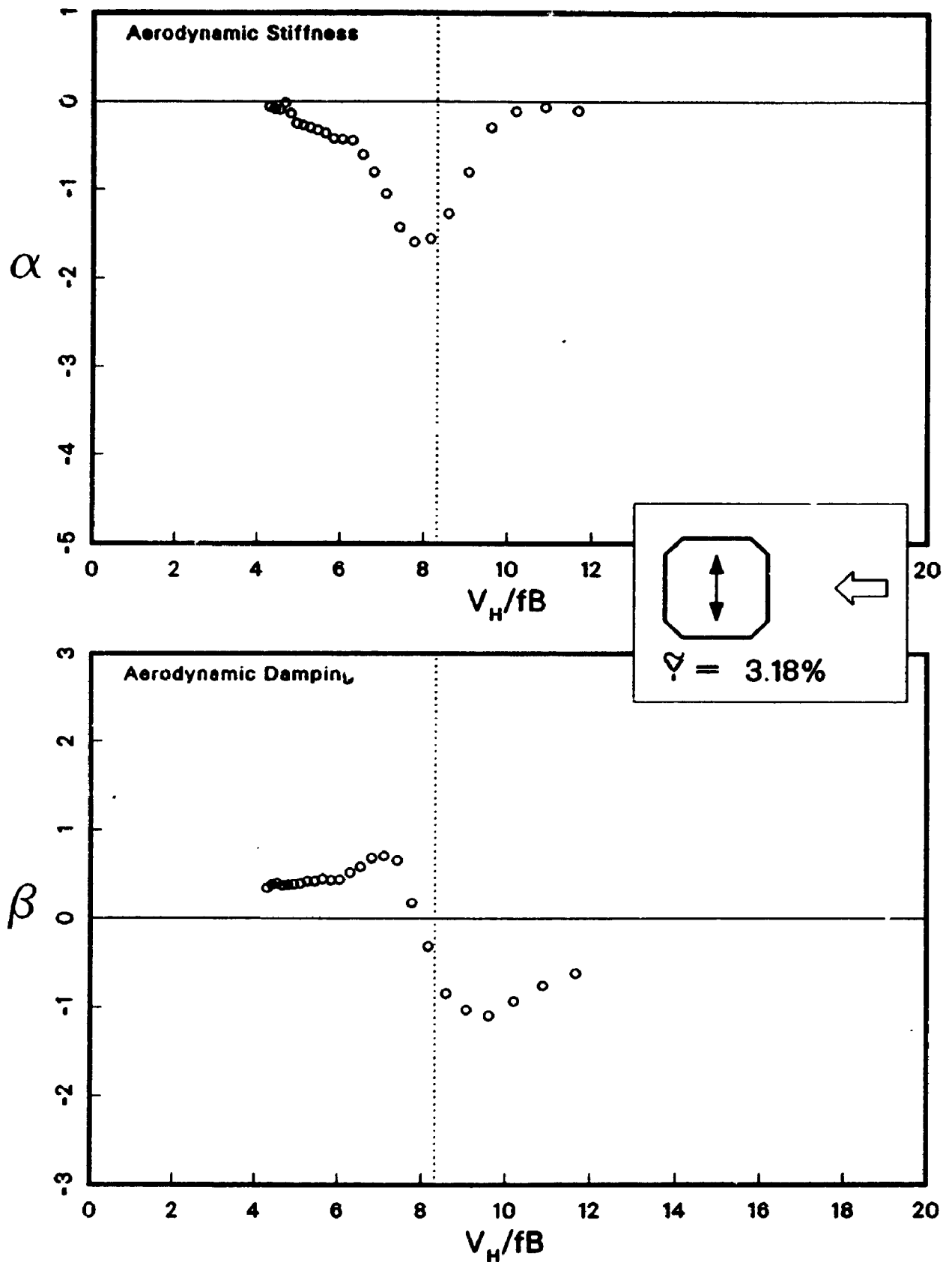
Figure 8.14: Aerodynamic Impedance for Worst Wind Direction For Shape C
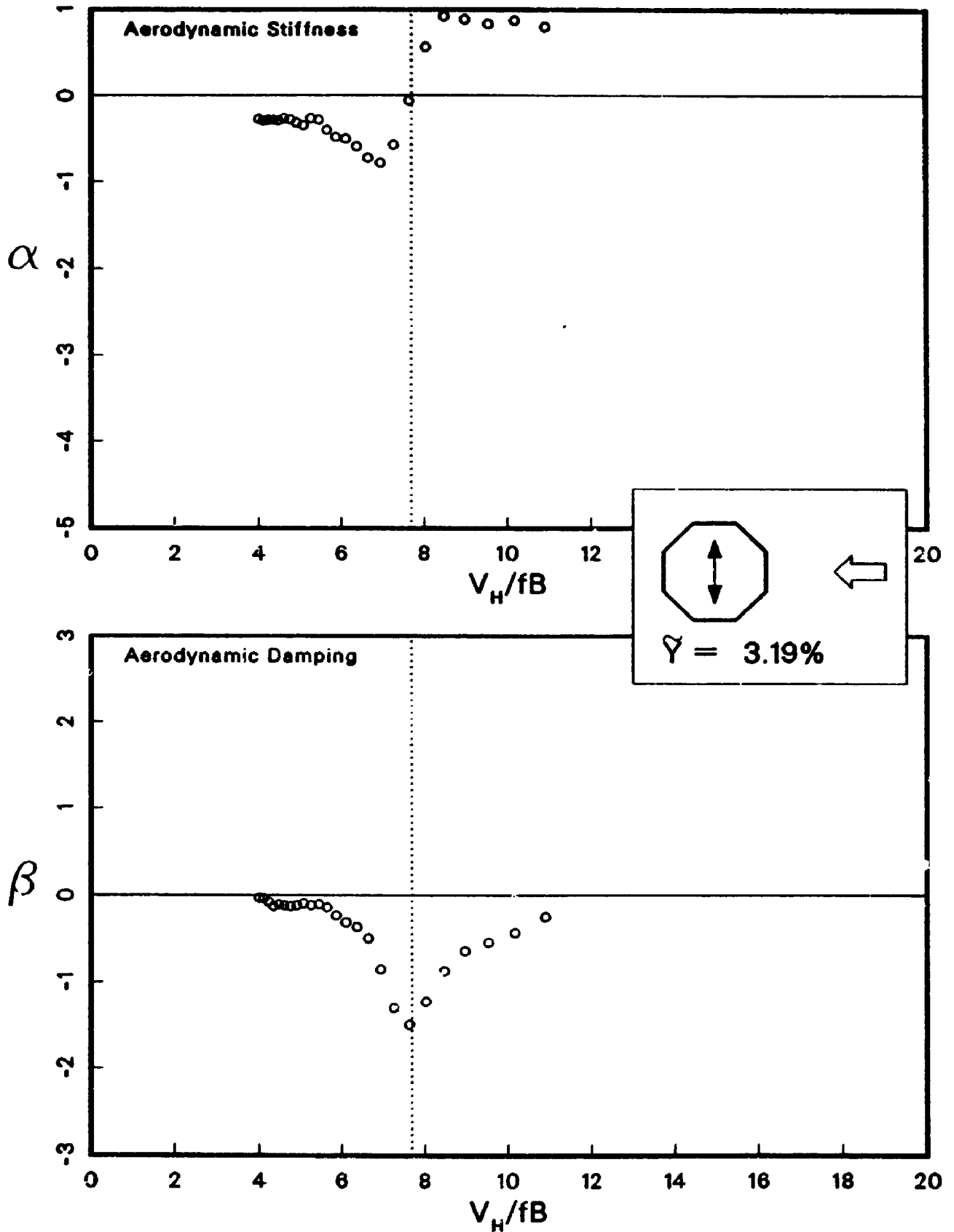
Figure 8.15: Aerodynamic Impedance for Worst Wind Direction For Shape D
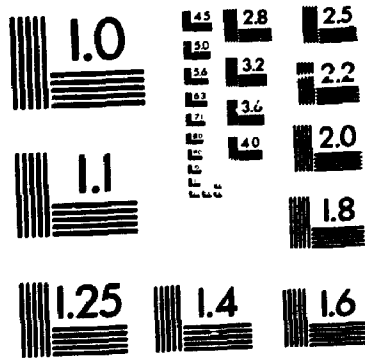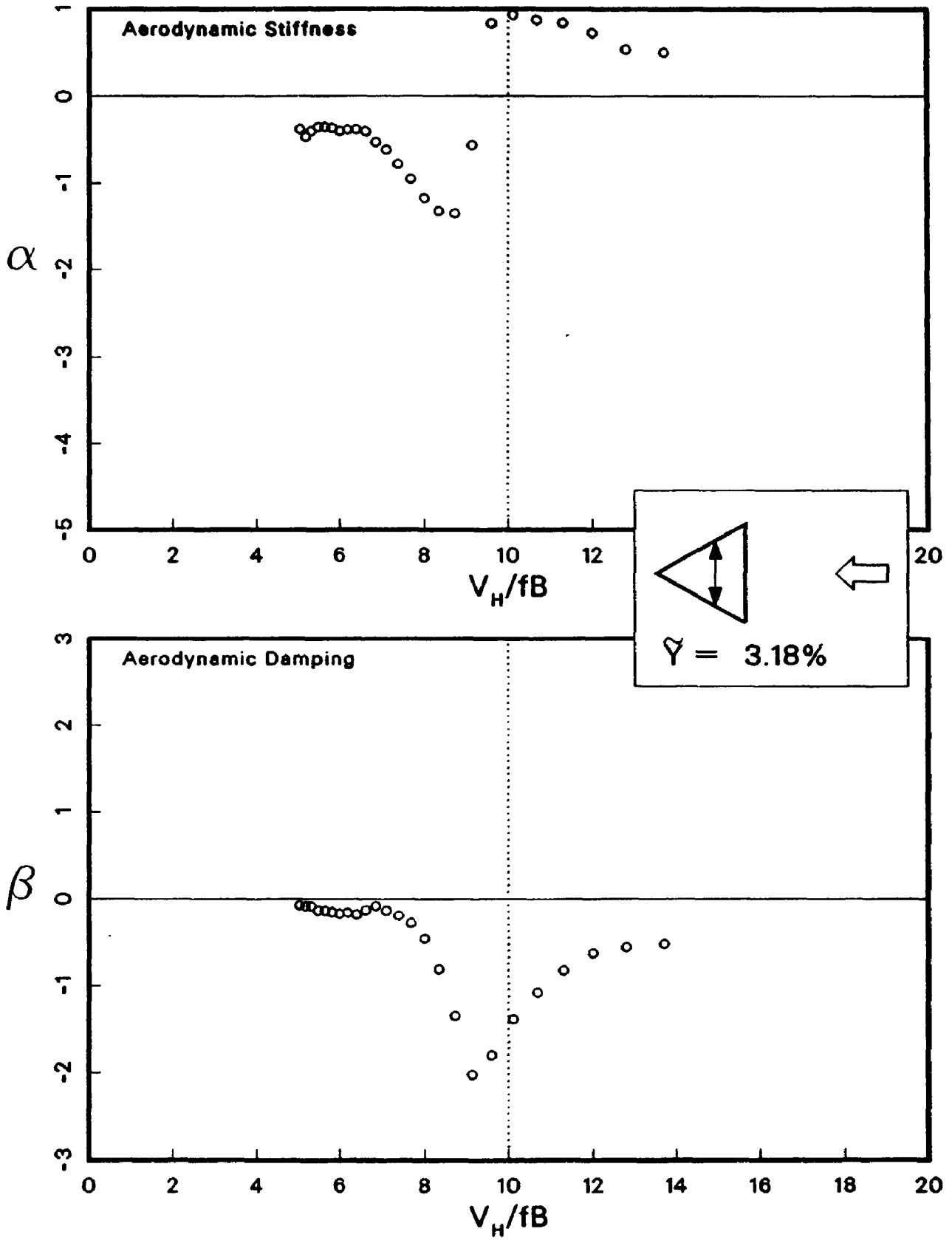
Figure 8.16: Aerodynamic Impedance for Worst Wind Direction For Shape E
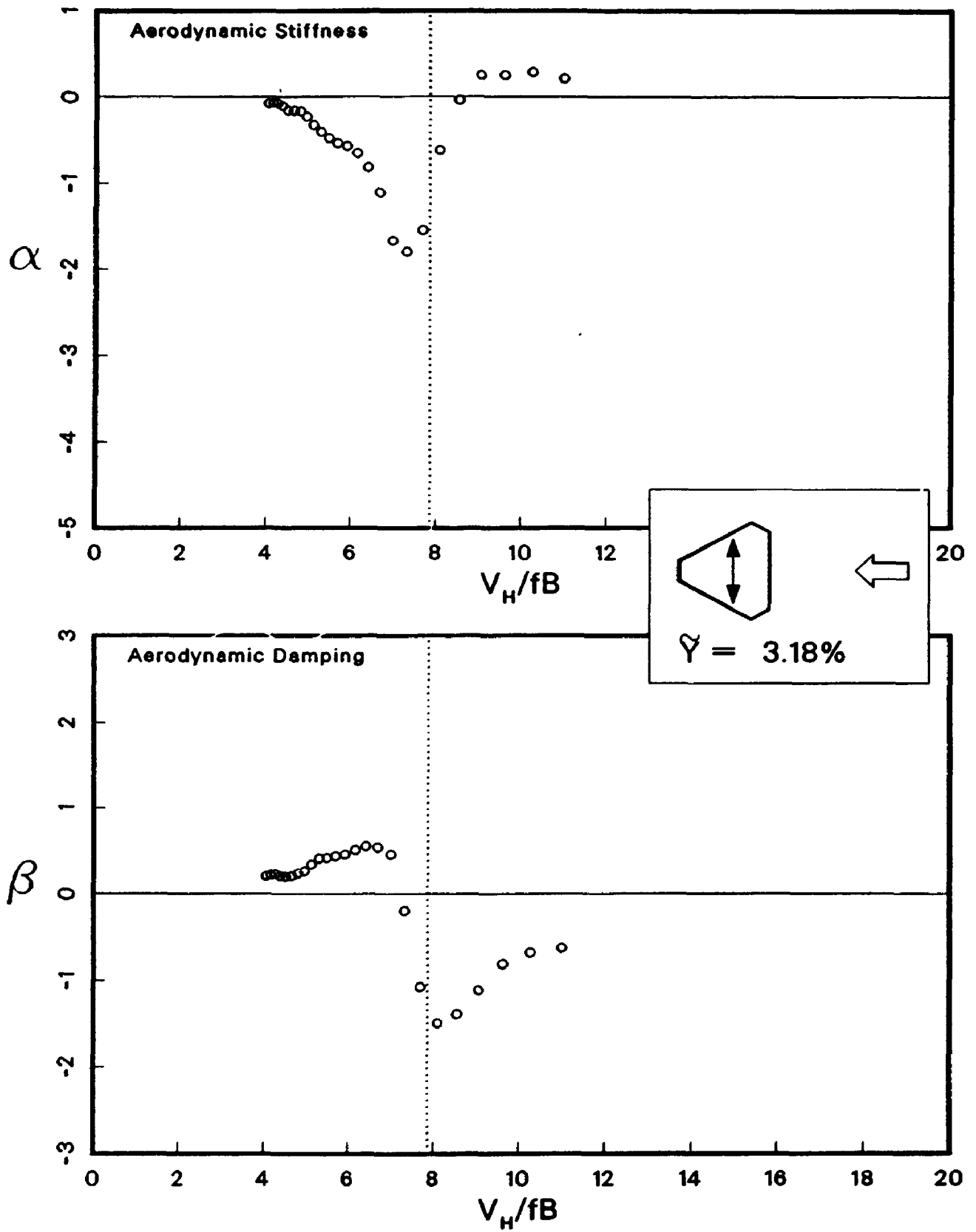
Figure 8.17: Aerodynamic Impedance for Worst Wind Direction For Shape F
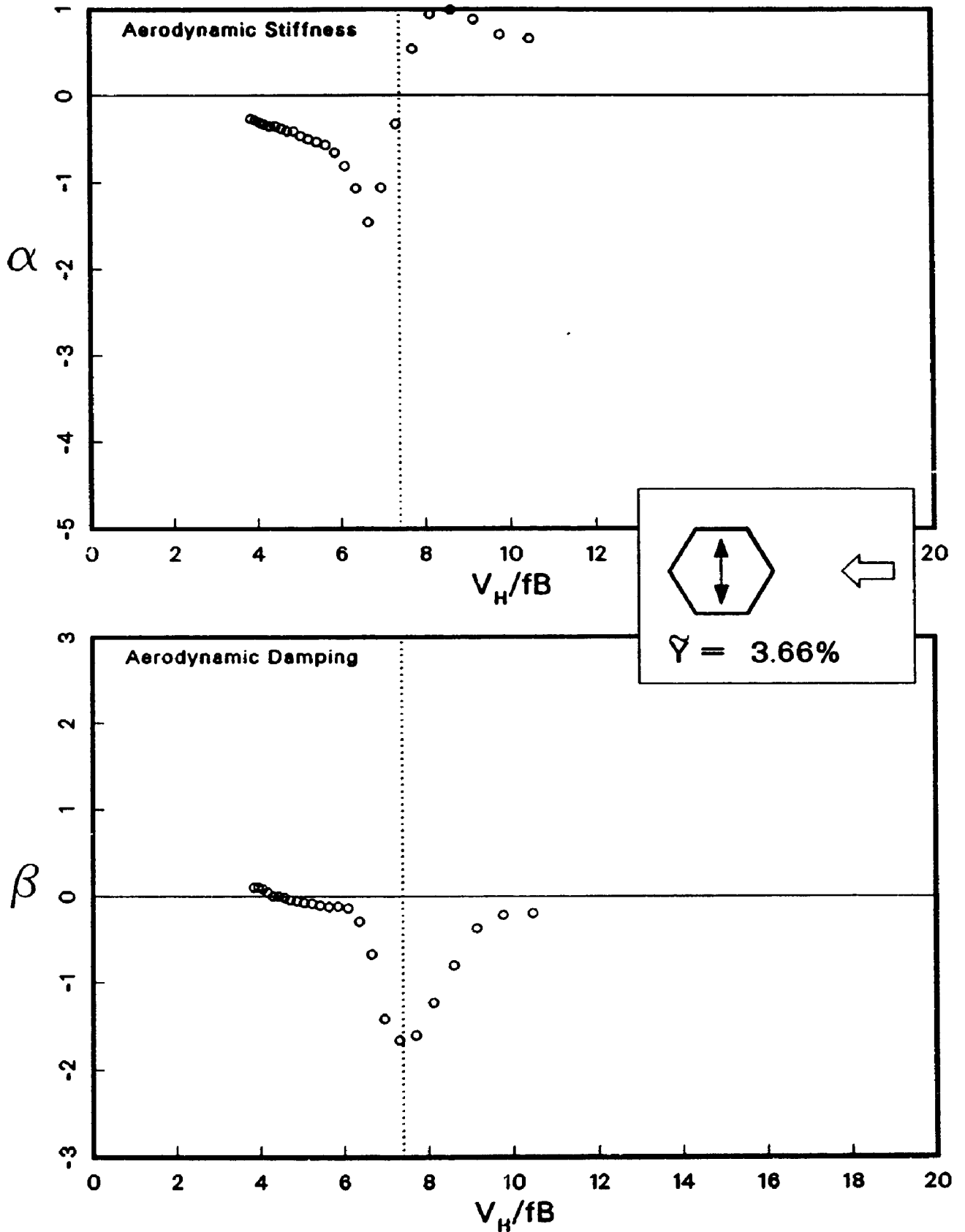
Figure 8.18: Aerodynamic Impedance for Worst Wind Direction For Shape G
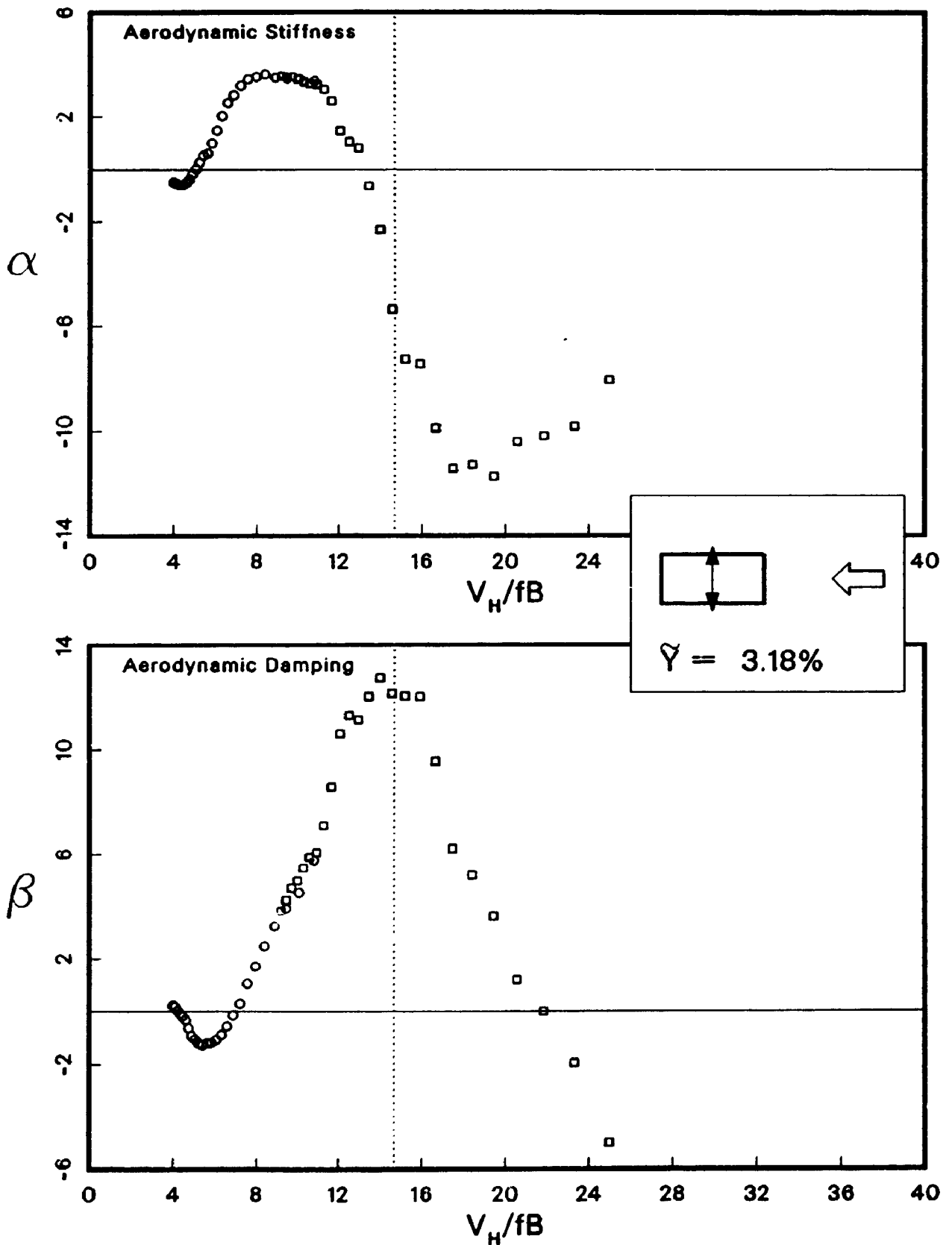
Figure 8.19: Aerodynamic Impedance for Worst Wind Direction For Shape H
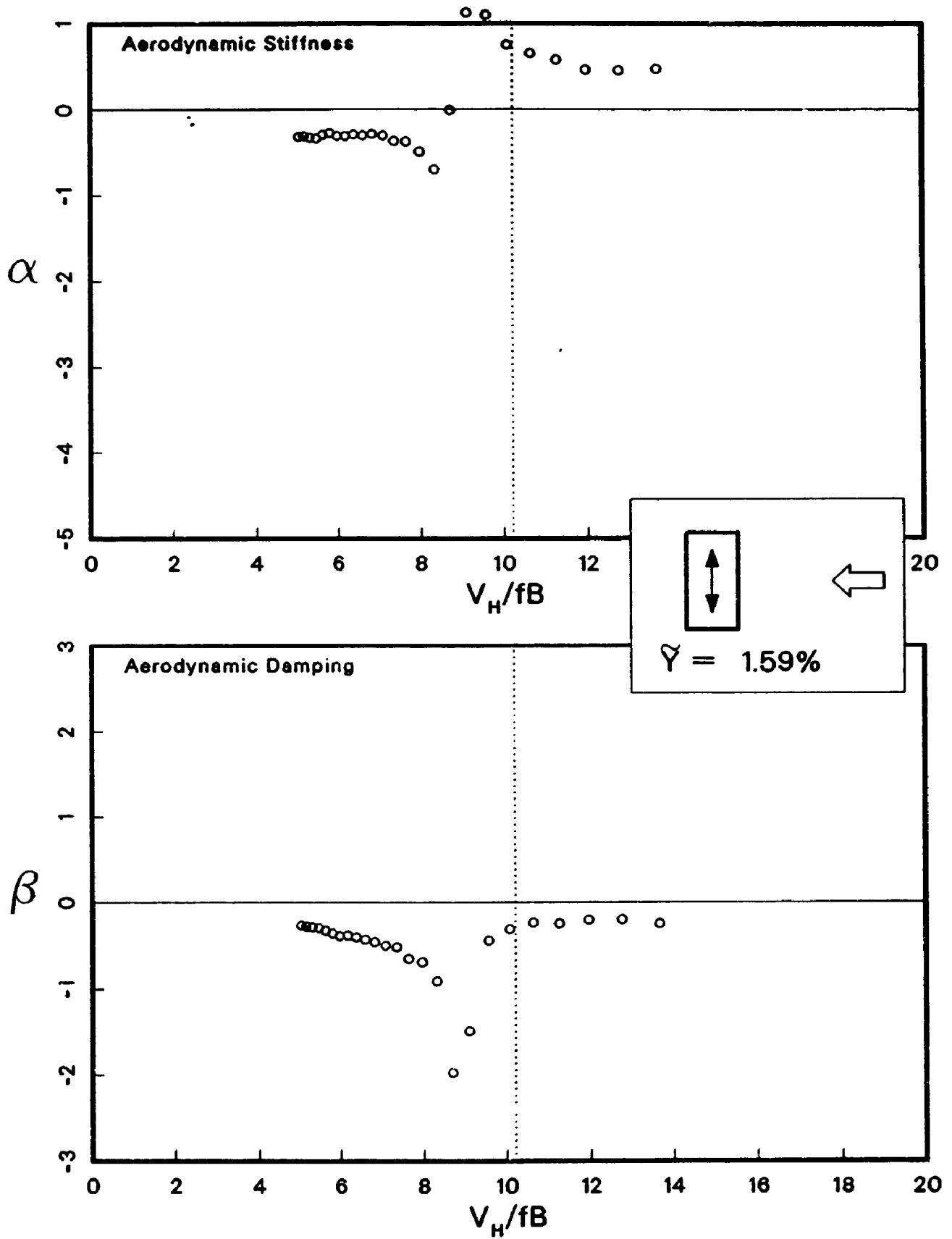
Figure 8.20: Aerodynamic Impedance for Worst Wind Direction For Shape I

researchers[55] have noted the existence of multiple Strouhal numbers for certain rectangular cross-sections. Again, the data are not matched well enough for direct comparisons, however, with these previous findings in mind, cursory examination of the data indicate that there may be a more direct relation between the Strouhal numbers obtained from direct measures of the action in the wake of the body and the *phasing* of the aerodynamic impedance rather than with the aerodynamic damping or stiffness considered separately. This is an area for future research.

Part IV

CONSPECTUS

Chapter 9

Conclusions and Recommendations

The initial aim of this study was the development of a routine method of measuring motion-induced forces acting on wind tunnel models of tall structures vibrating in a pivoting mode about their base. The impetus for this was the desire to refine the established base balance technique which is simply unable to account for these forces.

The Pivot Mode Activator System which has been developed for this purpose has surpassed the initial expectations and it is hoped that it will provide a means for expediting fundamental research into motion-induced force models as well as contributing to practical wind tunnel studies.

As a demonstration of the use of the system, two extensive experimental studies have been carried out. The first described in Chapter 7 was a comprehensive study of the square prism and included both forced oscillation and free oscillation aeroelastic experiments. The forced oscillation experiments involved the application of the designed system for measuring motion-induced forces acting on the whole structure and also the use of a pressure tap model to investigate the distribution

of the wind-induced loads in both the spatial and the frequency domains. The effects on motion-induced forces caused by variations in flow velocity, oscillation amplitude, turbulent shear flow conditions, and aspect ratio were all investigated. These experiments provide a comprehensive set of data obtained under matched conditions with which theoretical models may be compared. The ability to use the results of these data to provide predictions of response under prototype free oscillation situations was also demonstrated.

The second study involved the investigation of various shaped prisms representing potential cross-sections of tall chimneys. Base balance experiments were performed on these prisms for various turbulent exposures, aspect ratios and wind directions. In each case the worst wind directions from a design point of view were identified. The Pivot Mode Activator was then used to provide information on the character of the motion-induced forces which would be present in those situations.

Each study produced a substantial amount of valuable experimental data. The data from the study of the square prism, in particular that from the pressure model experiments, have not been used nearly to their full potential in the current study. The data for the various shaped prisms comprise a significant data set which can be of great practical use to designers. It is for these reasons that, while that data from each study pertinent to the goals and conclusions of the current work have been presented within this thesis, the data sets in their entirety have not. They are instead included in two separate reports which are available from the Boundary Layer Wind Tunnel Laboratory. The first is entitled "Forced Oscillation Experiments on a Pressure Model of A Square Prism", BLWT-SS17-89. The second is entitled "Design Data for Tall Chimneys of Various Cross-Sectional Shape",

BLWT-SS18-89.

9.1 Recommendations for Future Versions of the PMA System

While the current model of the pivot mode activator has proven to be quite adequate, there are a few improvements which might be incorporated should a second one be constructed. Briefly, the following recommendations are in order:

- The use of elastic flex-pivots should be reconsidered, particularly for the passive pivot locations. It appears that the use of these devices introduced vibration modes near the operating range of the system which has contributed to some of the non-ideal dynamics.

- The axis orientation of the model mounting plate can be currently adjusted from-below. It would be more convenient if this could be carried out from above.

- Analog filtering may be included in the PMA Signal Processor. This would reduce the need for additional equipment in the setup.

- A significant improvement in the current system would be made if an adequate turntable locking device could be designed to remove the lateral sway mode.

More significant alterations in the design of the system might include

- The design of a multiple load cell system which does not make use of load links or passive pivots at all, but transmits all loads from the mounted model through the piezo-electric cells. The overturning moment would then have to be extracted from the combination of signals. This would produce a significantly more rigid system.

- The redesign of the activator device to provide controlled pivoting motion in two orthogonal directions.

- The design of a signal processor which makes use of integrators to provide signals which are more direct measures of the aerodynamic impedance.

9.2 Main Findings of the Experimental Studies

A number of findings regarding the nature of the forces acting on a moving structure have been made as a result of the experimental portion of this work. Some of these were expected, based on previous research on square prisms. These are:

- Below the critical velocity associated with vortex shedding, the aerodynamic damping on a square prism is positive. There is a rapid change around the shedding velocity and the damping becomes negative for higher velocities.

- Both the real and the imaginary parts of the aerodynamic impedance, that is the aerodynamic stiffness and the aerodynamic damping, vary with the amplitude of the motion.

In addition, there are several findings which were anticipated and confirmed by the current work.

- The aerodynamic stiffness at velocities associated with vortex shedding, is negative and this produces a small change in the natural frequency of vibration of the structure. This is indicated by the forced vibration experiments and confirmed by the free oscillation experiments.

- Increased turbulence intensity and mean velocity variation over the height is associated with a smearing of the aerodynamic impedance functions. That is rates of change with respect to velocity are decreased and so extremes values of the functions are thereby diminished.

- A similar effect occurs with decreased aspect ratio; the peaks in the aerodynamic impedance occurring around vortex shedding are broadened and diminished.

The experiments on the forced oscillation pressure model have produced the following findings for oscillations less than about 15% of the tip diameter.

- The tip effect on the motion-induced forces on a model oscillating in a pivot mode is essentially restricted to about four diameters from the top of the model.

- The tip effect on the random or non-correlated forces on an oscillating model is essentially restricted to about three diameters from the top of the model.

- The (forced) motion organises the fluctuations in the loading at frequencies less than that of the oscillating motion so that there is a greater coherence over distance, and hence the correlation length for those frequencies increases.

- The (forced) motion does not so organise fluctuations occurring at frequencies greater than the motion.

- The spectral distribution of forces at smaller amplitudes ($\tilde{Y} < 5\%$ for a 13.3:1 prism) does not vary significantly.

- At some amplitude, however, the motion begins to redistribute the energy at higher frequencies down to the frequency of motion. This degree of redistribution then increases with amplitude. In the process, there is a greater organisation of the fluctuations since they are now occurring at the lower frequency. The associated effective correlation length therefore increases.

- The total energy of the fluctuations associated with frequencies other than that of the motion varies only weakly with amplitude, even during the redistribution process.

- The total rms of the fluctuations occurring at the frequency of motion, (the motion correlated forces) increases almost linearly with amplitude.

With respect to predictive methodology, the following has been found.

- The base balance technique, neglecting motion-induced forces, provides adequate or even conservative predictions of rms and peak responses for velocities up to about 80% of the critical vortex shedding velocity or Strouhal velocity.

Above this velocity it may underestimate the responses by a factor of two or more depending on the particular structural parameters and flow conditions.

- Based on the investigations of the effects of aspect ratio and turbulence intensity on the motion-induced forces, it would be expected that errors associated with the base balance technique would not be as severe for buildings of typical aspect ratio situated in built-up environments.

- Forced oscillation results from the pivot mode activator can provide a lower bound estimate for the response of a freely vibrating structure.

- The combined method using both base balance and pivot mode activator results and based on a stationary loading spectrum produces very good predictions of the rms response.

- The greatest uncertainties in these predictions are apparently due to the difficulty in accura ely determining the structural damping.

- When conditions are such that the n⌣ damping available is very small and the aerodynamic impedance is a locally constant function, then the response becomes very sensitive to the random forcing available from the turbulent flow.

- The experimental data available suggest that the potential exists for developing a theoretical approach to predict peak factors as well.

9.3 Practical Significance of Motion-Induced Forces

The results of the experimental studies confirm that motion-induced forces are generally not significant for typical buildings, ($H/B < 10$), whose reduced design velocities are typically <7. In this range, the magnitude of the aerodynamic damping tends to be small or positive. A built-up environment which increases the local turbulence, can be expected to further diminish the effects. For very tall slender buildings, such as the super tall skyscrapers which have been proposed from time to time, motion-induced forces would have to be given greater consideration.

For tall stacks and chimneys, the typical design velocities do fall in the range where motion-induced forces have been found to be significant, that is for $V_r > 10$.

The current study also indicates that for shapes other than a simple square, the aerodynamic damping may become negative at velocities below the Strouhal velocity as identified by the peak in the excitation spectrum acting on a stationary model. This consideration may play a role for the more common tall buildings as well as chimneys. In short, the peak occurring in the spectrum measured on a stationary body may suggest at what velocities aerodynamic damping may be negative, but it cannot be relied upon as a definitive indication of either the sign or the magnitude of the aerodynamic damping.

9.4   Practical Use of PMA System

The feasibility of measuring motion-induced forces with a high degree of resolution, using a typical base balance model has been demonstrated. In the simplest form a test with the Pivot Mode Activator System can ascertain the potential for negative aerodynamic damping for a particular wind direction of concern. This can be done by performing a single swept frequency experiment at a small amplitude and over the velocity range of interest.

A more concerted test effort can provide data which when combined with base balance results will provide good estimates of the rms response of a structure. Moreover since the measured data from both tests depend only on the geometry of the structure and the flow conditions, parametric studies providing response estimates as functions of structural properties are possible. This ability offers a particularly valuable advantage over a conventional aeroelastic test, although the full test effort for the two is comparable.

A third intermediate scenario is as follows. The Pivot Mode Activator System may be used to determine for a range of velocities, a small amplitude value of the aerodynamic damping (and stiffness). This can be done to whatever resolution is desired by choosing the type of test, swept or steady frequency, and the length of the data records. Assuming that the process is linear, that is that the impedance does not vary with amplitude, parametric predictions of response may be carried out. In this way the structural properties and velocities associated with excessive amplitudes or instability may be identified. This information in most cases will be

quite sufficient for design requirements as it indicates the conditions to be avoided. In more rare cases it may be desired to explore the variation in more detail. In that case a more elaborate test series may be carried out or perhaps an aeroelastic model study would be indicated.

The potential of developing an empirical method of predicting peak factors has been noted. This would further refine the procedures described above.

9.5 Recommendations for Further Studies

The Pivot Mode Activator System has been developed to the point that rather extensive test series may be carried out in a relatively routine manner. As an example, the test series investigating the effects of turbulence intensity was considered one evening as an addendum to the main test series. The complete set of tests were run automatically by the tunnel control computer during the night. The next morning, the complete processing of the data to the presentation stage took about four hours.

A number of possible research projects come to mind using both the complete Pivot Mode Activator System and just the mechanical activator with instrumented models. For example,

- An investigation of the relation between the shape of the force spectrum acting on a stationary body, and in particular, the location of the spectral peaks,

and the form of the aerodynamic impedance at low amplitudes.

- An investigation of the variation of aerodynamic impedance with afterbody length.

- Investigations of the variation of aerodynamic impedance with various geometric modifications, such as along wind and across wind holes, splitter plates, or strakes.

- The variation of mean and rms across wind (and along wind) forces acting on a moving body with various angles of attack — this may indicate when and how the quasi-steady assumptions of the galloping theory break down.

- A detailed study of the influences of tapering and of aspect ratio on the aerodynamic impedance.

In addition to these, further studies advancing the practical applications of the system may be carried out. For example

- The development of an empirical approach to predicting peak factors as was previously mentioned.

- The development and testing of empirical models to fit to the aerodynamic impedance functions with the purpose of extrapolating to untested amplitudes.

- Investigations to determine the effects and importance of modifying the force spectrum measured on a stationary model so as to represent that acting on a moving model.

Of course these suggestions barely scrape the surface.

9.6 Recess

Research is an open ended endeavor. It was very easy to let the initial scope of this work expand, however, there comes a point where one must, for peace of mind, say enough and package it up. It is certainly felt that the initial goals have been met. A routine system of measuring motion-induced forces has been developed. The use of the system has been demonstrated and the reliability of the results verified. In addition two significant data bases of experimental results have been accumulated. From these a great deal of valuable information regarding motion-induced effects has been gleaned and a great deal more remains... for another day.

Part V

APPENDICES AND REFERENCES

Appendix A

Complementary Representations
of Aerodynamic Impedance
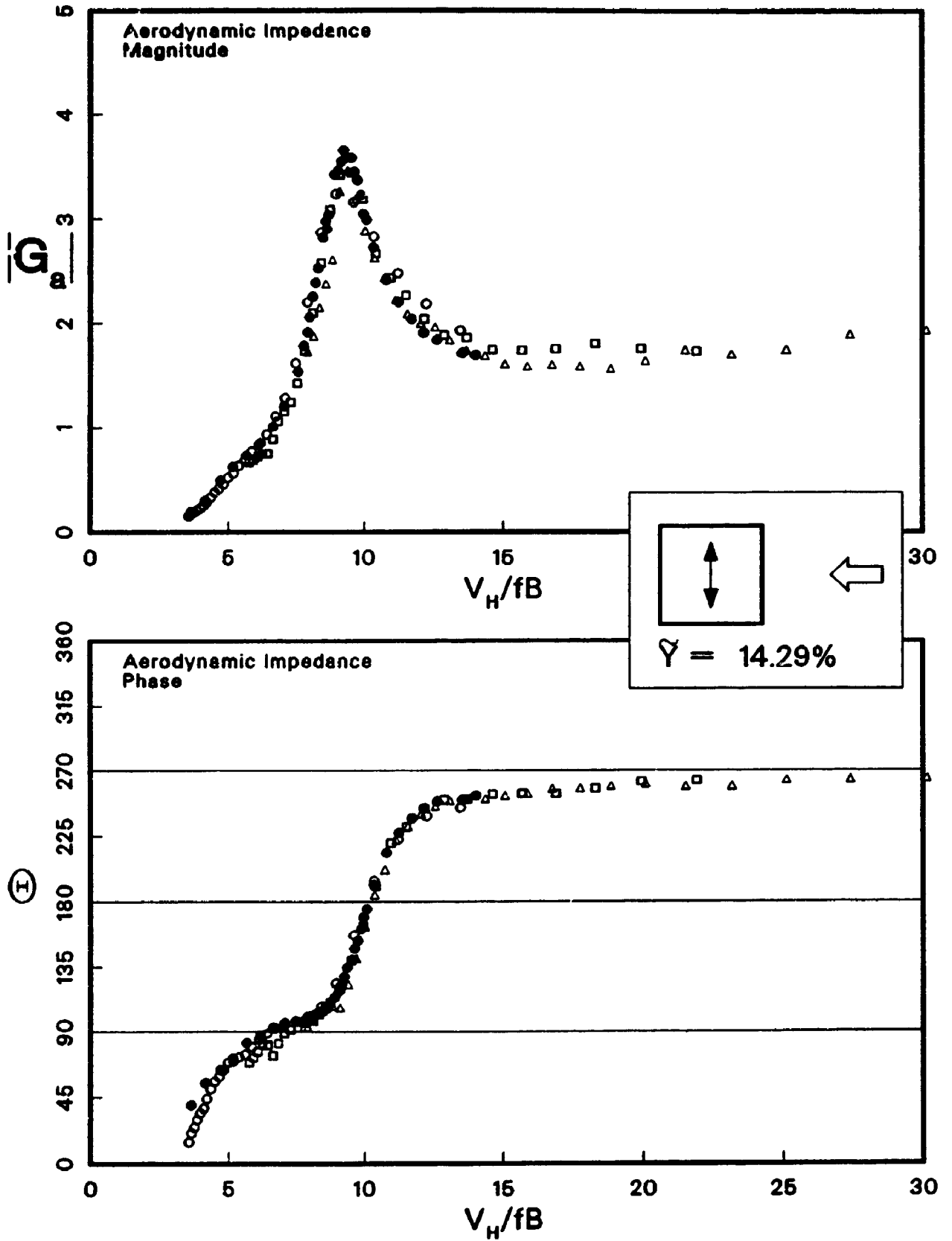
Figure A.1: Comparison of Results from Disparate Experimental Techniques and Analysis Methods, Large Amplitude
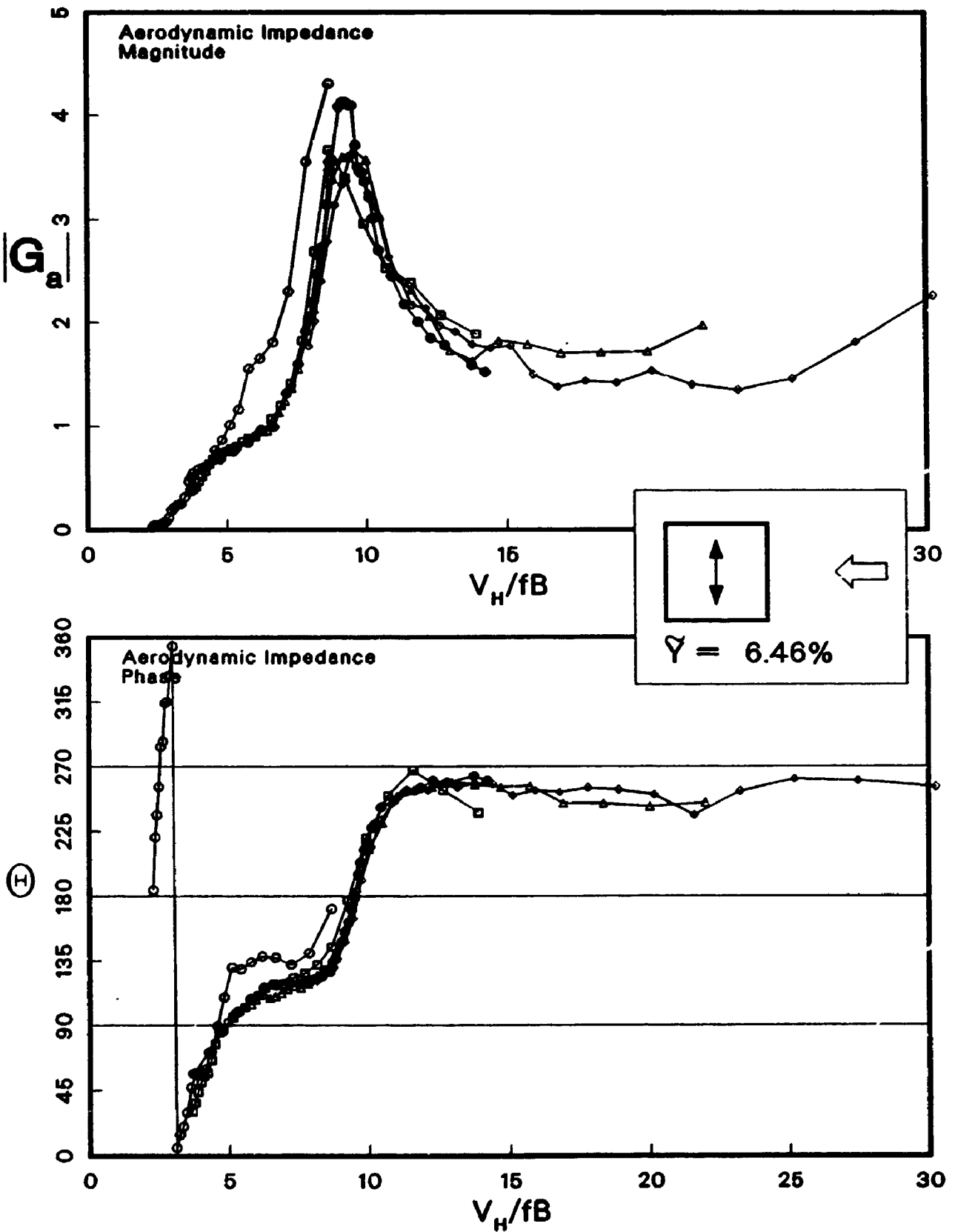
Figure A.2: Comparison of Results from Disparate Experimental Techniques and Analysis Methods, Medium Amplitude
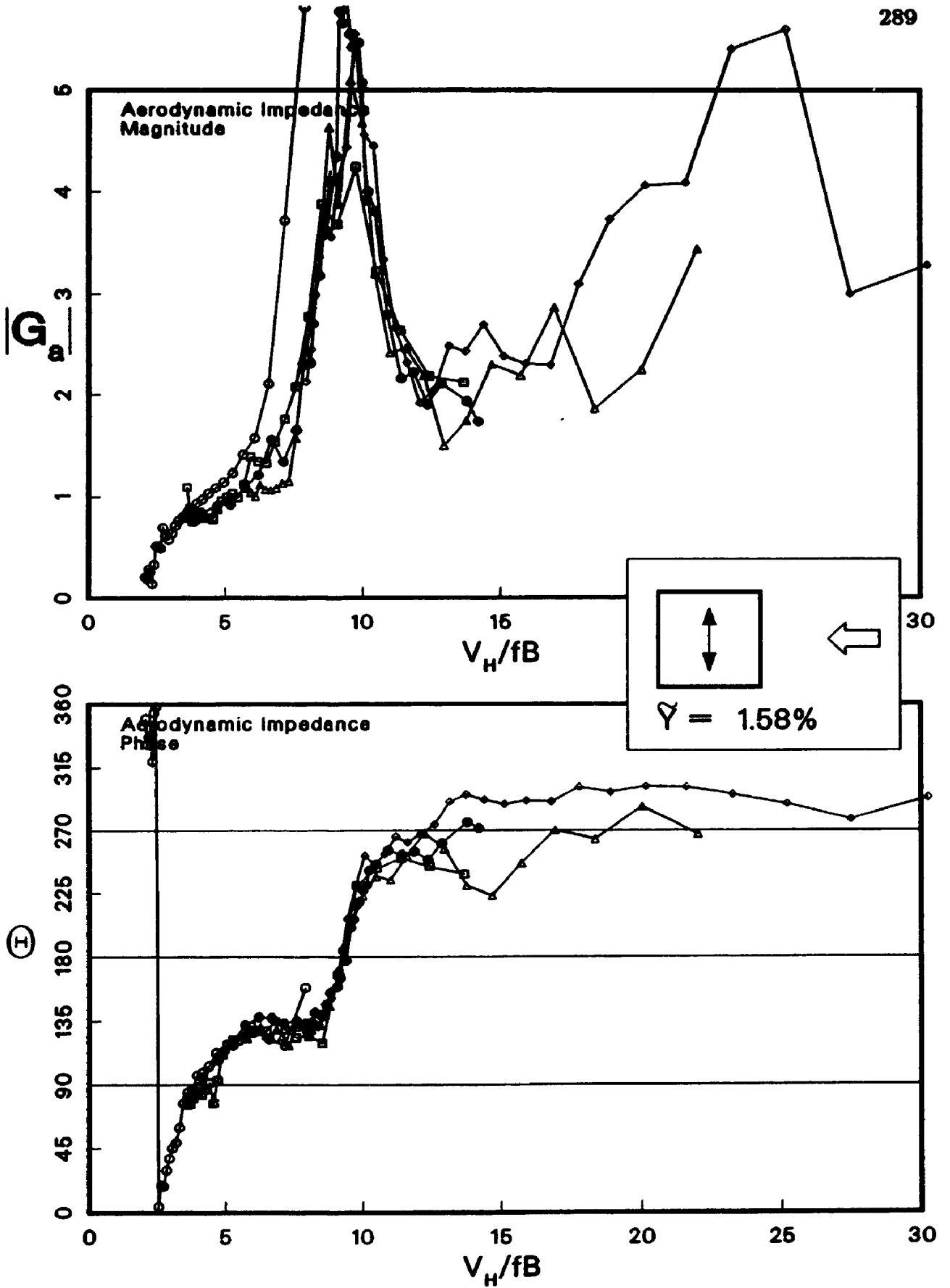
Figure A.3: Comparison of Results from Disparate Experimental Techniques and Analysis Methods, Small Amplitude
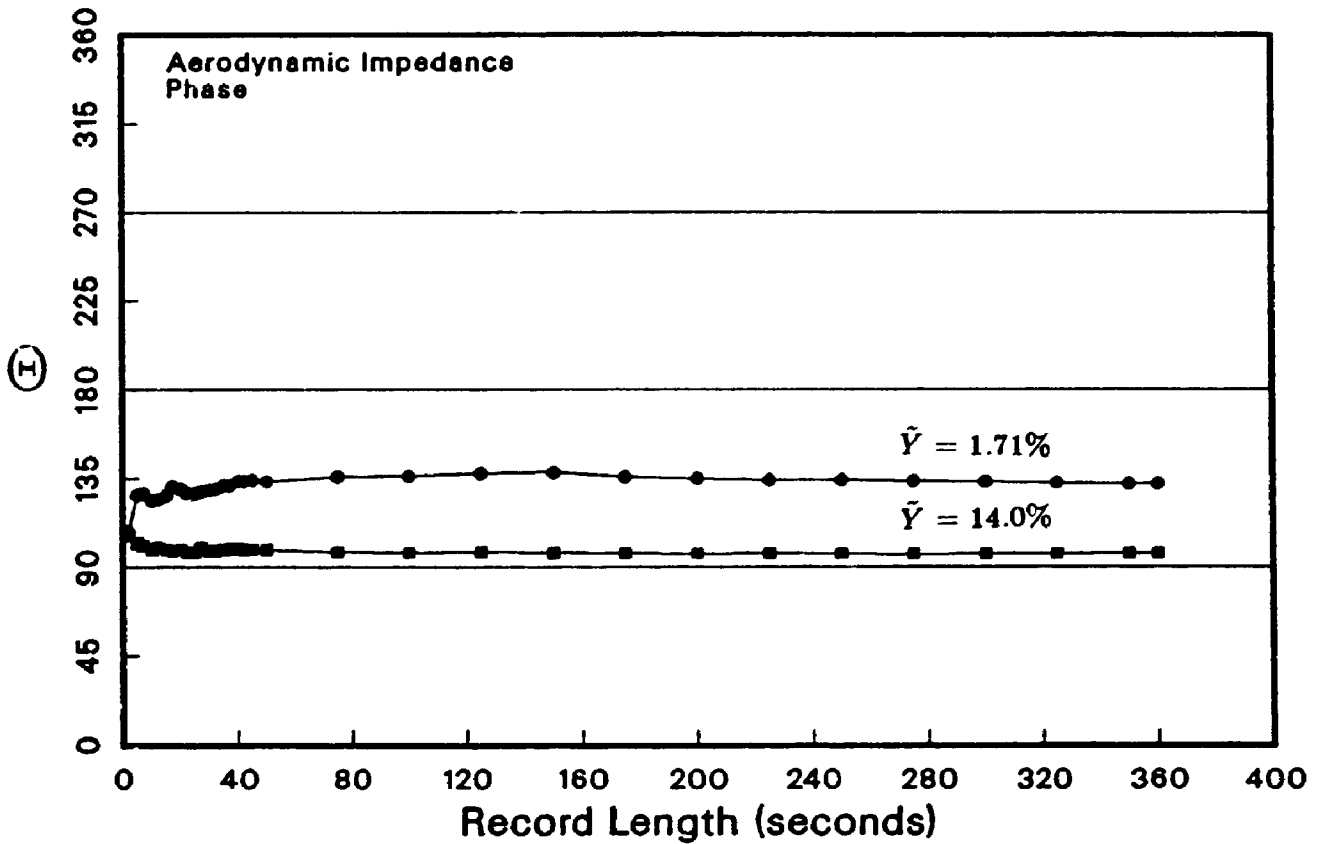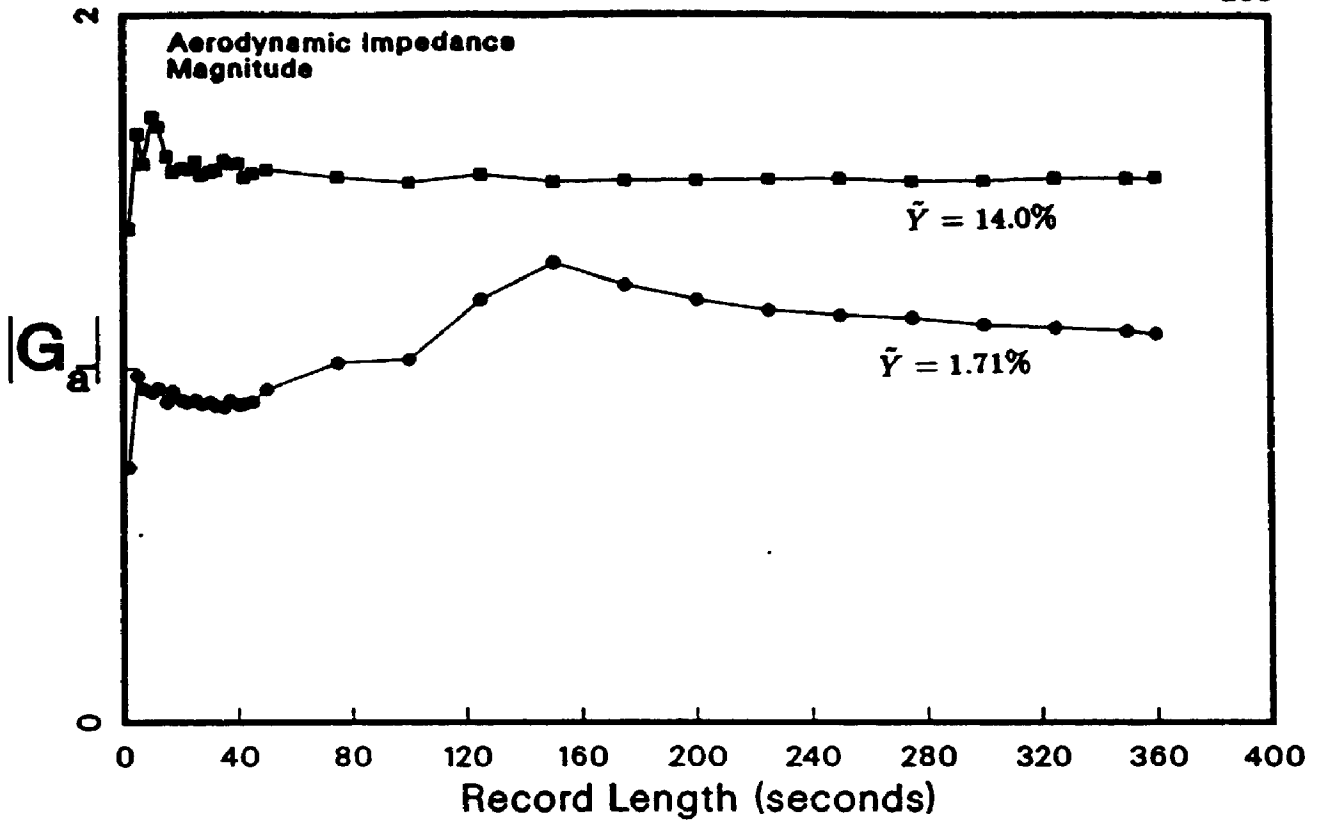
Figure A.4: Variation of Estimate with Record Length (Steady Frequency)
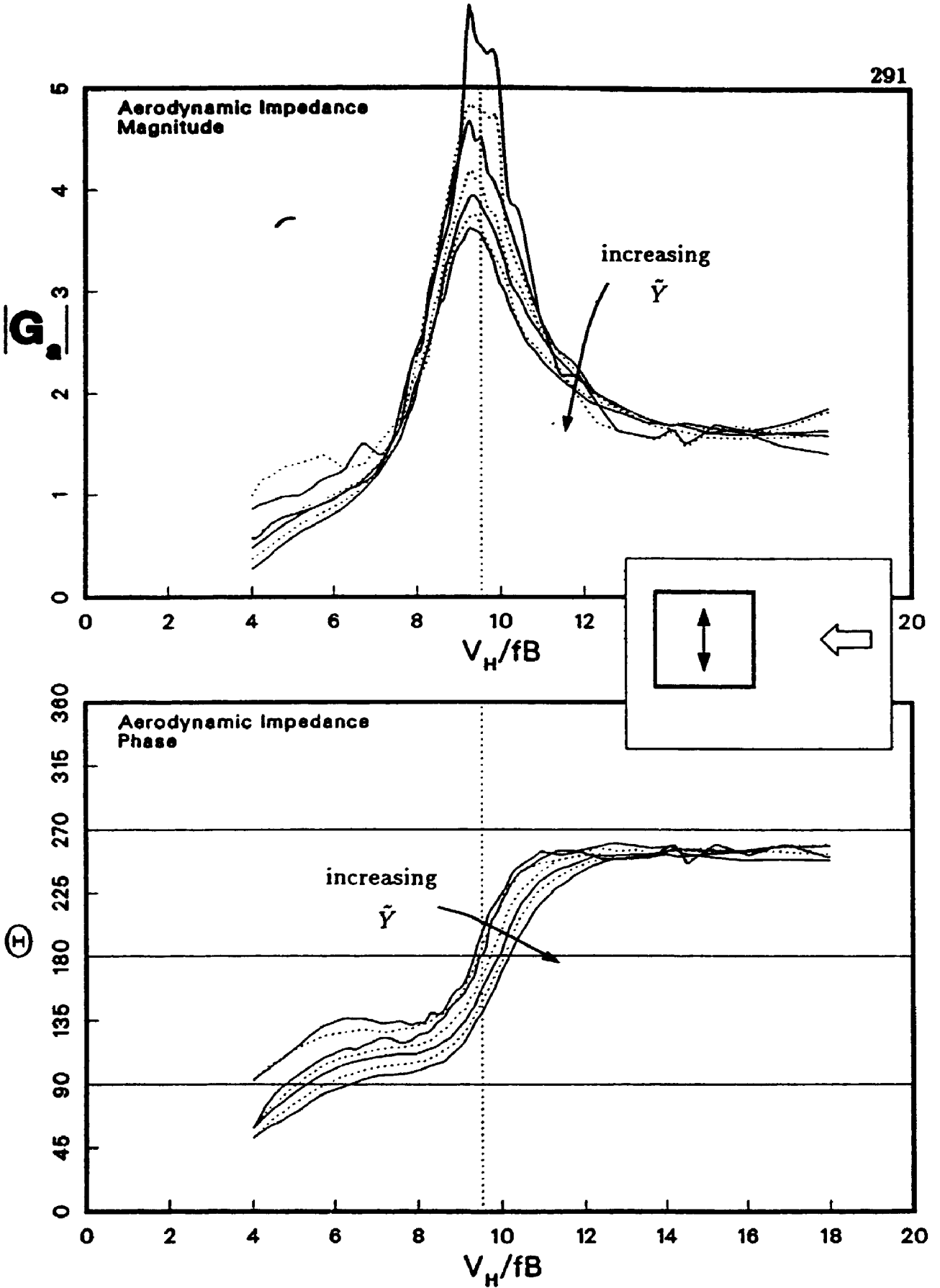
Figure A.5: Interpolated Curves Showing Variation of Aerodynamic Impedance with Amplitude ($\tilde{Y} = 2\%$ to 14% at 2% intervals)
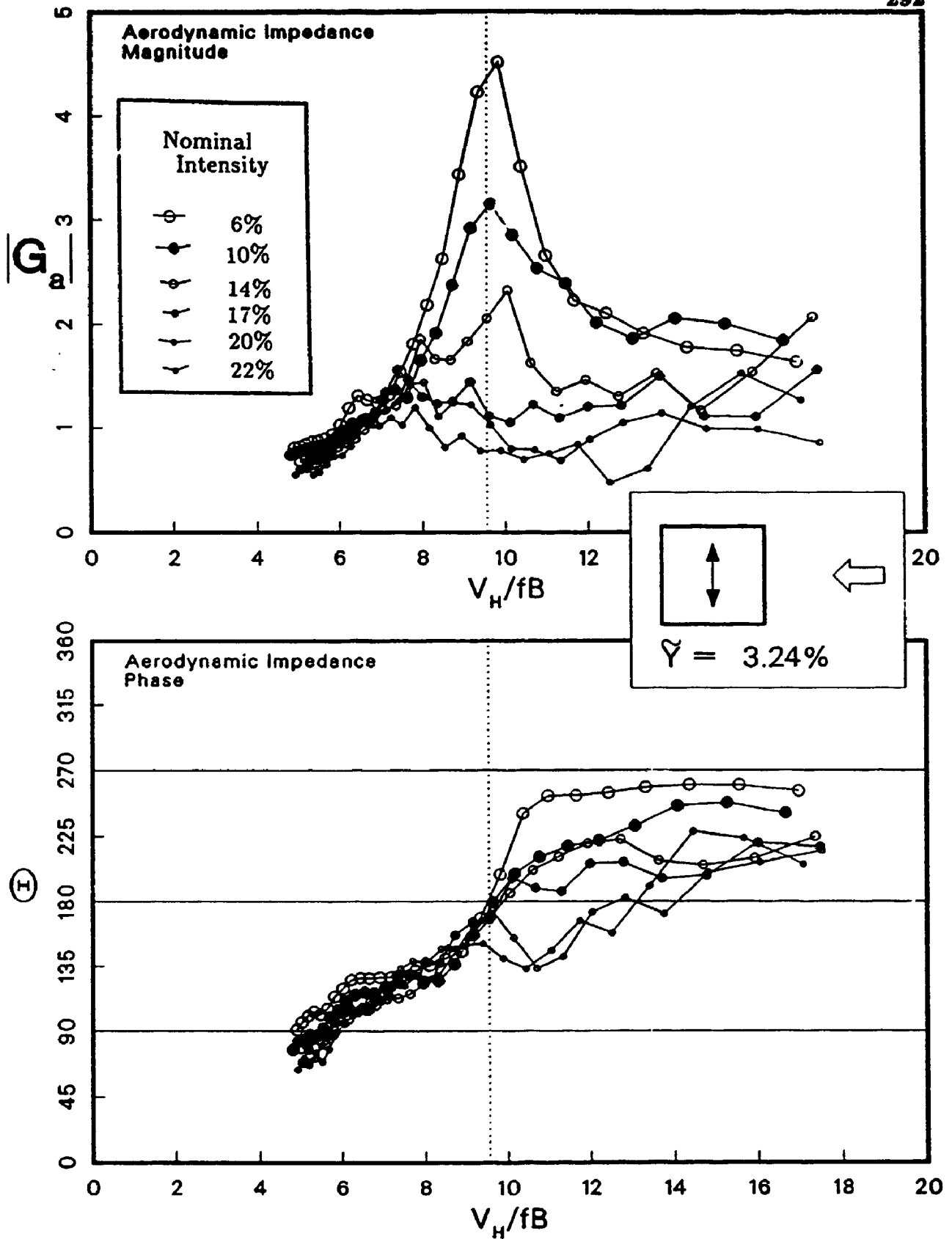
Figure A.6: Aerodynamic Impedance for Various Turbulent Shear Flows
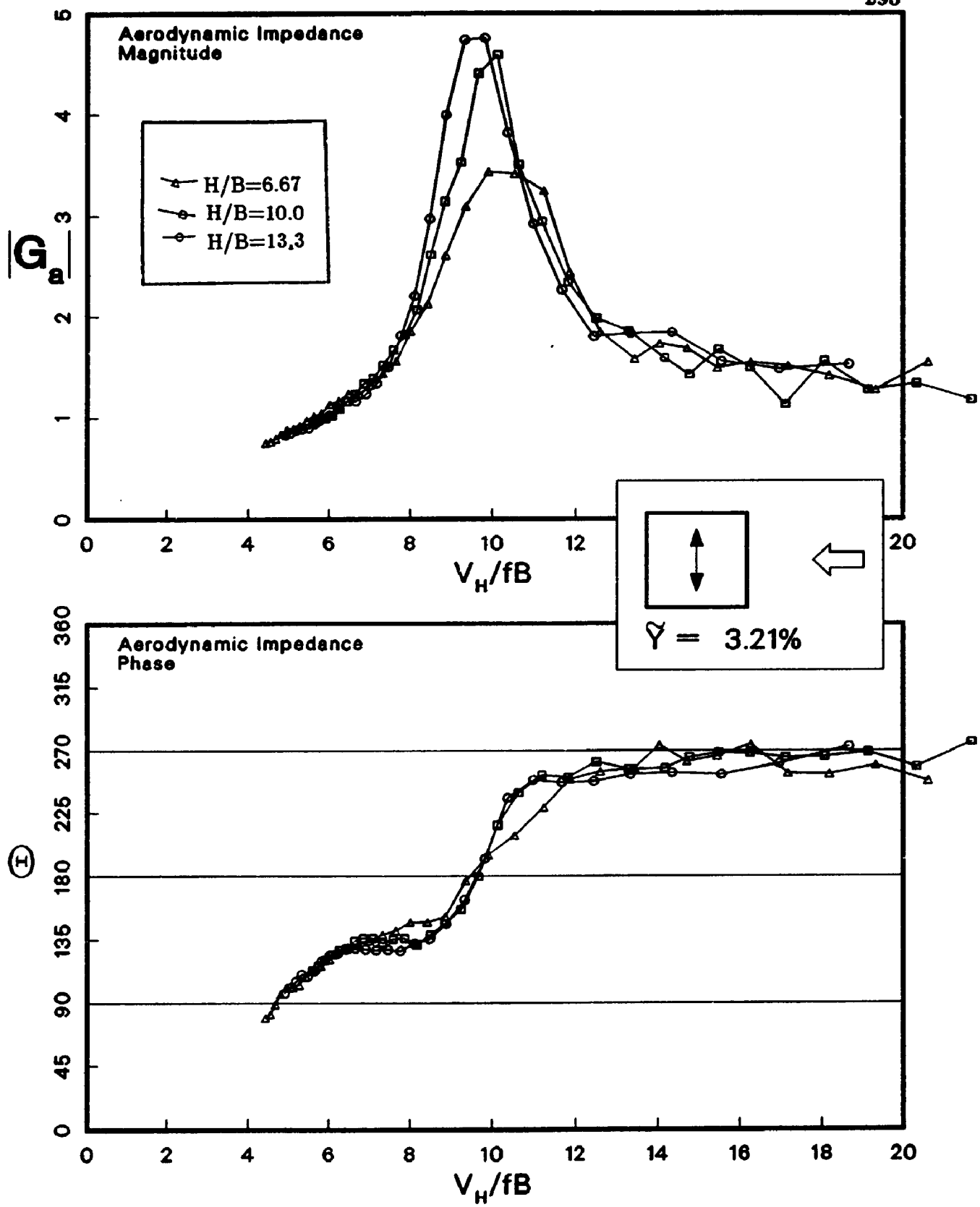
Figure A.7: Aerodynamic Impedance for Three Different Aspect Ratios (13.3:1, 10:1, 6.7:1)
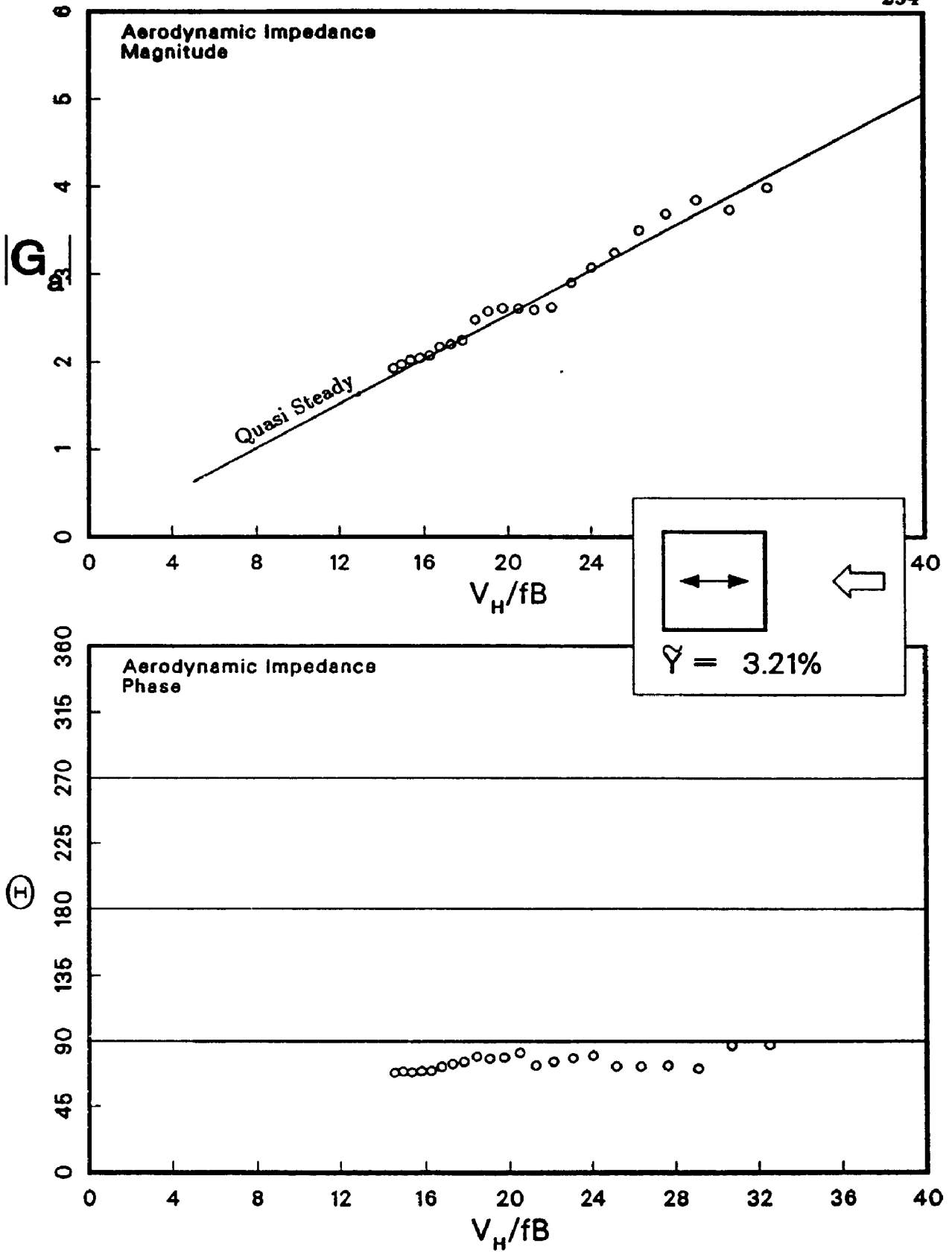
Figure A.8: Comparison of PMA Results with Quasi-Steady Theory for Along Wind Direction
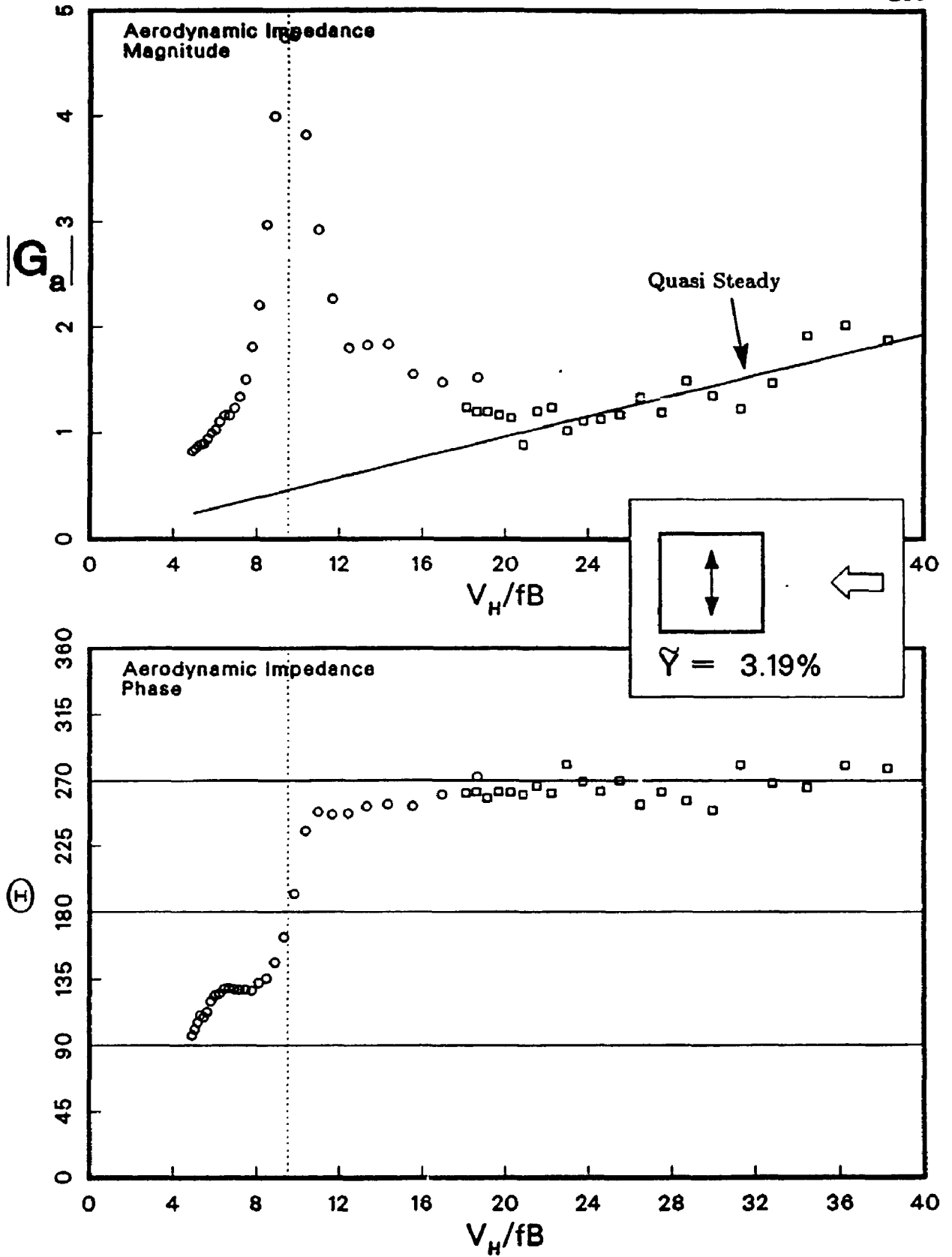
Figure A.9: Comparison of PMA Results with Quasi-Steady Theory for Across Wind Direction
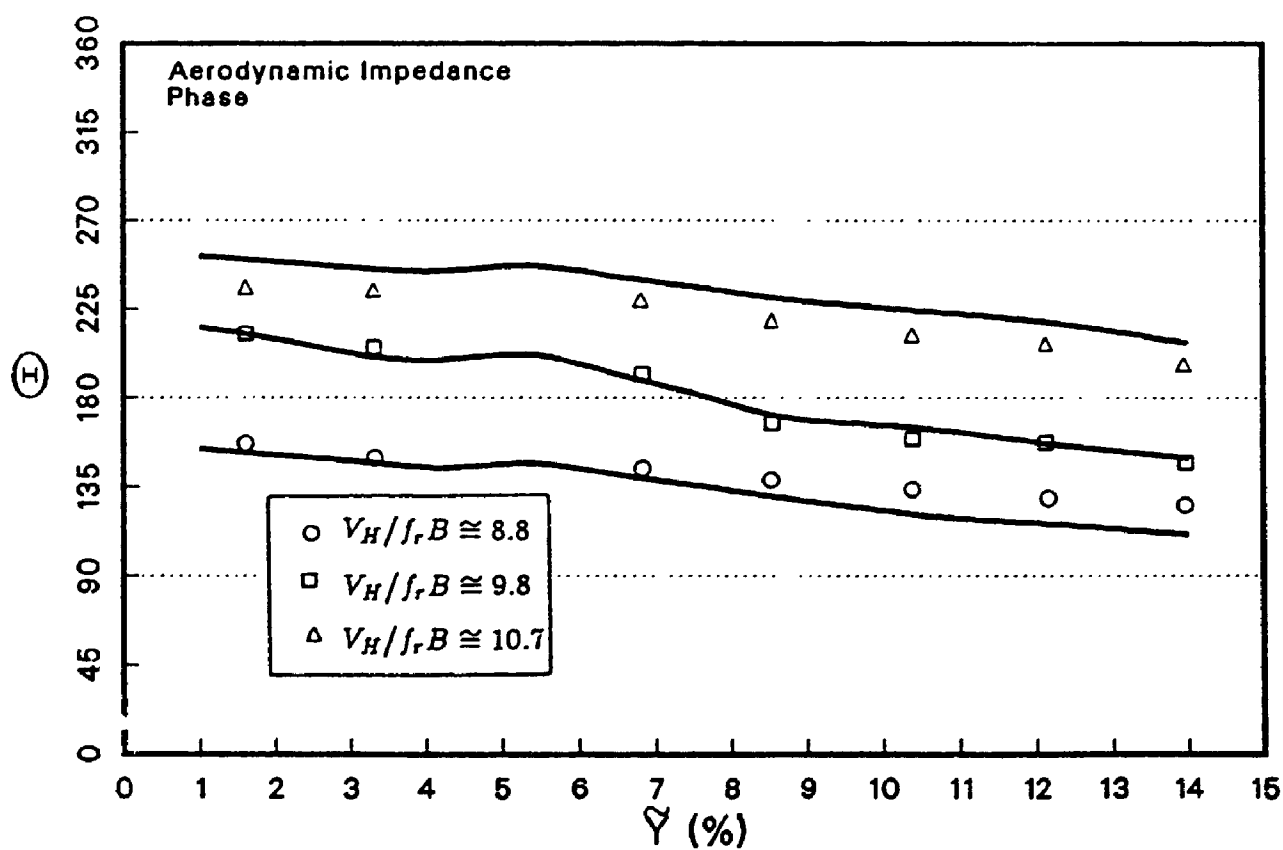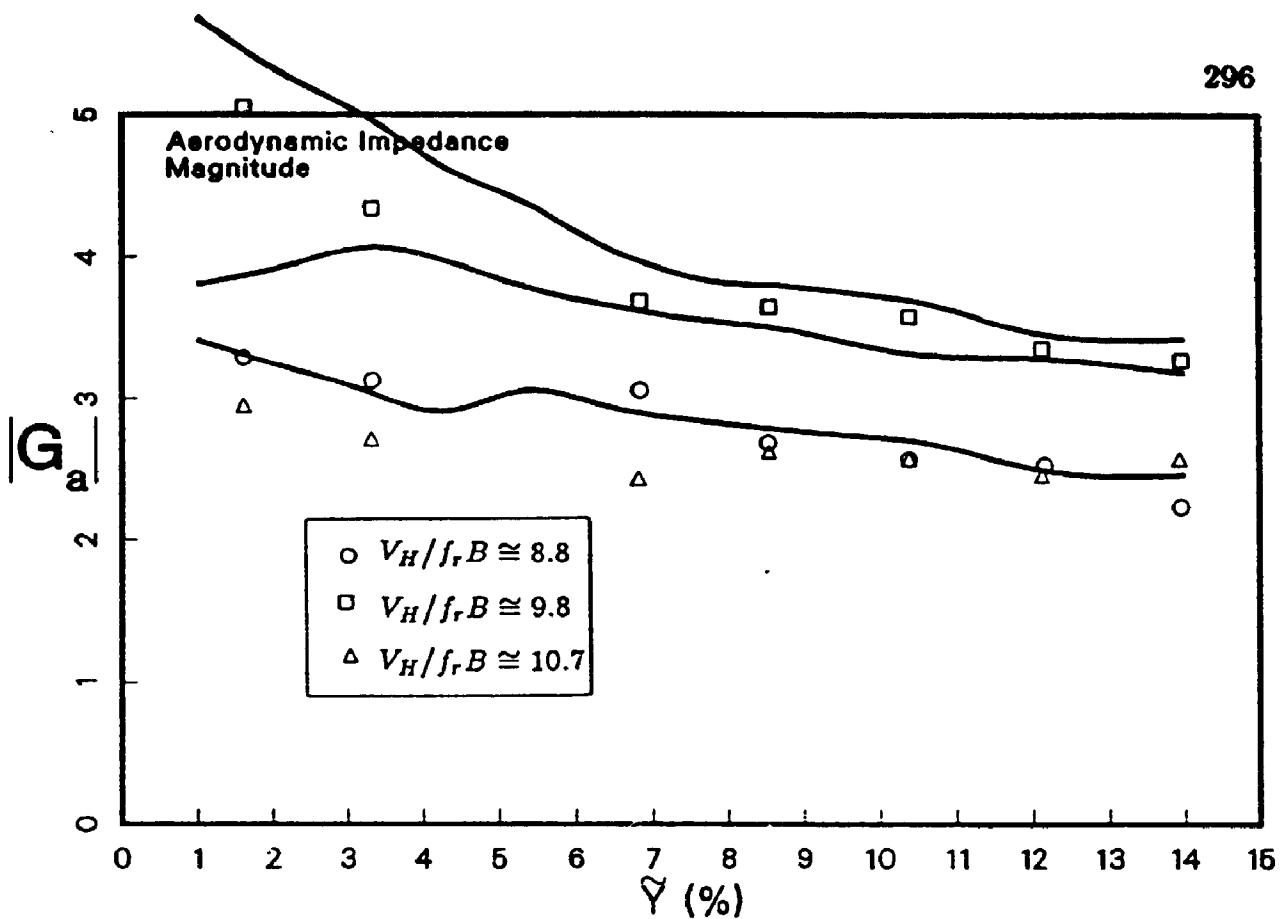
Figure A.10: Comparison of Aerodynamic Impedance Determined from the PP Experiments with the PMA Results
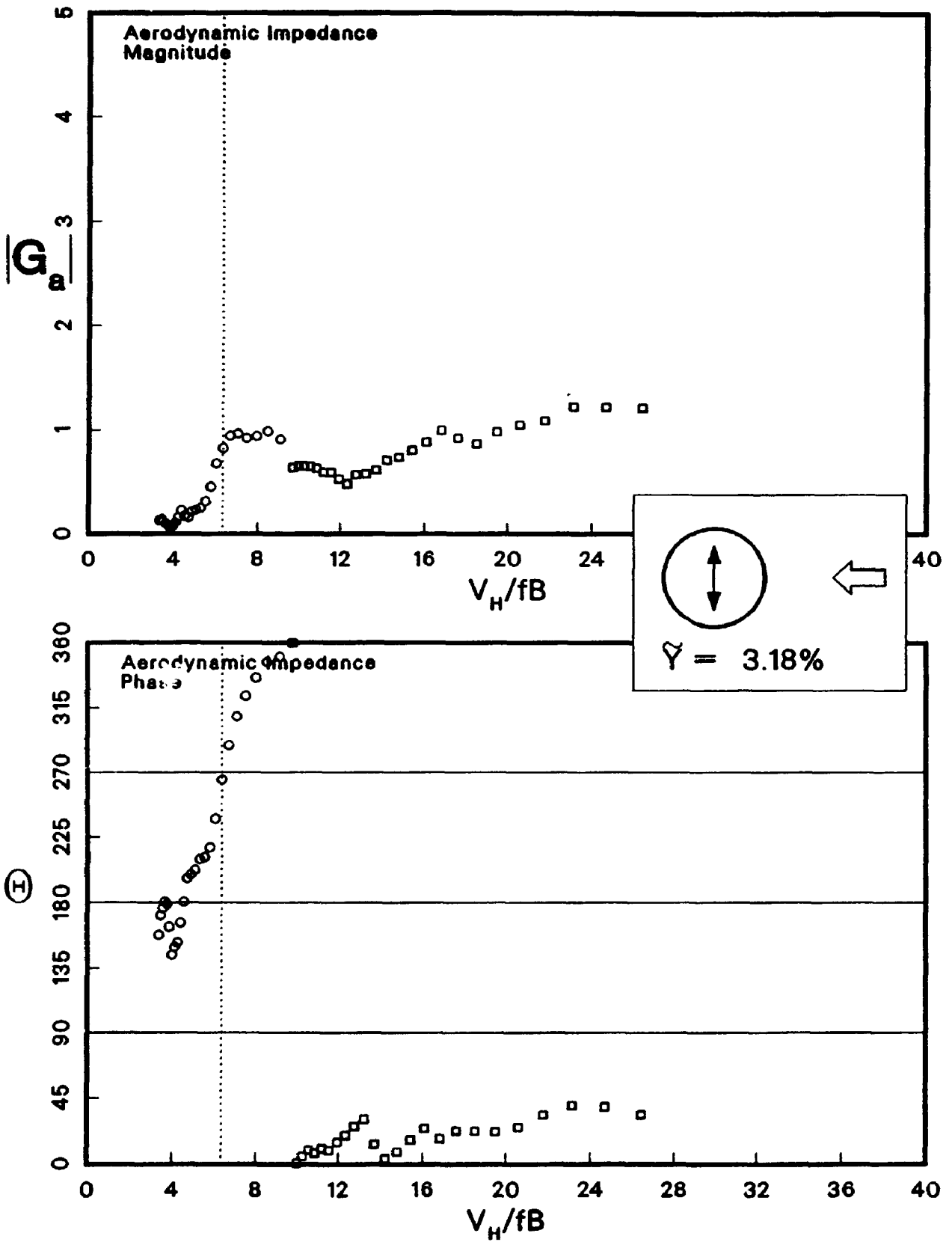
Figure A.11: Aerodynamic Impedance for Worst Wind Direction For Shape A
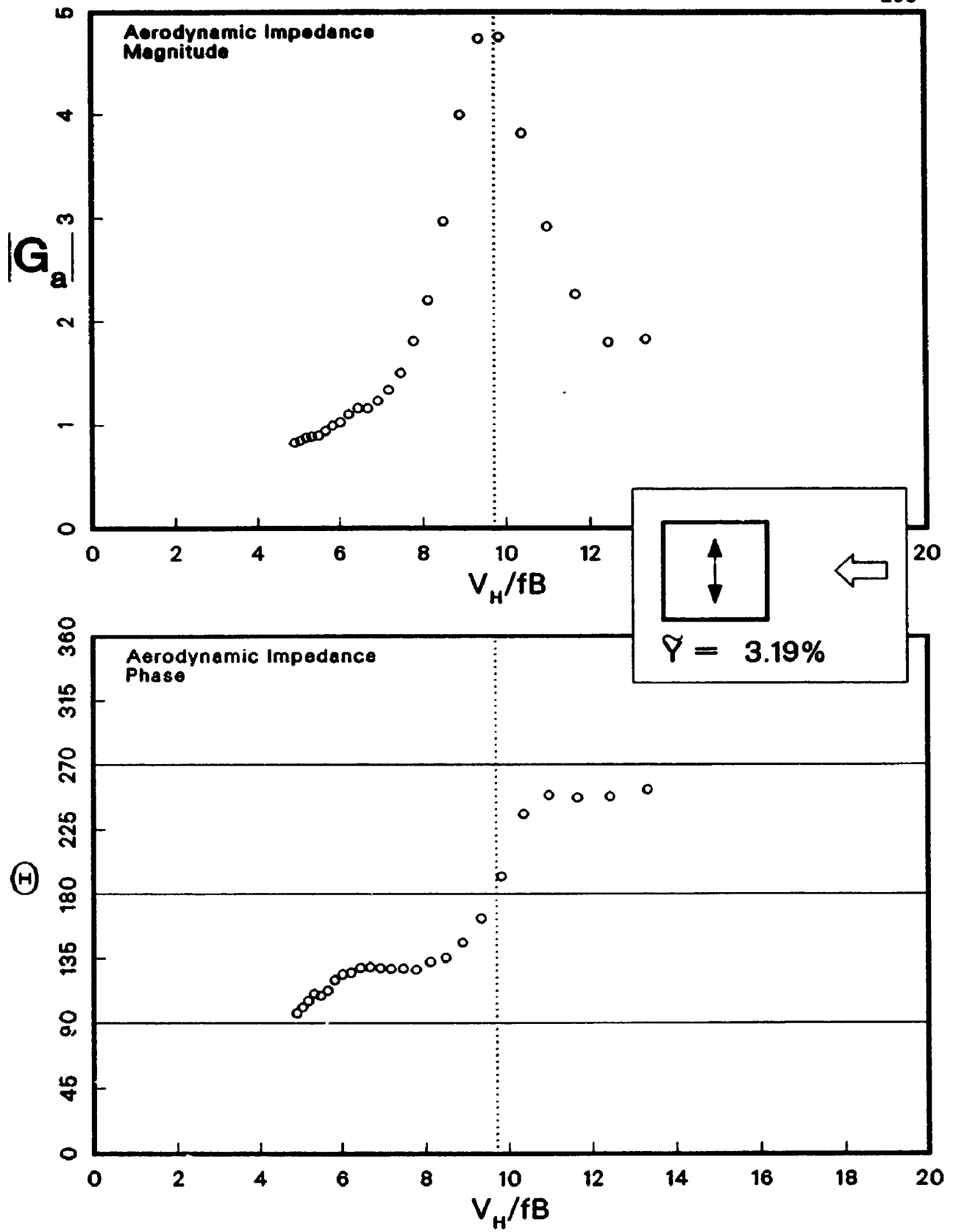
Figure A.12: Aerodynamic Impedance for Worst Wind Direction For Shape B
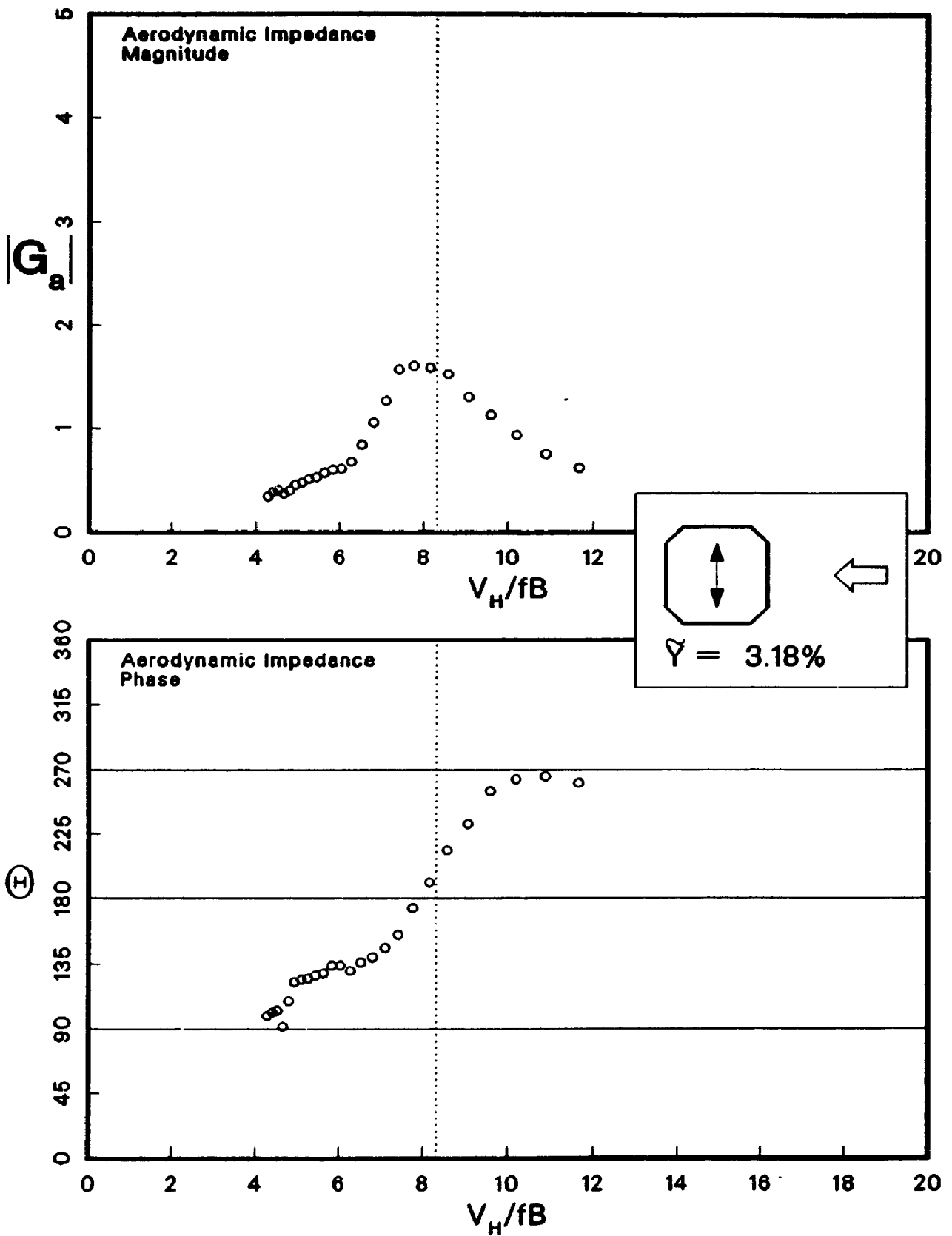
Figure A.13: Aerodynamic Impedance for Worst Wind Direction For Shape C
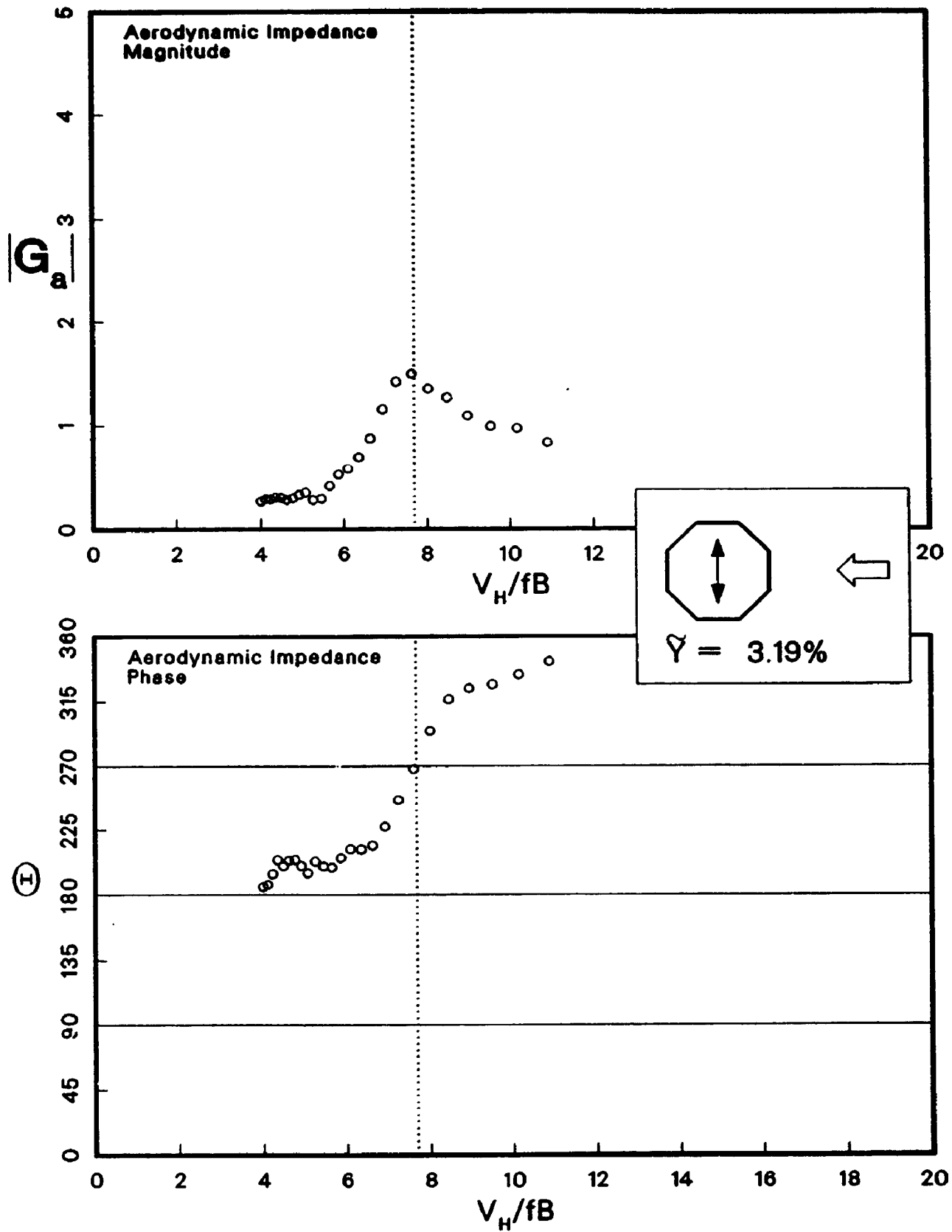
Figure A.14: Aerodynamic Impedance for Worst Wind Direction For Shape D
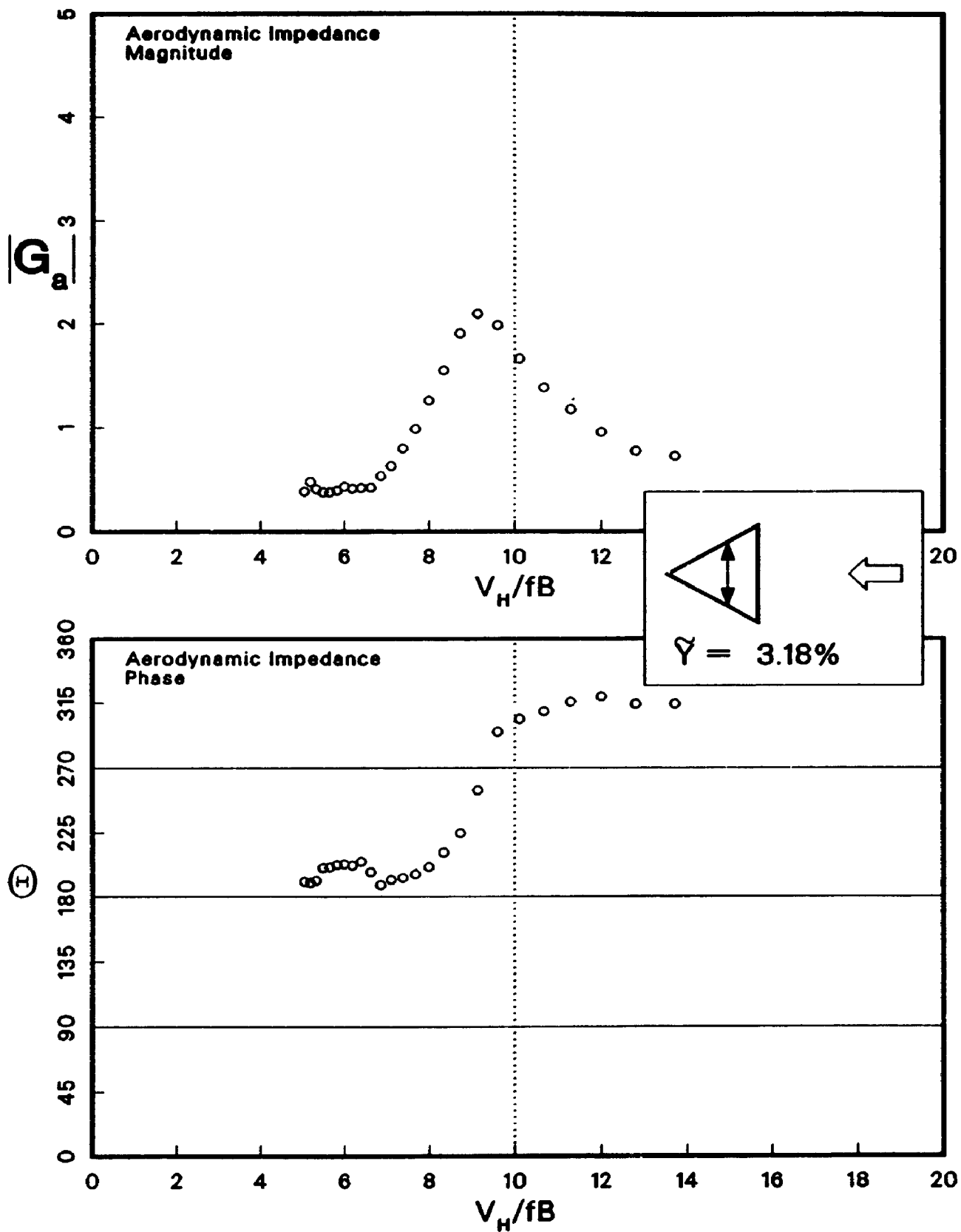
Figure A.15: Aerodynamic Impedance for Worst Wind Direction For Shape E
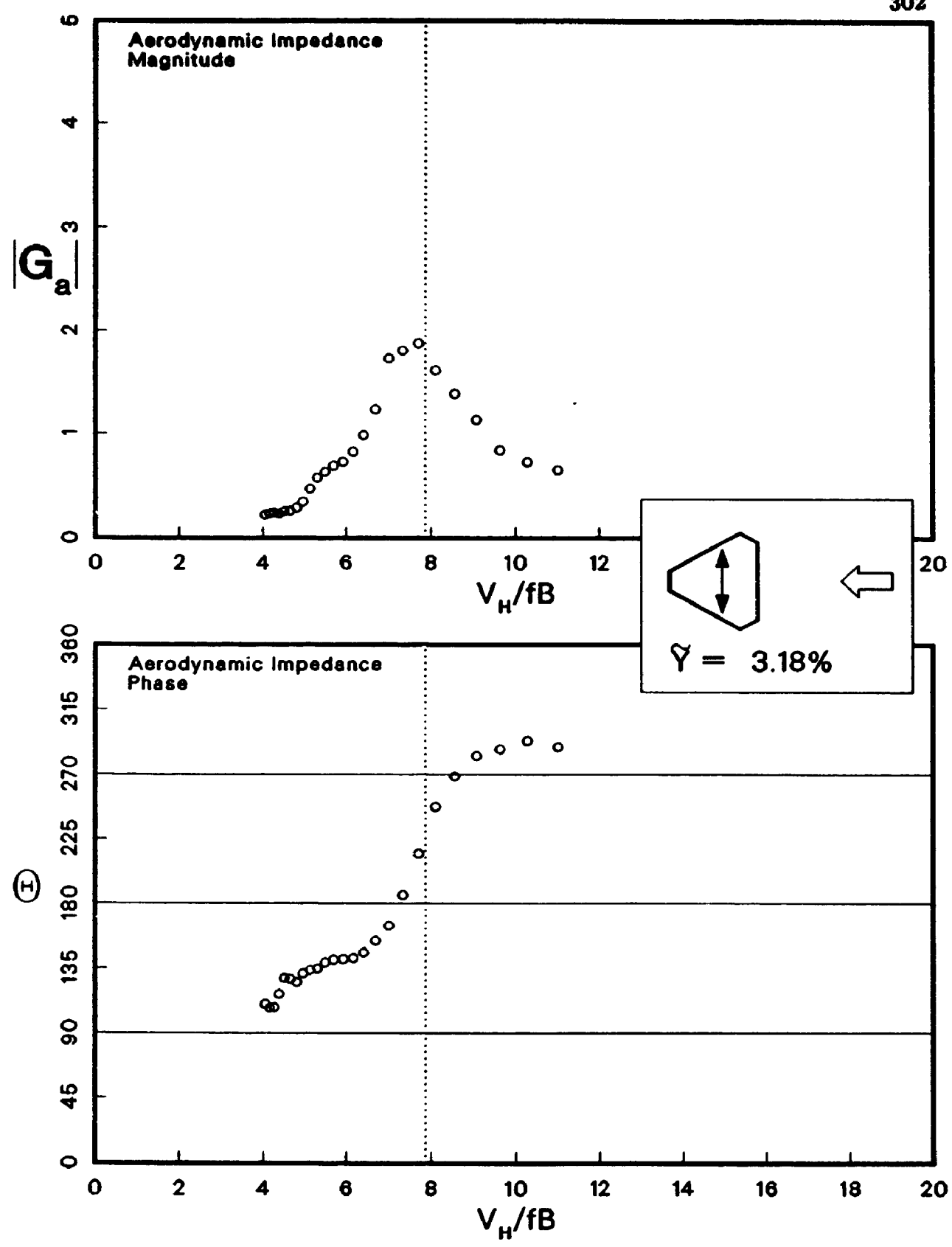
Figure A.16: Aerodynamic Impedance for Worst Wind Direction For Shape F
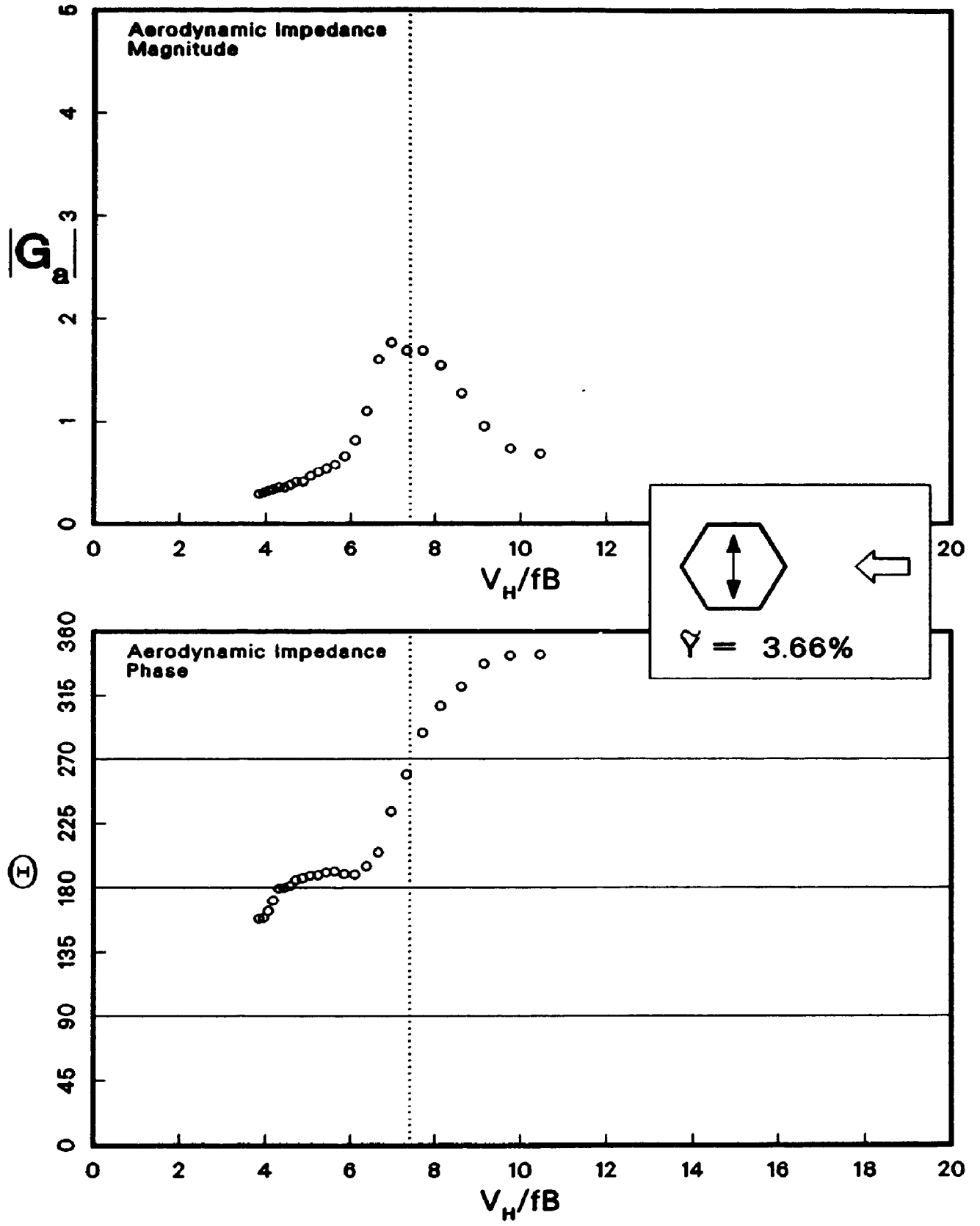
Figure A.17: Aerodynamic Impedance for Worst Wind Direction For Shape G
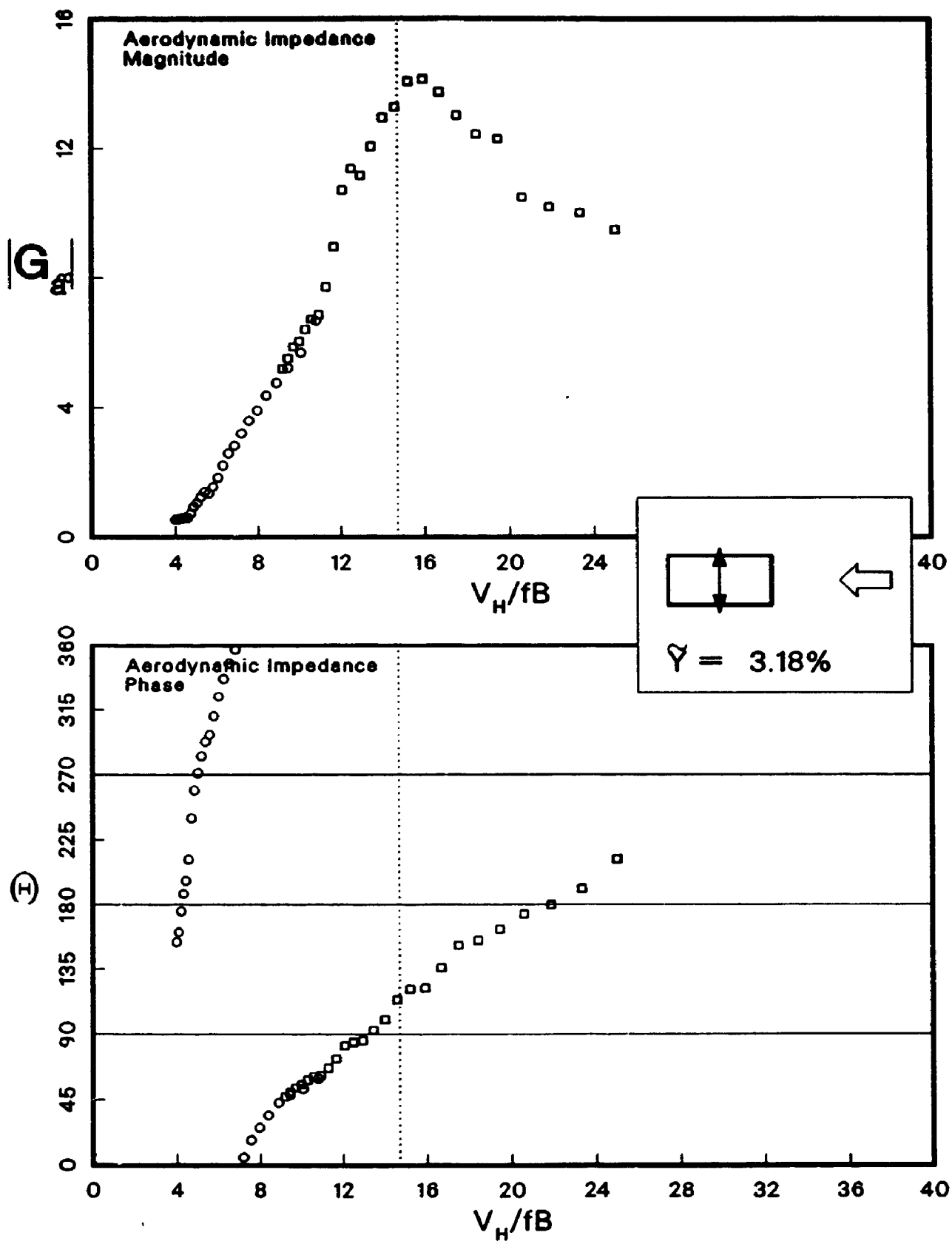
Figure A.18: Aerodynamic Impedance for Worst Wind Direction For Shape H
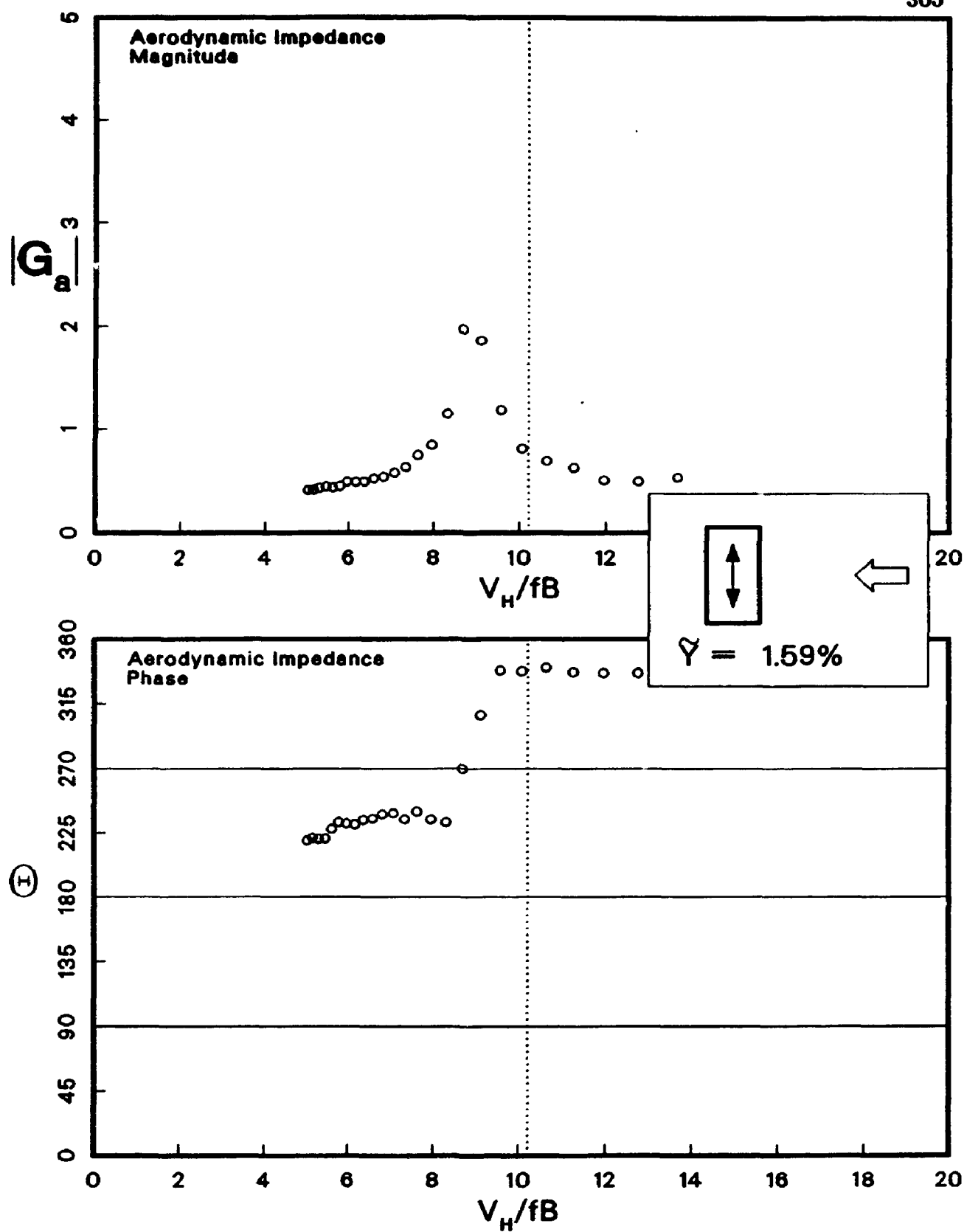
Figure A.19: Aerodynamic Impedance for Worst Wind Direction For Shape I

Appendix B

Spectra of the Wind
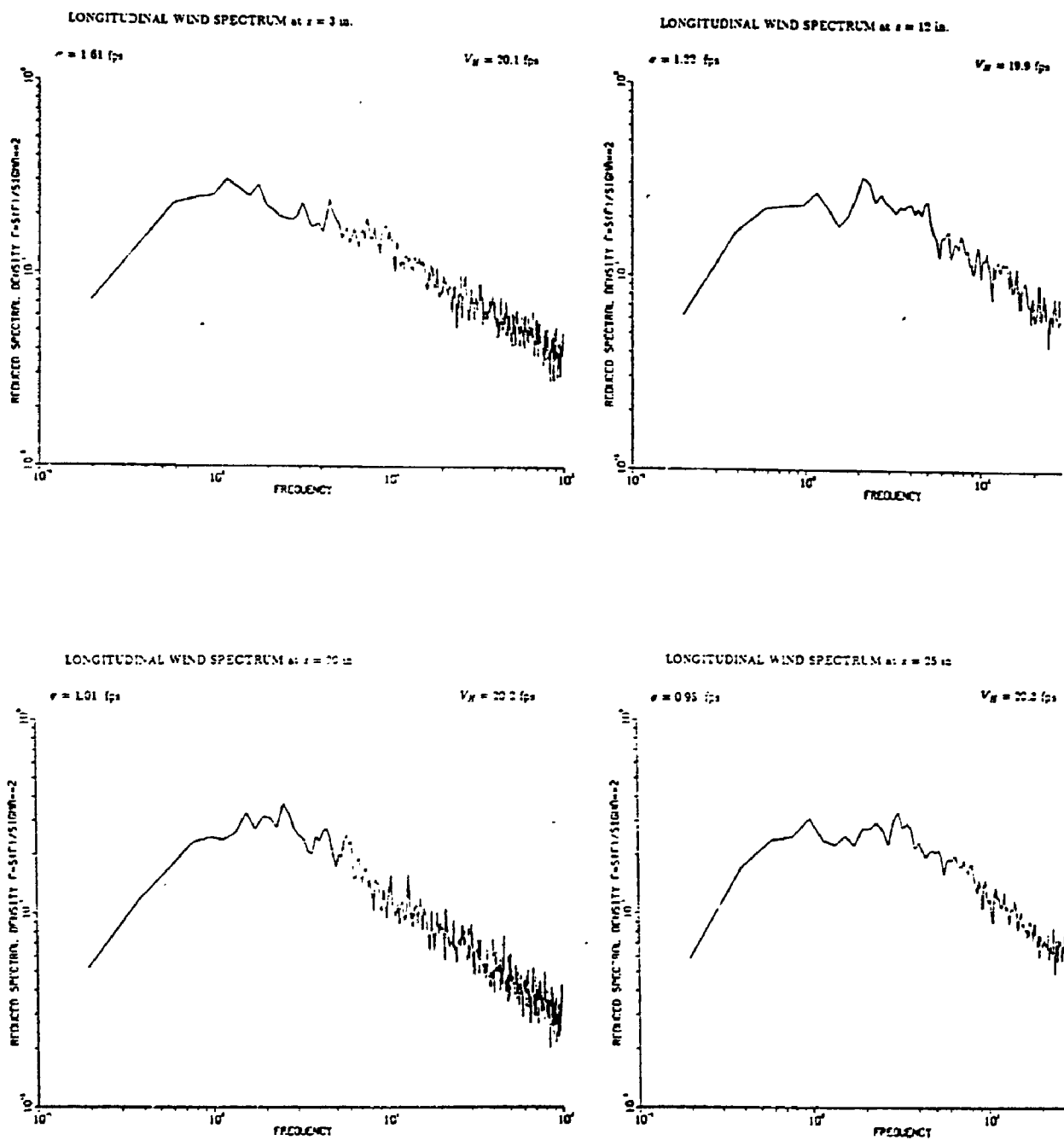
Figure B.1: Spectra of Longitudinal Wind at Four Heights for Main Test Exposure used with Tests on Square Prism

Appendix C

Aerodynamic Impedances For The Square Prism, α, β
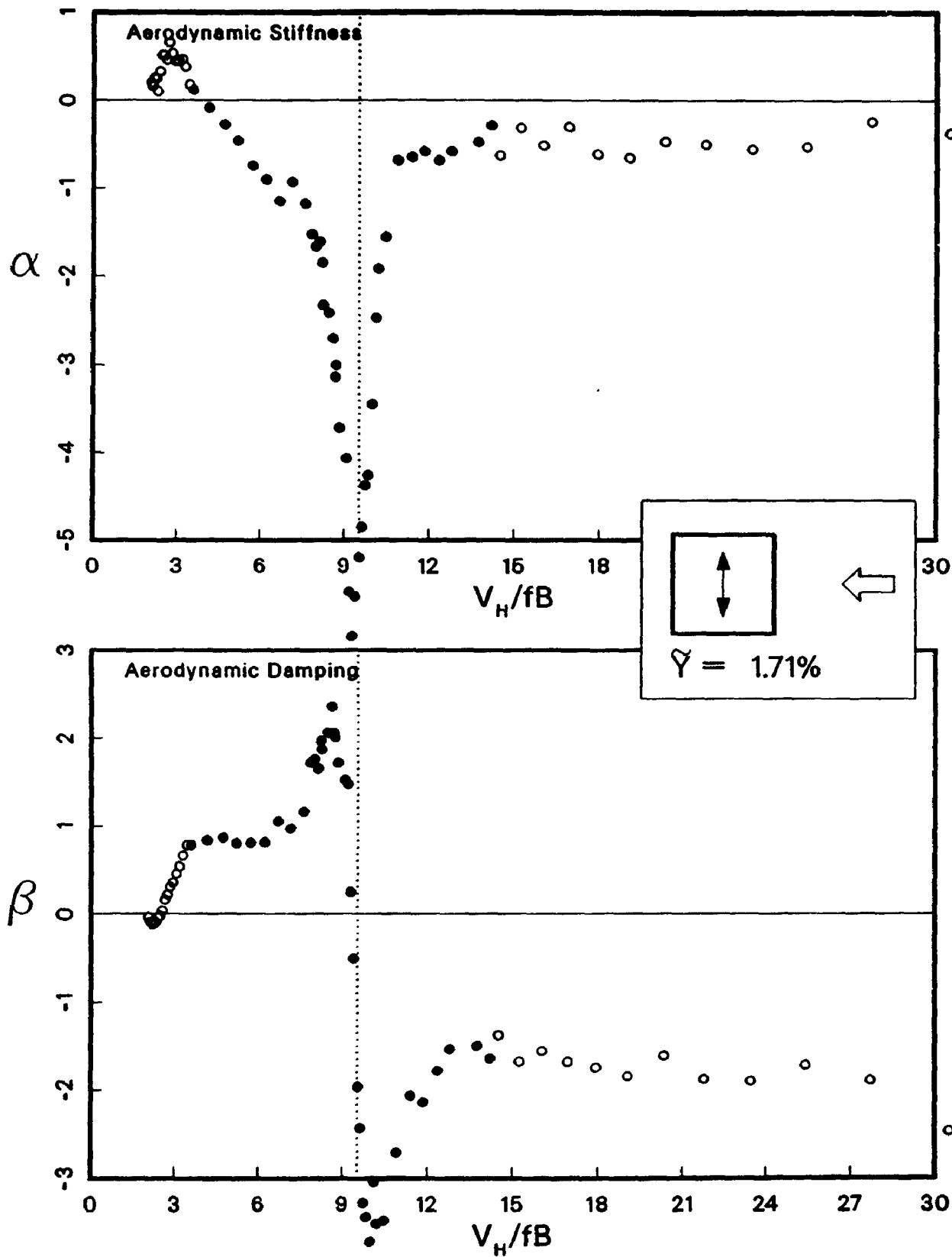
Figure C.1: Aerodynamic Impedance for $\ddot{Y} = 1.71\%$, α, β
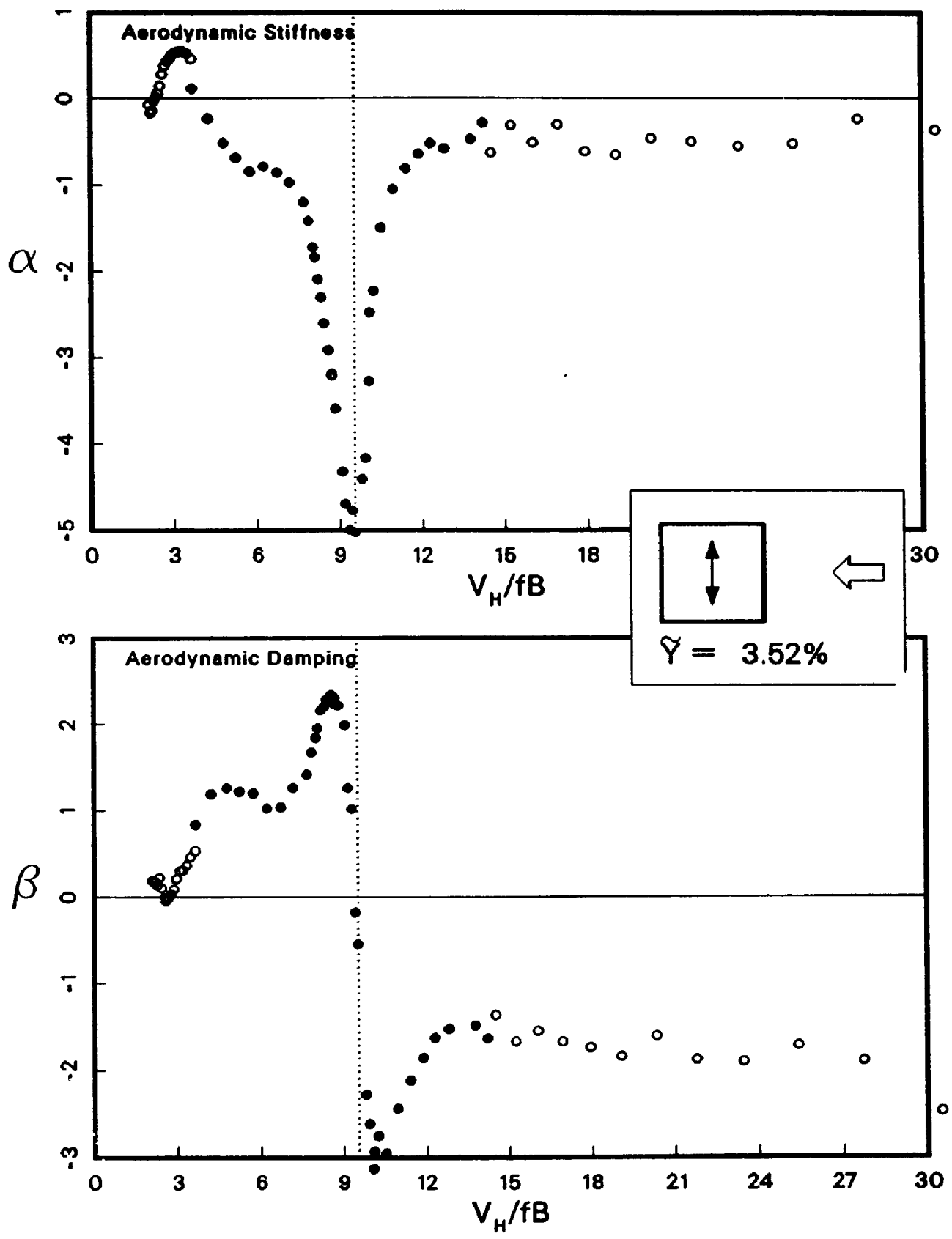
Figure C.2: Aerodynamic Impedance for $Y = 3.52\%$, α, β
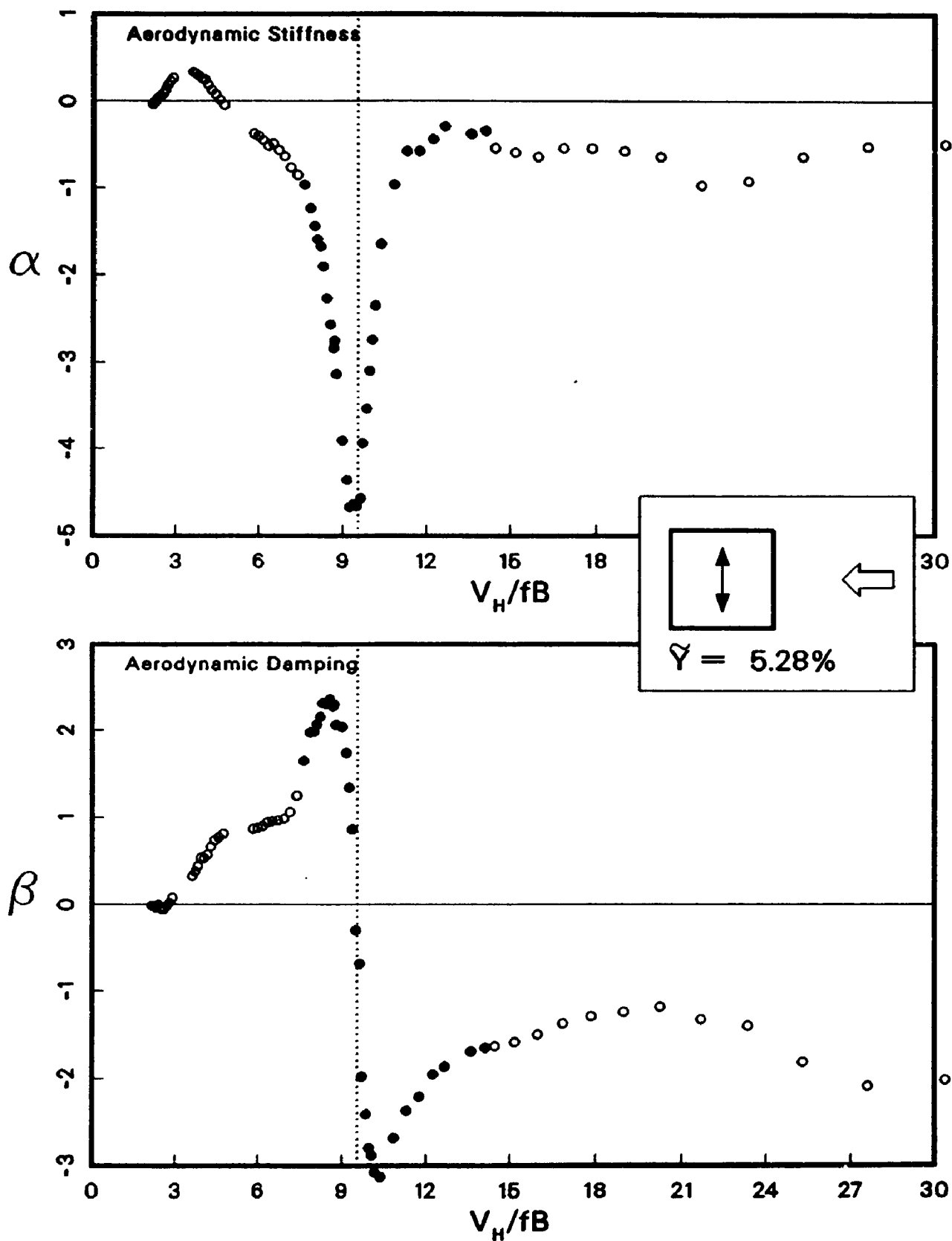
Figure C.3: Aerodynamic Impedance for $Y = 5.28\%$, α, β
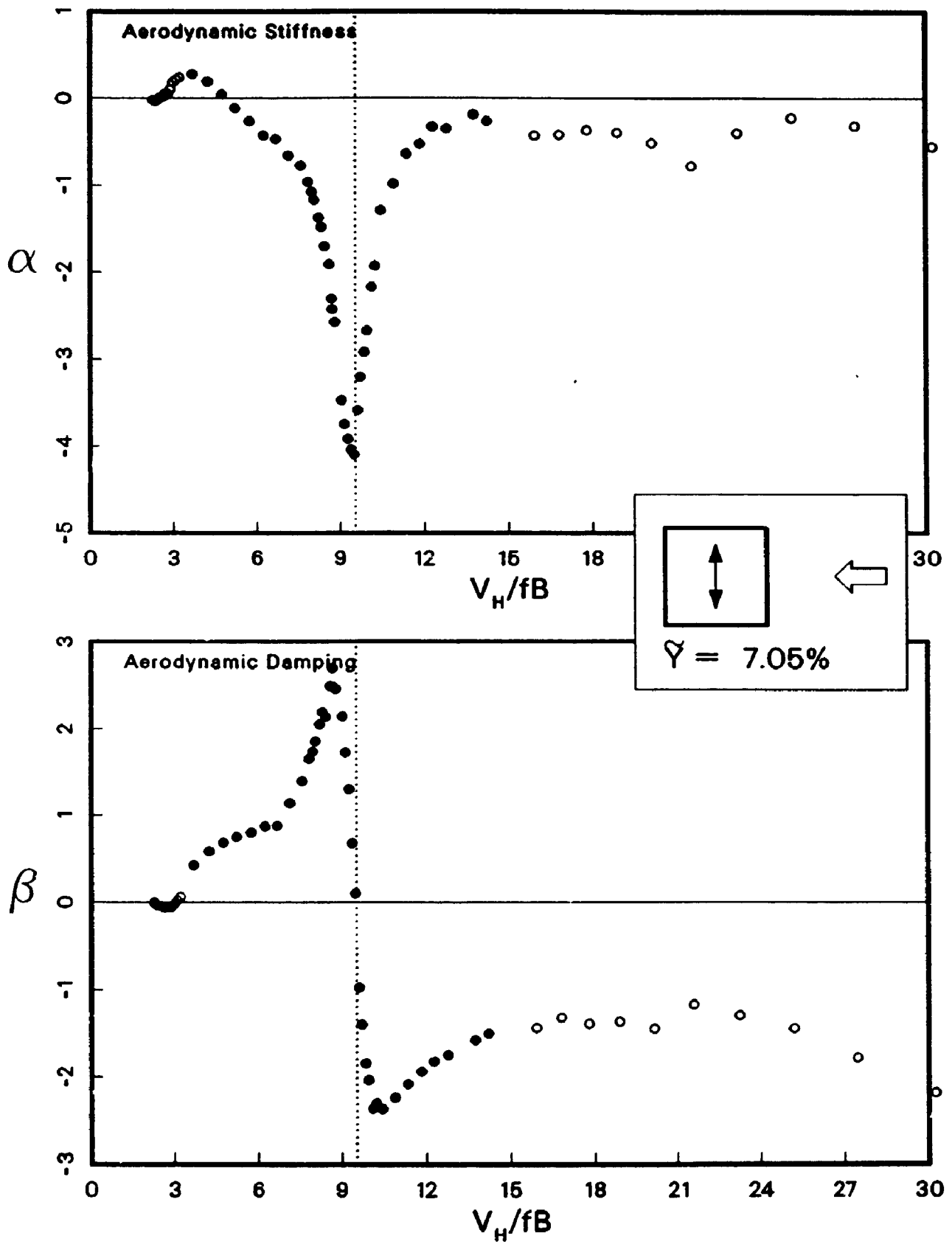
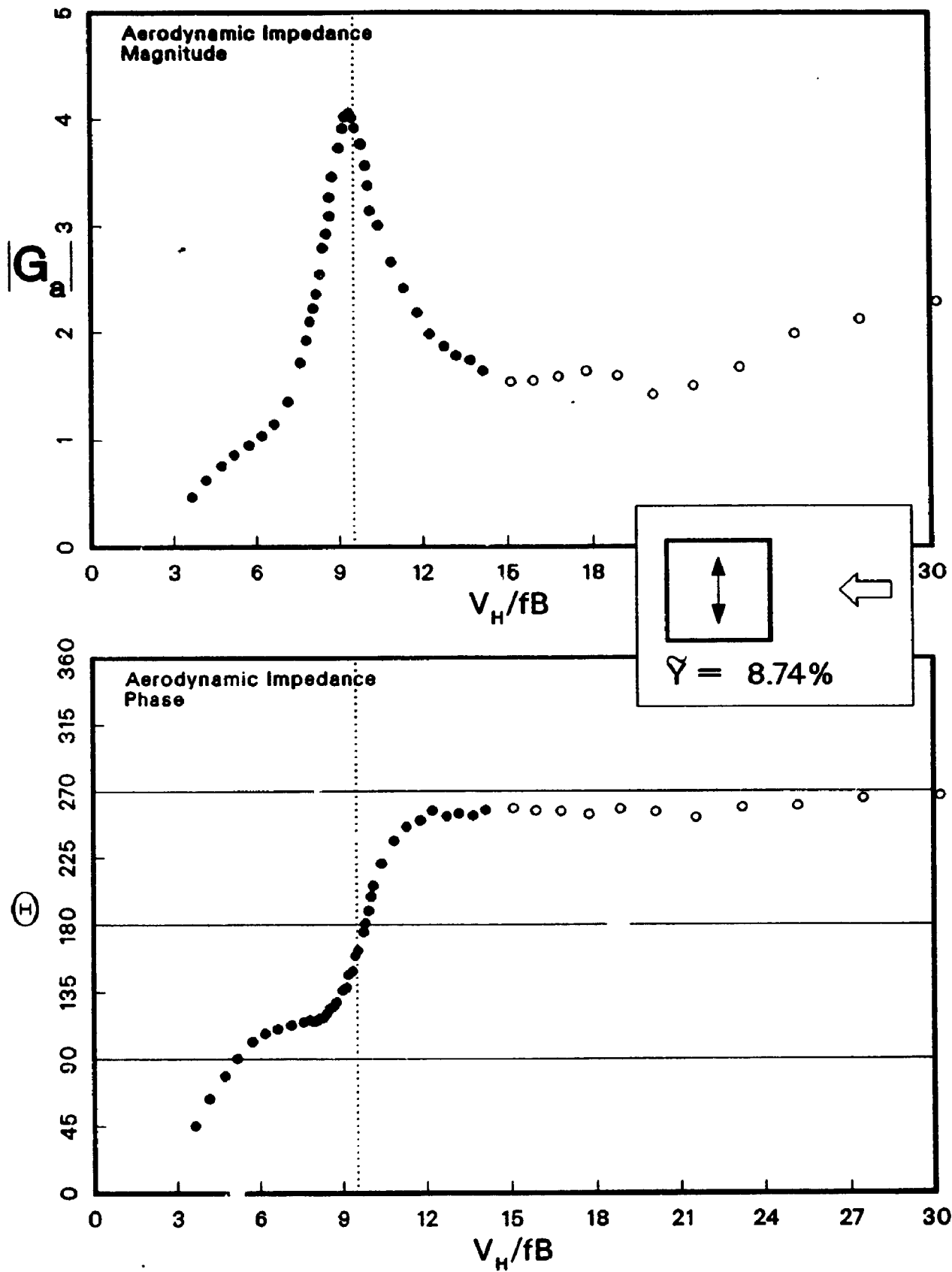Figure C.4: Aerodynamic Impedance for $Y = 7.05\%$, α, β
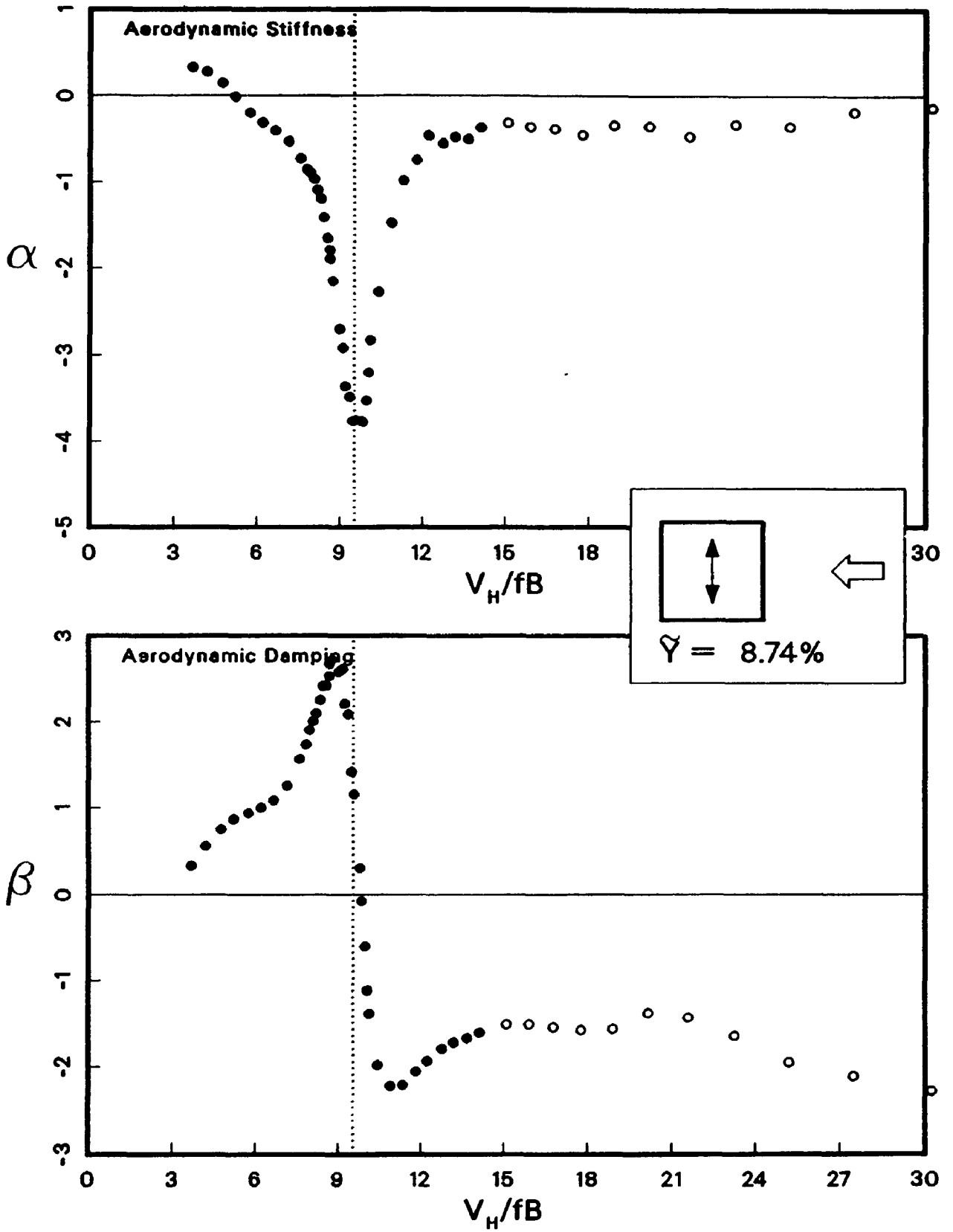
Figure C.5: Aerodynamic Impedance for $\tilde{Y} = 8.74\%$, α, β
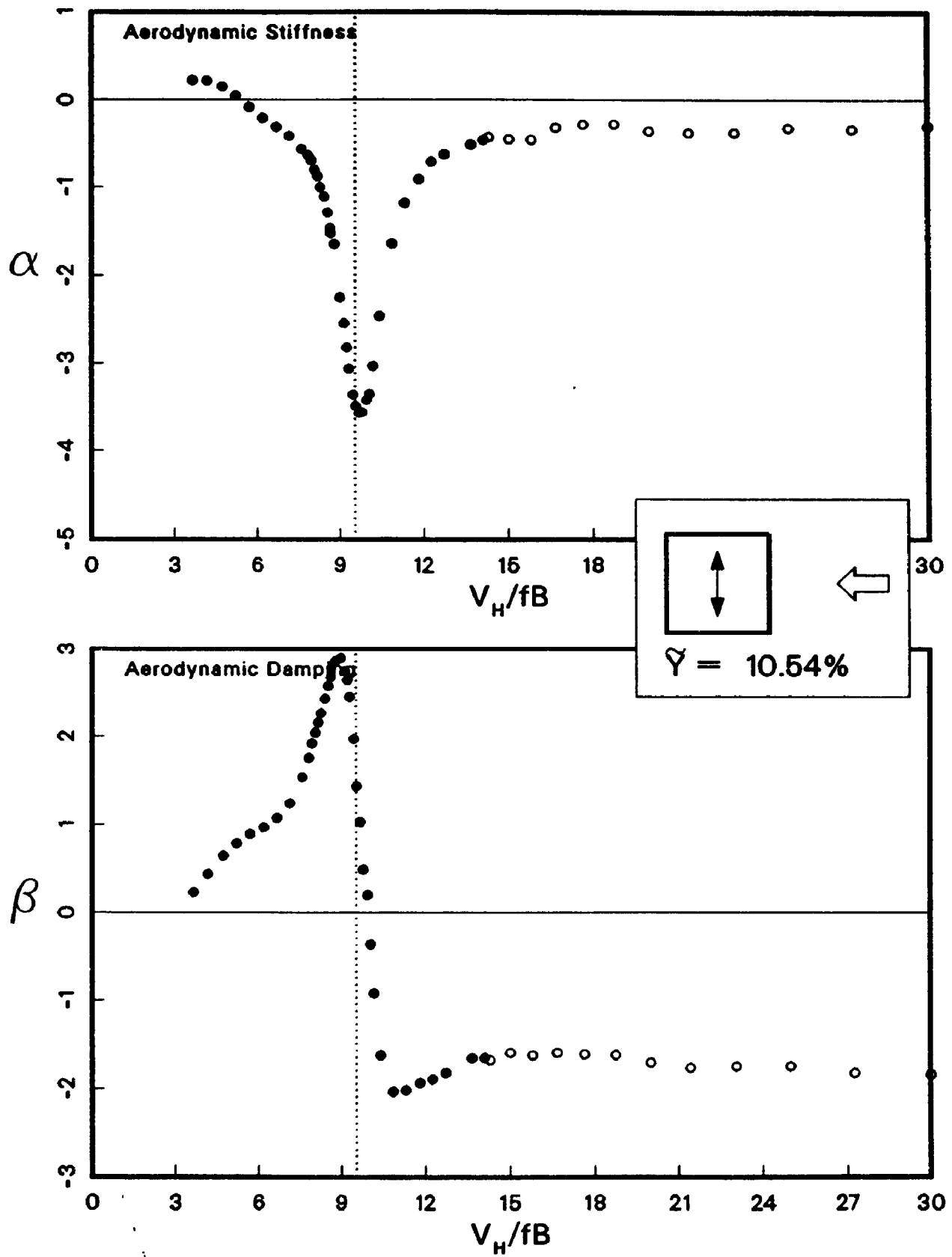
Figure C.6: Aerodynamic Impedance for $\tilde{Y} = 10.54\%$, α, β
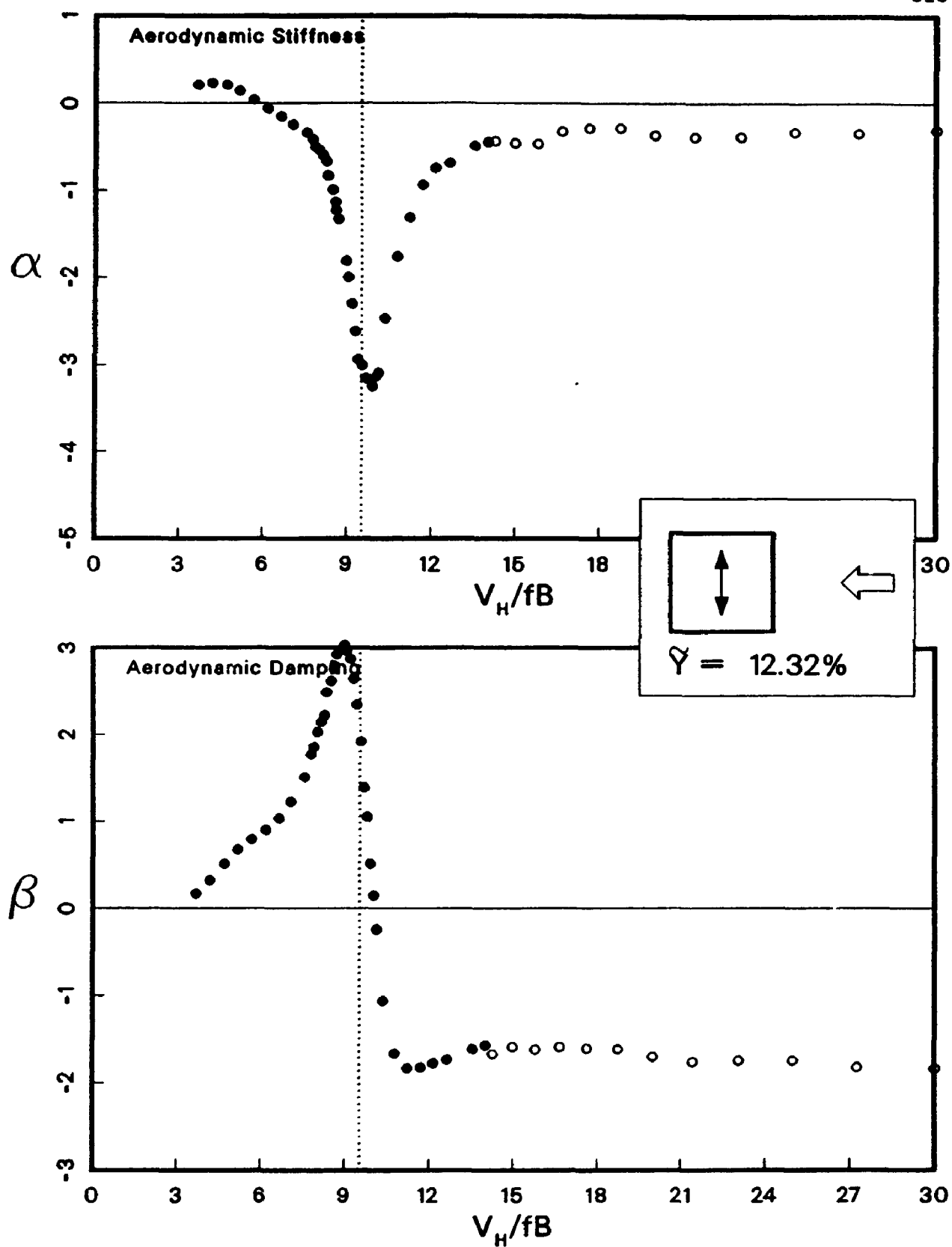
Figure C.7: Aerodynamic Impedance for $\tilde{Y} = 12.32\%$, α, β
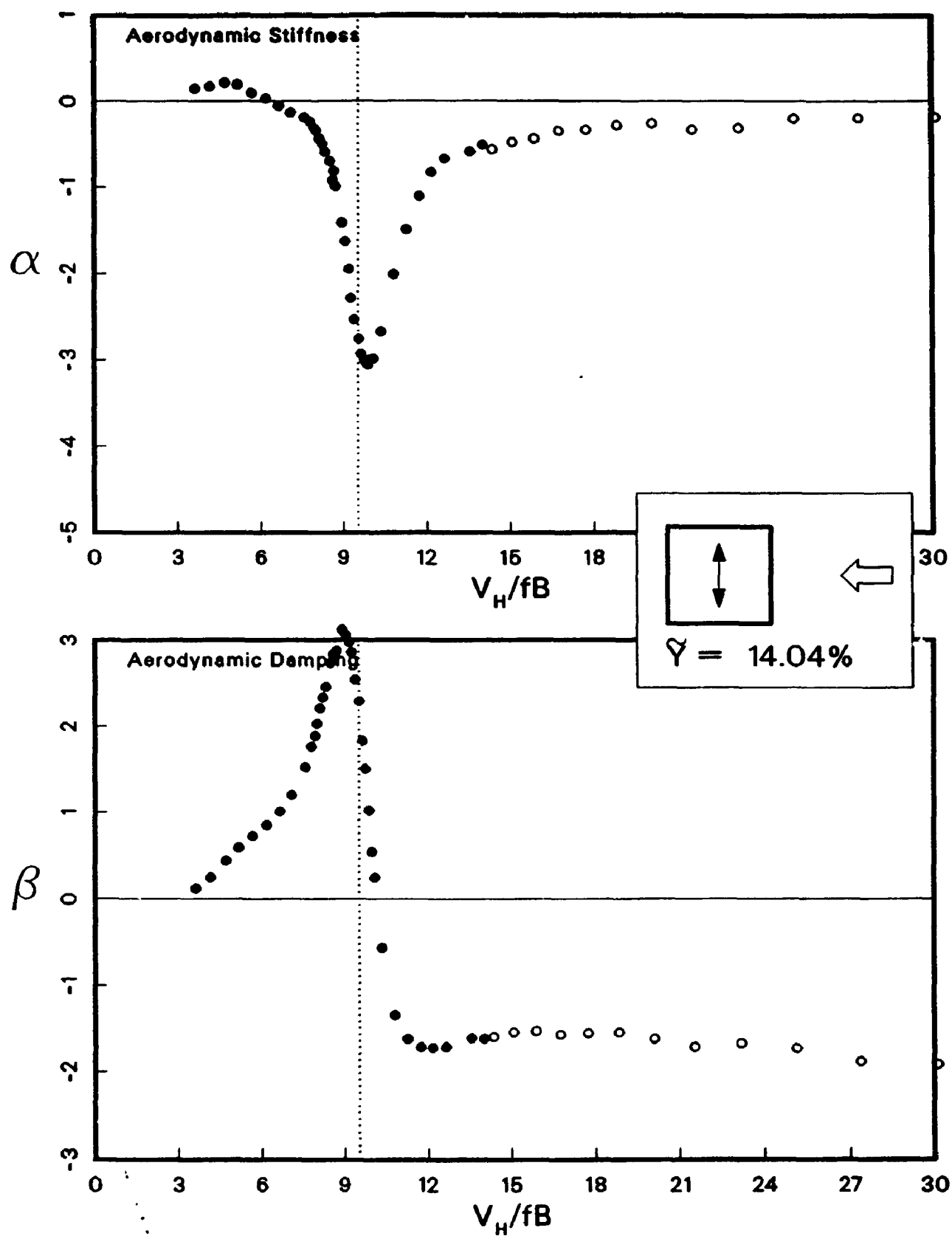
Figure C.8: Aerodynamic Impedance for $\tilde{Y} = 14.04\%$, α, β

Appendix D

Aerodynamic Impedances For The Square Prism, $|G_a|$, Θ
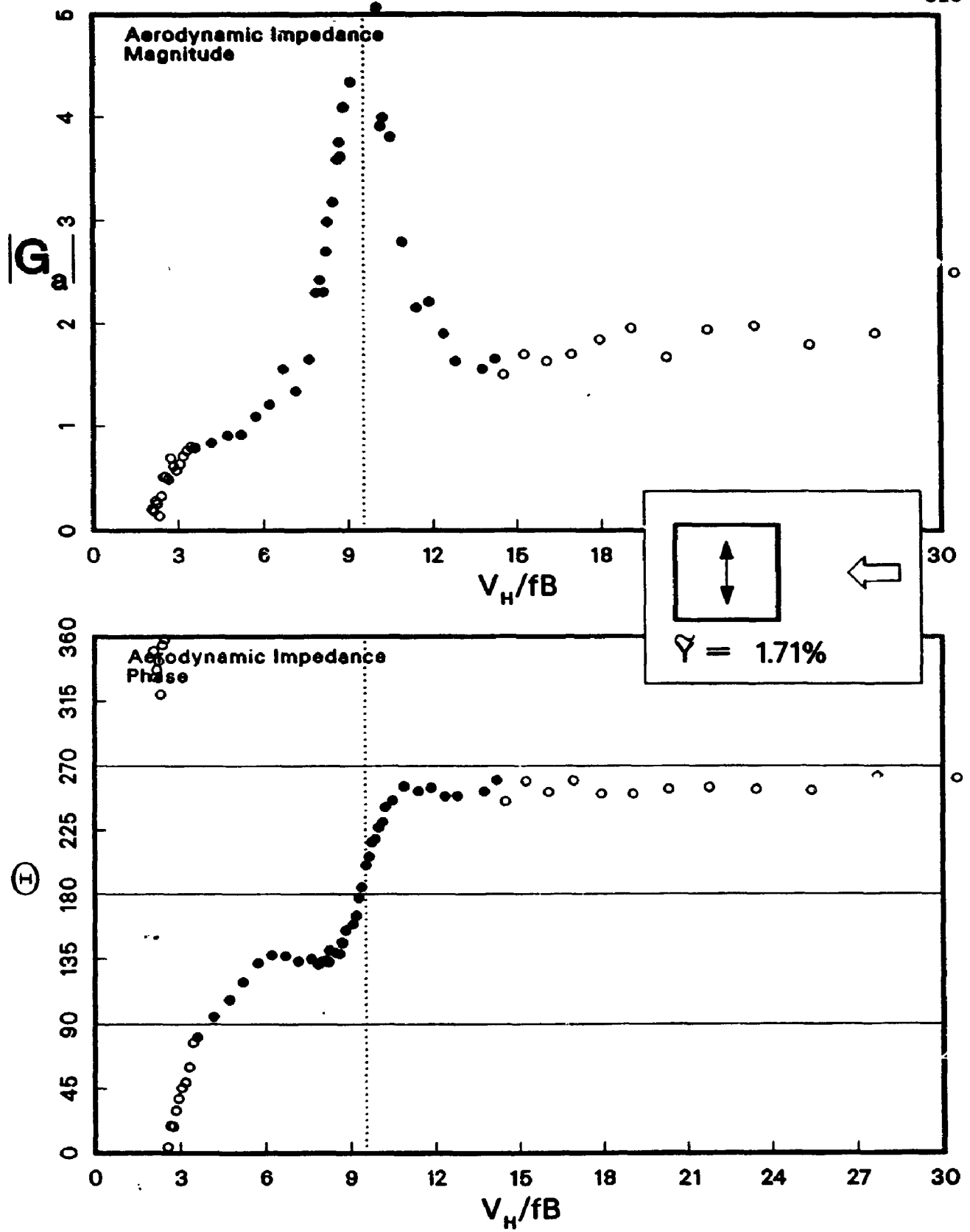
Figure D.1: Aerodynamic Impedance for $\tilde{Y} = 1.71\%$, $|G_a|$, Θ
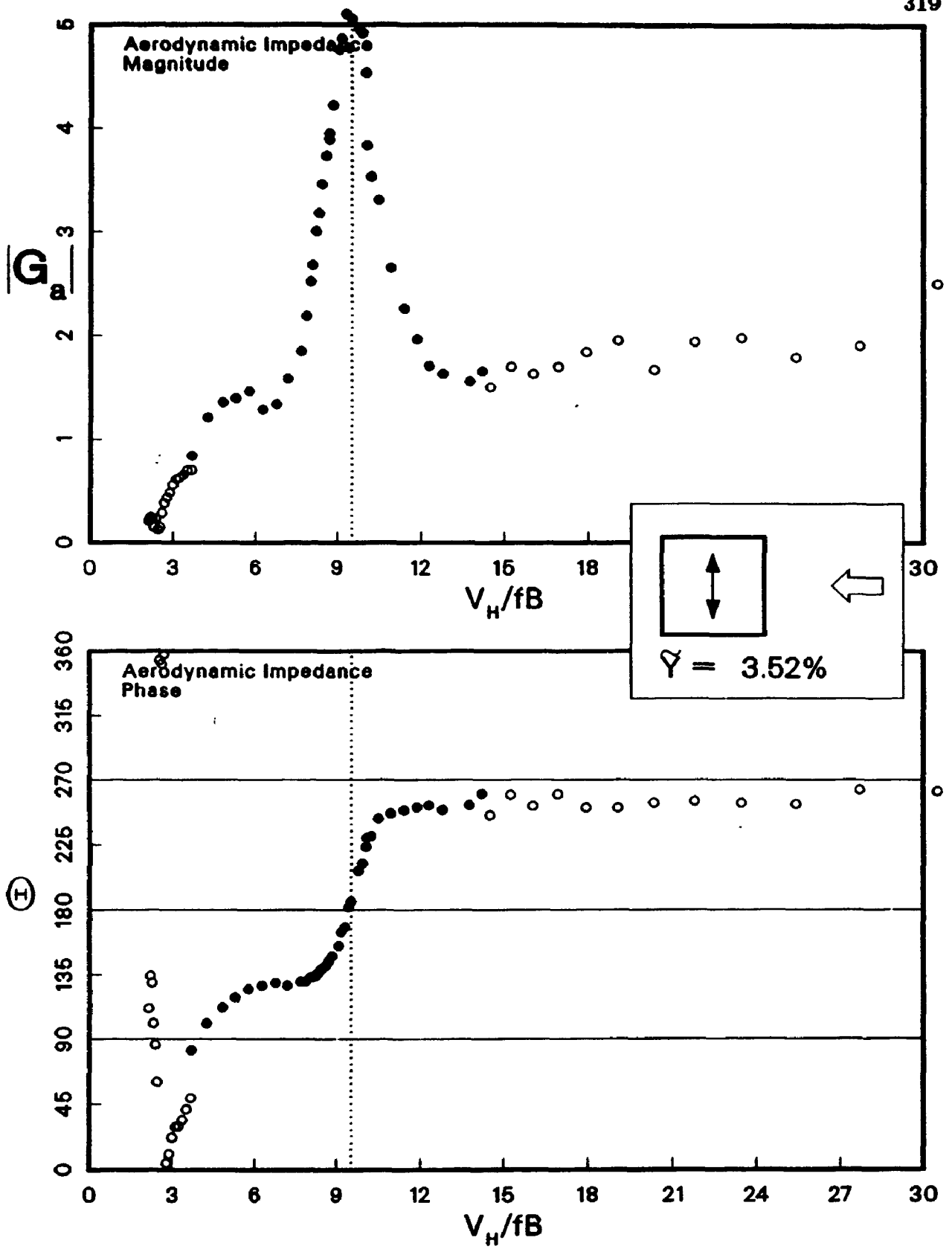
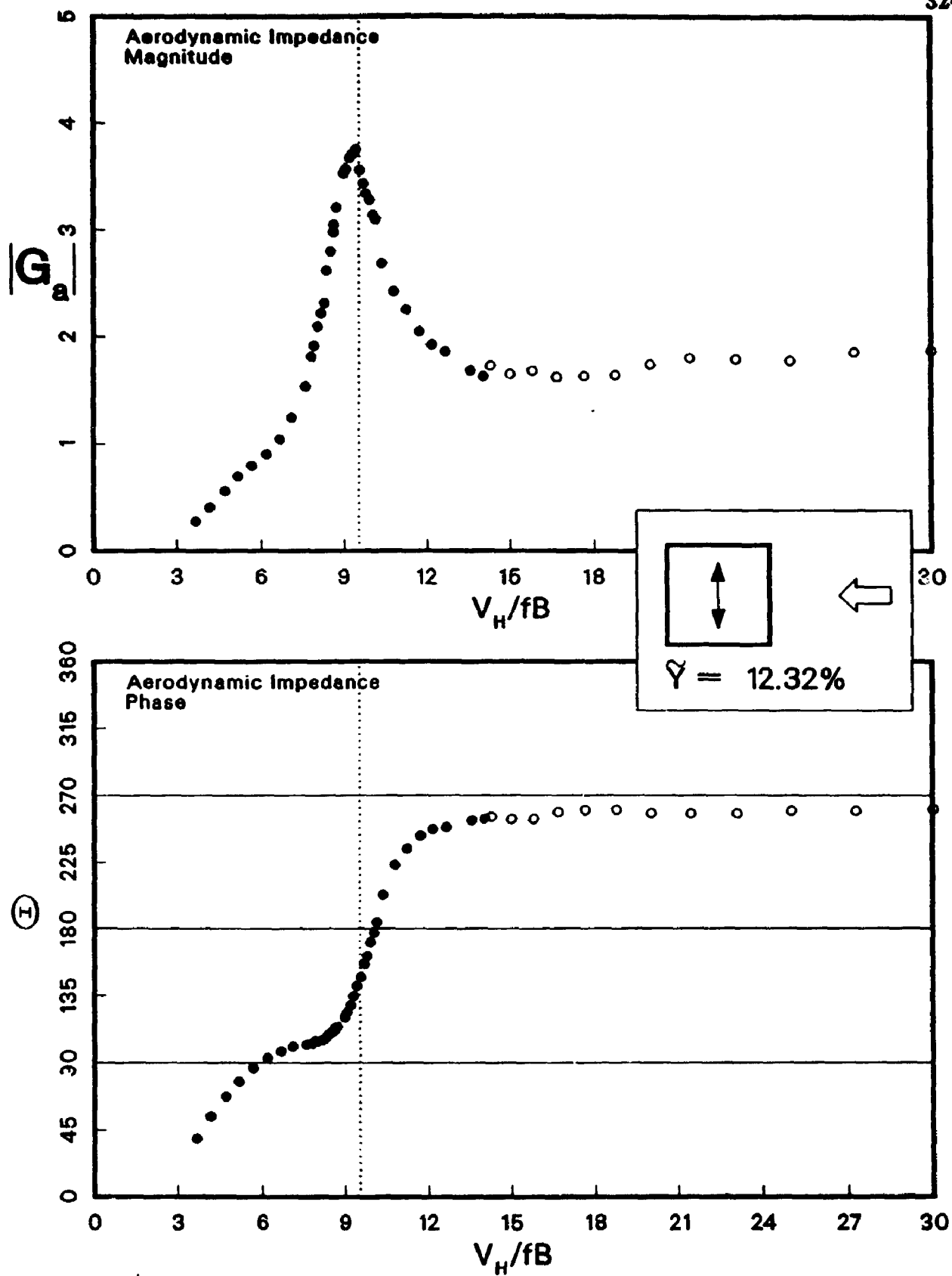Figure D.2: Aerodynamic Impedance for $\tilde{Y} = 3.52\%$, $|G_a|$, Θ
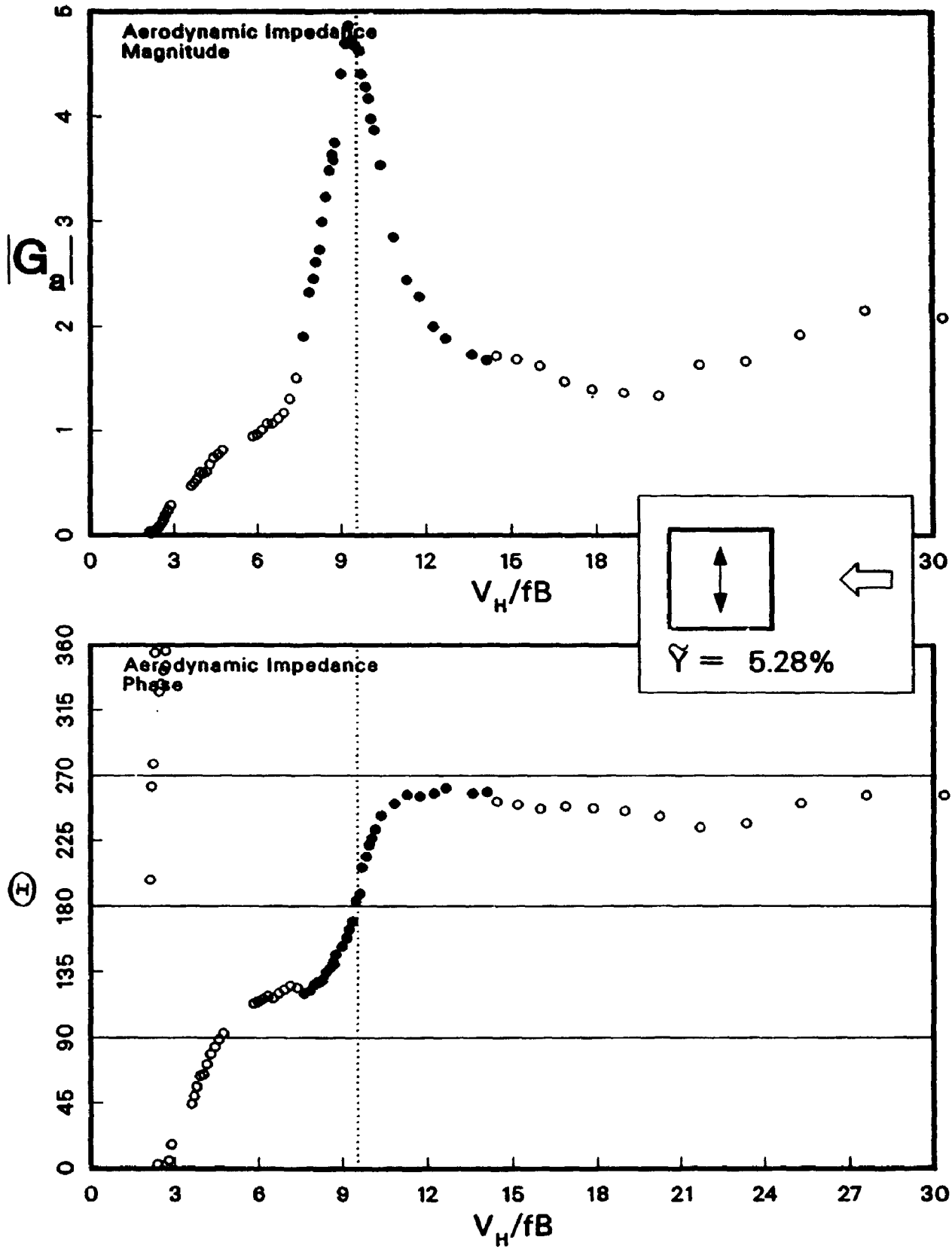
Figure D.3: Aerodynamic Impedance for $\tilde{Y} = 5.28\%$, $|G_a|$, Θ
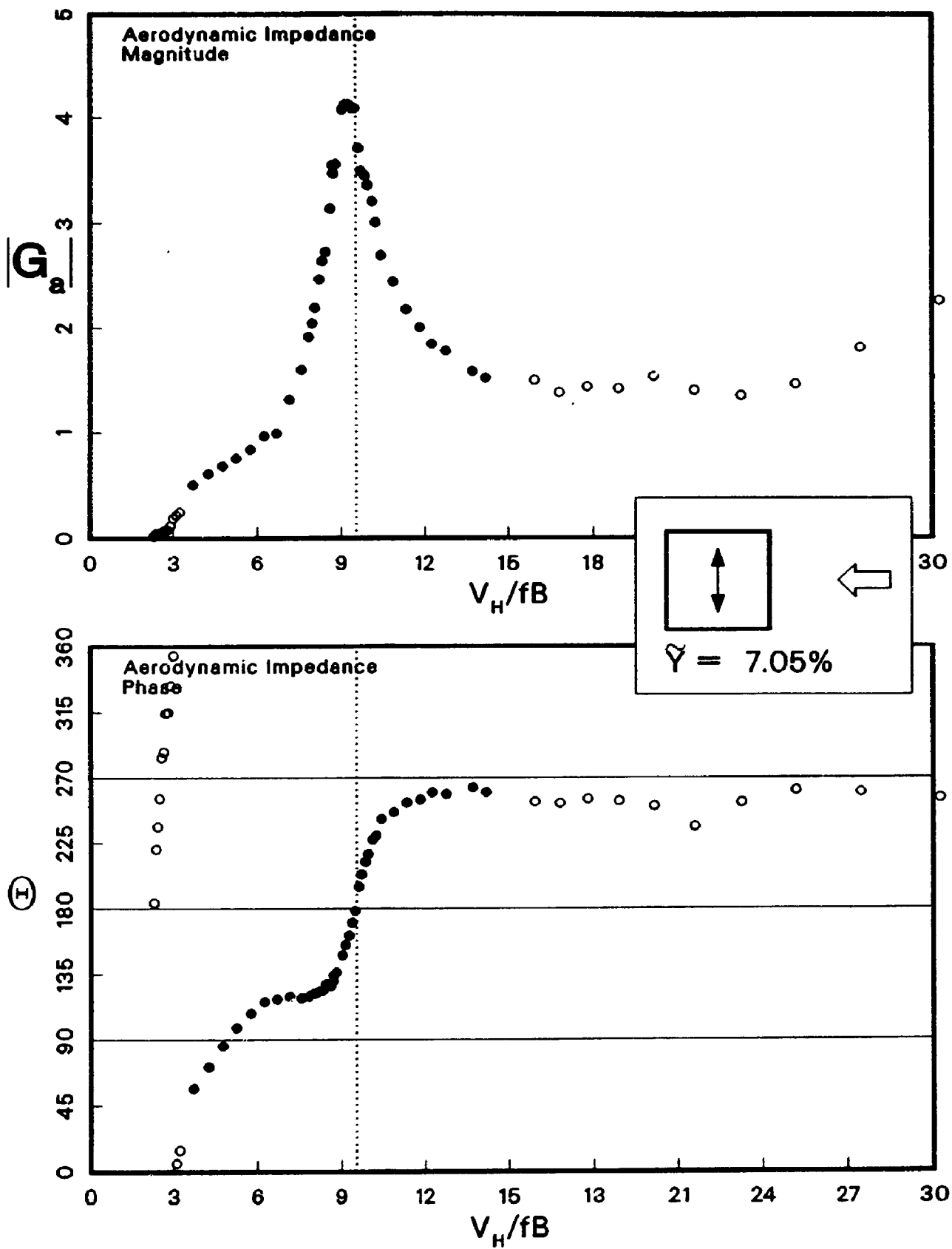
Figure D.4: Aerodynamic Impedance for $\hat{Y} = 7.05\%$, $|G_a|$, Θ

Figure D.5: Aerodynamic Impedance for $\tilde{Y} = 8.74\%$, $|G_a|$, Θ
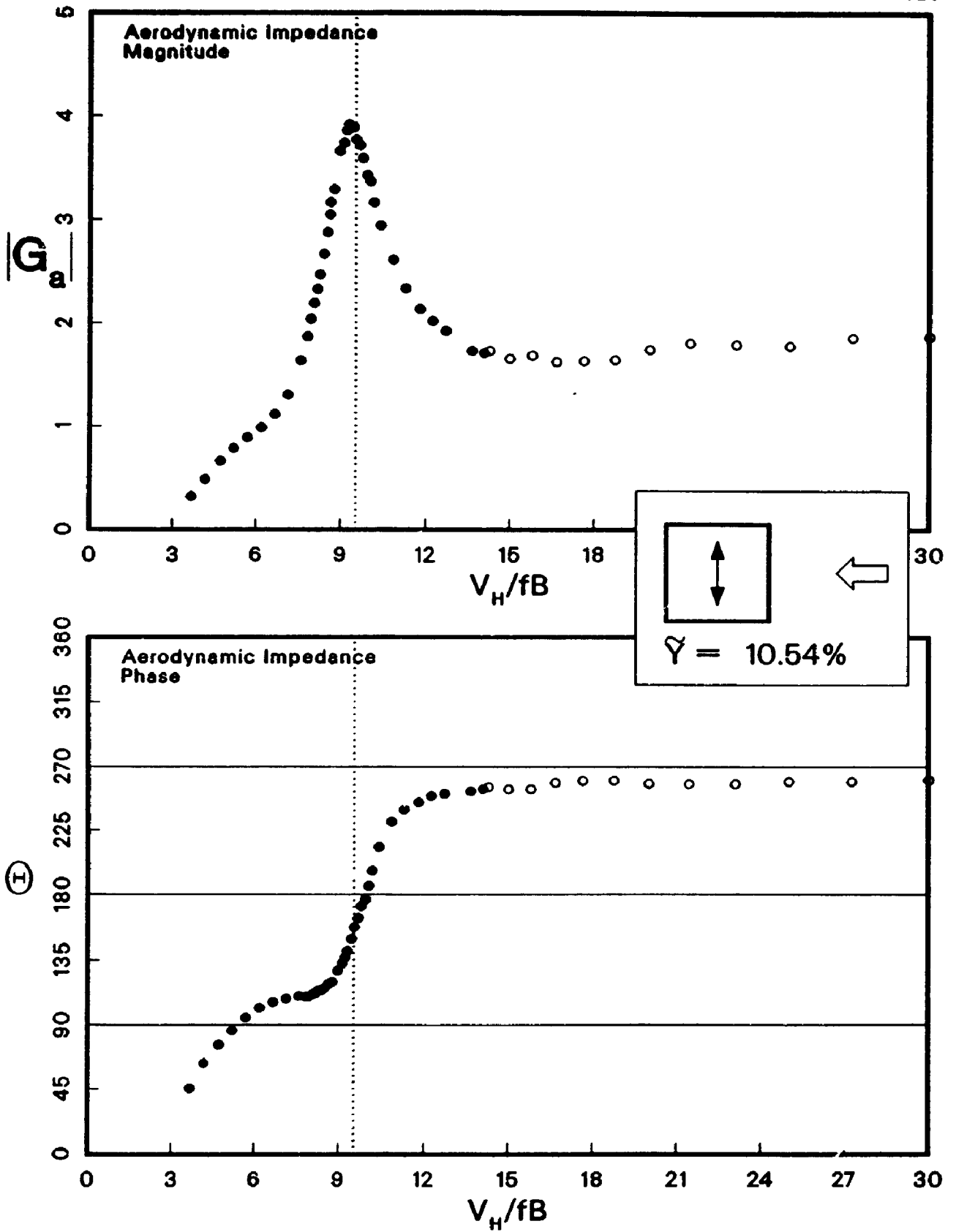
Figure D.6: Aerodynamic Impedance for $\tilde{Y} = 10.54\%$, $|G_a|$, Θ

Figure D.7: Aerodynamic Impedance for $\tilde{Y} = 12.32\%$, $|G_a|$, Θ
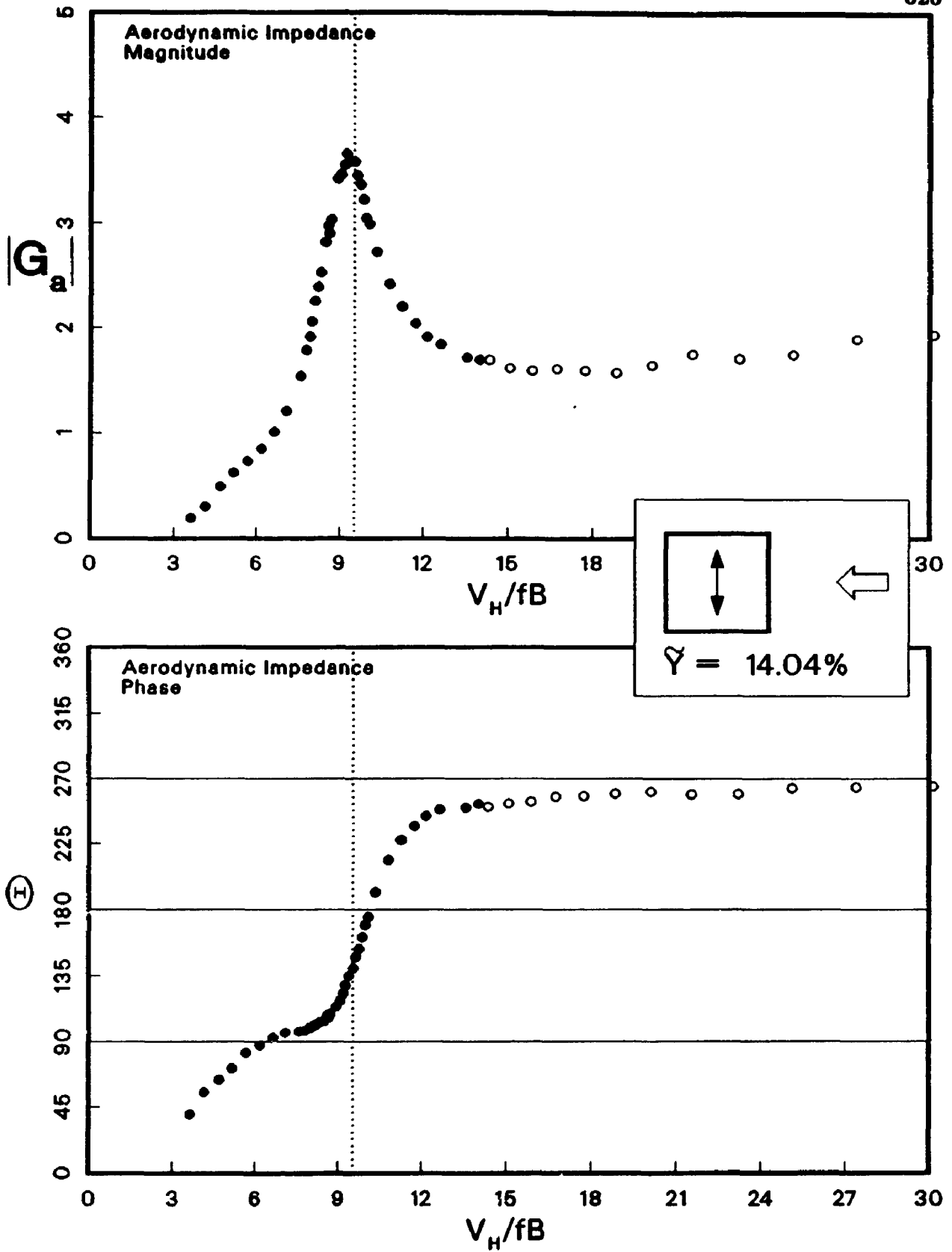
Figure D.8: Aerodynamic Impedance for $\tilde{Y} = 14.04\%$, $|G_a|$, Θ

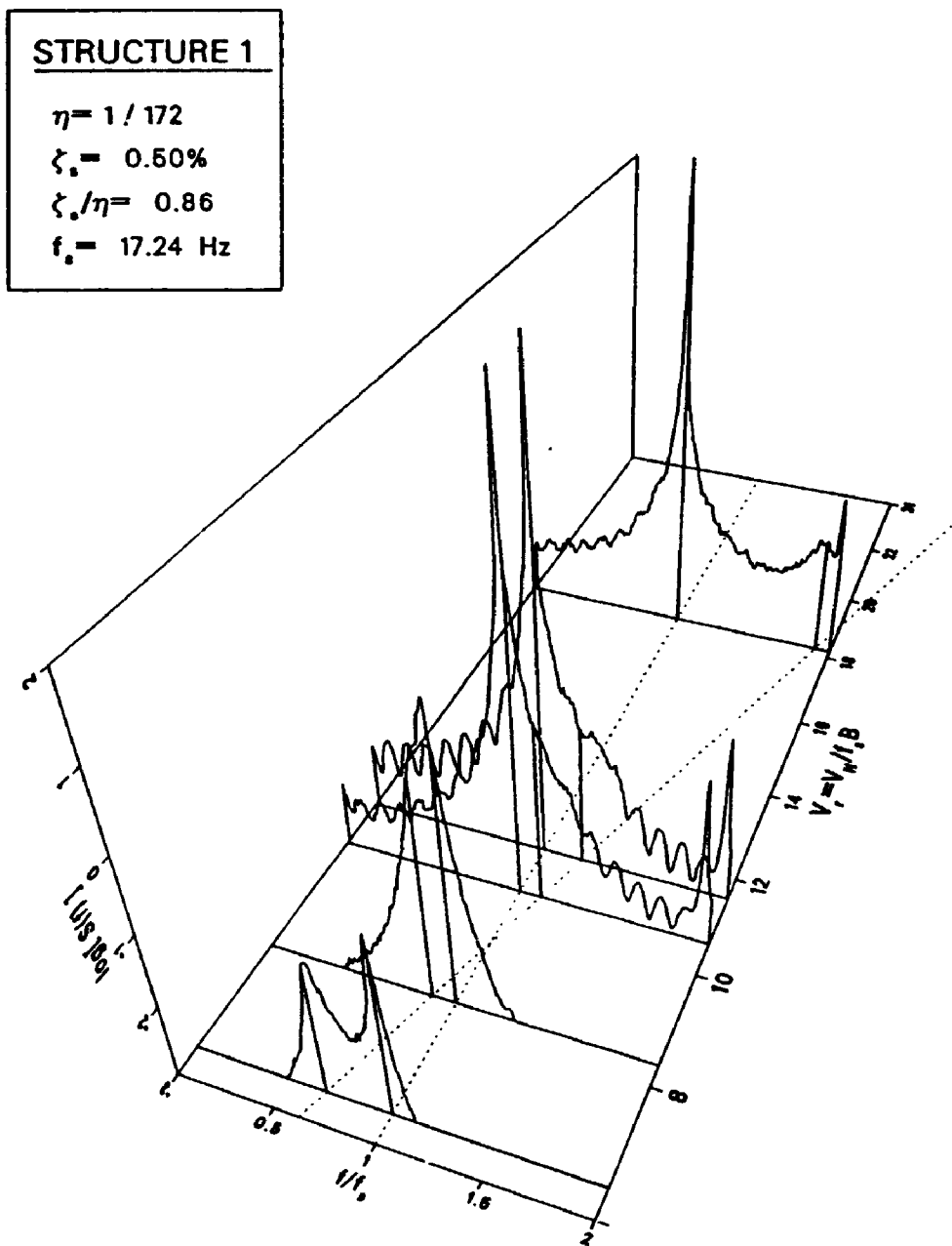# Appendix E

Auto-Spectra from the Aeroelastic Tests

STRUCTURE 1

$\eta = 1 / 172$

$\zeta_s = 0.50\%$

$\zeta_s/\eta = 0.86$

$f_s = 17.24$ Hz

Figure E.1: Auto-Spectra for Aeroelastic Model Structure 1

STRUCTURE 2

$\eta = 1 / 172$

$\zeta_{\bullet} = 1.08\%$

$\zeta_{\bullet}/\eta = 1.86$

$f_{\bullet} = 17.24$ Hz
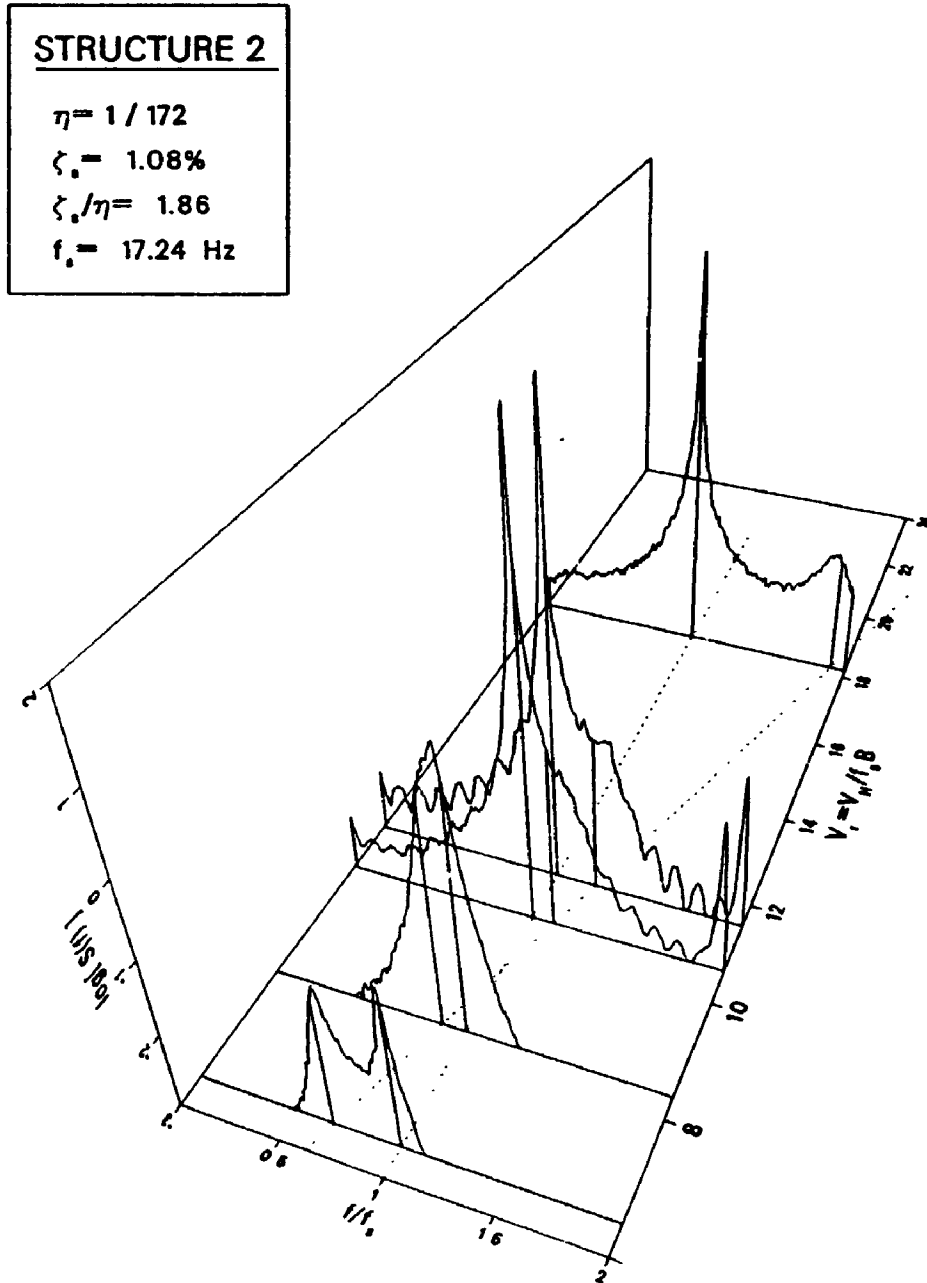
Figure E.2: Auto-Spectra for Aeroelastic Model Structure 2

STRUCTURE 3

$\eta = 1 / 172$

$\zeta_s = 2.44\%$

$\zeta_s/\eta = 4.20$

$f_s = 17.24$ Hz
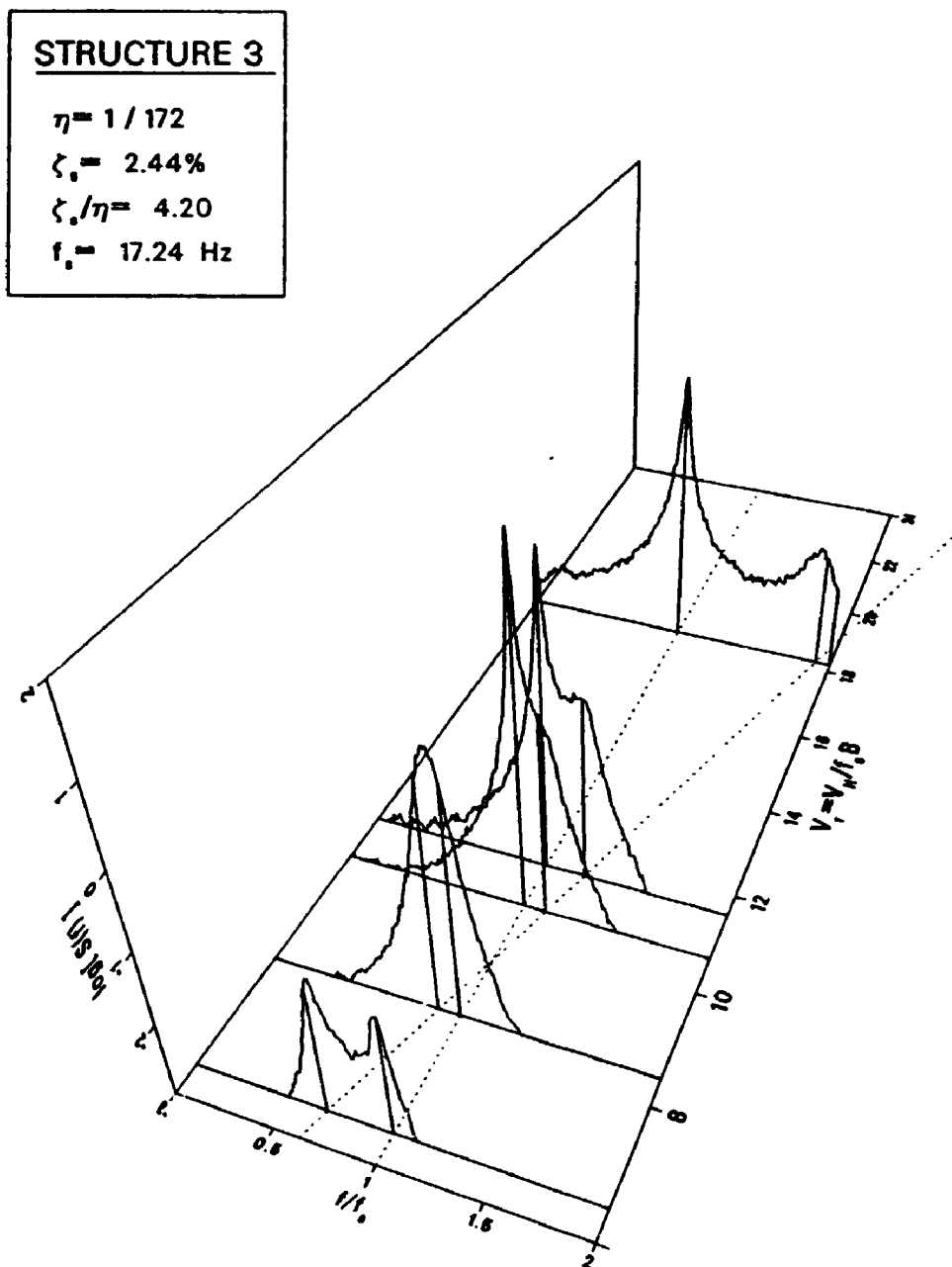
Figure E.3: Auto-Spectra for Aeroelastic Model Structure 3

STRUCTURE 4

$\eta = 1 / 284$

$\zeta_s = 4.75\%$

$\zeta_s/\eta = 13.49$

$f_s = 13.42$ Hz
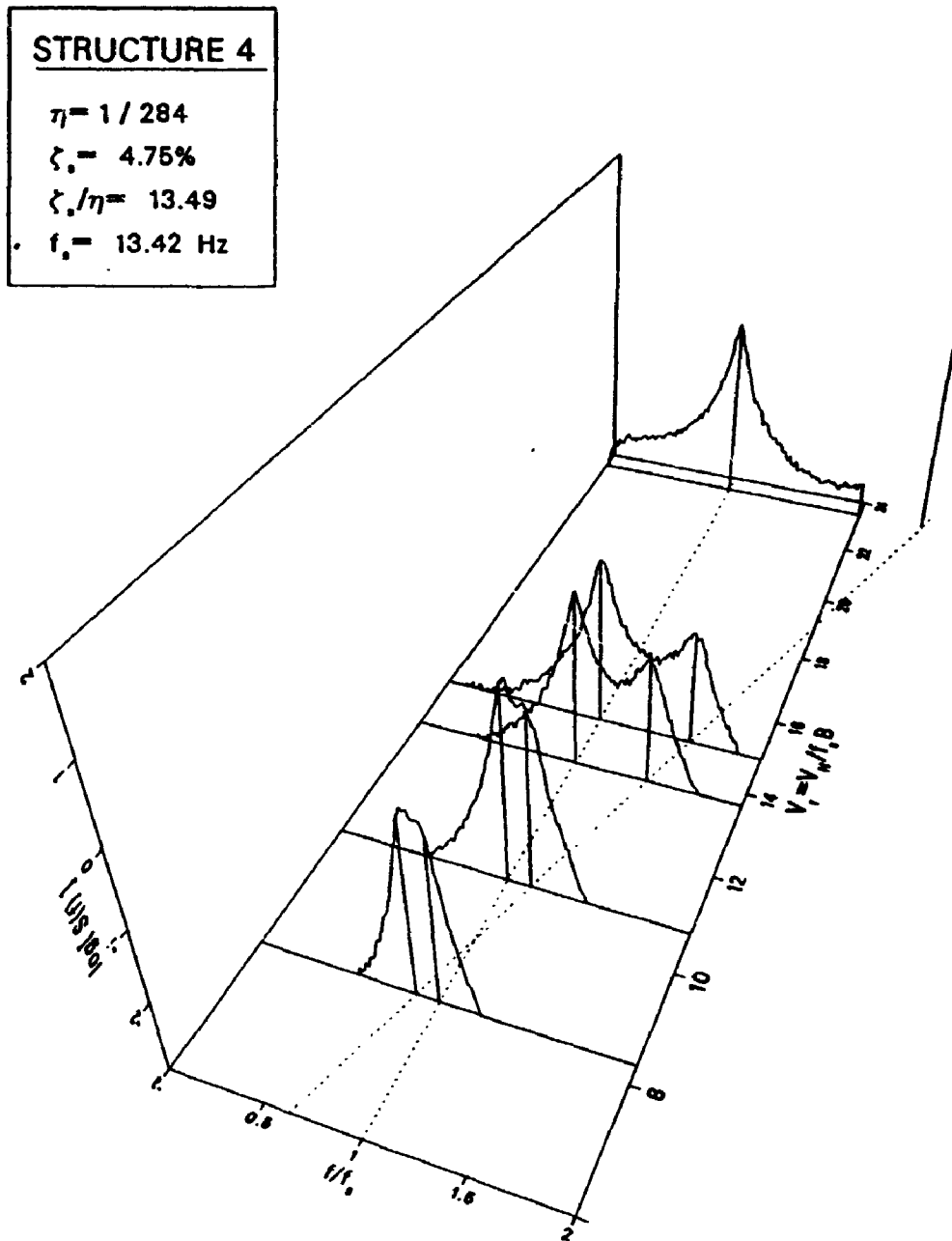
Figure E.4: Auto-Spectra for Aeroelastic Model Structure 4

STRUCTURE 5

η= 1 / 284

ζ_a= 8.80%
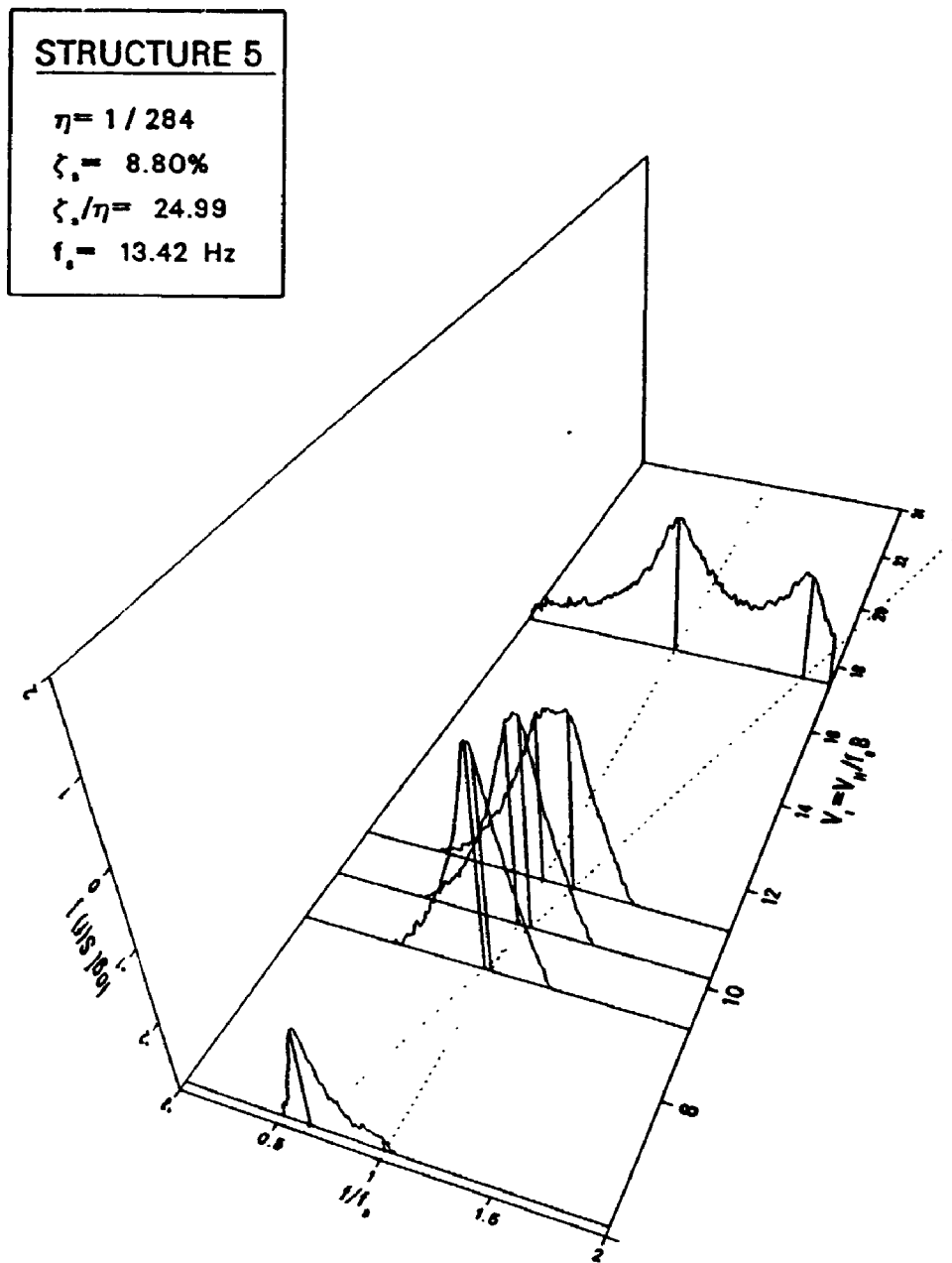
ζ_a/η= 24.99

f_a= 13.42 Hz

Figure E.5: Auto-Spectra for Aeroelastic Model Structure 5

Appendix F

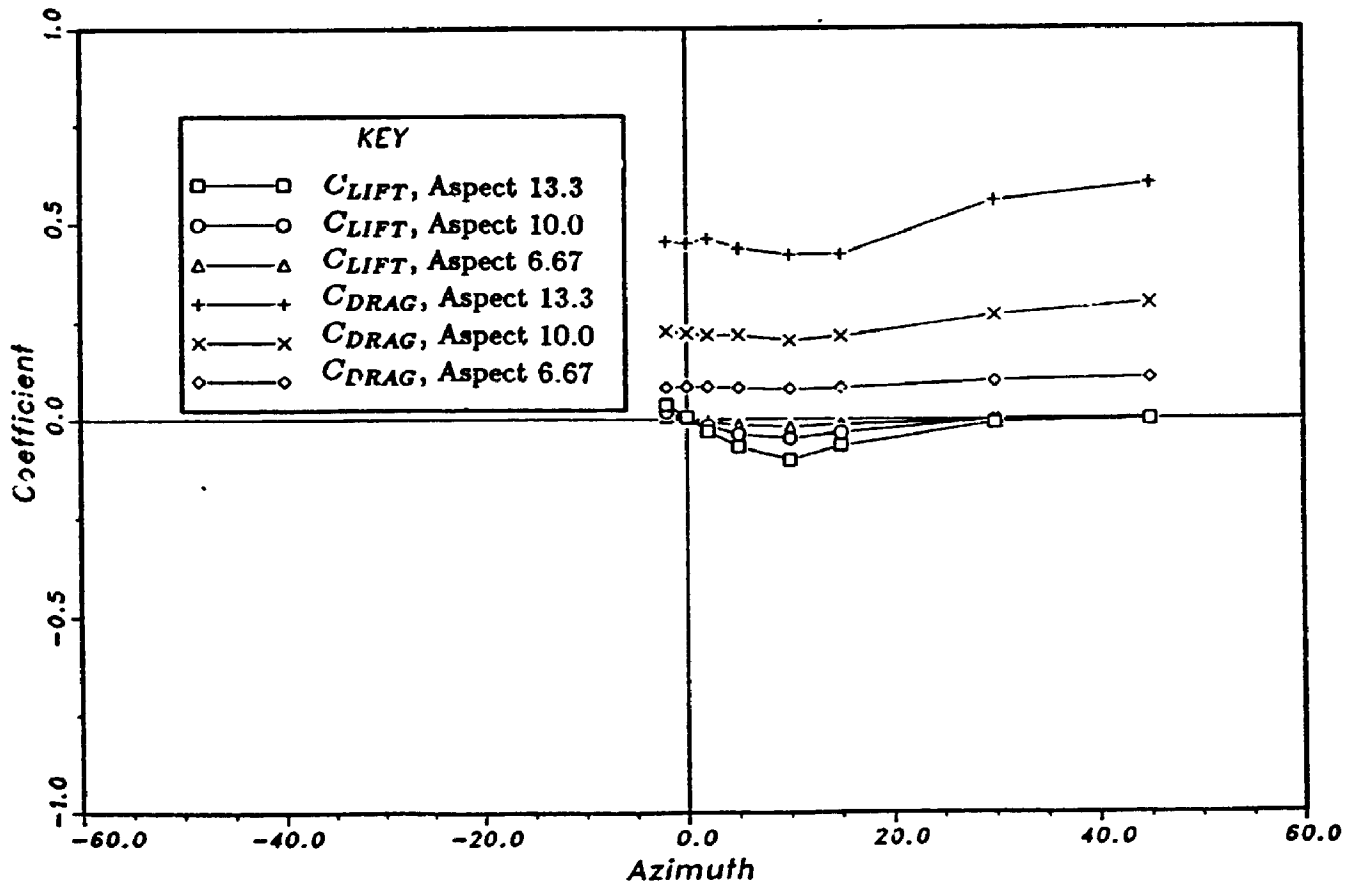# Moment Coefficients for Various Shaped Prism

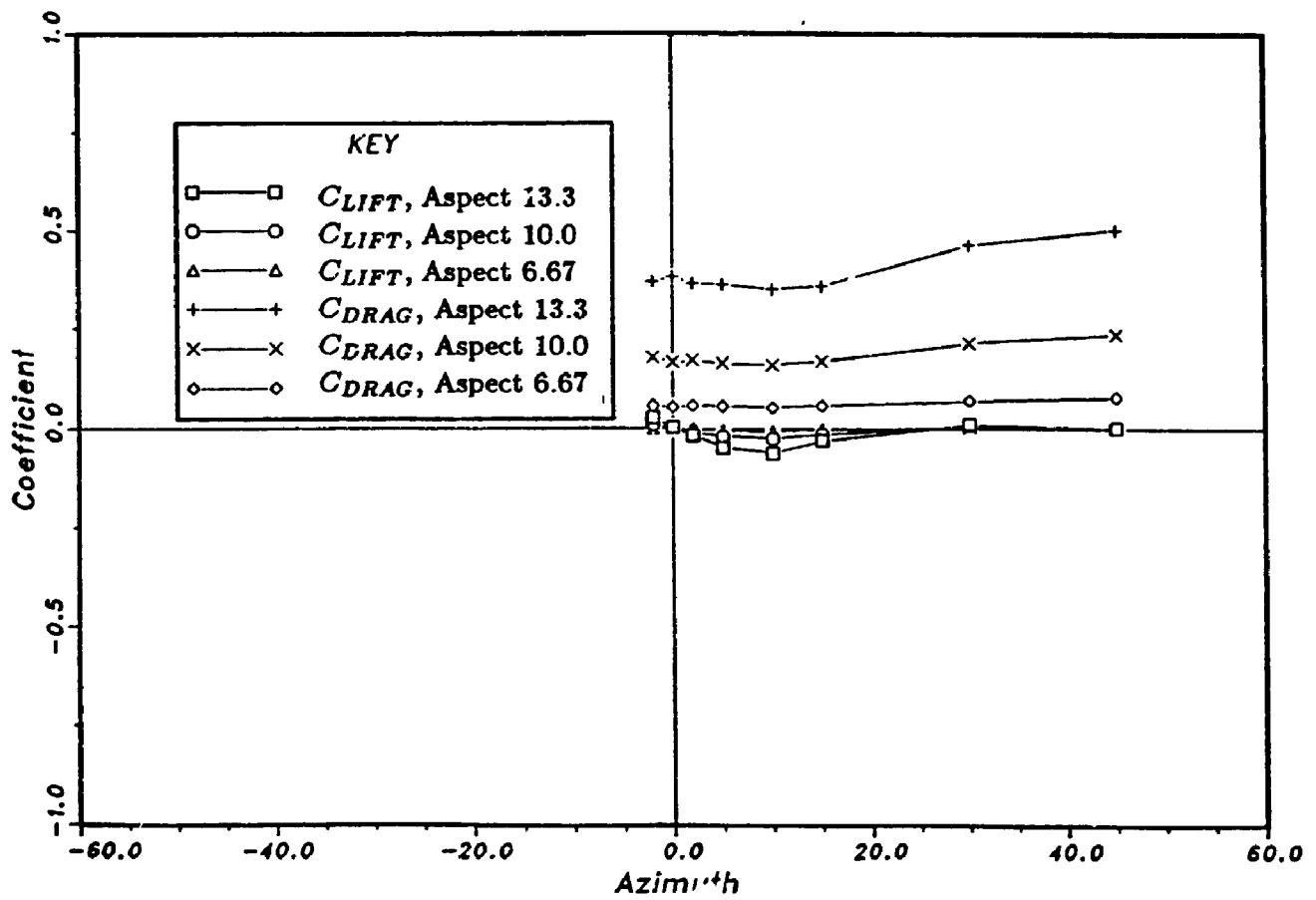Figure F.1: Moment Coefficients, Shape C, Exposure 1

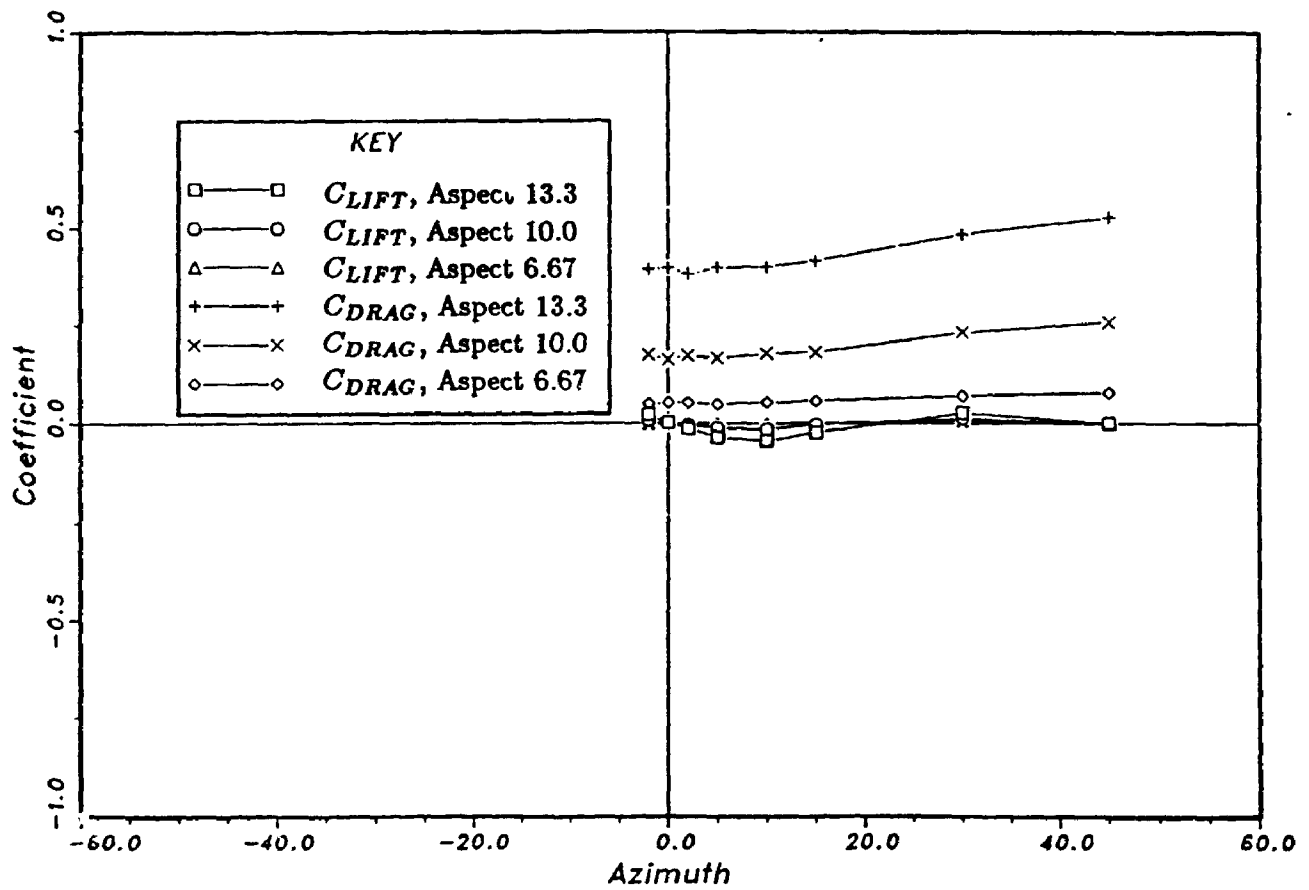Figure F.2: Moment Coefficients, Shape C, Exposure 2

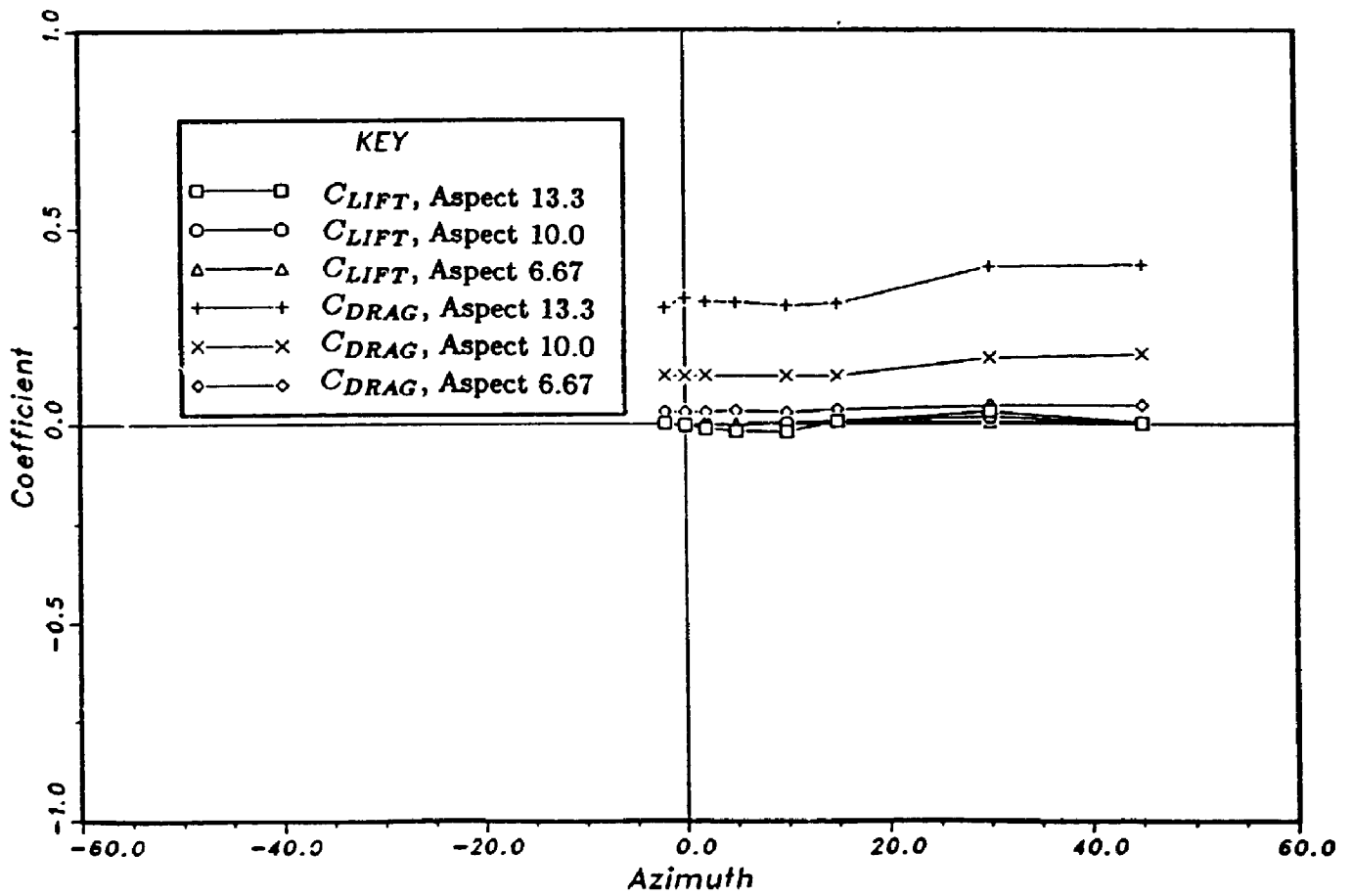Figure F.3: Moment Coefficients, Shape C, Exposure 3

Figure F.4: Moment Coefficients, Shape C, Exposure 4

Figure F.5: Moment Coefficients, Shape C, Aspect 6.67:1
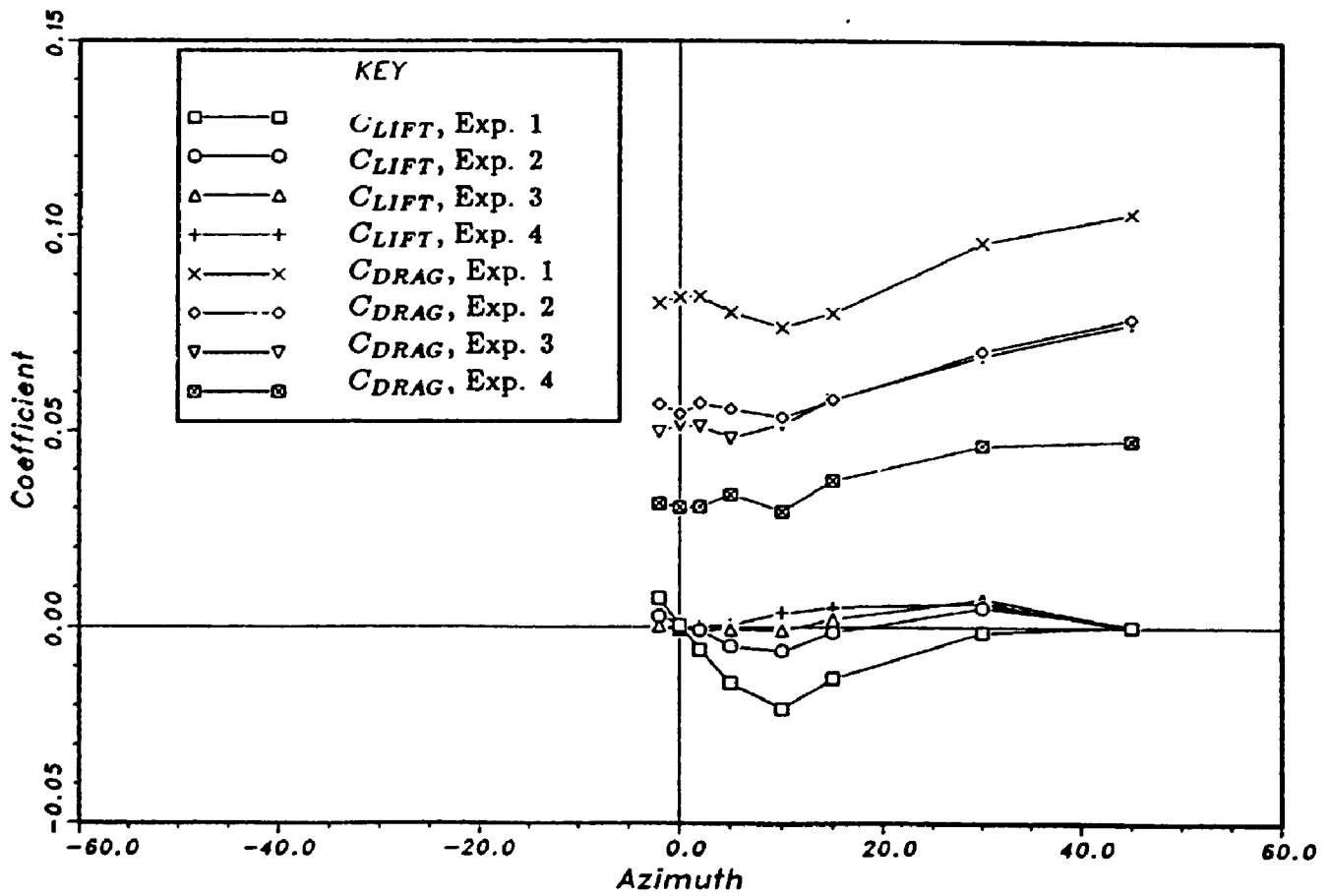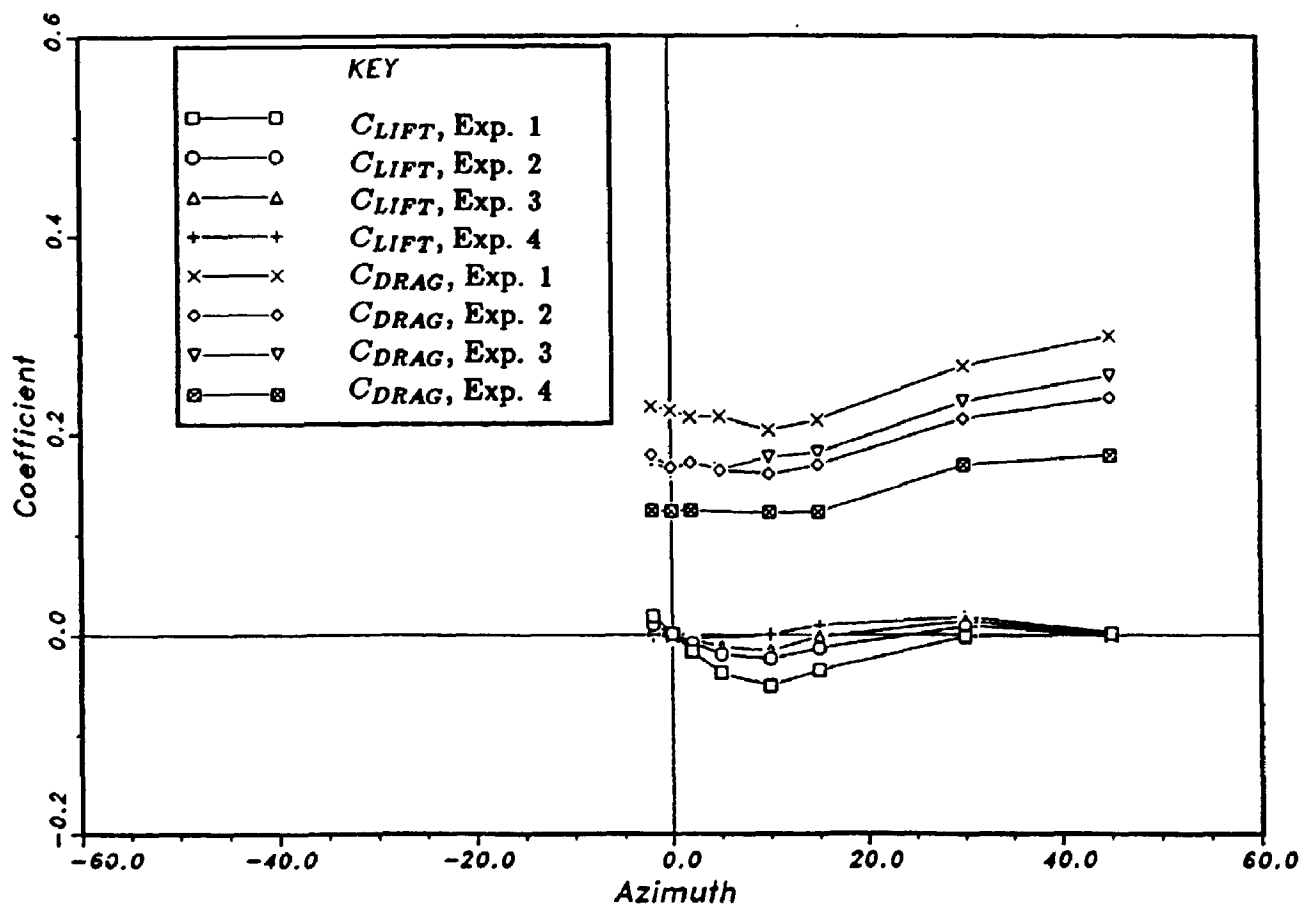
Figure F.6: Moment Coefficients, Shape C, Aspect 10:1

Figure F.7: Moment Coefficients, Shape C, Aspect 13.3:1

Figure F.8: Moment Coefficients, Shape B, Aspect 13.3, Exposure 2

Figure F.9: Moment Coefficients, Shape C, Aspect 13.3, Exposure 2

Figure F.10: Moment Coefficients, Shape D, Aspect 13.3, Exposure 2

Figure F.11: Moment Coefficients, Shape E, Aspect 13.3, Exposure 2

Figure F.12: Moment Coefficients, Shape F, Aspect 13.3, Exposure 2
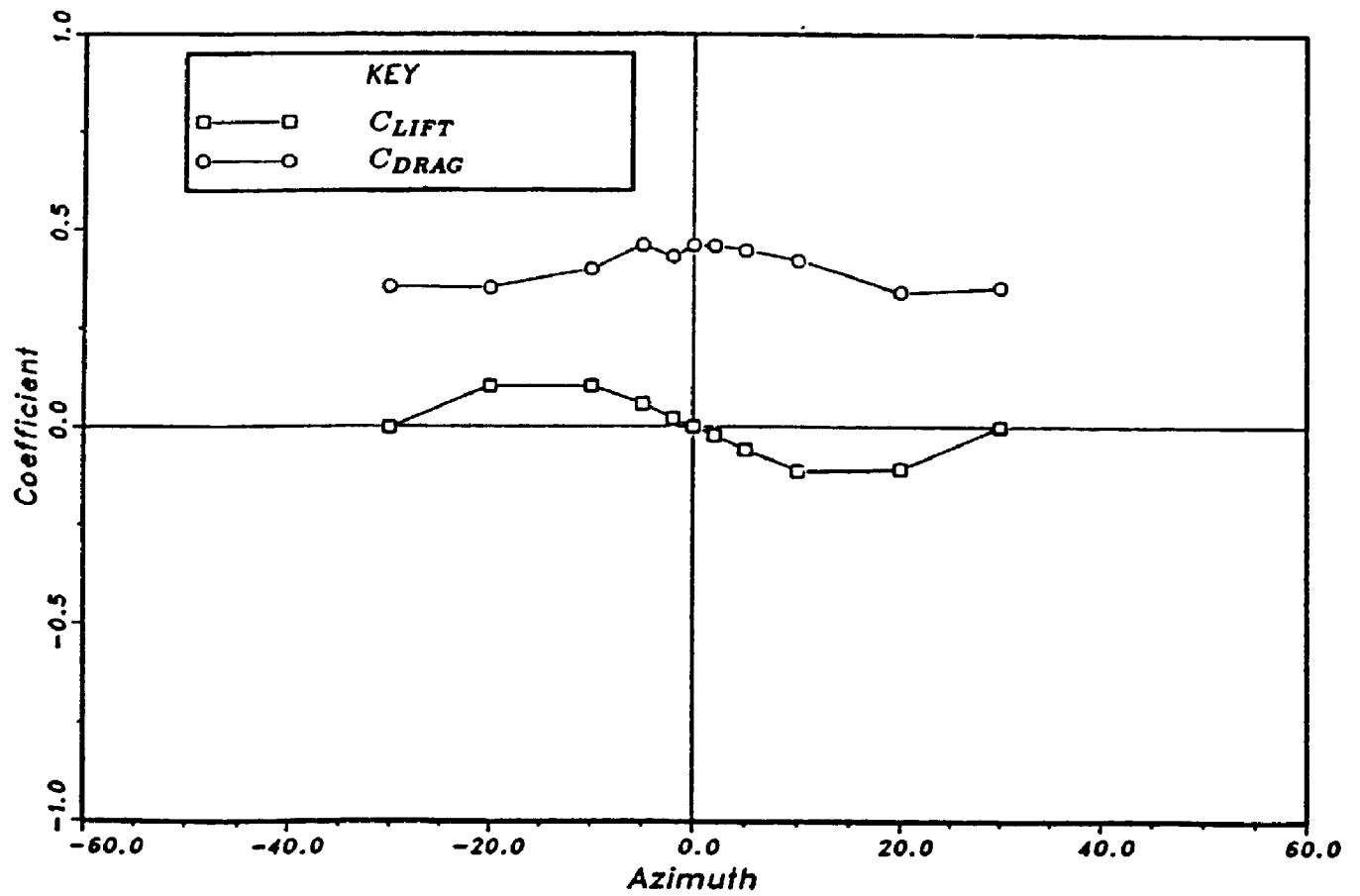
Figure F.13: Moment Coefficients, Shape G, Aspect 13.3, Exposure 2
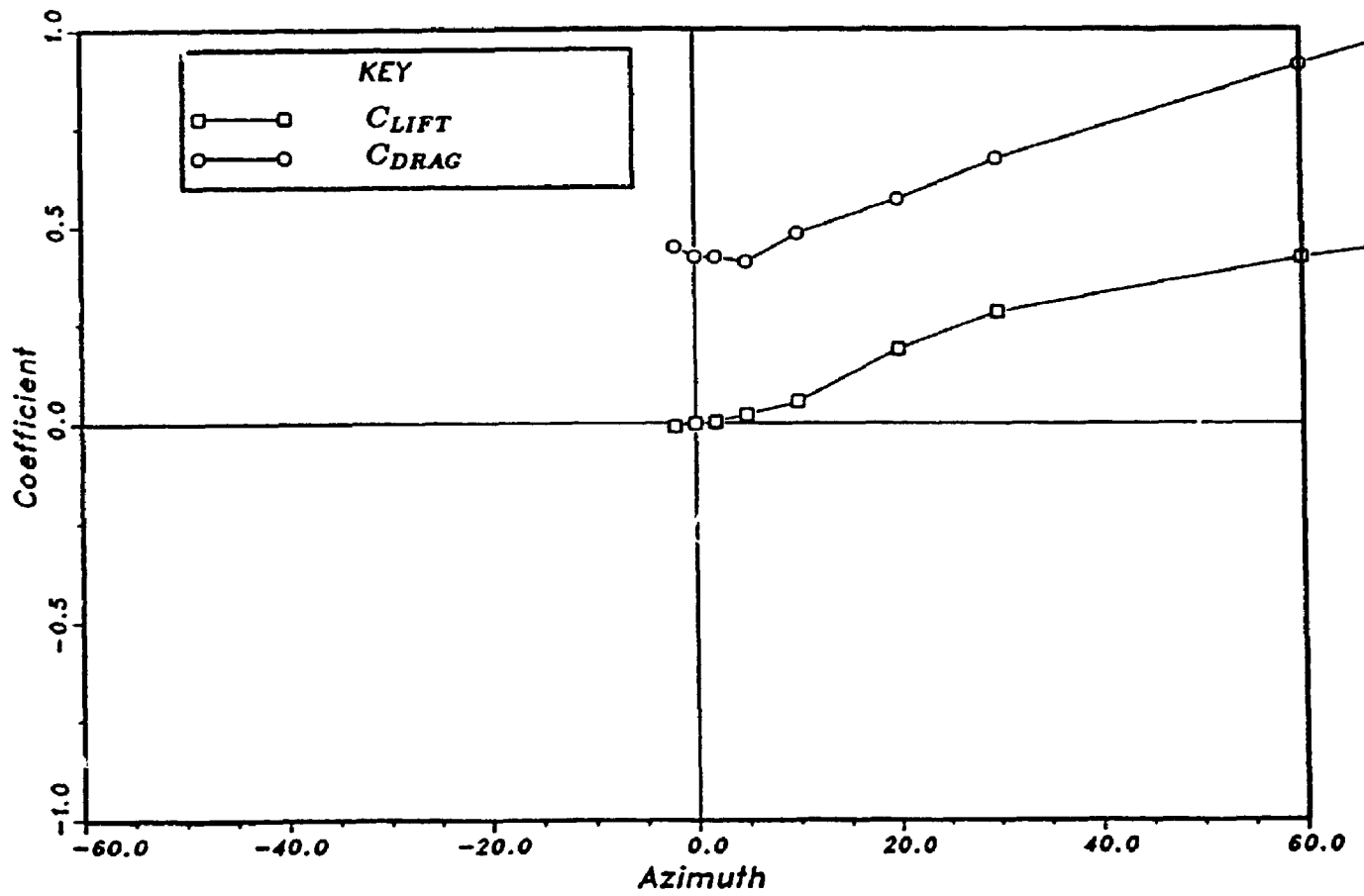
Figure F.14: Moment Coefficients, Shape H, Aspect 13.3, Exposure 2
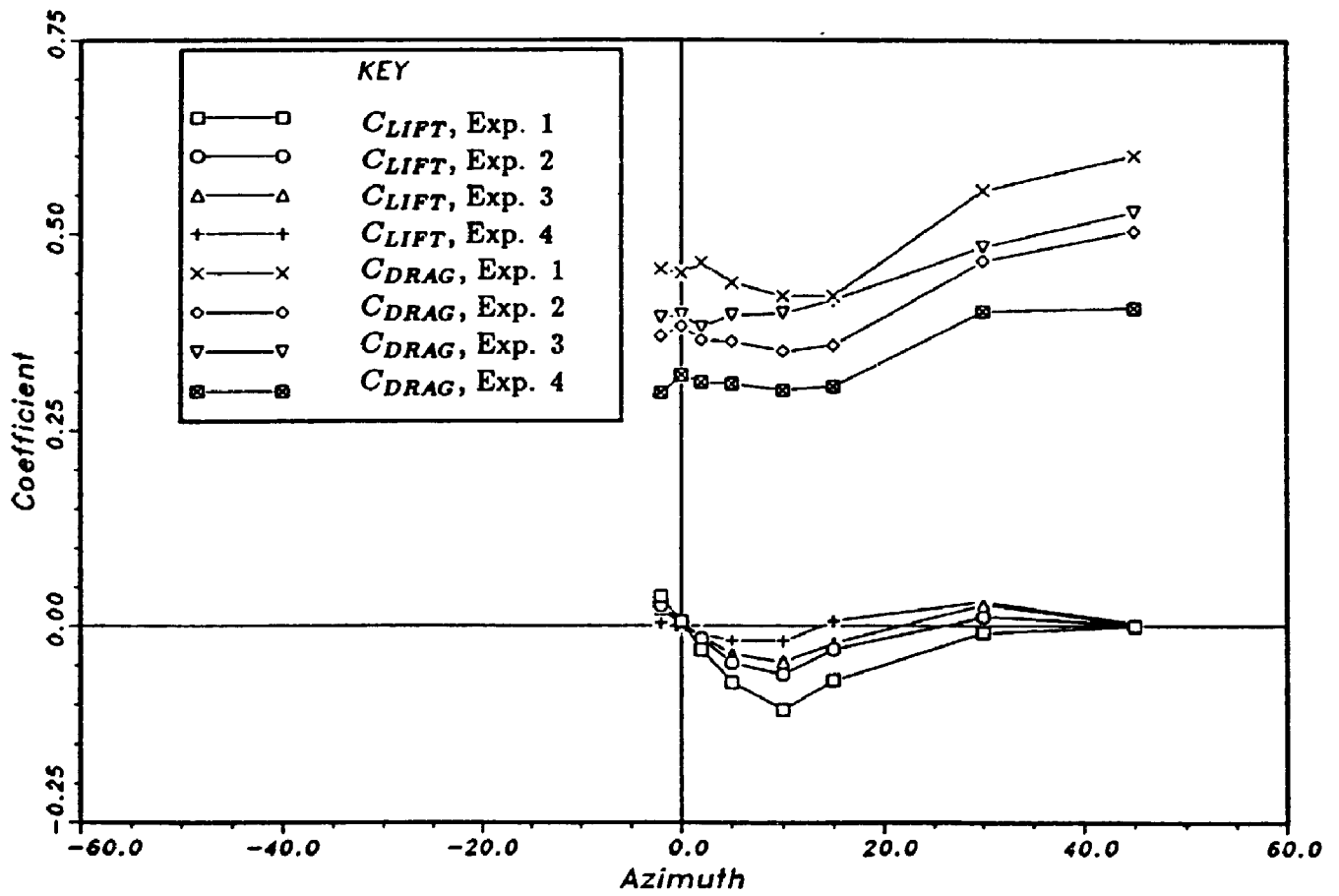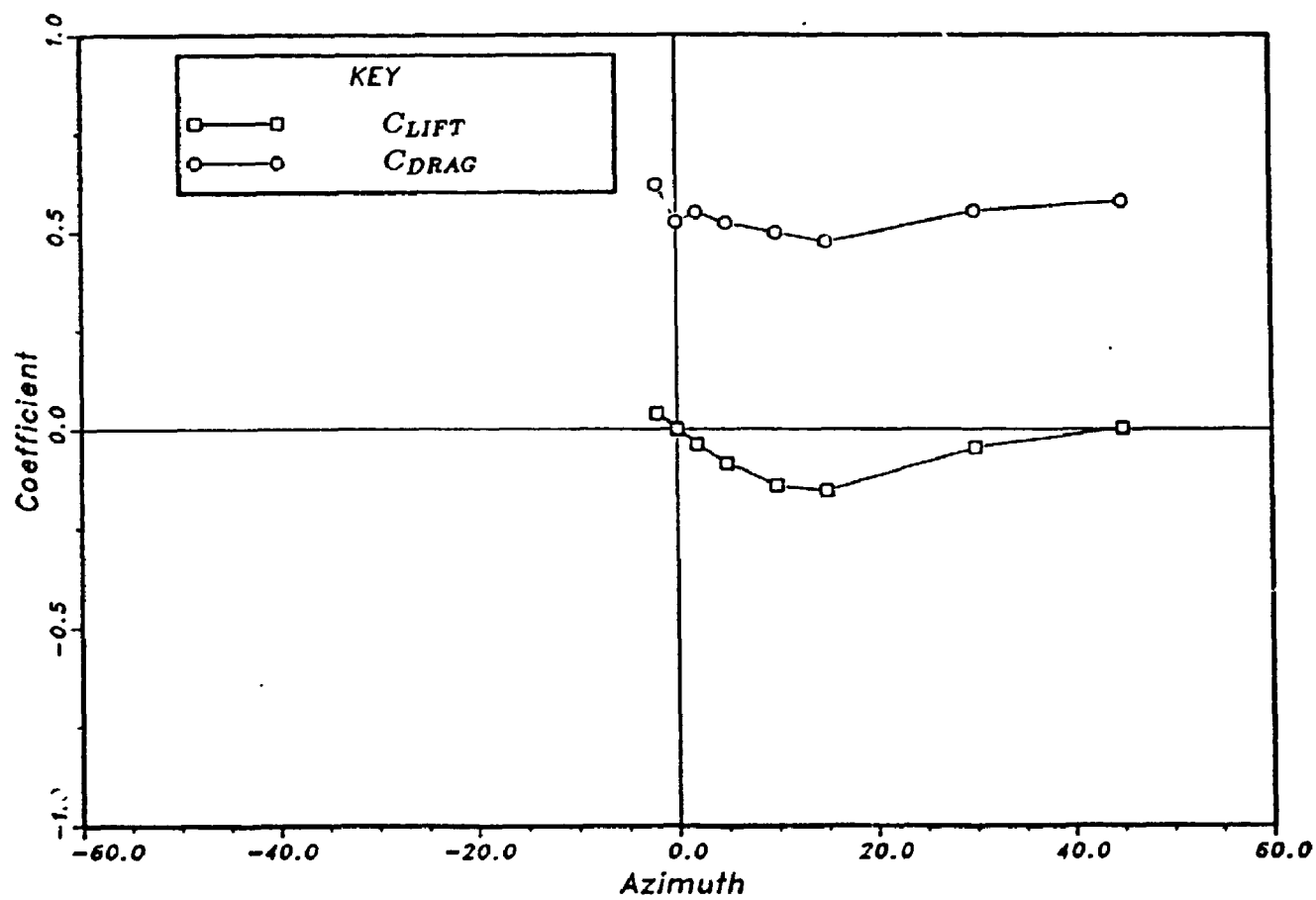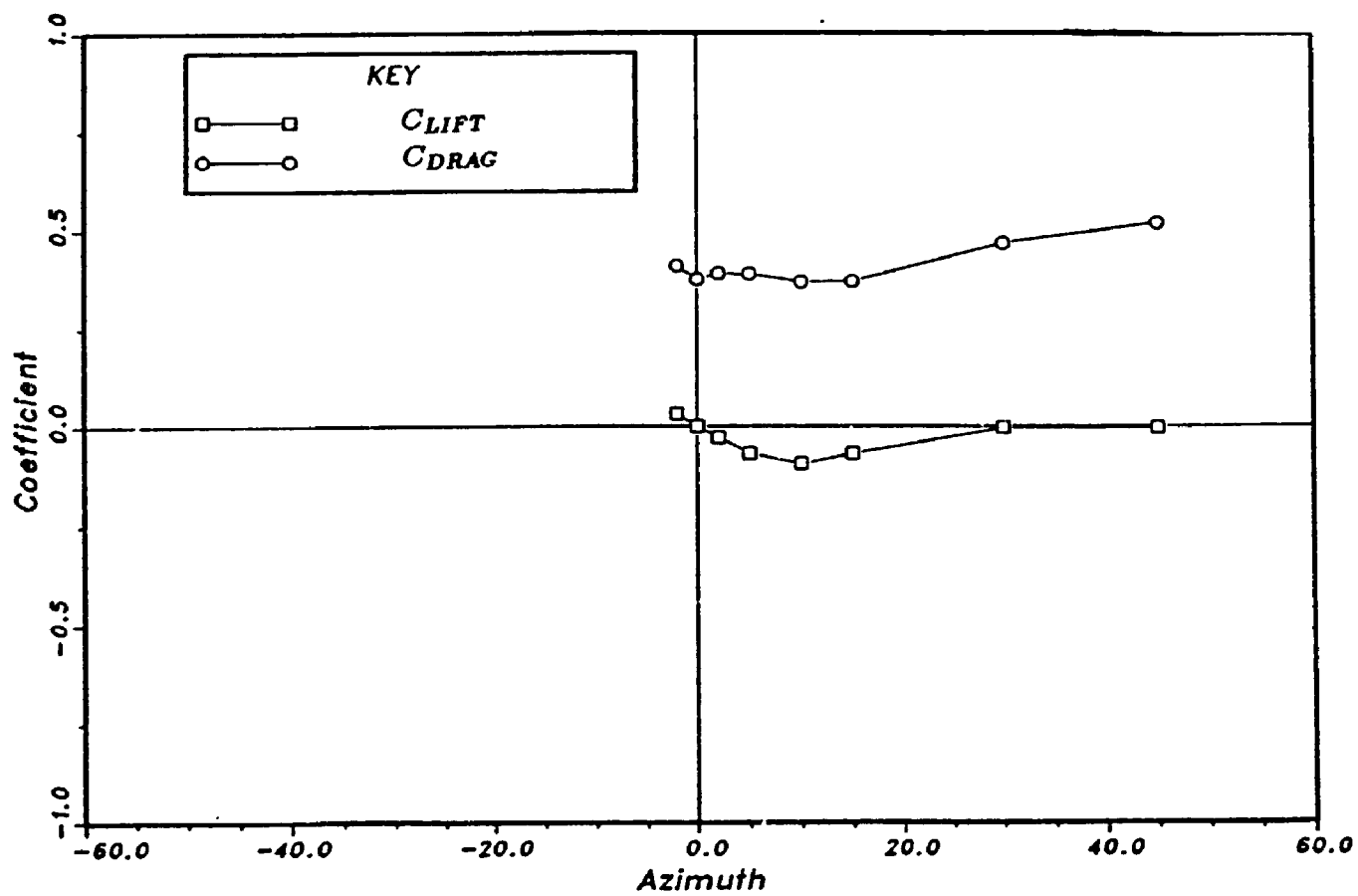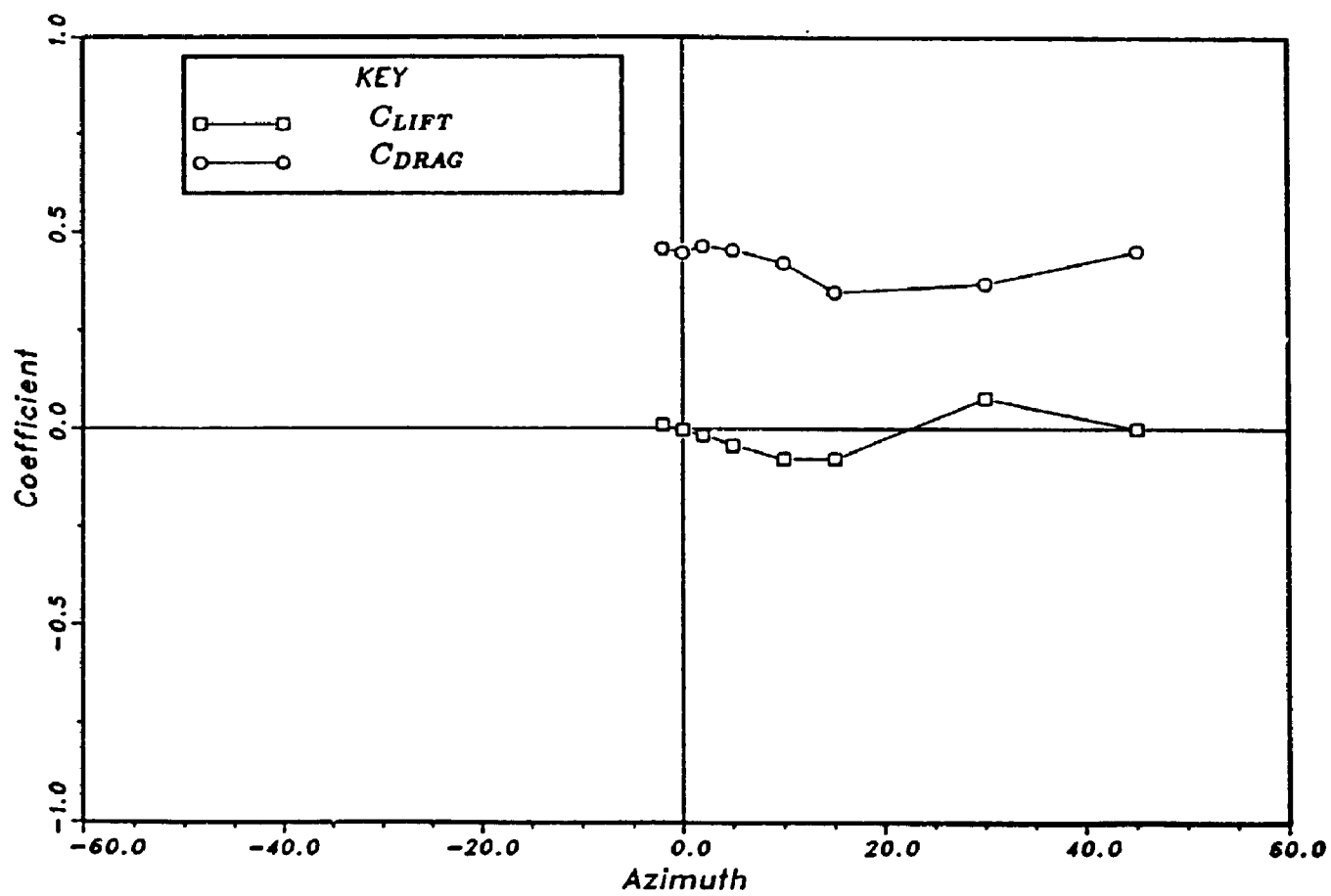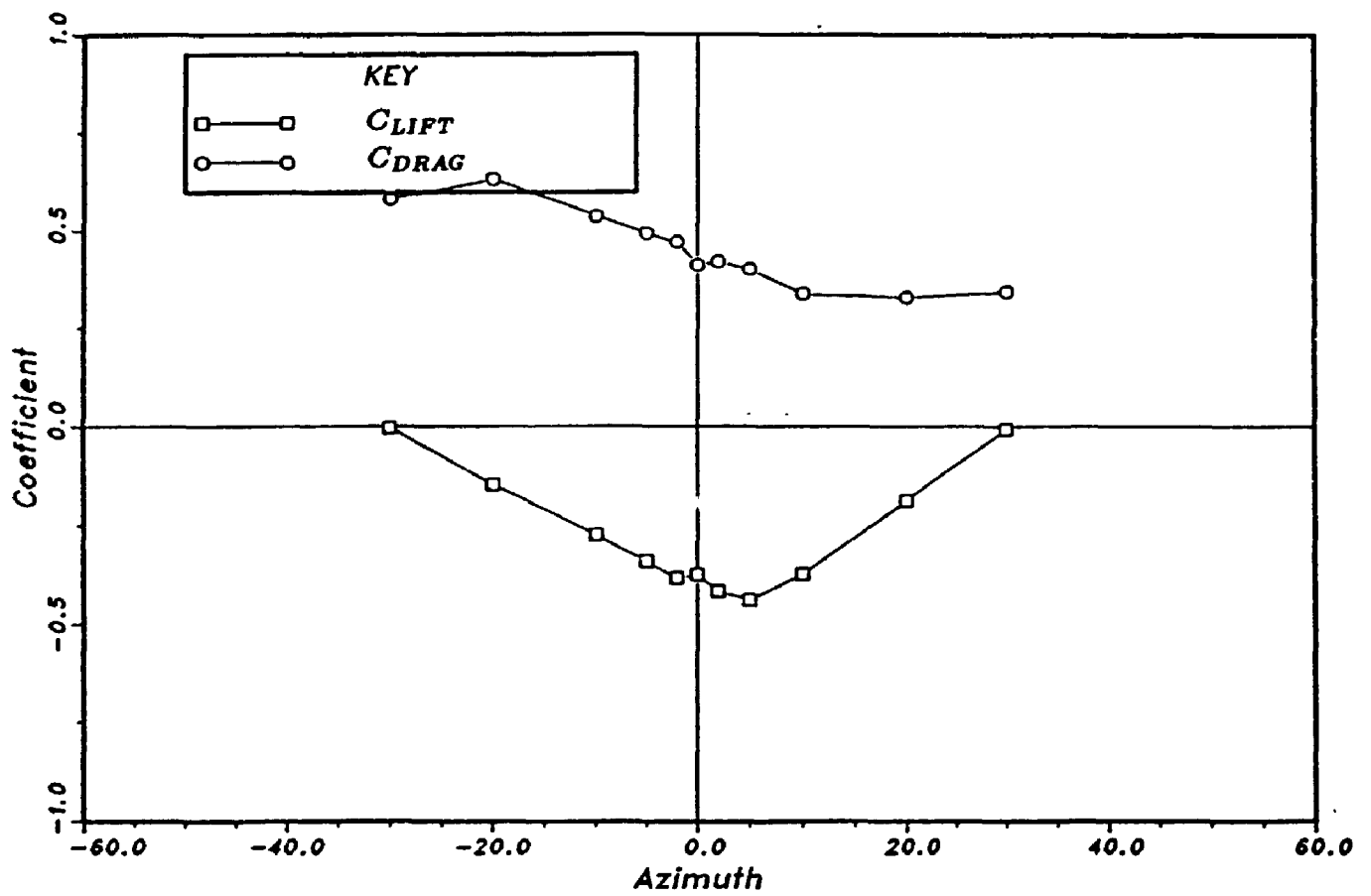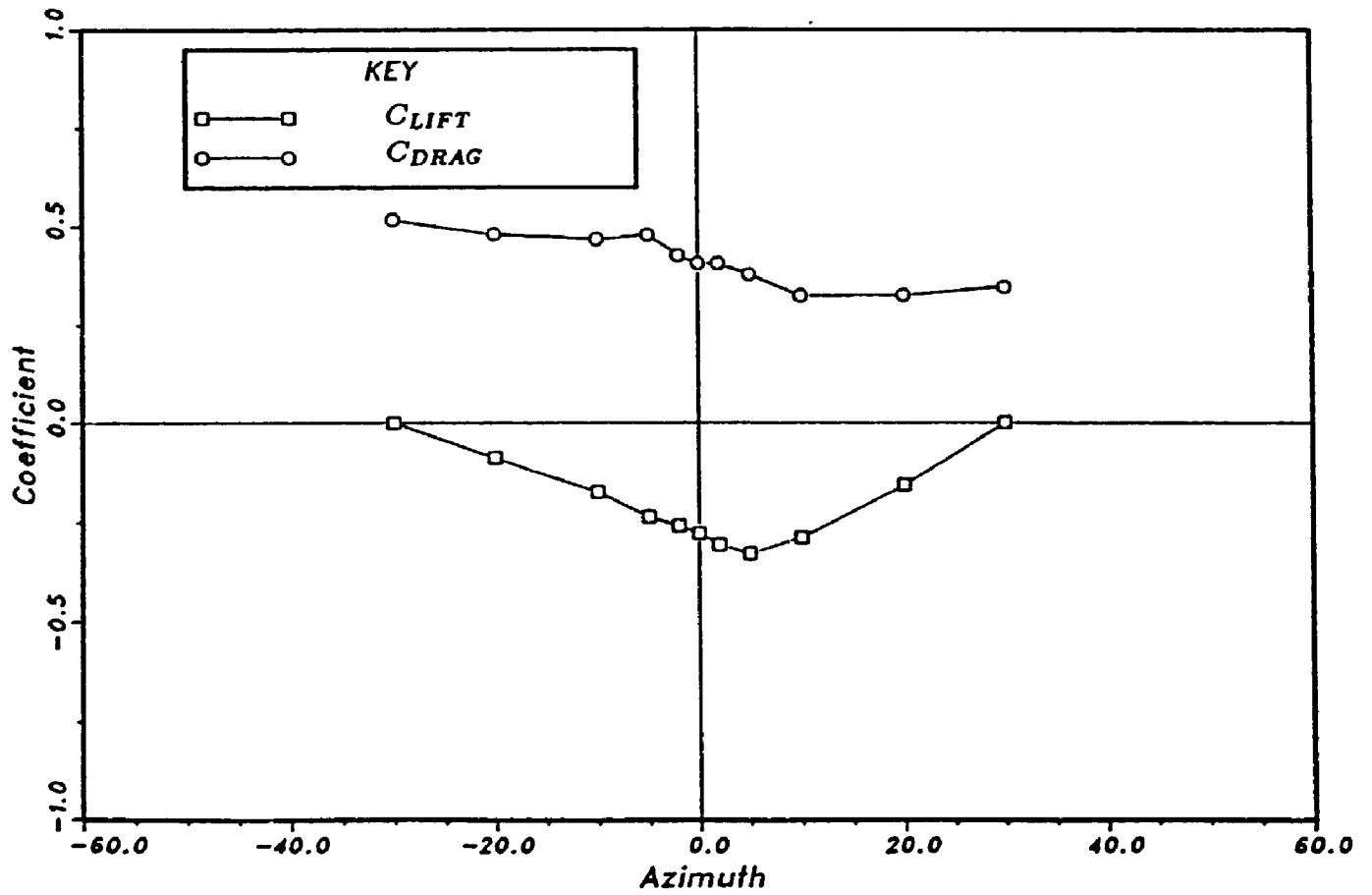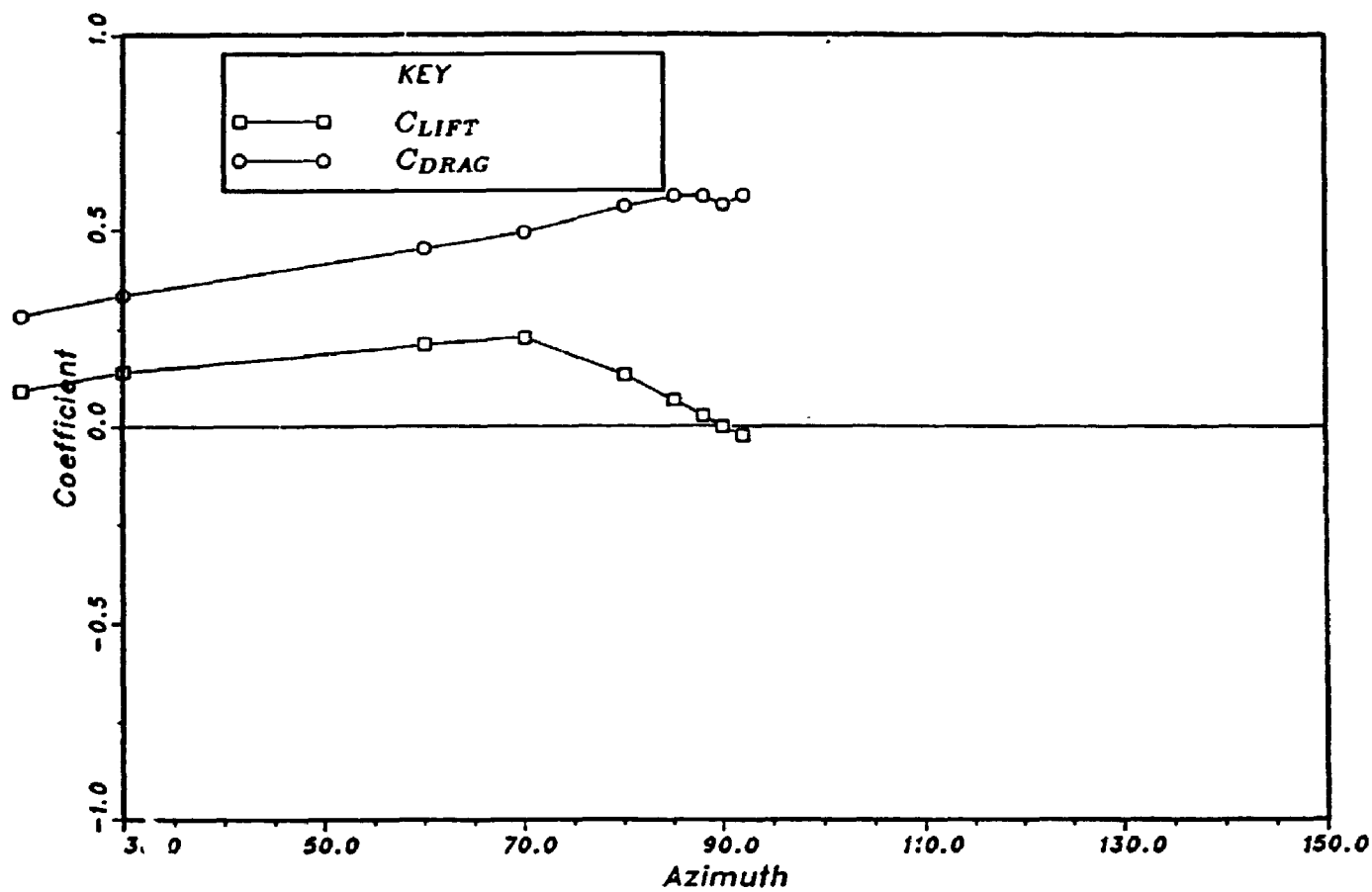
Figure F.15: Moment Coefficients, Shape I, Aspect 13.3, Exposure 2

References

[1] R.I. Basu and B.J. Vickery. Across-wind vibrations of structures of circular cross-section. part II. development of a mathematical model for full scale application. *Journal of Wind Engineering and Industrial Aerodynamics*, 12:75–97, 1983.

[2] P.W. Bearman, I.S. Gartshore, D.J. Maull, and G.V. Parkinson. Experiments on flow-induced vibration of a square-section cylinder. *Journal of Fluids and Structures*, 1:19–34, 19. 7.

[3] P.W. Bearman and S.C. Luo. Investigation of the aerodynamic instability of a square-section cylinder by forced oscillation. *Journal of Fluids and Structures*, 2:161–176, 1988.

[4] P.W. Bearman and E.D. Obasaju. An experimental study of pressure fluctuations on fixed and oscillating square-section cylinders. *Journal of Fluid Mechanics*, 119:297–321, 1982.

[5] H. Bénard. Formation de centres de giration á l'arrieére d'un obstacle en mouvement. *Comptes Tendues Acad. Sci. Paris*, 147:839–842, 1908.

[6] J.S. Bendat and A.G. Piersol. *Random Data: Analysis and Measurement Procedures*. Wiley-Interscience, John Wiley & Sons, 2nd edition, 1971.

[7] K.Y.R. Billah. *A Study of Vortex-Induced Vibration*. PhD thesis, Princeton University, 1989.

[8] G. Birkhoff. Formation of vortex streets. *Journal of Applied Physics*, 24:209–231, 1953.

[9] R.E.D. Bishop and A.Y. Hassan. The lift and drag forces on a circular cylinder oscillating in a flowing fluid. In *Proceedings of the Royal Society, Serial A*, pages 51–75, 1964.

[10] R. D. Blevins. Part I: vibration of structures induced by fluid flow. In C.M. Harris, editor, *Shock Vibration*, McGraw-Hill Book Company, 1988.

[11] D. W. Boggs and J. A. Peterka. Aerodynamic tests of tall buildings. *Journal of Engineering Mechanics*, 115(3):618–635, March 1989.

[12] N.N. Bogoliubov and Y.A. Mitropolsky. *Asymptotic Methods in the Theory of Non-Linear Oscillations*. Hindustan Publishing Corp., Delhi, India, 1961. translated from Russian.

[13] D.N. Bouclin. Hydroelastic oscillations of square cyiinders MASc. Thesis, University of British Columbia, 1977.

[14] E.O. Brigham. *The Fast Fourier Transform*. Englewood Cliffs, N.J.: Prentice-Hall, 1974.

[15] Ray W. Clough and Joseph Penzien. *Dynamics of Structures*. McGraw-Hill Book Company, 1975.

[16] R.M. Corless. *Mathematical Modelling of the Combined Effects of Vortex-Induced Vibration and Galloping*. PhD thesis, University of British Columbia, 1986.

[17] A. G. Davenport. The influence of turbulence on th aeroelastic responses of structures to wind. Symposium on Practical Experience with Flow Induced Vibrations, Karlsruhe, 1979.

[18] A. G. Davenport. The prediction of the response of structures to gusty wind. In *Safety of Structures under Dynamic Loading*, pages 257–284, TAPIR, Trondheim, Norway, 1978.

[19] A. G. Davenport. The response of slender line-like structures to gusty wind. In *Institute of Civil Engineers*, pages 389–408, 1962.

[20] A. G. Davenport, N. Isyumov, and T. Miyata. The experimental determination of the response of suspension bridges to turbulent wind. In *Proceedings of the Third International Conference on Wind Effects on Buildings and Structures, Tokyo*, pages 1207–1219, 1971.

[21] A. G. Davenport and T. Tschanz. The response of tall buildings to wind: effects of wind direction and the direct measurement of dynamic force. In *Proceedings of the Fourth U.S. National Conference on Wind Engineering Research*, pages 205–223, July 1981.

[22] A.G. Davenport. Probability, reliability, statistics, and safety. In *The Application of Wind Engineering Principles to the Design of Structures*, chapter 2, ZACE Services Ltd., Lausanne, Switzerland, 1987. A Short Course Taught by A.G. Davenport. B.J. Vickery, and J.A. Hertig.

[23] A.G. Davenport, N. Isyumov, J.P.C. King, M. Novak, D. Surry, and B J. Vickery. Blwt II: the design and performance of a new boundary layer wind tunnel. In K. C. Mehta and R. A. Dillingham, editors, *Proceedings of the Fifth U.S. National Conference on Wind Engineering*, Wind Engineering Research Council, Inc., Texas Tech University, Lubbock, Texas, November 1985.

[24] A.G. Davenport and J.P.C. King. *A Study of Wind Effects for the Sunshine Skyway Bridge, Tampa, Florida — Concrete Alternative.* Technical Report BLWT-SS24-82, Boundary Layer Wind Tunnel Laboratory, University of Western Ontario, 1982.

[25] A.G. Davenport and J.P.C. King. *A Study of Wind Effects for the Sunshine Skyway Bridge, Tampa, Florida — Steel Alternative.* Technical Report BLWT-

SS24-82, Boundary Layer Wind Tunnel Laboratory, University of Western Ontario, 1982.

[26] A.G. Davenport and M. Novak. Part II: vibration of structures induced by wind. In C.M. Harris, editor, *Shock Vibration*, McGraw-Hill Book Company, 1988.

[27] A.G. Davenport, P.J. Vickery, N. Isyumov, and M. Mikitiuk. *A Study of Wind Action on the Tel Aviv Transmission Tower, Tel Aviv, Israel.* Technical Report BLWT-SS19-84, Boundary Layer Wind Tunnel Laboratory, University of Western Ontario, 1984.

[28] J. P. Den Hartog. *Mechanical Vibrations.* McGraw-Hill Book Co., Inc., New York, 4th edition, 1956.

[29] J.P. Den Hartog. Transmission line vibration due to sleet. *Transactions of the American Institute of Electrical Engineering*, 51:1074, 1932.

[30] E.H. Dowell. Non-linear oscillator models in bluff body aeroelasticity. *Journal of Sound & Vibration*, 75(2):251–264, 1981.

[31] R. Dutton and N. Isyumov. Reduction of tall building motion by aerodynamic treatments. In A. Kareem, editor, *Proceedings of the Sixth U.S. National Conference on Wind Engineering*, Wind Engineering Research Council, Inc., University of Houston, Houston, Texas, March 1989.

[32] R. J. Dutton. An aerodynamic modification to reduce vortex shedding from a square prism. MESc. Tnesis, University of Western Ontario, 1989.

[33] L.E. Ericsson. Karman vortex shedding: friend or foe of the structural dynamicist? *Journal of Aircraft*, 23(8):621–628, August 1986.

[34] C.C. Feng. The measurement of vortex-induced effects in a flow past stationary and oscillating circular and d-section cylinders. MASc. Thesis, University of British Columbia, 1968.

[35] N. Ferguson and G.V. Parkinson. Surface and wake flow phenomena of the vortex-excited oscillation of a circular cylinder. *ASME Journal of Engg. Indus.*, 831–838, 1967.

[36] R.T. Hartlen and I.G. Currie. Lift-oscillator model of vortex-induced vibration. *Journal of the Engineering Mechanics Division, ASCE.* 96(EM5):577–591, October 1970. Proceedings Paper 7606.

[37] J. A. Hertig. Wind tunnel simulation, part I: on similarity rules for fluid modeling. In *The Application of Wind Engineering Principles to the Design of Structures*, chapter 7, ZACE Services Ltd., Lausanne, Switzerland, 1987. A Short Course Taught by A.G. Davenport, B.J. Vickery. and J.A. Hertig.

[38] E.L. Hixson. Mechanical impedance. In C.M. Harris. editor, *Shock Vibration*, McGra-v-Hill Book Company, 1988.

[39] J.C.R. Hunt. Recent developments and trends: physical and mathematical modelling. In J.E. Cermak, editor, *Wind Engineering, Proceeding· of the Fifth International Conference, Fort Collins, Colorado*, pages 957–964, Pergamon Press, July 1979.

[40] N. Isyumov. The aeroelastic modelling of tall buildings. In *International Workshop on Wind Tunnel Modelling Criteria and Techniques*, National Bureau of Standards, Gaithersburg, Maryland, April 1982.

[41] N. Isyumov and A. G. Davenport. *Wind Tunnel Study for the CN Tower.* Technical Report BLWT-SS01-74, Boundary Layer Wind Tunnel Laboratory, University of Western Ontario, 1974.

[42] N. Isyumov, A. Steckley, N. Amin, and H. Fatehi. Effects of the orientation of the principal axis of stiffness on the dynamic response of a slender square building. In A. Kareem, editor, *Proceedings of the Sixth U.S. National Conference on Wind Engineering*, Wind Engineering Research Council, Inc., University of Houston, Houston. Texas, March 1989.

[43] N. Isyumov, A. Steckley, and A. G. Davenport. *A Study of Wind Effects for the St. Chrischona Tower, Basel, Switzerland.* Technical Report BLWT-SS34-82, Boundary Layer Wind Tunnel Laboratory, University of Western Ontario, 1982.

[44] W.D. Iwan and R.D. Blevins. A model for vortex-induced oscillations of structures. *Journal of Applied Mechanics*, 41:581–586, 1974.

[45] D.W. Jordon and P. Smith. *Nonlinear Ordinary Differential Equations.* Claredon Press, Oxford. 1977.

[46] S.C. Luo. *A Forced Vibration Study of the Aerodynamic Instability of a Square Section Cylinder.* PhD thesis, Department of Aeronautics, Imperial College, 1985.

[47] N. Minorsky. *Nonlinear Oscillations.* R.E. Krieger, Florida, 1962.

[48] M. Novak. Aeroelastic galloping of prismatic bodies. *Journal of the Engineering Mechanics Division, ASCE*, 96(EM1):115–142, February 1969. Proceedings Paper 6394.

[49] M. Novak. Galloping oscillations of prismatic structures. *Journal of the Engineering Mechanics Division, ASCE*, 98(EM1):27–46, February 1972. Proceedings Paper 8692.

[50] M. Novak and A. G. Davenport. Aeroelastic instability of prisms in turbulent flow. *Journal of the Engineering Mechanics Division, ASCE*, 96(EM1):17-37, February 1970. Proceedings Paper 7076.

[51] M. Novak, A.G. Davenport, and H. Tanaka. Vibration of towers due to galloping of iced cables. *Journal of the Engineering Mechanics Division, ASCE*, 104(EM2):457-473, April 1978. Proceedings Paper 13706.

[52] M. Novak and H. Tanaka. Effect of turbulence on galloping instability. *Journal of the Engineering Mechanics Division, ASCE*, 100(EM1):27-47, February 1974. Proceedings Paper 10338.

[53] E.D. Obasaju. Forced-vibration study of the aeroelastic instability of a square section cylinder near vortex resonance. *Journal of Wind Engineering and Industrial Aerodynamics*, 12:313-327, 1983.

[54] E.D. Obasaju. *Pressure Fluctuations on Stationary and Oscillating Square Section Cylinders.* PhD thesis, Department of Aeronautics, Imperial College, 1977.

[55] Y. Otsuki, K. Washizu, H. Tomizawa, and A. Ohya. A note on the aeroelastic instability of a prismatic bar with square section. *Journal of Sound & Vibration*, 34(2):233-248, 1074.

[56] Y. Otsuki, K. Washizu, H. Tomizawa, A. Ohya, and K. Fujii. Experiments on the aeroelastic instability of prismatic bars with rectangular sections. In *Proceedings of the Third International Conference on Wind Effects on Buildings and Structures, Tokyo*, pages 891-898, 1971.

[57] G. V. Parkinson. Nonlinear oscillator modelling of flow-induced vibration. In E. Naudascher and D. Rockwell, editors, *Practical Experiences with Flow-Induced Vibrations*, pages 786-797, Springer-Verlag, Berlin, 1980.

[58] G. V. Parkinson and J. D. Smith. The square prism as an aeroelastic non-linear oscillator. *Quart. Journal of Mechanics and Applied Math.*, XVII(2), 1964.

[59] G.V. Parkinson. Mathematical models of flow-induced vibrations. In E. Naudascher, editor, *Flow-Induced Structural Vibrations*, pages 81–127, Springer-Verlag, Berlin, 1974.

[60] G.V. Parkinson and N.P.H. Brooks. On the aeroelastic instability of bluff cylinders. *Journal of Applied Mechanics*, 252–258, 1961. Transactions of the ASME.

[61] G.V. Parkinson and P.P. Sullivan. Galloping response of towers. *Journal of Industrial Aerodynamics*. 4:253–260, 1979.

[62] W.H. Press, B.P. Flannery, S.A. Teukolsky, and W.T. Vetterling *Numerical Recipes: The Art of Scientific Computing*. Cambridge University Press, 1987.

[63] L.R. Rabiner and B. Gold. *Theory and Application of Digital Signal Processing*. Englewood Cliffs, N.J.: Prentice-Hall, 1975.

[64] M. Rosales. A novel technique for measuring spatially averaged pressure:its development and application to low-rise buildings. MESc. Thesis, University of Western Ontario, 1983.

[65] T.V. Santosham. Force measurements on bluff cylinders and aeroelastic galloping of a rectangular cylinder. MASc. Thesis, University of British Columbia, 1966.

[66] T. Sarpkaya. Vortex-induced oscillations: a selective review. *Jornal of Applied Mechanics*, 46:241–256, 1979.

[67] J. W. Saunders and W. H. Melbourne. Tall rectangular building response to cross-wind excitation. In *Proceedings of the Fourth International Conference*

on Wind Effects on Buildings and Structures, pages 369–379, Cambridge University Press, London, Heathrow, U.K., 1975.

[68] C. Scruton. On the wind-excited oscillations of stacks, towers, and masts. In *Symposium on Wind Effects on Buildings and Structures, Teddington, England*, 1963.

[69] E. Simiu and R.H. Scanlan. *Wind Effects on Structures.* Wiley-Interscience, John Wiley & Sons, 2nd edition, 1986.

[70] R. A. Skop and R. A. Griffin. On a theory for the vortex-excited oscillations of flexible cylindrical structures. *Journal of Sound & Vibration*, 41(3):263–274, 1975.

[71] J.D. Smith. An experimental study of the aeroelastic instability of rectangular cylinders. MASc. Thesis, University of British Columbia, 1962.

[72] T. Staubli. Calculation of the vibration of an elastically mounted cylinder using experimental data from forced oscillation. *ASME Journal of Fluid Engineering*, 105:225–229, 1983.

[73] A. Steckley. Evaluation of a new area load measurement technique. BASc. Thesis, University of Toronto, 1984.

[74] A. Steckley. *Forced Oscillation Experiments on a Pressure Model of a Square Prism.* Technical Report BLWT-SS17-89, Boundary Layer Wind Tunnel Laboratory, University of Western Ontario, 1989.

[75] A. Steckley and N. Isyumov. *An Investigation of Wind Effects for the McMahon Stadium Expansion Project, Calgary, Alberta.* Technical Report BLWT-SS3-87, Boundary Layer Wind Tunnel Laboratory, University of Western Ontario, 1987.

[76] A. Steckley and N. Isyumov. *Wind Tunnel Model Study of Wind Loads for the Husky Stadium Expansion Project, Calgary, Alberta.* Technical Report BLWT-SS3-87, Boundary Layer Wind Tunnel Laboratory, University of Western Ontario, 1987.

[77] A. Steckley, G. R. Lythe, N. Isyumov, and A. G. Davenport. *Aeroelastic Wind Tunnel Model Study of the New Bank of China Building, Hong Kong.* Technical Report BLWT-SS37-85, Boundary Layer Wind Tunnel Laboratory, University of Western Ontario, 1985.

[78] A. Steckley and B.J. Vickery. *Design Data for Tall Chimneys of Various Cross-Sectional Shape.* Technical Report BLWT-SS18-89, Boundary Layer Wind Tunnel Laboratory, University of Western Ontario, 1989.

[79] V. Strouhal. Über eine besondere art der tonerregung. *Ann. Phys.*, V:216–250, 1878.

[80] P.P. Sullivan. Aeroelastic galloping of tall strucutures in simulated winds. MASc. Thesis, University of British Columbia, 1977.

[81] David Surry and Gary R. Lythe. The atlantic palace - part II: the application of wind tunnel/force balance techniques. In Gary C. Hart and Richard B. Nelson, editors, *Dynamic Response of Structures*, pages 357–364, Engineering Mechanics Division of the American Society of Civil Engineers, ASCE, UCLA, California, March 1980.

[82] A. Tallin and B. Ellingwood. Analysis of torsional moments on tall buildings. *Journal of Wind Engineering and Industrial Aerodynamics*, 18:191–195, 1985.

[83] Y. Taniike. Unsteady aeroelastic base moments on a high-rise building. In A H-S Ang., editor, *Structural Design Analysis and Testing, Structures Congress '89, San Francisco*, pages 599–608, ASCE, ASCE, May 1989.

[84] T. Tschanz. *The Base Balance Measurement Technique and Applications to Dynamic Wind Loading of Structures.* PhD thesis, University of Western Ontario, 1983. BLWT-5-83.

[85] B.J. Vickery and R.I. Basu. Across-wind vibrations of structures of circular cross-section. part I. development of a mathematical model for two-dimensional conditions. *Journal of Wind Engineering and Industrial Aerodynamics*, 12:49–73, 1983.

[86] B.J. Vickery and A. Steckley. Wind loads on chimneys with non-circular cross-sections. In *Proceedings for the Sixth International Chimney Conference, CICIND, Brighton, England*, 1988.

[87] P. J. Vickery and T. A. Reinhold. Second generation force balance. In A. Kareem, editor, *Proceedings of the Sixth U.S. National Conference on Wind Engineering*, Wind Engineering Research Council, Inc., University of Houston, Houston, Texas, March 1989.

[88] P. J. Vickery, A. Steckley, N. Isyumov, and B. J. Vickery. The effect of mode shape on the wind-induced response of tall buildings. In K. C. Mehta and R. A. Dillingham, editors, *Proceedings of the Fifth U.S. National Conference on Wind Engineering*, Wind Engineering Research Council, Inc., Texas Tech University, Lubbock, Texas, November 1985.

[89] T. von Karman. Über den Mechanismus des Widerstands, den ein bewegter Korper in einer Flüssigkeit erfährt. *Göttinger Nachrichten, Math. Phys. Kl.*, 547–556, 1912.

[90] T. von Karman. Über den Mechanismus des Widerstands, hartogden ein bewegter Korper in einer Flüssigkeit erfährt. *Göttinger Nachrichten, Math. Phys. Kl.*, 509–517, 1911.

[91] M. A. Wawzonek. Aeroelastic behavior of square section prisms in uniform flow. MASc. Thesis, University of British Columbia, 1977.

[92] R. E. Whitbread. The measurement of non-steady wind forces on small-scale building models. In *Proceedings of the Fourth International Conference on Wind Effects on Buildings and Structures*, pages 567–574, Cambridge University Press, London, Heathrow, U.K., 1975.